UNIVERSIDAD POLITÉCNICA DE MADRID
Escuela Técnica Superior de Ingenieros de Telecomunicación

Development of Spatially-fed Reflective Planar Devices with Enhanced Capabilities for Emerging mm-Wave Wireless Networks based on Liquid Crystal Technology

DOCTORAL THESIS

Submitted for the degree of Doctor by:

Roberto Guirado Liñan
Master's Degree in Telecommunications Engineering

Madrid, 2025

UNIVERSIDAD POLITÉCNICA DE MADRID
Escuela Técnica Superior de Ingenieros de Telecomunicación

Doctoral Degree in Communication Technologies and Systems

Development of Spatially-fed Reflective Planar Devices with Enhanced Capabilities for Emerging mm-Wave Wireless Networks based on Liquid Crystal Technology

DOCTORAL THESIS

Submitted for the degree of Doctor by:

Roberto Guirado Liñan
Master's Degree in Telecommunications Engineering

Under the supervision of:
Dr. Gerardo Pérez Palomino
Dr. Eduardo Carrasco Yépez

Madrid, 2025

Title: Development of Spatially-fed Reflective Planar Devices with Enhanced Capabilities for Emerging mm-Wave Wireless Networks based on Liquid Crystal Technology
Author: Roberto Guirado Liñan
Doctoral Programme: Communication Technologies and Systems

Thesis Supervision:

Dr. Gerardo Pérez Palomino, Profesor Contratado Doctor, Universidad Politécnica de Madrid

Dr. Eduardo Carrasco Yépez, Profesor Contratado Doctor, Universidad Politécnica de Madrid

External Reviewers:

Thesis Defense Committee:

Thesis Defense Date:

The project that gave rise to these results received the support of a fellowship from ”la Caixa” Foundation (ID 100010434). The fellowship code is LCF/BQ/DR21/11880029. The work was also partially funded by the Spanish Ministry of Science and Innovation within the project ENHANCE-5G under Grant PID2020-114172RB-C22/AEI/10.13039/501100011033.

I would like to dedicate this work to all the teachers and professors I have had during my academic career

Acknowledgement

En primer lugar, me gustaría dar las gracias a mis supervisores por la implicación en este trabajo. Creo que desarrollar una tesis doctoral y a su vez mantener una buena salud mental solo es posible si uno sabe que puede confiar plenamente en quienes le dirigen. Eduardo, gracias por tu soporte y paciencia, y por ser un referente como investigador y como profesor. Gerardo, tu experiencia y tus consejos, y cada una de las discusiones técnicas que hemos tenido, me han hecho aprender mucho más allá de lo que hubiera esperado. Gracias a los dos por hacer que estos años fueran mentalmente apasionantes, y por transmitirme vuestros valores personales y científicos. Me siento muy afortunado de haberos tenido como supervisores.

El día a día en la universidad no hubiera sido lo mismo sin los compañeros del Grupo de Electromagnetismo Aplicado, y concretamente sin los habitantes del gueto. Quiero agradecer especialmente a Pablo, quien más que un compañero ya es un gran amigo, su increíble predisposición para ayudarme o para discutir ideas desinteresadamente aunque no fuese el mejor momento para ello. Y a los demás habitantes: Enrique, Rebo, Bárbara, Juan Diego, por hacerlo todo más entretenido.

No puedo estar más agradecido con los miembros del Grupo de Fotónica Aplicada, que me han acogido como uno más y me han puesto todas las facilidades para poder fabricar dispositivos en la cámara limpia. A Xabi, por tu inigualable experiencia en cristales líquidos y sus procesos de fabricación. A Morten, por tus sabios consejos y tus ideas. A Lolo, por ser el mejor maestro de cámara limpia que pude tener. A Ricardo, por estar siempre dispuesto a echar una mano. Y a Javi, Byron, y compañía, por ser grandes personas y compañeros.

I would also like to be grateful to the Huawei colleagues from Munich, who taught me their understanding about liquid crystals from other points of view, and overall helped me have a great time in Germany. Thank you Grischa, Markus, Veysel, Sumanyu and Ivan.

També vull donar les gràcies a qui espero que siguin els meus amics per tota la vida. Ja sigui volent o sense, heu estat de gran ajuda des de Barcelona: Dani, José, Marc, Arnau, Pol i Montes. Finalment, als meus pares i a la meva germana, amb qui sempre puc comptar. I a l'Alba, la persona amb qui he compartit cada patiment i cada alegria, aquesta tesi també és teva.

Abstract

The work presented in this thesis results of an effort to improve the current capabilities and limitations of spatially-fed planar devices which are electronically reconfigurable by means of liquid crystal technology. Among the different devices that this encompasses, the focus is put on reflectarray antennas and reconfigurable intelligent surfaces, given their foreseeable usefulness in next-generation networks, which will rely on high-frequency bands.

Using liquid crystals is not the only possible way to achieve reconfigurability in these devices, since tunable surfaces based on diodes, MEMS, graphene, and other technologies have already been proposed. However, they present a set of advantages which make them unique, and that positions them as a promising alternative capable of overcoming most of the limitations that other technologies face. By means of an applied bias voltage to the liquid crystal, its anisotropic molecules rotate, which provides a change in the material permittivity. Amid other advantages, liquid crystals can operate at a wide frequency range, their manufacturing cost is low, and they provide continuous tunability. Notwithstanding, they are not free from issues, which makes them an immature technology yet. The research carried out in this work tries to shed light into these issues, and to propose and examine possible solutions.

One of these issues is the lack of unit cells exhibiting complex functionalities. In this work, a W-band reflectarray antenna based on liquid crystal which controls independent beams for orthogonal linear polarizations is designed, manufactured and measured in an anechoic chamber. The antenna provides 25dBi of gain and can scan both beams from 5º to 40º with a minimum SLL of 9dB.

Another existent limitation in liquid crystal devices operating below optical frequencies is the slow response time they exhibit, around several seconds, which comes from a thicker material cavity. During this thesis, the dynamics of the transient states of the mixtures upon changing external excitations are studied, and a model capable of predicting them is proposed. Then, three different methods to reduce such response times are proposed.

The first method consists of engineering the device biasing signals by predicting the instantaneous rotation of the molecules. The proposed approach is experimentally validated with measurements from a reflectarray antenna, achieving response time reductions up to 250X and 2X, in rising and decay transitions respectively. Unfortunately, the decay transition is the slowest and most limiting one, so another acceleration technique is desired.

The second method consists of utilizing a novel material, namely polymer network liquid crystal, instead of conventional liquid crystals. A mixture showing significant temporal reduction while providing enough dielectric tunability is proposed, and an effective anisotropic permittivity model is developed to facilitate designing structures containing it. A reflectarray cell based on polymer network liquid crystal is designed, manufactured and measured, showing decay times as low as 200ms. However, there is a trade-off between time reduction, required voltage levels and dielectric tunability, which limits its practical usefulness.

The third evaluated method consists of using dual-frequency liquid crystals, capable of fast switching both in rise and decay transitions if biasing waveforms of varying frequency are properly designed. Four of these mixtures are identified and used to manufacture periodical unit cells, which yield a measured response of 10ms in both rise and decay transitions if used together with the first method.

Finally, the suitability of liquid crystal to reconfigure an electrically large intelligent surface at 27 GHz, whose radiation can be electronically modified, is also tested. It is experimentally demonstrated that such device can improve the system-level metrics of demodulated signals by dynamically reconfiguring the beam.

Resumen

El trabajo presentado en esta tesis resulta de un esfuerzo para mejorar las capacidades y limitaciones actuales de dispositivos planares alimentados espacialmente y reconfigurables electrónicamente mediante cristal líquido. Entre los distintos dispositivos que esta nomenclatura engloba, se pone el foco en las antenas reflectarray y en las superficies inteligentes reconfigurables, dada su utilidad en redes de próxima generación, que usarán bandas de alta frecuencia.

El uso de cristales líquidos no es la única forma posible de lograr reconfiguración en estos dispositivos, pues se han propuesto superfícies sintonizables basadas en diodos, MEMS, grafeno y otras tecnologías. Sin embargo, estos presentan un conjunto de ventajas que los hace únicos, y que los hace capaces de superar la mayoría de las limitaciones de otras tecnologías. Mediante un voltaje aplicado al cristal líquido, sus moléculas anisótropas pueden ser rotadas, lo que proporciona un cambio en la permitividad del material. Entre otras ventajas, los cristales líquidos pueden funcionar en un amplio rango de frecuencias, su coste de fabricación es bajo y ofrecen sintonización continua. No obstante, no están exentos de problemas, lo que los convierte en una tecnología aún inmadura. Este trabajo trata de identificar estos problemas, así como de examinar posibles soluciones.

Uno de estos problemas es la falta de celdas que proporcionen funcionalidades complejas. En este trabajo se diseña, fabrica y mide en cámara anecoica una antena reflectarray de banda W basada en cristal líquido que controla independientemente haces de polarizaciones lineales ortogonales. La antena proporciona 25dBi de ganancia y puede escanear ambos haces entre 5º y 40º con un SLL mínimo de 9dB.

Otra limitación existente en los dispositivos de cristal líquido que operan por debajo de frecuencias ópticas es su tiempo de respuesta, de varios segundos, debido al grosor de la cavidad de cristal líquido. En esta tesis se estudia la dinámica del material al cambiar el voltaje aplicado, y se propone un modelo capaz de predecirlos. Luego, se proponen tres métodos diferentes para reducir dichos tiempos.

El primer método consiste en diseñar las señales aplicadas al dispositivo, prediciendo la rotación instantánea de las moléculas. El método propuesto se valida experimentalmente con una antena reflectarray, consiguiendo reducciones de tiempos en transiciones ascendentes y descendentes de hasta 250X y 2X, respectivamente. Desafortunadamente, la transición descendente es la más limitante, por lo que se requiere otra técnica de aceleración.

El segundo método consiste en utilizar cristal líquido de redes poliméricas, en lugar de cristal líquido convencional. Se propone una mezcla que reduce significativamente los tiempos a la vez que proporciona suficiente sintonización, y se desarrolla un modelo de permitividad anisotrópica efectiva para facilitar el diseño de estructuras que la contengan. Se diseña, fabrica y mide una celda reflectarray basada en cristal líquido de redes poliméricas, consiguiendo tiempos de respuesta de hasta 200 ms. Sin embargo, existe un compromiso entre la reducción del tiempo, los niveles de tensión requeridos y la sintonización, lo que limita su utilidad.

El tercer método evaluado consiste en utilizar cristal líquido de frecuencia dual, capaz de

conmutar rápidamente tanto en las transiciones ascendentes como descendentes si se diseñan adecuadamente señales de control con frecuencia variable. Se identifican cuatro de estas mezclas, y se fabrican celdas periódicas con las que se obtiene una respuesta medida de 10 ms en ambas transiciones, si se utilizan junto con el primer método.

Por último, también se analiza el uso de cristal líquido para reconfigurar una superficie inteligente eléctricamente grande a 27 GHz, cuya radiación puede modificarse electrónicamente. Se demuestra experimentalmente que dicho dispositivo puede mejorar las métricas de señales demoduladas, mediante la reconfiguración del haz.

Table of Contents

List of Figures

List of Tables

Abbreviations and acronyms

3GPP	3rd Generation Partnership Project
AC	Alternating Current
ACA	Anisotropic Conductive Adhesive
AM	Active Matrix
AWG	Arbitrary Waveform Generator
CEMDATIC	Centro de materiales y dispositivos aplicados a las TIC
DFLC	Dual-Frequency Liquid Crystal
DC	Direct Current
DUT	Device Under Test
EVM	Error Vector Magnitude
ITO	Indium Tin Oxide
LC	Liquid Crystal
LCD	Liquid Crystal Display
PBCH	Physical Broadcast Channel
PNLC	Polymer Network Liquid Crystal
PSS	Primary Synchronization Signal
PWM	Pulse-Width-Modulation
RF	Radiofrequency
RM	Reactive Mesogen
RMS	Root mean square
SFPS	Spatially-Fed Planar Surface
SINR	Signal-to-Noise-plus-Interference Ratio
SR	Selection Ratio
SSS	Secondary Synchronization Signal

TRL	Thru-Reflect-Line
TRM	Thru-Reflect-Match
OD	Overdrive
UPM	Universidad Politécnica de Madrid
VNA	Vector Network Analyzer

Chapter 1

Introduction

The novel engineering challenges appearing in wireless communications are giving rise to unconventional solutions through the entire protocol stack to face them, including the physical layer. Recently, the use of Spatially-Fed Planar Surfaces (SFPS) is gaining attention to tackle some of these problems [1, 2].

For instance, with the space exploration entering to a new era, and the development of massive constellations of nanosatellites, the research is pushing towards the onboarding of planar antennas, known as reflectarray antennas, on them, and even making them unfoldable, reducing weight and costs as compared to traditional reflectors [3]. In terrestrial networks, the more and more densely populated areas, with unseen traffic demands, are starting to force network operators to deploy more and more cellular base stations to maximize their coverage. Besides, these environments are dynamic, for which beam adaptability could be very useful. As a consequence, planar reflective surfaces, known as reconfigurable intelligent surfaces (RIS), are being proposed as a way to improve the service quality while reducing such massive base station deployment [4].

Moreover, the incessant increase in capacity needs requires the pursuit of available bandwidth at the mm-wave bands, where higher propagation losses must be overcome with high-gain reconfigurable pattern antennas. However, achieving electronic reconfigurability at high-frequency bands remains as an open problem, with very few candidate technologies keeping the pace. Operating at these bands entails other problems too, such as greater sensitivity to steering angle deviations, thus requiring accurate electronic scanning capabilities.

The currently available tunability methods are mostly based on microwave reconfigurable circuits, and thus suffer from increasing the operating frequency, mainly in terms of losses or manufacturing difficulties. In the last decade, the research of alternatives in the realm of tunable materials has proliferated, being the Liquid Crystal (LC) one of the most significant candidates. Since LCs are engineered for the optical spectrum, their usage in the sub-THz bands does not represent a drastic technological challenge, and given its wide adoption in optic reconfigurable devices, the manufacturing is uncomplicated.

Nonetheless, there are still some aspects in which this technology has to be further developed, mainly the large switching times, biasing strategies, lack of advanced functionalities and losses. As a consequence, they are estimated to currently have a low technology readiness level, of 3-4. This work is focused on enhancing the current capabilities of LC-based SFPS such as reflectarray antennas and RIS, predominantly in terms of reducing switching times and introducing advanced functionalities, such as the independent control of two orthogonal polarizations.

1.1 Spatially-fed Planar Surfaces

Quasi-periodic planar structures have focused the attention of the research community for many years, due to their ability to manipulate electromagnetic waves when propagating through the free space. Among the different SFPS that one can imagine, reflectarray and transmitarray antennas, frequency selective surfaces and RIS are the ones centering most of the interest. These devices locally modulate the properties of the periodic structure (in each unit cell) according to the illumination conditions from the feed, to obtain a specific functionality.

Reflecting SFPS, such as reflectarray antennas and RIS, are devices capable of re-radiating the incoming electromagnetic waves, similar to parabolic reflectors, but with a specifically designed radiation pattern [5]. The physical operating principle of reflectarrays and RIS is fundamentally the same, but their feeding strategy, application scenarios and functions are quite different. These structures manipulate the radiation characteristics of the outgoing electromagnetic waves by introducing a specific reflection coefficient profile throughout their surface, tailored to the impinging wave. These reflection coefficients can be then designed so that the reflection has an arbitrary radiation pattern. Although it is possible to tune both the phase and amplitude of such reflection coefficients, they typically work by modifying only the phase, in order to avoid the introduction of losses to the reflected electric field, and to avoid using amplifiers.

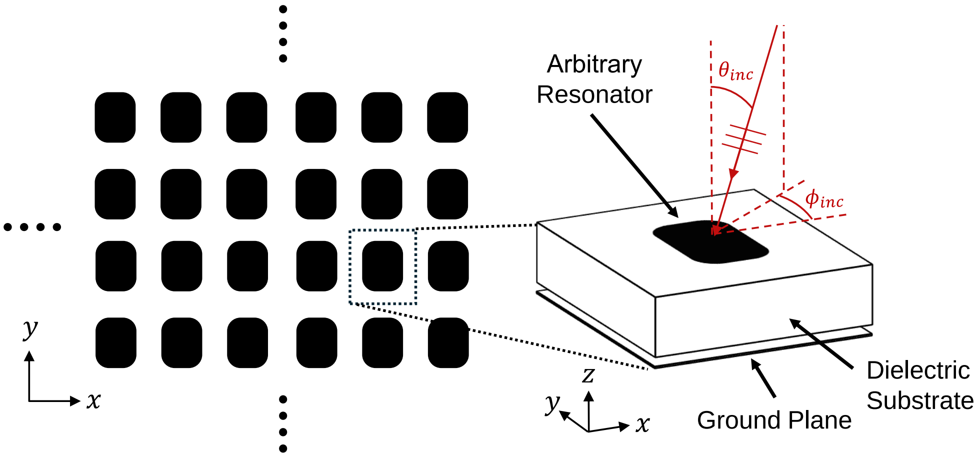

Figure 1.1: Periodic surface array (top view) with a detail of its unit cell (3D view).

Their structure is typically composed of a dielectric substrate containing a patterned metallization array, which is loaded on top of a metallic ground plane, as shown in Figure 1.1. This creates a resonant structure which introduces abrupt phase-shifts in the reflection coefficient of each element of the array. By controlling certain parameters through the surface, such as the dimensions of the metallizations or the materials, the phase-shifts of the reflection coefficients can be locally controlled. The patterned metallizations are usually quasi-periodic, dividing the surface in unit cells (see Figure 1.1) to facilitate their design and analysis, using the local periodicity approach [5]. The structure is said to be quasi-periodic because it is composed of an array of the same the unit cell, but with slight modifications to achieve the different phase shifts in each cell.

One of the most basic unit cells, for instance, consists of a rectangular patch metallization printed on top of a grounded low-loss dielectric. The different phase-shifts are obtained by slightly modifying the length of the patch, which shifts the reflection coefficient resonances in frequency, and consequently the phase can be chosen. However, there exist alternative structures, such as aperture-coupled patches [6], in which the phase-shifts are intended to be controlled by the length of a delay line to introduce a true time delay, or multi-layer structures [7], with several dielectric and sets of metallizations. The resonant element can also be varied, such as adding stubs to the rectangular patch, or designing different resonating shapes (circular patches, rings, cross-shaped, and so on [8]). In all these, an improvement of a certain property of the response is sought, such as wideband operation or polarization diversity.

Reflectarray antennas are fed from a close source, such as a horn antenna, and their purpose and applications are similar to reflector antenna. Figure 1.2(a) shows a reflectarray antenna and two unit cells, in which the dimensions of the resonant elements change to locally generate different phase shifts. The aperture illumination on these antennas is optimized so that most of the power coming from the feed can be re-radiated and the total efficiency is maximum, in a simlar way as in parabolic reflectors. On the contrary, the expected use-cases behind RIS devices (Figure 1.2(b)) are most of the times opportunistic, in the sense that they are thought to improve the coverage of certain areas by reflecting a very small portion of the radiated energy from the source, since in this case, the feed is located far-away (e.g. a cellular base station). Therefore, while the former must work with an spherical impinging wave, a quasi-planar impinging wave can be assumed for the latter.

The unit cells exhibit a different response depending on the angles of incidence of the impinging wave. In the case of an incident plane wave, these angles are defined as in Figure 1.1, where the elevation and azimuth incident angles are denoted by θ_{inc} and ϕ_{inc}, respectively. When the illumination comes from a close feed, this results in an incident spherical wave, by which each cell perceives a different incidence angle. However, a local plane wave of the corresponding incidence angle from the feed phase center can be assumed at the unit cell level, facilitating the local periodicity approach analysis. Related to this, the cell response is also polarization-dependent in general. Thus, the behaviour of a reflective unit cell is described by the following S-parameter matrices, depending on the used coordinate system.

$$\overline{\overline{S}} = \begin{pmatrix} S_{TETE} & S_{TETM} \\ S_{TMTE} & S_{TMTM} \end{pmatrix}, \quad or \quad \overline{\overline{S}} = \begin{pmatrix} S_{XX} & S_{XY} \\ S_{YX} & S_{YY} \end{pmatrix}, \tag{1.1}$$

where TE and TM denote the transversal electric and transversal magnetic components of the polarization, if the feed coordinate system is used, and X and Y denote the Cartesian components of the polarization considering the surface coordinate system. For a given unit cell, these matrices are dependent on the angle of incidence.

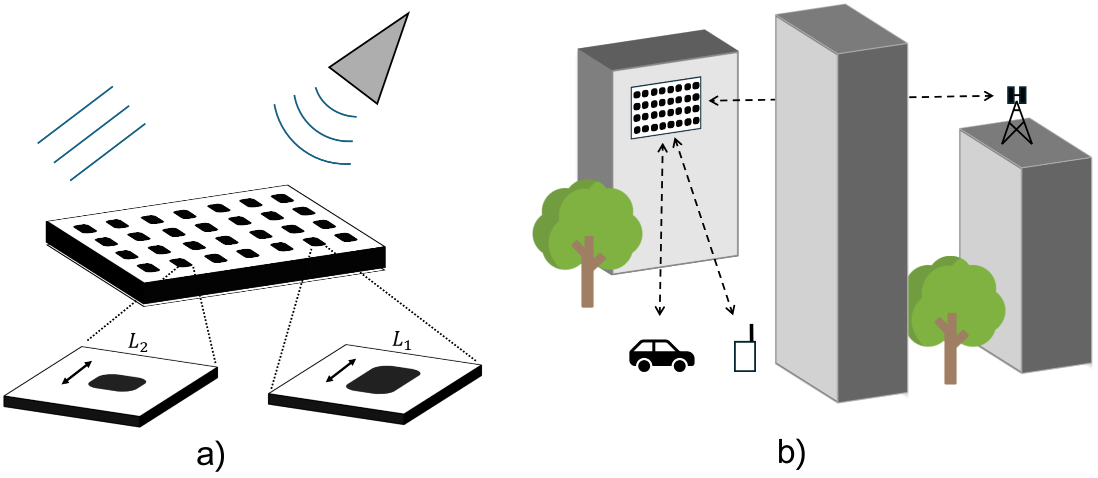

Figure 1.2: a) Reflectarray antenna b) RIS application example in an urban scenario.

1.1.1 Reconfigurable Spatially-fed Planar Surfaces

The previously introduced SFPS can be classified, depending on whether they can exhibit reconfigurability or not, as passive or active devices. Active SFPS can modify the phase shift that each cell introduce, generating different phase profiles of the reflected field and therefore obtaining different radiation patterns. On the contrary, in passive devices their functionality is fixed once they are designed, such as the reflectarray shown in Figure 1.2(a). In the literature, although in most of the cases RIS are presented as reconfigurable devices capable of modifying their re-radiation pattern, passive (static) devices are sometimes referred to as RIS as well [9].

Reconfigurable structures must, therefore, include in their cells some mechanism to vary the phase by means of a control signal. Among the technologies capable to provide reconfigurability to SFPS, varactor diodes, PIN diodes, microelectromechanical systems (MEMS) and other materials have been successfully implemented. However, in high-frequency applications, none of these provide a definitive solution yet.

Diode implementations are commonly found in reconfigurable reflectarray designs due to their fast switching speeds, although they are not practical above few dozens of GHz due to high losses. Different works rely on PIN diodes to implement single-bit reconfiguration [10, 11, 12], since multi-bit implementations require complex biasing networks and introduce great losses. In [13], a 1-bit reconfigurable surface based on PIN diodes that operates at 7.45 GHz is designed, with reduced switching times but introducing significant losses. In [14], a varactor diode implementation of a circular polarization reflectarray with 300º phase shift is introduced, which operates at dual band 11.3/14.7 GHz. Another example is the reflecting surface of [15], also based on fast-switching varactors, which shows 320º of phase shift at 23.5 GHz,

MEMS-based designs exhibit reduced losses as compared to diodes [16, 17]. Their energy consumption is low, although the number of required devices increases exponentially if a fine phase shift quantization is needed. Their integration is not trivial, and their practical usability is limited below the K-band. For instance, in [18], a fast reconfigurable reflectarray introducing losses of 0.5dB is presented, although its phase range is limited to 180º and it operates at 11.2 GHz. Moreover, reconfigurability by means of discrete elements does not scale with size, requiring a quadratic increase in the number of switching devices.

Mechanical reconfigurability through moving parts, actuators or magnetic forces has also been demonstrated. However, they present large energy consumption levels, low reliability and large switching times [19, 20].

The use of tunable materials in the development of high-frequency reconfigurable SFPS is at its infancy, with very few materials having demonstrated success in functioning prototypes. Some of them can exhibit a change in their electrical properties by means of an electrical excitation, while others require a temperature change. The use of graphene has been proposed as a reconfigurable material for reflectarrays [21, 22], due to its ability to operate at high frequencies and the possibility to miniaturize designs. However, its electromagnetic model is not completely developed, the required manufacturing processes are arduous, and empirical results are not available.

Ferroelectric-based designs [23, 24] work by tuning the dielectric constant of a ferroelectric film through a DC biasing voltage. They feature high-speed switching, low energy consumption and large tunability, although they require impractically high voltages above 300V and very few prototypes have been reported.

Vanadium dioxide (VO_2) is a phase-change material whose crystalline structure can be changed by means of temperature, transitioning between insulator and metallic phases. Given its heat exchange nature, its switching speed is low. Although theoretical work suggests its usefulness for SFPS design, practical results are still very limited [25, 26].

Designs based on liquid metal technology have also been proposed [27, 28]. These structures consist of a patterned cavity in which a liquid with metallic properties can be pumped in and out, in order to empty or fill certain regions with such material, showing reconfigurability. Although promising, they are lossy, its manufacturing is impractical, and their switching speeds are excessively slow.

Therefore, all the aforementioned technologies present important issues that hinder their practical implementation. LC-based SFPS, on the contrary, although not being a fully deployable technology yet, can overcome most of these issues.

LC presents tunability throughout most of the electromagnetic spectrum, from DC to the optical regime, being the only technology whose performance improves when increasing the frequency. This tunability is continuous, and contrary to other discrete elements, this comes naturally without extra effort in the design stage. The manufacturing procedures are well known and fully adopted in production lines, especially by the optics industry. This also translates into reduced costs. For instance, when fabricating a thousands-of-elements device, a single filling process suffices to provide all elements with reconfigurability at once, which is significantly easier than welding discrete elements one by one. The required voltages for a normal operation are in the range of 0-5V, which is compatible with most electronics, and their power consumption is negligible. However, there are still some challenges to overcome at mm-wave, such as significant losses and slow switching speed.

1.2 Liquid Crystals

The key of the thesis comes from the use of LC materials, which are employed as dielectrics in reflective SFPS to provide reconfigurability. A LC is in fact a state of matter which presents certain properties of liquids, such as fluidity, but also of crystalline solids, such as order. The main attribute of LC materials is their anisotropy, given by the shape of the nanometric molecules which constitute them.

Among the different kinds, thermotropic LCs are the most commonly used, since depending on the temperature their molecules show different phases [29, 30]:

- At high temperatures, beyond a threshold temperature called clearing point, they are isotropic and behave like liquids, showing no orientational or positional order. The clearing point typically lies between 80ºC-200ºC.
- Below the clearing point, the LC enters the nematic phase, at which the molecules show large orientational order (oriented in the same average direction) and short positional order (molecules can move with certain viscosity), being locally homogeneous. This phase is used in most of the applications of LC, from displays to antennas, and also in the devices of this thesis.
- Further reducing the temperature, the LC can first reach the smectic phases, in which the molecules arrange in layers, and finally the crystal solid phase where they show both large positional and orientational order.

Although there exist different kinds of anisotropic LC molecules (e.g. discotic), the most typical ones are calamitic, which are elongated like rods and therefore are uniaxial. This uniaxial nature makes such molecules highly anisotropic, which allows denoting two macroscopic permittivities: a parallel permittivity ($\epsilon_{||}$) for the long axis, and a perpendicular permittivity for the short axes ($\epsilon_{\perp}$), as can be observed in Figure 1.3(a). Through the thesis, these permittivities are treated as relative permittivities. The difference between $\epsilon_{||}$ and $\epsilon_{\perp}$ is defined as the dielectric anisotropy ($\Delta\varepsilon$), and is a key parameter of LCs as it is a measure of their tunability.

Because of the large orientational order, nematic LCs show a preferential orientation towards a certain direction. This direction is indicated by a unit vector, known as the LC director ($\hat{n}$), which is a macroscopic parameter that accounts for the average direction of the molecules in an infinitesimal volume. Besides, because of their anisotropy, the macroscopic permittivity of the material must be represented by a tensor, which will depend on such director. Therefore, given a fixed coordinate system, the permittivity is given by:

$$\overline{\overline{\varepsilon}}(\vec{r},t) = \varepsilon_{\perp}\overline{\overline{I}} + \Delta\varepsilon\overline{\overline{N}}(\vec{r},t), \tag{1.2}$$

where $\overline{\overline{I}}$ is the 3x3 identity matrix and $\overline{\overline{N}}(\vec{r},t) = \hat{n}(\vec{r},t) \otimes \hat{n}(\vec{r},t)$, being $\hat{n}(\vec{r},t)$ the LC director that defines the local orientation of the LC molecules at a certain point and time:

$$n_x = cos(\theta(\vec{r},t))cos(\phi(\vec{r},t)); \quad n_y = cos(\theta(\vec{r},t))sin(\phi(\vec{r},t)); \quad n_z = sin(\theta(\vec{r},t)); \tag{1.3}$$

where in the chosen coordinate system θ is the molecule rotation angle between the XY plane and the z axis, and ϕ is the rotation angle between the x and y axes.

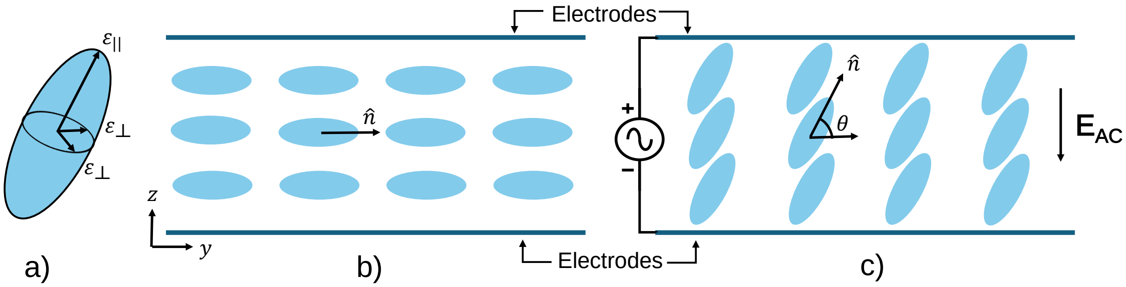

Figure 1.3: a) LC molecule and its permittivity representation. b) Sketch of a LC cavity in repose state. c) Sketch of a LC cavity with an applied intermediate AC electric field.

As a consequence of the short positional order that LCs show at the nematic phase, the molecules can be rotated by means of external excitations, such as an AC electric field (DC component should be avoided as it can have long-term damaging effects to the mixtures). As can be deduced from Equation (1.2), the rotation of the molecules will entail a change in such tensor, and therefore the volumetric permittivity of the cavity where the LC is enclosed will be modified. In Figure 1.3(b-c), a LC cavity in repose and with an external excitation are shown, where molecules can rotate in the YZ plane.

When an external AC electric field is applied through the LC, different deformation forces (twist, splay and bend) appear on the molecules, which cause their reorientation [29]. In the most common case of nematic LCs with positive dielectric anisotropy, the molecules will align parallelly to this AC electric field. Since the magnitude of the electric field can be analoguely controlled, the rotation and thus the permittivity can be continuously tuned. The specific impact of such forces into the molecules rotation, and how to predict it, will be described in detail in Chapter 3. However, in the extreme cases of a null electric field (OFF state) and of a strong electric field (ON state), the permittivity tensor can be easily predicted from Equation (1.2) as:

$$\overline{\overline{\varepsilon}}_{OFF} = \begin{pmatrix} \varepsilon_{\perp} & 0 & 0 \\ 0 & \varepsilon_{||} & 0 \\ 0 & 0 & \varepsilon_{\perp} \end{pmatrix}; \qquad \overline{\overline{\varepsilon}}_{ON} = \begin{pmatrix} \varepsilon_{\perp} & 0 & 0 \\ 0 & \varepsilon_{\perp} & 0 \\ 0 & 0 & \varepsilon_{||} \end{pmatrix}, \tag{1.4}$$

where the molecules are assumed to be oriented towards y in the repose state and their rotation plane is YZ, as in Figure 1.3. Different assumptions such as zero pretilt and homogeneous electric field biasing have been made. In Chapters 3 and 4, a more realistic model including pretilt and inhomogeneity will be considered.

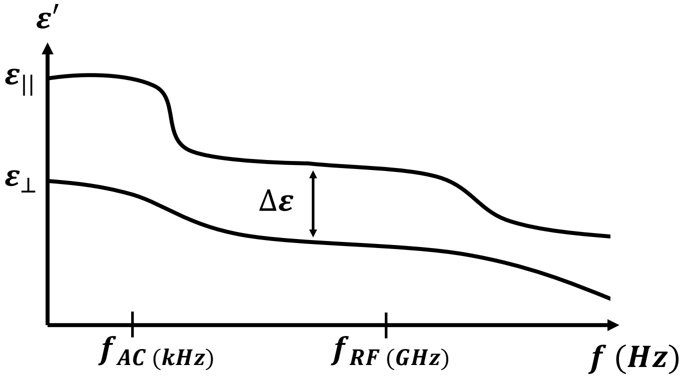

Figure 1.4: Dependence with frequency of the LC real permittivity component.

1.3 LC as a reconfigurable technology in SFPS

It is important to notice that $\epsilon_{||}$ and $\epsilon_{\perp}$, and therefore the dielectric anisotropy and the resulting permittivity tensors, are highly dependent on the frequency, as represented in Figure 1.4. While rotating the molecules could significantly alter the permittivity tensor for the electric fields at a certain spectrum region, it could at the same time be almost unnoticeable at another range of frequencies.

Because of the great tunability of LC in optics, their usage is widespread in devices such as Liquid Crystal Displays (LCD) [31], Spatial Light Modulators (SLM) [32] or Augmented Reality/Virtual Reality (AR/VR) glasses [33]. In these devices, the dielectric anisotropy (or birefringence, as known in optics) of commercial LC is significantly large, and several 2π cycles of phase shifts can be achieved by simply transmitting light through the mixture and properly biasing it, without the need of resonators. In such cases, the phase shifts come from the large differences in optical paths ($\Delta\phi = 2\pi \cdot d \cdot (\sqrt{\varepsilon_{||}} - \sqrt{\varepsilon_{\perp}})/\lambda_0$), which are attainable with physically thin ($h_{LC} = 5 - 20\mu m$), but electrically enormous ($10 - 30\lambda$) LC cavities.

In mm-wave frequencies, common values of LC dielectric anisotropy are $\Delta\varepsilon = 0.8 - 1.2$. Therefore, obtaining full 2π cycles by a simple material transmission would require millimetre-thick cavities, which are not practical in terms of cost, manufacturing or biasing, leading to enormous response times. As a consequence, similarly to passive SFPS, resonant elements providing abrupt phase shifts are used. In this case, the varying metric along the surface, by which different phase shifts are introduced, is not the physical dimension of the resonant element but the dielectric permittivity tensor, which in the end tunes the electrical lengths as well.

The physical structure of a LC-based SFPS and its unit cells (or pixels) is shown in Figure 1.5, where the angle of incidence (elevation) of the cells is shown. The structure resembles the passive SFPS ones, but with important modifications. Firstly, the dielectric substrate, homogeneous, isotropic and low-loss in passive SFPS, is substituted by a lossy and highly

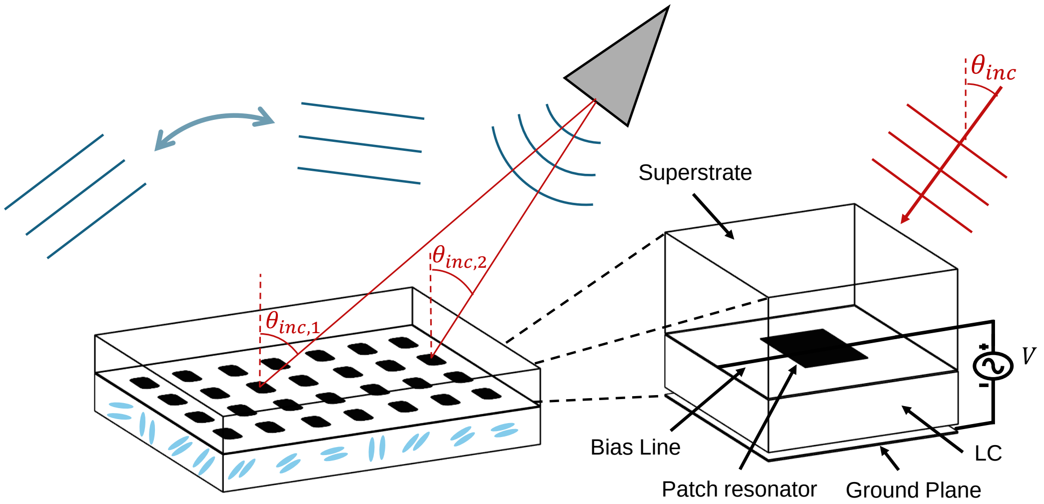

Figure 1.5: Sketch of a LC-based reconfigurable reflectarray antenna and its unit cell detail. The impinging spherical wave from the feed can be considered a locally plane wave at the unit cell level.

inhomogeneous and anisotropic LC cavity. As already mentioned, the thickness of this cavity is electrically thin ($\lambda/20 - \lambda/100$), which leads to the existence of non-evanescent higher-order modes. This cavity is reconfigurable, which requires synthesizing the correct voltages for the desired phase-shifts. Secondly, the resonator elements play an important role both in RF, as they as responsible for the reflection coefficient phase-shifts, and in AC, as they act as electrode for the biasing voltage that rotates the LC molecules. In order to do so, conductive biasing lines are connected to the resonators (as in Figure 1.5), which must be designed such that its impact to the RF response is minimum. Thirdly, the resonators must be printed below a superstrate, in order for the LC cavity to be formed and properly enclosed. This adds a top dielectric interface which was not present in passive SFPS. Fourthly, the use of multi-layer cells, which can provide great benefits as shown in passive SFPS, is discouraged in LC-based designs, as the manufacturing complexity vastly increases. Instead, additional resonators in the same layer can be used.

For the LC director to have a preferential alignment direction in the repose state, a surface treatment in both the enclosing cavity plates is needed, known as surface anchoring. Since the LC is aligned with the AC electric field direction, in the absence of it the mixture could relax in any direction, not being controllable and, in average, behaving as isotropic, which would diminish the effective tunability of the devices. There are different methods for achieving this alignment, such as rubbing and photoalignment. Rubbing consists on creating micro-grooves at the surfaces with a specific direction. To do so, a material sensitive to this rubbing, such as certain types of polyimide or nylon, must be first deposited on the surfaces, and then, the grooves are physically created by means of a velvet cloth. Alternatively, photoalignment consists on producing these grooves by illuminating a photosensitive material with polarized light, which is considered a better solution as it is a cleaner, more repeatable, and re-writable procedure. The anchoring forces of physical rubbing are generally stronger than in the photoalignment case, which results in smaller response time but higher inhomogeneity. Although the planar alignment, where the LC in both surfaces are aligned parallelly, is the most commonly used in LC-based SFPS, different applications can require more exotic alignments such as twisted nematic (perpendicular alignment in each surface), or vertical alignment (LC is aligned orthogonally to the surface plane), or even to align different regions of the surfaces in different ways. In Figure 1.6, an example of a LC cavity containing an alignment layer is shown, where its influence in the molecules rotation can be observed for two states. These surface anchorings pre-define a boundary condition for the LC molecule rotation, which not only promotes a specific orientation at the repose state ($\vec{n_0}$) but also influences their rotation at the excited states, creating inhomogeneous molecule rotation throughout the volume ($\vec{n_0}, \vec{n_1}$, and $\vec{n}(z)$ in general). This requires an inhomogeneous permittivity tensor description $\overline{\overline{\varepsilon}}(z)$, which even in the extreme cases slightly differ from those in Equation (1.4). This must be considered for an accurate model, as will be seen in the following chapters.

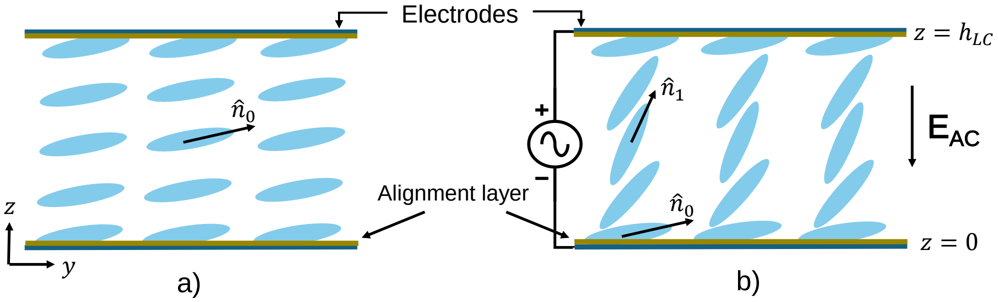

Figure 1.6: LC cavity with an alignment layer (planar alignment) in a) repose state b) applied AC electric field.

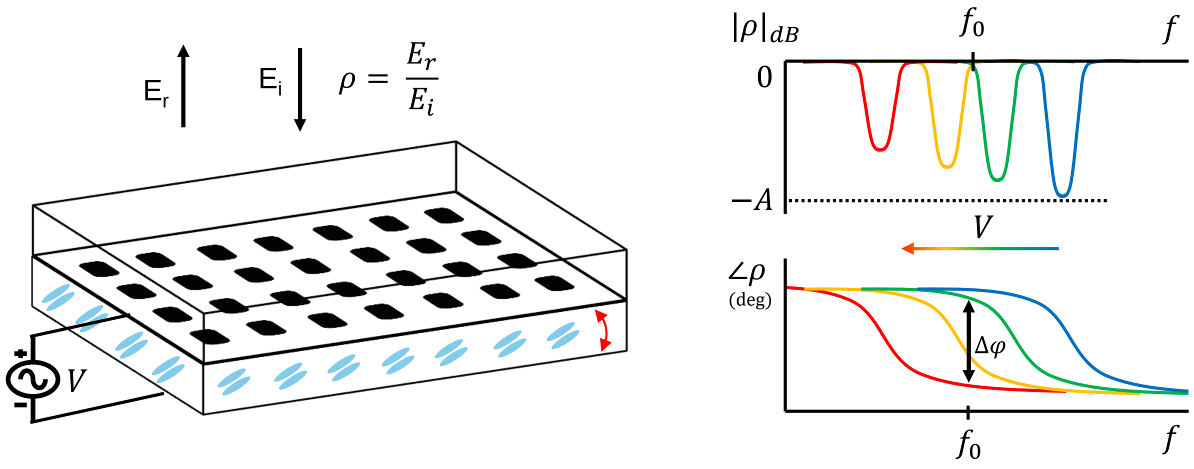

Figure 1.7: Tuning the reflection coefficient of an LC-based SFPS by means of a varying voltage V. The shifting of the resonances through the frequency spectrum makes the phase-shift introduced by the reflection coefficient at a certain frequency f_0 to vary.

The operation principle of the LC in reflecting SFPS is shown in Figure 1.7, where both the phase and amplitude of the electric field reflection coefficient (ρ, or S_{XX} or S_{YY} for one polarization) as a function of the frequency are shown for varying biasing voltages. The modification of the biasing voltage in the unit cell rotates the LC molecules, altering the volumetric permittivity in the cavity. This varies the electrical length of the resonator. In turn, this shifts the resonance, both in phase and amplitude. As can be observed, the amplitude loss is generally not negligible due to the significant LC complex permittivity. The phase range $\Delta\varphi$ (i.e. the difference between the maximum and minimum achievable phase shift at a certain frequency f_0) is also indicated. It is worth remarking that, apart from the frequency and the biasing voltage, given a fixed coordinate system the reflection coefficient is dependent on the angle of incidence and the electric field polarization. For all of the above, a careful characterization of the LC and its impact on the unit cell behaviour is essential for properly designing and controlling these devices.

Depending on how the biasing is organized through the surface, the device features different focusing and steering capabilities. On one hand, if 1D addressing is chosen, the biasing voltages can only be tuned along the rows or columns, but there is not the option of individually tuning each pixel. This leads to single plane focusing and steering. On the other hand, in the most generic case of 2D addressing, there is independent biasing for each unit cell, so arbitrary phase patterns can be generated. Whereas the former is much simpler to design and manufacture, the second provides more degrees of freedom in radiation pattern terms.

Although, as already mentioned, this technology is still under development, in the recent years is has focused the attention of researchers and significant advancements have been made. The first prototypes of LC reflectarray antennas were presented in 2006 [34, 35], and succeeding pioneer works showed its potential [36, 37]. These preliminary designs used LC mixtures that were designed with optical purposes, and as such, were not optimized for mm-wave operation. In [38], a LC reflectarray surface of 16 × 16 patch elements, showing high loss resonances around 77 GHz, was presented. Consequently, more advanced unit cells were developed. In [39], a 35 GHz multi-resonant cell showed wide bandwidth and large phase-shift capabilities. In those designs, the LC was modelled as an isotropic material of varying scalar permittivity, which is a simplistic strategy that does not contemplate all the mixture complexity. The extreme states were considered only, and a control of the device was complicated. In [40, 41], a more accurate technique for modelling the LC in those devices was introduced, which allowed accounting for the anisotropy and inhomogeneities in all states. This leads to a better control of the the introduced phases, and thus of the final radiation pattern [42]. In the last decade, different unit cells targeting an improved performance in terms of scan range [43] and losses [44, 45] were introduced. In this case, the lossy behaviour of the mixture usually forces complex metallizations or multi-layer designs [46].

Given the reduced complexity as compared to 2D scanning, most of these prototypes consist on 1D addressing, which enables structures with a larger number of resonant elements. A 2D scanning capability in a 10×10 reflectarray has been shown in [43] by means of hundred independent biasings, although this method does not scale for larger devices. Similarly, [47] presented a 9.55 GHz 12×12 LC reflectarray antenna capable of 2D beam-steer, which requires a complex biasing network and multi-layer structure. Other electrically small surfaces capable of steer a beam in both planes, in Ka-band, are shown in [48, 49, 50], although in some of those cases only 1D scan in two separate planes is shown.

Prior to the commencement of this thesis, the response time of those devices was very slow, in the order of seconds, due to the large LC cavity thickness and their viscous nature. Although not many works tackle it or even measure it, there have been recent efforts, in parallel to the development of this thesis, to improve it [51]. In [46], a thin LC layer is supposed to improve the dynamic reconfiguration of the device, but the specific times are not provided. Very recently [52], a 62 GHz delay lines RIS based on LC showed 72ms of switching time due to a 4.6μm-thick only LC cavity. Different bias structures, which significantly complicate an accurate LC model and control, have also been investigated. In [53], perpendicular alignments and stripped electrodes reduce the switching time with limited effectiveness. Similarly, in a recent work [54], a complex ground plane with alternating biasings tries to reduce the switching time below 200ms.

1.4 Challenges of Liquid Crystal mm-wave devices

Even though the usage of LC in mm-wave devices, and specifically in SFPS, is nowadays already present in the research community, there exist several challenges to be overcome.

1.4.1 Lack of advanced functionalities

Passive periodic surfaces, and specifically reflectarray antennas, feature numerous and diverse electromagnetic functionalities such as independent polarization manipulation, polarization conversion, dual-band operation, multiple beamforming, sophisticated radiation patterns other than pencil beams, or multi-panel configurations, among others. In contrast, the development of LC-based periodic surfaces is still immature and none of these functionalities are implemented, being the basic single-resonant unit cell the common choice. Moreover, as already mentioned, the small dielectric anisotropy that LCs show at mm-wave frequencies aggravate these difficulties.

1.4.2 Slow temporal response

The thick cavities required in LC-based mm-wave devices result in an excessively slow response time after a change of bias voltage. Although the reaction to an increasing electric field intensity is quick, the relaxation of the molecules when reducing such electric field intensity is very slow, with typical time responses in the order of the seconds or even minutes. However, final devices operating in practical scenarios might require to be reconfigured at the millisecond scale.

1.4.3 High losses

In the last decade, novel LC mixtures specifically designed for mm-wave devices have been developed, improving the previous ones mainly in loss and viscosity reduction. However, their losses are still too large compared to passive dielectric materials, which hinders a low-loss response in final devices. Therefore, new strategies to reduce them are essential to increase the efficiency of the final devices. These strategies can either be focused on the material, using new mixtures with lower $tan\delta$ or higher dielectric anisotropy, or be focused on improving cell designs.

1.4.4 Manufacturing and measuring difficulties at low frequencies

The LC manufacturing processes are well developed at the optical regime, where the industry readiness is at a very advanced level, even to obtain devices with millions of cells. However, the differences in requirements, application scenarios, manufacturing sizes, material properties, cavity thicknesses and other aspects make these processes increasingly hard to apply to devices operating at frequencies far from the optic ones, which usually rely on resonant structures. Similarly, measuring SFPS below the optic frequencies entails many issues that must be considered for obtaining reliable results, such as proper calibration and conscious sample illumination. At those bands, since the dimensions of the resonators are comparable to the operating wavelength, which does not occur in the optic devices, new phenomena appear.

1.4.5 2D addressing techniques

Periodic surfaces capable of focusing and steering in two orthogonal planes require a complete independent control of the reflection coefficient in each pixel. In the case of LC devices, this requires applying an independent voltage to each cell, also known as 2D addressing. Given the difficulty to do so, current works tackle this problem by either limiting the devices to 1D addressing, which restricts the focusing and steering to a single plane, or by implementing direct addressing, which consists on connecting each cell to a different voltage source and does not scale. However, the most elegant solution, and the only one known enabling the control of large arrays beyond 20×20 elements, would consist on adding a tailored active matrix controller capable of driving the pixel voltages by sweeping complex engineered signals in the interconnected rows and columns.

1.5 Objectives of the thesis

After having identified the previous challenges for the LC-based SFPS devices, this thesis will be focused on the following objectives:

1.5.1 Method for manufacturing and measuring LC-based SFPS

As already mentioned, the manufacturing of planar LC devices in optics has well standardized procedures. Some of this knowledge can be used to manufacture LC devices that operate at RF bands, although significant disparities appear. Given that throughout the thesis several prototypes are fabricated, a complete standardized manufacturing procedure is to be developed.

Additionally, defining a procedure for accurately measuring the manufactured samples under periodical environment is required. This must consider relevant aspects such as angles of incidence, illumination levels at the surface, calibration approach and the imperfect planar front.

1.5.2 Demonstrating improved switching times by means of different techniques

To overcome the slow response of the LC-based devices in RF, a strategy to develop fast switching devices must be found. As known from the LC industry in the optics regime, three possible solutions are identified, whose effectiveness at mm-waves was unknown:

- **Overdrive and Underdrive.** Consists of driving the LC with engineered signals in the time domain, which allows a specific control of the molecule rotation and its acceleration. A method to design the driving signals, and the corresponding temporal improvement must be developed and experimentally validated.
- **Polymer Network Liquid Crystal mixtures.** Certain LCs can be doped with other materials to achieve complex mixtures with specific features. In the case of Polymer Network Liquid Crystal (PNLC), a polymer introduces strong anchoring forces through the volume in the cavity, which can theoretically reduce the molecule relaxation times by orders of magnitude. Such mixtures must be characterized, and a prototype must be manufactured and measured to test the feasibility of such improvements.
- **Dual-Frequency Liquid Crystal.** Although generally nematic LC molecules align parallel to the cavity electric field, Dual-Frequency Liquid Crystal (DFLC) mixtures can be designed such that depending on the driving frequency their molecules align either parallel or perpendicular to such field. Therefore, this can enable the quick rotation of the molecules in either direction. To test the behaviour of such mixtures, different DFLC materials must be identified and tested in resonant unit cells at mm-wave frequencies.

1.5.3 Development of unit cells with reduced losses achieving sufficient phase range

The currently available mixtures lead to devices introducing high losses in the reflection coefficient. This phenomenon not only occurs because of the mixture loss, but also because of the resonant behaviour of the structures. To alleviate such issue, and given the lack materials with low ohmic loss or higher anisotropy, novel unit cells specifically targeting this problem must be investigated.

1.5.4 Accurate electromagnetic modelling of LC in novel devices

The appearance of novel LC devices demands for efficient electromagnetic models that allow accurate designs. For instance, unit cells capable of providing more than a single functionality, which can be developed with similar strategies as in passive unit cells but with the LC as dielectric, cannot be considered homogeneous in the plane parallel to the surface. However, a complete volumetric description is unreasonably complex. Therefore, an efficient strategy to model the mixture in such a way that the RF responses can be predicted with enough accuracy must be developed.

Similarly, when devices implementing strategies to reduce their response time are designed, such as overdrive, static LC models do not suffice. The static modelling of the LC in a cavity, which relates the quasi-static electric field intensity with the corresponding volumetric permittivity tensor, is known and can be well predicted, given that a complete information of the mixture and the structure is provided. However, the dynamics of electric field transitions and their impact on the responses of RF devices including resonant elements are not properly predicted.

1.5.5 Complete development of LC devices operating at mm-wave for enhanced networks

As a demonstration of a LC SFPS consisting of multi-functional unit cells, an electrically large W-band reflectarray antenna capable of independently steering the beam of two orthogonal polarizations by means of LC is to be investigated and experimentally tested. Since the purpose of the device is to prove the multi-functional unit cells and the aforementioned model, the prototype should be simple to manufacture and to drive.

The potential of LC-based SFPS to act as a RIS will be examined by proposing a specific device. An electronically reconfigurable unit cell will be designed and measured, and the impact of using a dynamic RIS panel based on those unit cells in a realistic system will be evaluated.

1.6 Thesis organization

This document is divided into seven chapters, including this introduction, which are detailed next.

Chapter 1 introduces the thesis and summarizes the key technologies involved. Important background information on LC mixtures and nomenclature is given, and a state-of-the-art on planar structures based on LC is carried out. Furthermore, the identified challenges of this technology, as well as the objectives of the thesis, are detailed.

In Chapter 2, first the manufacturing processes related to the devices developed in this work are exhaustively presented. Secondly, the free-space measurement procedures are explained, as well as their implication in the results. As a useful example, a LC mixture is experimentally characterized to obtain its permittivity tensor.

A novel dual-polarization LC antenna at W-band is introduced in Chapter 3. A detailed LC modeling in statics, required for this device, is described. The complete development is explained, from its design and manufacturing to its operation and measurement.

Chapter 4 focuses on the temporal response of mm-wave devices which are based on LC. First, a dynamic model for predicting transitions in conventional LC is presented. Then, the model is used to develop a specific biasing technique to reduce their response time. Two additional techniques, based on polymer network and dual frequency LCs, are also examined. The Chapter also includes an analysis on the dynamic impact of realistic biasing effects, and the far-field prediction of the transitions.

A RIS LC device is presented in Chapter 5. The design and manufacturing of the device is detailed, and a system-level measurement including standardized 5G signals is carried out.

Finally, Chapter 6 presents a discussion on the results of the thesis, and Chapter 7 concludes and provides future research lines, as well as a summary of the main publications derived from the thesis.

Chapter 2

Fabrication and characterization of periodic surfaces based on liquid crystals

2.1 Manufacturing of LC-based SFPS

The manufacturing of planar LC devices is not new. In fact, the optics industry has well standardized procedures to mass-produce LC devices, with completely automatized production lines, thus achieving very reduced costs. However, apart from obvious prototype differences between optics and RF, the wavelength disparity alone leads to divergent design choices with relevant impact in all the fabrication steps.

The LC mm-wave devices designed during the thesis have been manufactured at the clean room facilities of the CEMDATIC I+D Center at UPM. Given the microscale dimensions required for implementing the LC technology in the devices, any external agents, such as the presence of dust or changes in temperature or humidity, could alter significantly the fabrication processes of the devices. The clean room provides a controlled environment where these are minimized as much as possible.

Considering the standard LC reflective structure introduced in Figure 1.5, the two basic surfaces required to the start manufacturing processes are a backplane and a top plane.

The backplane behaves as device ground plane for the RF and as bottom electrode for the LC addressing, and can be continuous or segmented. If segmented, it can either be split in stripes (columns or rows) for 1D addressing, or even in individual cell pixels for 2D addressing. As such, it must be metallic, commonly made of gold or aluminium. Copper should be avoided since its direct contact with certain LC mixtures leads to long-term instabilities.

The top plane consists of a dielectric with protruding metallic resonant elements in RF, which will also act as top electrodes for the LC addressing. These can either be interconnected by stripes (if the backplane is continuous) or be short-circuited in all elements (if the segmentation is made in the backplane). The dielectric material is typically quartz or low-loss microwave substrates.

The assembly of the backplane and top plane, leaving a LC cavity in between, will form the LC-based SFPS structure. The cavity thickness is one of the most sensible parameters in the device design, with small deviations leading to large reflection coefficient variations. This is because of their extremely reduced electrical size ($\sim \lambda/20 - \lambda/100$) as compared to passive reflectarray designs, imposed by the LC technology. Therefore, the surfaces of the structures must be as flat as possible and with the smallest possible roughness. Moreover, the thickness should be as uniform as possible throughout the surface to keep the cell periodicity.

2.1.1 Sputtering

In order to metallize a flat dielectric substrate, such as glass or quartz, a physical vapor deposition technique called sputter deposition is used, as shown in Figure 2.1. Its operating principle is based on the use of an electrically excited gas plasma, such as argon, in a vacuum chamber. The accelerated gas ions eject the atoms from the metal source (target) and these are sputtered across the chamber, including the dielectric substrate. This allows a controlled thin film deposition.

The backplane and top plane of the fabricated LC antennas are based on gold, given its excellent compatibility with LC. Depending on the frequency of operation of the antenna, the thickness of the gold layer should be adjusted considering the penetration depth. In order for the gold to adhere to glass or quartz, a thin layer (15nm) of chromium or titanium is used. Depending on the conditions of the deposition (i.e., the substrate roughness, the vacuum levels, gas concentration, electrical excitation), the gold adhesion will be of higher or lower quality.

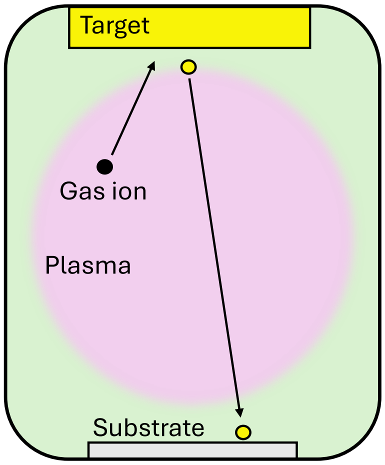

Figure 2.1: Schematic of the sputter deposition process.

2.1.2 Photolithography

A photolithography process through wet etching is followed to pattern the metallic planes, as summarized in Figure 2.2. The top electrode must be patterned with the designed resonant elements and connector pads, and segmentation could be required in the backplane. Alignment marks can also be included in the metallic patterning edges to facilitate the assembly.

A Microposit S1818 positive photoresist is spin-coated at 4000rpm for 30s and softbaked at 120°C for 60s (step 2 in the figure). In order to avoid undesired gold residues at the edges of the surfaces, the photoresist at the boundaries is removed with acetone. Then, it is exposed to UV using the desired pattern mask (step 3). Even though the optimal exposure time depends on the mask mounting material, as a reference, 20s exposure (5 mW/cm^2 at 400nm) is used when the substrate is glass. The photoresist is developed with RS Universal Developer for 45s (step 4) and finally the substrate is rinsed with deionized water.

The last step is to etch the metals with their specific reactants (step 5), such as a iodine solution for gold, and to remove the remaining photoresist with acetone (step 6).

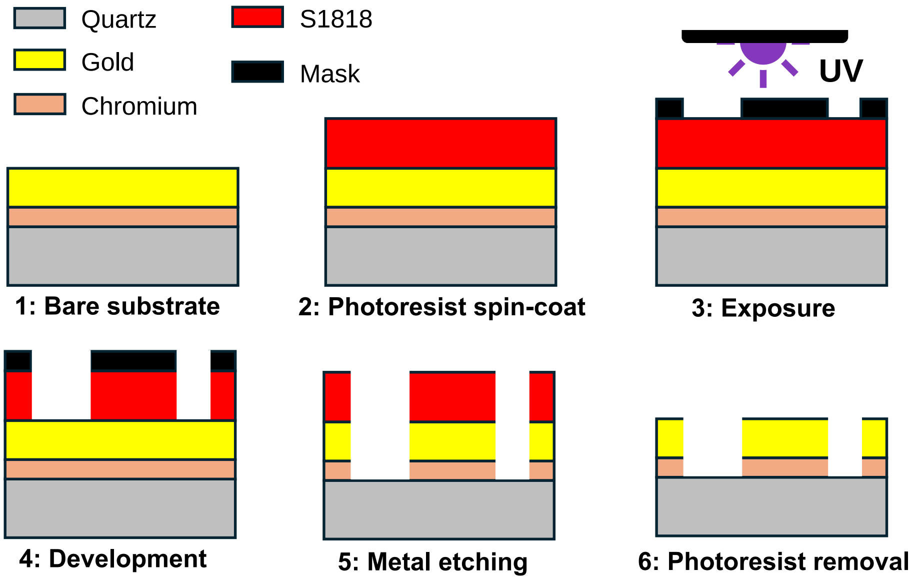

Figure 2.2: Photolithography process followed for manufacturing the patterned surfaces of LC-based SFPS.

2.1.3 Alignment layer

On top of both the metallic electrodes, a polyimide polymer is used as alignment layer. The process of adding such layer is depicted in Figure 2.3. This layer anchors the molecules at the top and bottom of the cavity, so that the molecules stay at the desired rotation plane even without any external excitation (see Figure 1.6). In order to deposit such layer, on top of the bare substrate (step 1) polyimide (Chisso LIXON aligner PIA2304) is first spin-coated at 2500rpm for 30s. Then, it is heated at 150°C for 1min and baked in the oven at 200°C for

45min. This results in a 100nm-thick layer coating of polyimide on top of the substrate (step 2).

Once the polyimide is hardened, it should be rubbed to a specific direction to promote the correct planar alignment of the LC molecules in the rest state. To do so, the surfaces are slid below a rotating cylinder covered in a micro-fibered velvet cloth (step 3), which creates parallel grooves in the polyimide (step 4). This rubbing generates the boundary conditions for the LC at the surfaces, including the molecule tilt angle at $z = 0$ (bottom electrode) and $z = h_{LC}$ (top electrode). This tilt angle is known as pretilt. The resulting pretilt depends on the specific polyimide mixture, which will ultimately have an impact on the inhomogeneity, LC orientation and the response time to external fields. For a correct alignment with consistent pretilts, the rubbing direction of each substrate should be parallel but opposite, commonly known as anti-parallel rubbing.

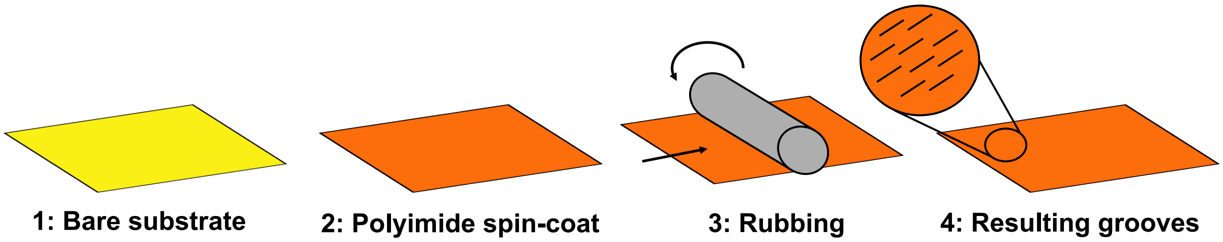

Figure 2.3: Treatment of a substrate with a polyimide alignment layer.

Considering that in SFPS most of the RF electric field will be concentrated underneath the resonator edges inside the LC cavity, and that its main component will be z (perpendicular to the surface), the specific rubbing direction is not a crucial factor. That is, rubbing in either x or y directions will lead to a similar behaviour, since the ε_{zz} component of the electric field will be equally affected upon rotation of the molecules. Small divergences will exist since the multiple excited RF modes in the cavity lead to small, but non-zero, x and y components.

2.1.4 Spacers

The common cavity thicknesses between the electrode planes is in the order of $50 - 150\mu m$. These are obtained by placing spacers in one of the electrode planes, typically the backplane. In optics manufacturing, where the cell gaps are much smaller, plastic or silica micro-spheres are deposited in the surface prior to sealing the cavity. However, the large-diameter versions of those are either non commercially available or showing excessively large variance in size. Thus, pillar spacers made of SU8-2050 epoxy based photoresist are implemented as alternative.

Figure 2.4 shows the process to growing spacers on the substrate, which starts by spin-coating the SU8 photoresist in the electrode plane (step 1). The spinning speed program depends on the desired spacer thickness. Then, the photoresist at the boundary of the surface must be removed to avoid inhomogeneities from edge effects. Next, a soft bake of 10min at 65°C, and a posterior bake of 30min at 95°C, are carried out in a hot plate.

Afterwards, the negative photoresist is exposed to UV light (5mW/cm^2 at 400nm) during

120s for curing (step 2). Previously, a specific mask is to be designed for each device to consider the cell periodicity and avoid placing spacers in a region with high RF impact. The masks allow the UV light to cure the photoresist only where a spacer is to be placed. Then, a post exposure bake of 10min at 95°C is carried out, and finally the resist is developed with propylene glycol methyl ether acetate (PGMEA), during 8 minutes with slow agitation, until the excess of SU8 is completely removed (step 3).

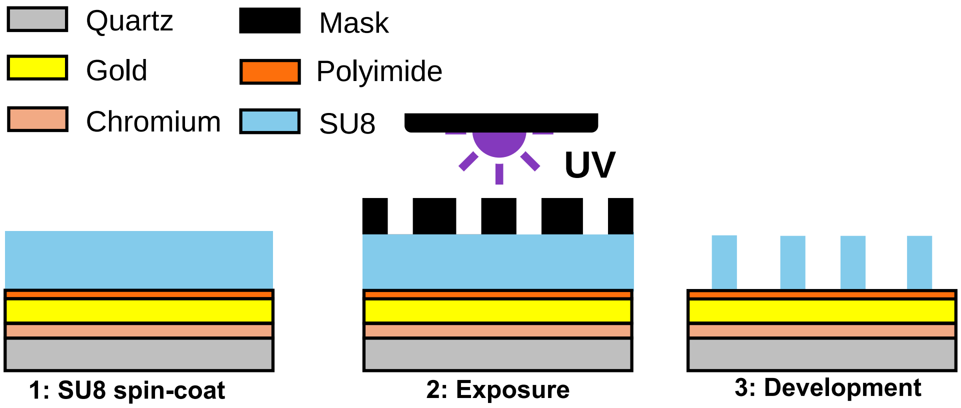

Figure 2.4: Process followed to obtain SU8 spacers on top of a substrate to create the LC cavity.

SU8 spacer thickness characterization

Given that the thickness of the SU8 spacers is one of the most important parameters of the process, a specific characterization of it depending on the spinner speed is carried out periodically. Even though the manufacturer provides reference values, the specific conditions of each laboratory will lead to different results, so testing and adapting the procedures for each clean room becomes necessary for accurate and repeatable results. In addition, the solvents present in the SU8 material will slowly evaporate over time, so this characterization must be done periodically and for each material recipient.

The characterization consists on following the previously mentioned process at different spin speeds and measuring the resulting thicknesses using a surface profiler (Dektak 150). The spinning program starts with a speed ramp of 10s and stabilizes at a target speed during 35s. For each final spinning speed, at least three samples are generated. For each sample, the spacers height is measured at different regions. After removing the data from highly inhomogeneous or aberrant samples, the results for each spinning speed are averaged and a fitting curve like the one in Figure 2.5 is obtained.

It should be mentioned that for obtaining thicker cavities, placing fiber optics cores of $125\mu m$ has also been tested. However, the obtained repeatability was poor and the use of this technique was finally discontinued.

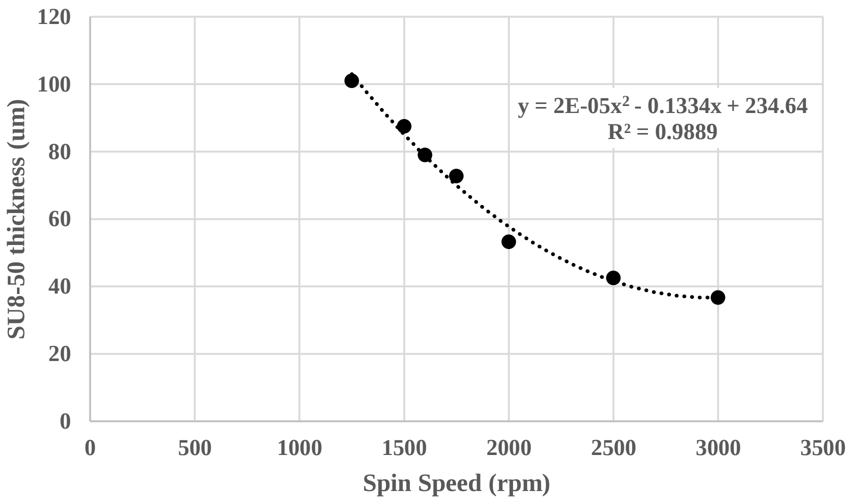

Figure 2.5: Characterization curve of the SU8-2050 thickness vs. spinning speed.

2.1.5 Antenna sealing, filling and connecting

When the patterning, alignment layer and spacer procedures are complete, the substrates must be assembled, as shown in Figure 2.6. This is done with the help of a built-in-house aligner, which ensures the correct relative position of the substrates. When both surfaces are aligned and in contact, they are held in place with plastic tweezers and magnets, and sealing glue is applied at two of the edges (step 1).

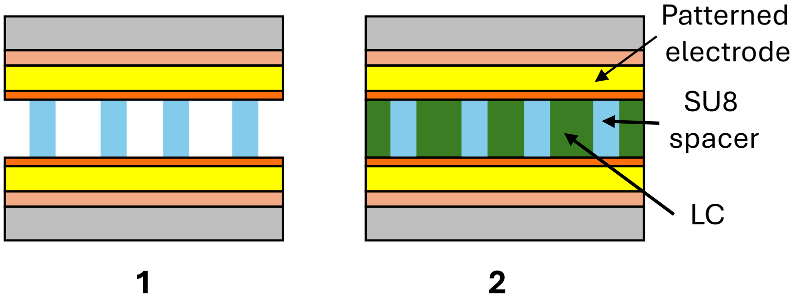

Figure 2.6: Cavity assembly and filling process. The top electrode plate, patterned with the array of resonant elements, together with the bottom electrode and separated by the SU8 spacers, create the cavity, which is later filled with LC material.

When the glue is dry, the cell is ready to be filled (step 2). To do so, it is heated in a hot plate. The LC mixture, which should also be heated to reduce its viscosity, is placed at one of the non-sealed edges with the help of a micropipette, and the cell is filled by capillary effect. Given the large filling area of the devices, the appearance of air bubbles inside the cavity is not infrequent. These can alter the device response in an unpredictable way, since they can flow around the surface depending on the position, pressure and temperature of the cells. In order to avoid them, the filling should be done homogeneously, using all the sample edge to introduce the LC. Additionally, vacuum conditions could also be used. Finally, when the cell

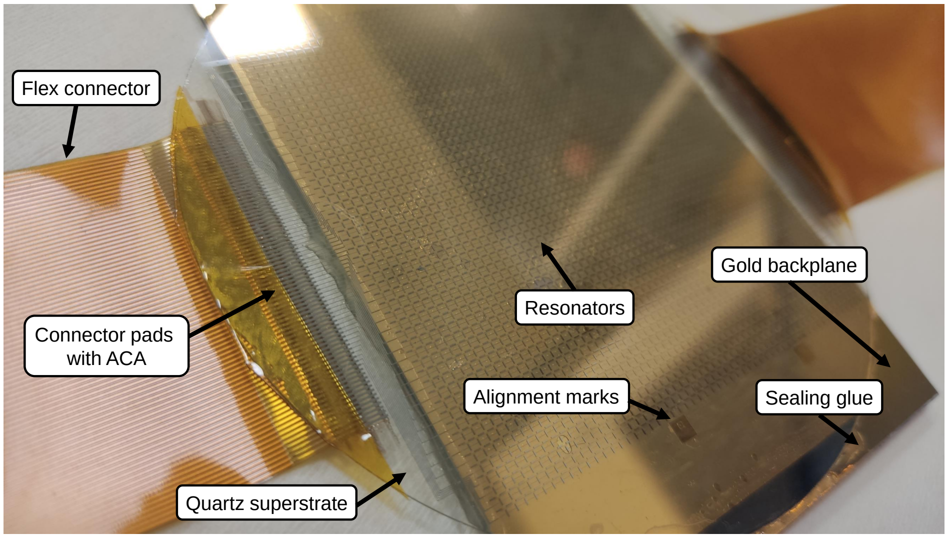

Figure 2.7: Picture of a finished manufactured antenna surface. The top superstrate, made of quartz, contains the patterned gold resonators obtained through photolithography, while the bottom plane is continuously covered in gold. The SU8 spacers and the alignment layer are indistinguishable.

is completely filled, the remaining edges are sealed. The sealing glue can be any compound that does not interact with the LC and that is viscous enough to not permeate into the cavity before it dries. Two used examples are optical adhesives, which can be quickly cured when briefly exposed to UV light, or fast two-component epoxy adhesives.

The last step is to facilitate a connection between the external voltage drivers and the electrodes connectors, as shown in Figure 2.7. For convenience, a flexible connector is used. First, the polyimide present on top of the electrode connectors must be removed with a rubber, as it is non-conducting. Then, an anisotropic conductive adhesive (ACA) is used to fix the flexible connector to the substrate pads. The ACA is the LCD industry-standard interconnect system and is much more convenient with respect to welding when making electrical connections to glass and quartz substrates. A specific bonding machine, equipped with microscope cameras, displays, bonding heads and temperature and pressure controls, is used for this purpose. Finally, the obtained device is ready to be operated through external biasing circuitry.

2.2 Characterization of spatially-fed periodic surfaces

Measuring and characterizing the behaviour of a SFPS is much more intricate than in most of the guided devices. In a SFPS, the measurement is made in free space, which means that the medium is not perfectly controlled. As compared to closed systems such as waveguide or stripline filters, or to semi-closed such as those based in microstrip technologies, where the power at the ports and throughout the structure is confined and can be easily predicted, measurements in open systems like SFPS is in general more challenging.

Let us consider a planar surface being fed by a standard rectangular horn antenna. The

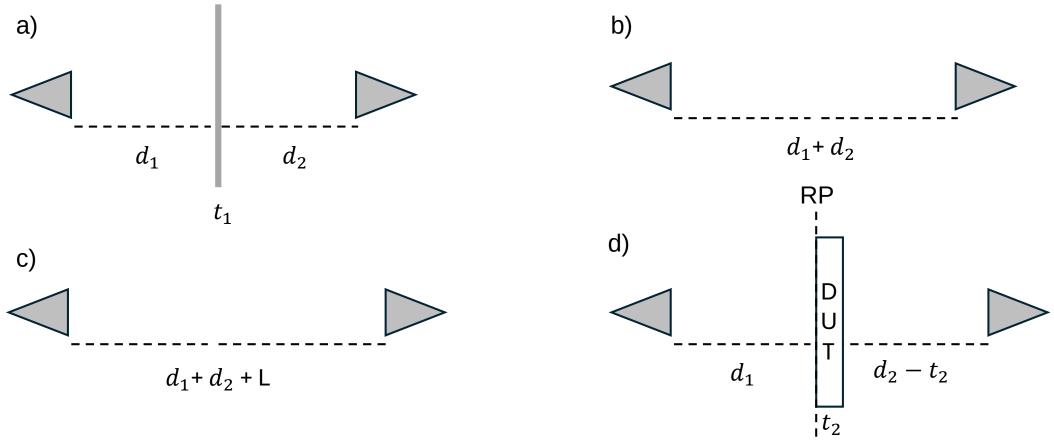

Figure 2.8: Reflect, through and line (TRL) calibration procedure (a-c), and device measurement (d) under normal incidence.

surface is at the near field of the antenna, and thus the incident wave is a spherical wave and not a planar wave. Since the illumination at the edges decays slowly (e.g. with a cos^q curve model, where q is related to the beamwidth), a decision must be made in terms of aperture levels. For instance, in reflectors, a typical strategy that optimizes the efficiency trade-off between illumination losses and amplitude homogeneity consists of a 10dB taper between the center and the surface border. This means that there is a significant scatter happening at the sample edges, and that there is power being radiated outside the surface. Therefore, this information must be known before any measurement is performed, otherwise it can affect substantially not only in transmissive setups, but also in the reflective ones, and artifacts could mask the real surface behaviour.

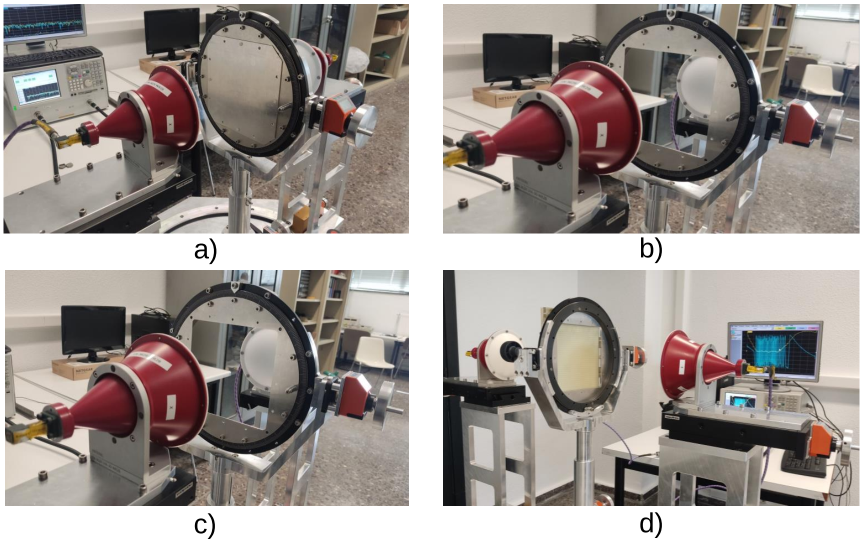

Figure 2.9: Implementation of a TRL calibration procedure in free-space at Ka band. a) Reflect b) Thru c) Line d) Sample measurement.

In free space, the same calibration techniques with the same standards as those from guided

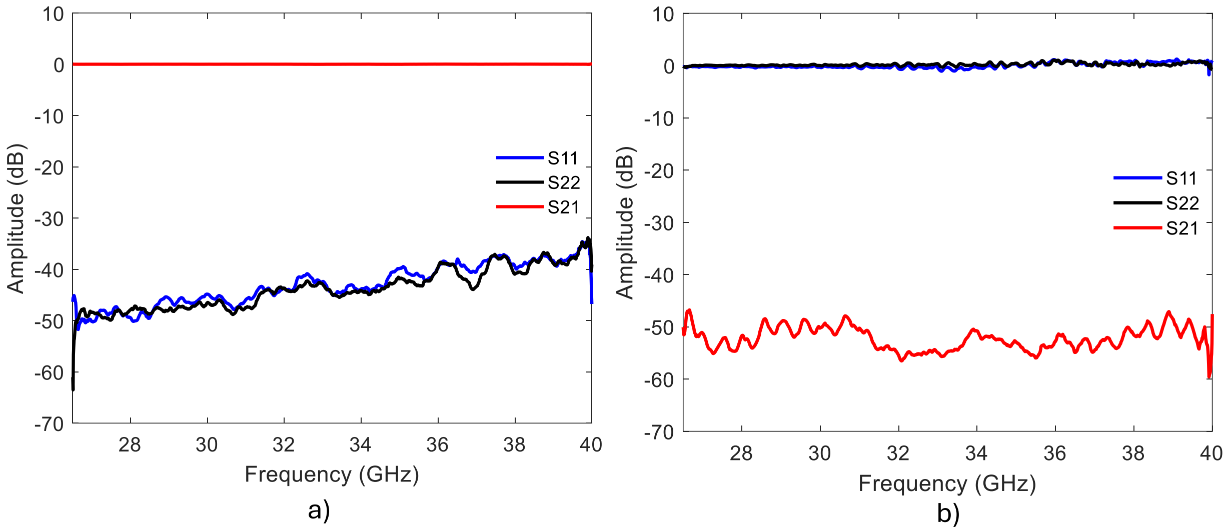

Figure 2.10: Measurement of the S-parameters in a) through standard b) reflect standard scenario after a TRL calibration.

systems can be used, such as Thru-Reflect-Line (TRL) or Thru-Reflect-Match (TRM). However, the difference lies on the physical implementation of each standard. For example, a reflect standard is implemented in free-space as a metallic plate of the same size as the device under test (DUT).

In this thesis, several surfaces are measured in free-space. The followed TRL calibration procedure in a vector network analyzer (VNA) for measuring SFPS under normal incidence, and the corresponding standards, are shown in Figure 2.8. First, a reflect standard is considered by placing a metallic plate of thickness t_1 and the same dimensions as the sample in between the horn antennas. Note that the distances d_1 and d_2 can be different. The thru standard is then considered by removing the metallic plate and bringing closer the antennas a distance t_1. Then, the line standard consists on separating them a distance L, for instance corresponding to $\lambda_0/4$. Finally, the device under test, of thickness t_2, can be measured by placing the sample at a distance d_1 and d_2 from each antenna to the reference plane (RP) respectively. Figure 2.9 shows the real implementation setup of these standards, to perform TRL calibration at Ka band.

However, as mentioned, the free-space calibration is more problematic, in general, than in guided structures, and raises several concerns to be considered. For instance, after following a 2-port VNA calibration procedure in a closed system, such as TRL, the short standard (reflect) can provide an isolation of hundreds of dB, at the numerical error range. On the contrary, following a similar procedure in free-space provides limited isolation only. Besides, free-space calibration is affected by all the surrounding elements of the measurement facilities, which can alter the results. When the distance between the horn antennas is changed, as in Figure 2.8(b-c), the surface illumination is also changed, which distorts the calibration. This is worsened if there are elements close to the sample, such as the holders of the structure. In this regard, a TRM calibration is also possible, by means of absorber materials, which avoids this modification of the illumination conditions. Finally, a generalization of a calibration

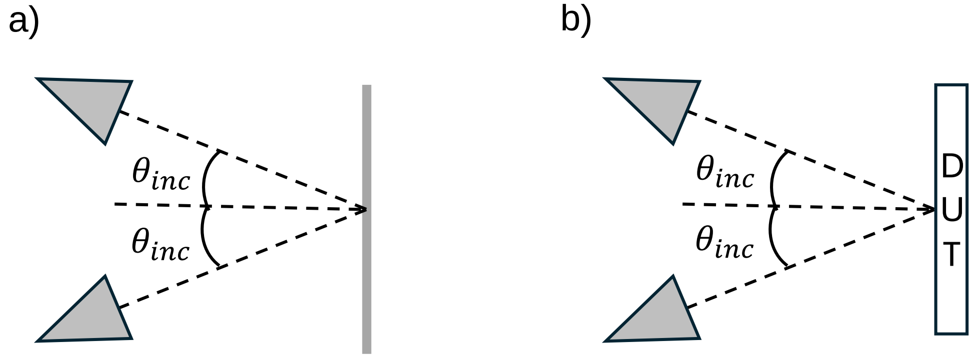

Figure 2.11: Calibration and measurement of a SFPS in a reflection setup.

procedure for oblique incidence is unknown, as it would require different physical ports, in reflection and transmission.

The measurements taken after the aforementioned TRL calibration, as seen in Figure 2.10, of the reflect and thru standards, show that the procedure is valid enough for reasonable measurements. However, the results are far from perfect: at the thru standard measurement, the S_{21} has a 0.03dB ripple variation, and the S_{11} and S_{22} are above -50dB. At the reflect standard, the S_{11} and S_{22} have a 0.5dB variation, and the phase varies $\pm 20°$ from 180°.

Although measurements could be acquired at an anechoic chamber, the real devices will operate in practice in uncontrolled environments. In fact, the main issue revolves around having a very precise knowledge of the feed illumination in the sample, which still persists in a perfectly supervised environment. To begin with, the measurement system alone, as well as scattering at the surface edges, could already distort the results if the illumination on the sample is not perfectly controlled. This affects all spatially-fed surfaces, not only reflectarray antennas or RIS, but also devices such as frequency selective surfaces. However, this remains an open problem that is commonly solved empirically.

To measure in oblique incidence conditions, and given the impossibility to perform 2-port calibration, a single S-parameter (S_{21}) is usually measured, after performing the corresponding thru calibration. In the case of transmissive devices, this does not provide the full description of the device. In the case of reflective devices, the scheme is shown in Figure 2.11, where the thru calibration and the measurement of a SFPS are performed at an elevation angle θ_{inc}, which is in practice limited by the physical dimensions of the horn antennas. The reference is taken from a metallic plate of the same dimensions and at the same plane of the sample. In this case, the thru calibration procedure can provide a complete information about the device response.

Most of the devices are designed assuming a planar wave front. This has enormous benefits for the analysis of periodical SFPS, as unit cell boundary conditions (Floquet modes) under the assumption of infinite surface and local periodicity approach can be set. However, as previously mentioned, many SFPS are fed from a nearby antenna, and thus the illumination is in fact spherical. Among other aspects, the angle of incidence is therefore varying along the

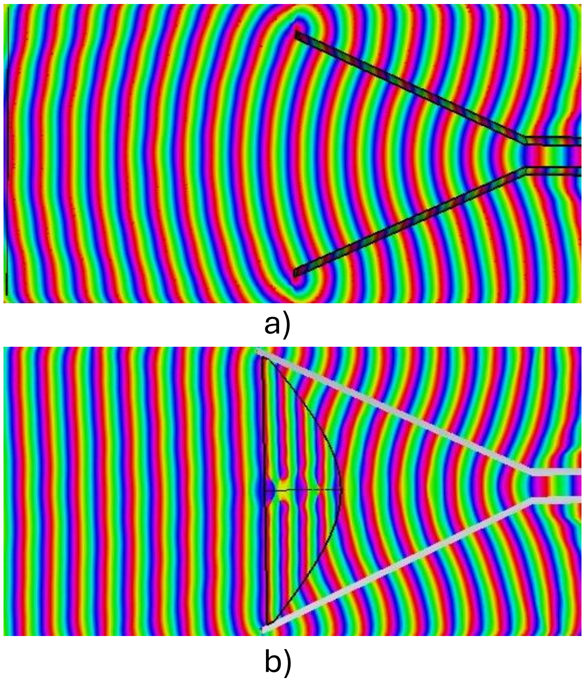

Figure 2.12: a) Cross-section of the electric field (E_y phase) in a standard conical horn antenna. b) Cross-section of the electric field (E_y phase) in a conical horn antenna loaded with a lens.

surface, which is typically modelled under the local periodic assumption by assuming different plane wave illumination for all the corresponding incidence angles. This can be observed in Figure 1.5, where although the impinging wave on the array surface is in fact spherical, a local plane wave of different angles can be assumed at the unit cells. The implications of these approximations have not been accurately resolved, although empirical results and simulation comparisons demonstrate that an accurate design can be made following these assumptions. In general, most of the designs consider the local periodicity approach, and measurement procedures are then followed without considering these effects, or assuming the potential errors that this generates. Nevertheless, this is empirically validated and, in general, there is great agreement between the simulated (pure plane wave) and measured (local plane wave) results. In [55], the impinging electric field at a reflectarray surface is computed by means of a discrete plane wave expansion, which provides a set of truly plane waves that can be multiplied by their corresponding reflection coefficients considering the different wave propagation constants. This makes the local periodicity approach to be slightly more realistic, as compared to considering a single incident plane wave. Some works also analyze the complete structure in a full-wave simulator [48], although this is in general a huge problem in computational terms.

For a finer comparison, when the local periodicity approach is used, it would be necessary to measure the devices in a periodic environment at each angle of incidence. Since the feeder is usually a horn antenna, the only way to approximate a plane wave at the surface, and alleviate such spherical illumination problem, consists on using lenses, which force a planar

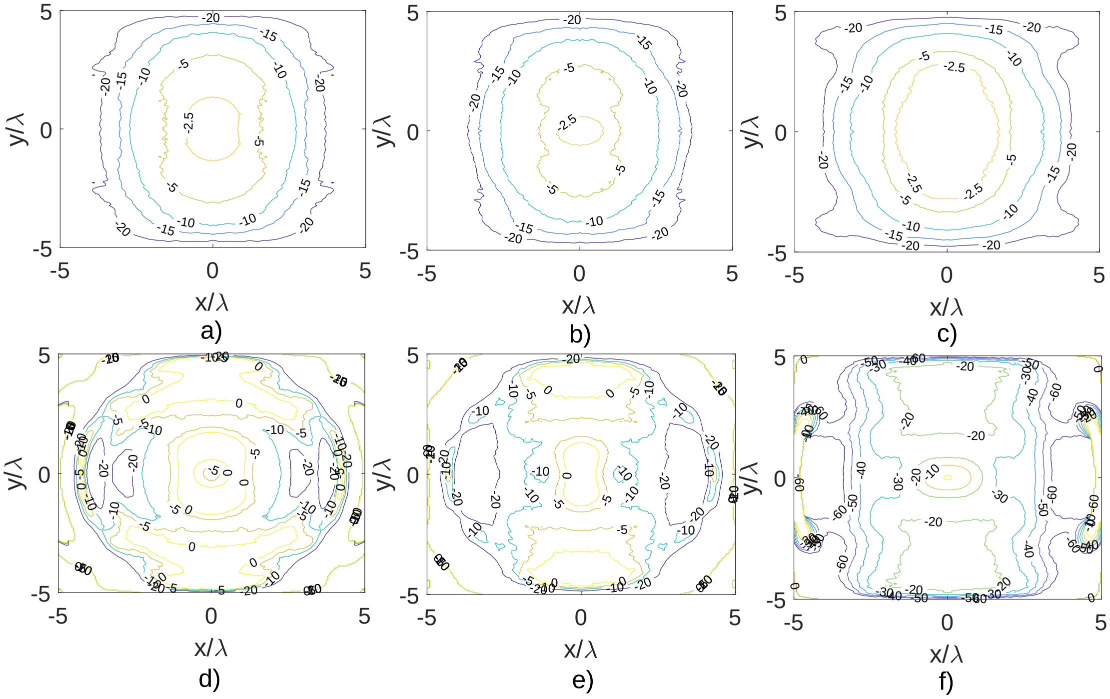

a) b) c) d) e) f)

Figure 2.13: Normalized amplitude (dBV/m, top) and phase (deg, bottom) of the incident electric field excited from a 10λ aperture horn antenna with lens. The distances from the antenna aperture to the surface plane are 5λ (a,d), 7λ (b,e) and 10λ (c,f).

wave front at a close distance of the aperture (see Figure 2.12). However, the generated wave is still not a true plane wave, and the planar wave front is only kept at a certain distance. The incident electric field to a $10\lambda \times 10\lambda$ surface, using a 10λ aperture conical horn antenna with a lens is shown in Figure 2.13. This information can be used as a reference to properly illuminate the SFPS considering the phase and amplitude variations. As can be seen, the planar phase starts to be distorted for large distances.

The previous discussion makes reference to co-polar measurements. When cross-polar measurements are required, or when the sample generates significant levels of cross-polarization, the characterization becomes much more complex. Calibrating in co-polar radiation conditions and measuring the cross-polar components (S_{TETM}, S_{XY}) implies rotating one of the antennas after calibration, which changes not only the illumination but also the loads of the system, both in transmission and reflection measurements, as shown in Figure 2.14. When one of the antennas is rotated, to capture the cross-polarization component excited from the device, it reflects the orthogonal component, which can influence the measurement. Therefore, these measurements must be done with extreme caution and considering these drawbacks.

2.2.1 Electromagnetic characterization of a LC mixture

The scenario of a SFPS in reflection is going to be measured in this section to obtain an electromagnetic characterization of a LC mixture (GT7-29001 by Merck [56]), which will be used later on in the thesis. The anisotropic complex permittivity tensor, that is, $\varepsilon_{||}$ and

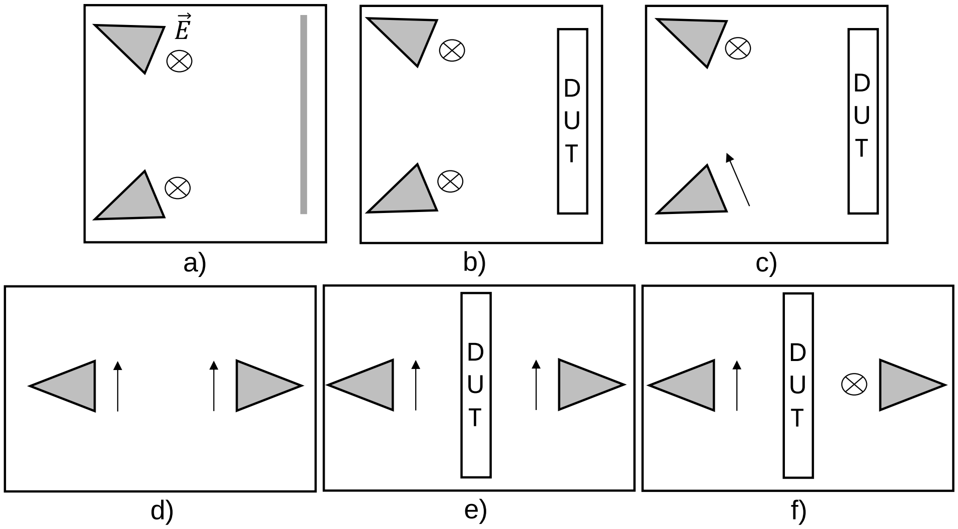

Figure 2.14: a) Co-polar reflection calibration. b) Co-polar reflection measurement. c) Cross-polar reflection measurement. d) Co-polar transmission calibration. b) Co-polar transmission measurement. c) Cross-polar transmission measurement.

$\varepsilon_{\perp}$ and the respective losses, are to be found at W-band, given that the manufacturer only provides these data at 19 GHz. In general, there is a lack of electromagnetic knowledge of many LC materials [57], so this procedure could often be used.

In order to obtain such information, an experimental extraction process is performed, in which the measured unit cell reflection coefficient of a manufactured device is iteratively compared to the simulated one, in the whole band, varying the complex permittivity. The simulation conditions consist of a full-wave simulator (CST Studio [58]) under unit cell boundary conditions (infinite periodic assumption), considering a single incident plane wave. This process has been validated by several works [59].

First, two sample reflectarray surfaces have been manufactured containing the studied LC. The unit cell used for this characterization, shown in Figure 2.15(a), is a well known multi-resonant single polarization cell. Its detailed geometry can be found in [40].

The samples are identical apart from the LC cavity thickness, which are 42 μm in one case and 50 μm in the other. The surfaces consist of 50 × 50 cells, and their unit cell reflection coefficients are measured in a setup like the one shown in Figure 2.11, with $\theta_{inc} = 30°$. The distance from the standard gain horn antennas to the reflectarray surface considers an illumination taper of at least 10dB. The reflection coefficients are extracted for both samples, throughout the entire band and at two different voltage states (V=0V and V=10V, AC square 1kHz), considering a constant fit (pole-zero) dispersive model in CST, centered at 90 GHz. This is done to provide enough redundancy. Note that when obtaining a macroscopic measurement of the unit cell, the entire surface must be equally biased with the same voltage. This results in a periodical surface reflecting in the specular direction, a scenario comparable to the calibrated one. The applied voltage is an AC waveform in order to avoid any DC components.

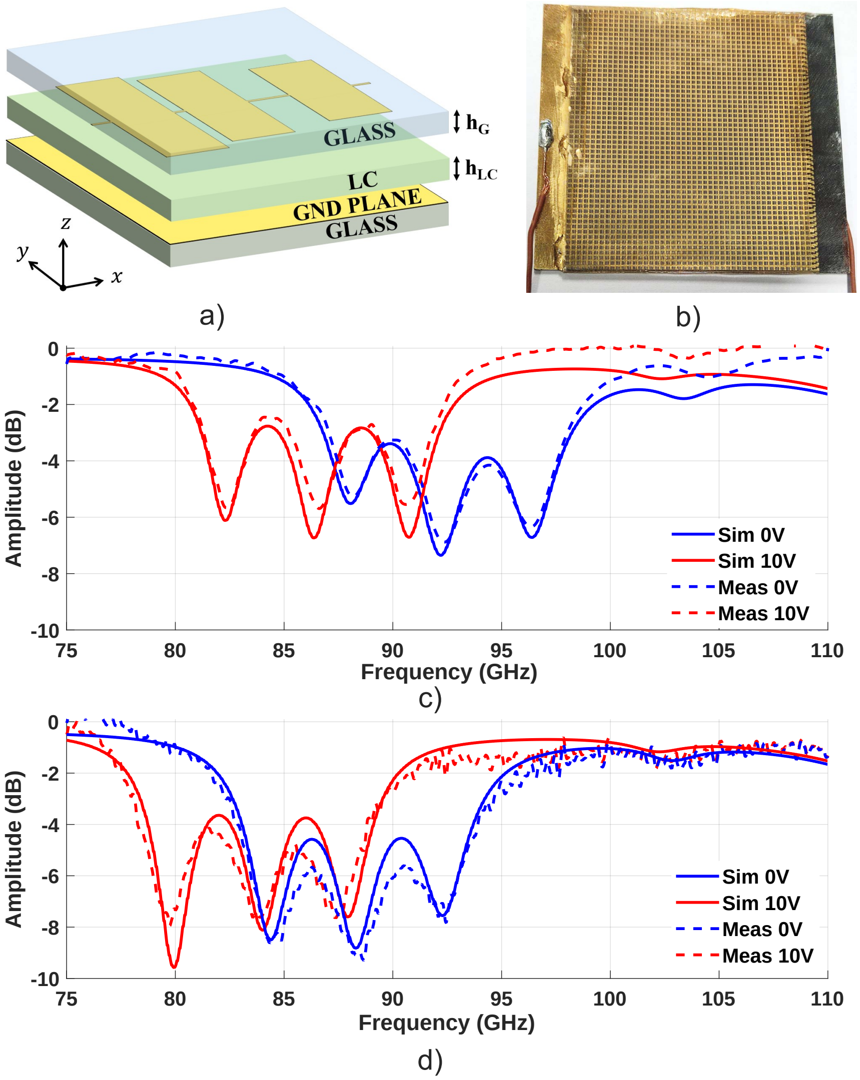

a) b) c) d)

Figure 2.15: LC cells used for characterization of the GT7-29001 mixture at W-band, and their measured and simulated S-parameters using the extracted permittivities. a) Geometry of the used unit cell ($h_G = 0.7mm$). b) Picture of one of the manufactured sample cells. c-d) Measured and simulated reflection coefficients (incidence angle $\phi_{inc} = 0°, \theta_{inc} = 30°$) using the extracted permittivity values once the iterative characterization process has finished for two cells with different LC thicknesses, $h_{LC,(c)} = 42\mu m$ and $h_{LC,(d)} = 50\mu m$.

Finally, the simulated complex permittivity values that best match those measurements, as shown in Figure 2.15, are the extracted values. In this case, the extracted W-band permittivities are $\varepsilon_{||} = 3.5$, $tan\delta_{||} = 0.015$ and $\varepsilon_{\perp} = 2.47$, $tan\delta_{\perp} = 0.02$, which slightly differ from those provided at 19 GHz, as can be observed in Table 2.1.

There exist many different LC materials [60, 61], and while most of them are synthesized targeting optic devices, specific developments for mm-wave frequencies are on-going, with several commercially available options. In Table 2.1, a collection of LC materials and their properties are summarized.

Material	**Frequency**	$\varepsilon_{\|\|}$	$\varepsilon_{\perp}$	$tan\delta_{\|\|}$	$tan\delta_{\perp}$
E7 [62]	19 GHz	2.98	2.53	0.009	0.022
BL006 [62]	19 GHz	3.16	2.58	0.0069	0.0191
TUD-566 [63]	30 GHz	3.11	2.32	0.0021	0.0066
GT3-23001 [42]	100 GHz	3.27	2.47	0.015	0.02
GT3-23001 [64]	19 GHz	3.28	2.46	0.0038	0.0143
GT3-24002 [65]	19 GHz	3.3	2.5	0.0032	0.0123
GT5-26001[64]	19 GHz	3.27	2.39	0.0022	0.007
GT7-29001 [64]	19 GHz	3.53	2.46	0.0064	0.0116
GT7-29001	100 GHz	3.5	2.47	0.015	0.02

Table 2.1: Properties of different available LC materials.

Chapter 3

Independent Dual-Polarization Beam-Steering Reflectarray Antenna based on LC

3.1 Introduction

The designs of existing LC-based SFPS unit cells in the literature are comparable, in complexity, to the first unit cells introduced for passive devices. They target a single functionality, such as beam-steering in a single polarization and a single frequency band. Nevertheless, as shown by the developments of the research community in passive SFPS, it is possible to design unit cells that simultaneously manipulate electromagnetic fields for more than one completely independent functionality [66, 67], and even to make them reconfigurable [68, 13]. Although the reflective case is much simpler, given the number of ports to be considered (2 if both polarizations are studied, 2×2 S-parameter matrix), than the transmissive case (4 ports, 4×4 S-parameter matrix), there are examples of both scenarios [69, 70]. However, in the LC case, there are important implications in terms of modeling, and a space limitation in terms of a single layer if cost and manufacturing complexity are considered.

One of such functionalities consists on distinguishing between orthogonal polarizations. Manipulating the polarization of an incoming electromagnetic wave by using LC entails several difficulties, and few works tackle it. The LC anisotropic molecules introduce an intrinsic interaction between polarizations, which complicates achieving a single-layer design with sufficiently low cross-polarization terms that allows for an accurate phase control and sufficient isolation. In [71], a LC reflectarray capable of converting a 45º incident linear polarization signal to circular or orthogonal linear polarization was presented by modifying only one electric field component through a dipole-like unit cell pattern oriented along TE. There are also examples of beam scanning for two polarizations but dependently, such as in [48], using a cross-shaped patch unit cell, and similar to [72]. In [73], an entire 20×20 reflectarray is simulated in full-wave targeting circular polarization. In [74], a unit cell with through-quartz vias aiming at polarization conversion is presented. A complex 15-layer structure containing two independent LC cavities and polarizers, introduced in [50], independently manipulates two orthogonal polarizations. However, a simple single-layer reflectarray based on LC with an independent control of each polarization in the same unit cell, and how to efficiently model it, can not be found in literature. Moreover, most of the aforementioned works are electrically small. Nevertheless, this would be very valuable in a LC reflectarray antenna, and it is crucial for the operation and reduced cost manufacturing of a LC-based RIS, as it allows to independently control two separate beams for two orthogonal polarizations in a simple manner, enabling a vast increase in the channel link capacity.

In this Chapter, a LC-based reflectarray antenna which is electrically large and is capable of independently operating two orthogonal linear polarizations is introduced. Considering the frequencies at which LC is more advantageous, W-band operation is targeted. The design contemplates the unit cell geometry and its proper modeling including the LC, as well as the required bias lines for the LC switching. Then, the complete antenna configuration is designed, manufactured and measured.

3.2 Unit cell design

The operating principle to design a unit cell capable of independently introducing phase shifts to different polarizations is to enable separate biasing connections to resonant elements sensible to those polarizations. Since the LC can be locally biased, different volumes within the same unit cell can, in principle, be biased in a different way. Then, the different voltages applied to one polarization element will modify the reflection coefficient of that polarization, by rotating the LC molecules under it, but its impact to the orthogonal polarization should be minimal, and vice-versa. Figure 3.1 shows two configurations which are studied next, which can provide such functionality.

However, there are several challenges associated to this design. In a reflectarray antenna, the different unit cells will perceive different angles of incidence from the main feed, which results in varying reflection coefficients. This effect can be significantly diminished if the period of the unit cell is reduced. However, when introducing multi-functional elements to a single unit cell, the required area to fit them increases. A way to solve this consists on shrinking the resonant elements, which allows reducing the cell period and also limits the coupling between the elements. However, this can deteriorate their response by introducing unwanted effects such as sharp resonances with higher losses and an increase on the specular behaviour as the cell begins to resemble a ground metallic plane. Moreover, increasing the number of resonant elements requires adding extra metallic biasing lines to connect each unit cell area to the proper voltages, which take more space and can also alter the RF response. This forces the cell period to be large, which entails the need to have an accurate control of the reflection coefficient.

The area of the unit cell containing resonant elements has additional implications apart from the relation with the period size. First, since the resonators are also used as electrodes for the AC electric field to bias the LC, the larger this area is the more LC volume will rotate when biased. This has an impact on the effective tunability of the cell. Second, the different resonators being driven at different voltages at the same cell generate inhomogeneity in the LC molecule rotation in the transversal direction (parallel to the surface). In all nematic

LC cells, there exists a longitudinal inhomogeneity (perpendicular to the surface) due to the pretilt and anchoring strengths at the enclosing plates, which can be accurately modelled. However, a relevant transversal inhomogeneity is not common and its model is not properly studied. Finally, it can also have an impact on the reconfiguration time.

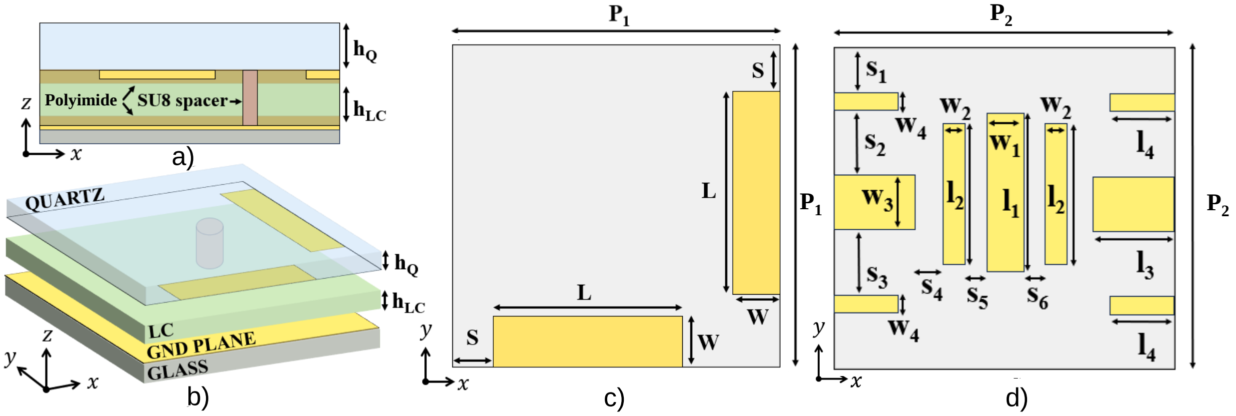

Figure 3.1: Dual-polarization unit cells. a) Side view b) 3D view and c) Top view of the proposed single-resonant unit cell. Dimensions (mm): $P_1 = 1.25$, $L = 0.77$, $W = 0.15$, $S = 0.165$, $h_Q = 0.4$, $h_{LC} = 0.08$. d) Top view of the proposed multi-resonant unit cell. Dimensions (mm): $P_2 = 1.6$, $l_1 = 0.801$, $l_2 = 0.745$, $l_3 = 0.396$, $l_4 = 0.365$, $w_1 = 0.189$, $w_2 = 0.142$, $w_3 = 0.284$, $w_4 = 0.0945$, $s_1 = 0.16$, $s_2 = s_3 = 0.407$, $s_4 = 0.1$, $s_5 = s_6 = 0.071$, $h_Q = 0.38$, $h_{LC} = 0.056$.

Another challenge appears when minimizing the cross-polarization effects of the cell. Even if the resonant elements are symmetrically designed, the varying incidence angles and the LC anisotropy itself will distort such symmetry and facilitate the coupling between polarizations. This is already important in a single-polarization unit cell, as that shown in Figure 2.15, in order to minimize the amount of energy that is lost towards other polarizations, but in the case of a unit cell aiming at manipulating both polarizations this not only represents energy losses but also a worsened behaviour to the other polarization. If cross-polarization levels are not reduced, the influence in the phases of the reflection coefficients of the opposite polarization could completely modify the phase profile on the surface, thus leading to important errors and degraded radiation patterns. In [75], these effects are studied, and a rotation of elements is proposed for passive devices. Another possible strategy to avoid the coupling between polarization consists on maximizing the distance between the resonant elements of each polarization in the unit cell, which again has repercussions on the period size. Therefore, a trade-off between period size, sensitivity to angle of incidence, and cross-polarization levels must be found.

Considering all the aforementioned effects, two different dual-polarization LC reflectarray unit cells operating at W-band have been designed: one containing a single resonant element per polarization, and another one with multiple resonant elements per polarization (see Figure 3.1, where the used materials and final dimensions are detailed). The LC mixture chosen for both unit cells is GT7-29001 (by Merck), as it is specifically designed to minimize losses and show large dielectric anisotropy at mm-wave bands. The LC manufacturer does not provide the electromagnetic specifications of such mixture at W-band, and an in-house characterization had to be carried out before designing the cell, as detailed in Section 2.2.1.

As can be observed, the resonant elements of the unit cell are dipole-shaped and are perpendicularly oriented one to the other. The specific dimensions and placing of the resonators, as well as the cell period and thickness, are chosen to minimize as much as possible the cross-polarization. These are first manually adjusted to find a reasonable structure, which is taken as a starting point for a finer design. Then, a light optimization is performed under a specific angle of incidence and the extreme biasing states, and finally analyzed under different pairs of voltage states and angles of incidence. The placing of the elements also considers the fact that keeping certain symmetry leads to closer results in both polarizations, which is desired. However, as previously mentioned, the LC anisotropy itself will result in an unavoidable variation in the reflection coefficient response of each polarization (S_{XX} and S_{YY}). This has a larger effect in the multi-resonant design than in the single-resonant design, due to the stronger couplings present in the first case. The design of the LC thickness considers a trade-off between losses and phase range. Whereas a thinner cavity increases the phase range and diminishes response time, it comes at the cost of increased losses.

It is worth mentioning that the two designs have been carried out separately, given the different limitations in each of them. Regarding the multi-resonant unit cell, closely spectrally concatenated resonances will lead to a significantly linear variation of the reflection coefficient phase, and to a large phase range. To achieve such behaviour, each set of dipoles is independently designed and finally combined and fine-tuned in a single cell. During the unit cell design, the choice of w_i will affect the width of the resonances, l_i affects their spectral location and s_i plays a role in the coupling between them.

Figure 3.2 shows the reflection coefficient as a function of the frequency for the two polarizations (S_{XX} and S_{YY}) at incidence angle $\phi_{inc} = 0°, \theta_{inc} = 25°$. As can be observed, the multi-resonant cell provides a larger course of phase ($\Delta\phi = 450°$) than the single-resonant one ($\Delta\phi = 200°$) and a larger instantaneous bandwidth, but its period is larger to fit more elements and thus its tolerance to different incidence angles is much lower and higher order modes could appear.

Note that the cavity thickness of the single-resonant unit cell is chosen to be relatively large ($h_{LC} = 80\mu m$). Typically, a thinner thickness could provide enlarged phase ranges at the cost of dealing with higher losses. In this case, and considering that a single dipole resonance is anyway limited to less than a full phase cycle, a thick cavity is considered to reduce losses and avoid critically coupled resonances

3.3 Impact of LC bias lines

The previously depicted cells do not consider the LC biasing required to alter the molecules state. In order to drive each resonant element with a low frequency electric field, thin metallic lines are added, which interconnect such dipoles with a connector outside of the array. The addition of these lines should have a minimum impact in the RF response of the cell. However, in practice these can add in-band resonances and unwanted effects, so their design must be done carefully.

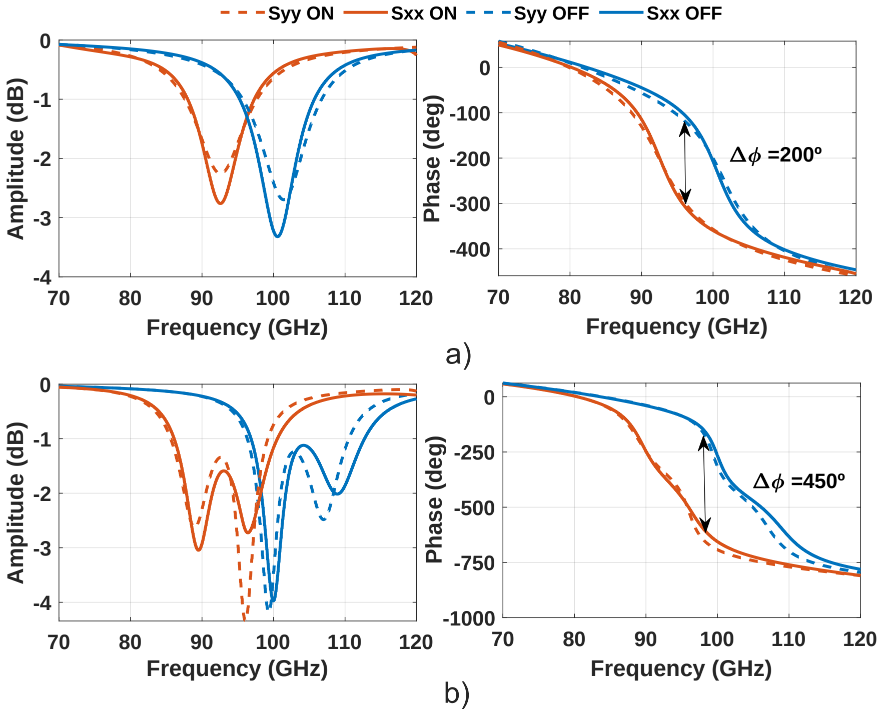

Figure 3.2: Simulated amplitude and phase of the S_{XX} and S_{YY} reflection coefficients of the (a) single-resonant and (b) multi-resonant unit cells for OFF (V=0) and ON (V>>10V) states. Incidence angle: $\phi_{inc} = 0°, \theta_{inc} = 25°$.

Considering this, a specific bias lines analysis has been carried out. To begin with, the biasing of the multi-resonant unit cell is extremely challenging and, after several unfruitful attempts of adding metallic biasing lines into their structure, it is concluded that an alternative strategy, in terms of materials, would be needed to be able to drive such cell without altering the RF response. Using a material which is conductive for AC signals but transparent to RF could help to simplify the problem, similar to indium tin oxide (ITO) for optical frequencies. This is the case of PDOT, although its related manufacturing processes are complex and it has not been successfully used for this purpose yet. For this technological reason, the following of the design considers only the single-resonant cell, which is easier to bias and to manufacture, and still serves to prove the multi-functionality purpose and to scan independent polarization beams, dealing with a narrow bandwidth.

Following the biasing study with the single-resonant cell, three different kind of bias geometries (A, B and C) have been analyzed and compared to the non-biased (ideal) geometry of Figure 3.3(a). In all geometries, the biasing is done interconnecting all the elements in the same column, so that only 1D scanning and focusing in possible, which greatly simplifies the addressing.

In geometry A (Figure 3.3(b)), metallic lines are added parallel to the y axis, in such a way that the x-oriented dipole is interconnected perpendicularly but the y-oriented dipole is interconnected parallelly to the lines. Because of this, the effect on S_{XX} is almost unnoticeable, but S_{YY} is significantly altered. In fact, in this case the resonance is completely out of band and, as a consequence, the phase is distorted by more than 200°.

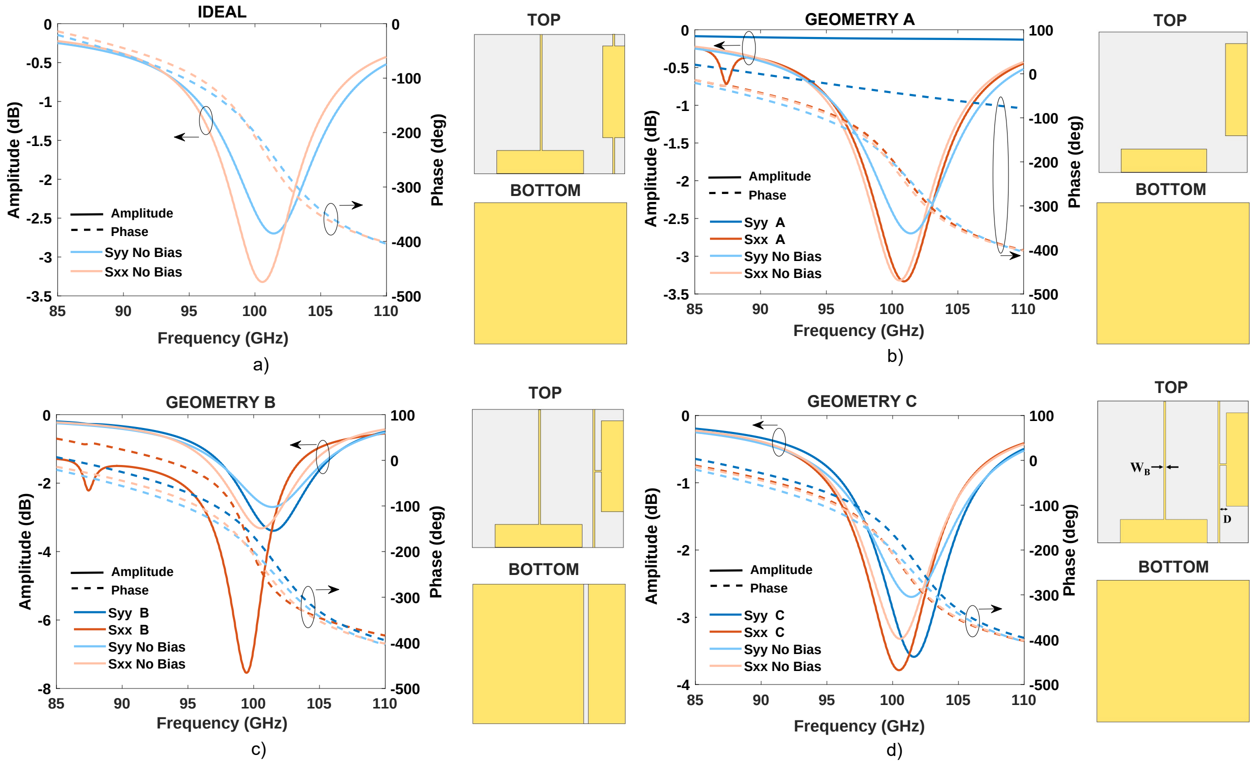

a) b) c) d)

Figure 3.3: Main conclusions of the analysis on the addressing bias geometry. The amplitude and phase of S_{XX} and S_{YY} are compared to the original unit cell for each geometry (Vx=Vy=0V state) under oblique incidence ($\phi_{inc} = 0°, \theta_{inc} = 25°$). a) Original unit cell without bias lines. b) Addressing geometry A. c) Addressing geometry B. d) Addressing geometry C ($D = 0.06$mm, $W_b = 0.02$mm).

Contrary to the previous geometry, in which the ground plane is continuous and the addressing is performed at the top electrode, in geometry B (Figure 3.3(c)) the different voltages are applied at the ground plane. This is possible because the bias signals are AC, and because the LC only reacts to the absolute magnitude of the low-frequency electric field, thus the molecule rotation is independent from the electric field sign. Therefore, whether the addressing of the columns is performed at the top electrode (the dipole voltage connections are segmented by columns and the RF ground plane acts as AC ground plane) or at the bottom electrode (the bottom metallic plane is segmented in columns connected to a different voltages, and all the dipoles are short-circuited in AC acting as ground plane) does not impact the performance in any way. This is, in fact, how the different pixels in LCDs and other optical devices are addressed. In this design, this requires segmenting the ground plane row-wise, with a gap along y. At the top electrode, bias lines interconnecting all the resonant elements are still required. However, an elbow-like turn is introduced in the bias lines of the y-oriented dipole, in order to interconnect both dipoles perpendicularly. The study reveals that using this ground plane segmentation has important implications in RF, as it introduces unwanted resonances in the RF ground plane, mostly on S_{XX}, which can fall in band. As can be observed, the S_{XX} resonance is amplified by more than 4dB and the phase slope becomes less linear.

It should be mentioned that a slightly modified version of this architecture should be used if a full 2D beam scanning is desired, provided that isolated back-plane segments are considered per each cell with proper via-holes and at the expense of the spurious resonances that this type of segmentation introduces, thus requiring a proper and complex design of the electrodes.

Similarly to geometry A, geometry C (Figure 3.3(d)) performs addressing at the top electrode with a continuous ground plane, but introduces the elbow-like turn of geometry B at the bias to interconnect both dipoles orthogonally. In fact, the connection is done in a region where the electric field tends to be small, close to the center of the dipole. The analysis showed that any other connection point enhances the superficial currents in the bias lines, which generates noticeable effects in the reflection coefficients and degrades cross-polarization. This turn slightly breaks the symmetry of the cell and marginally modifies S_{XX}. Nevertheless, the effects of this addressing on both S_{XX} and S_{YY} are very limited (Figure 3.3(d)), due to the continuous bottom plane and an optimal position of the bias connection.

Considering all these points, and given that the segmented ground plane (geometry B) introduces spurious resonances, the interconnection strategy of geometry C is finally chosen because its bias lines layout, perpendicularly connecting the dipoles at their center, yields the best results. Regarding the line thickness, a width of the lines (W_B) as thin as 20 μm is a reasonable trade-off between RF impact and manufacture restrictions.

3.4 Unit cell modeling

To engineer the phases at the reflectarray surface requires knowledge about the unit cell response in terms of its reflection coefficients, and their relation with the applied voltages. In the previous Figures 3.2 and 3.3, an anisotropic and homogeneous model is considered, which is valid for the extreme bias states, as in Equation (1.4). However, controlling the antenna requires predicting the behaviour in intermediate states and different pairs of voltages, which entail inhomogeneity, as well as on different electric field incidence angle and polarization, which adds up to a very large number of possibilities. Therefore, a modeling tool capable of solving these responses in an efficient manner is required. However, the efficient and accurate modeling of a LC unit cell operating at mm-wave is a complex task. In the design and analysis processes of antennas and microwave devices, equivalent circuits capable of reproducing the behaviour of such structures with analytical or quasi-analytical expressions are a great tool to save time and computational expenses. Instead of solving the real electromagnetic problem in a volumetric space, this represents a much more efficient way of finding a very good approximation of the device response. In fact, this is one of the best ways to design and predict the response of passive structures [76, 77] and is possible even for designs including certain reconfigurable elements. However, in structures including LC, the cavities are electrically very thin, and a number of high order non-evanescent modes are excited, which cannot be ignored. This makes the equivalent circuit very challenging to find, and forces performing full-wave simulations of the unit cell. Some works try to approximate the resonant LC cavities with simplistic circuit modelings, which are finally not used for design as they cannot fully predict the device behaviour.

The second great challenge of modeling these structures comes from the aforementioned LC inhomogeneity. Because of the anchoring forces at the enclosing plates, the molecules show great longitudinal inhomogeneity across z, especially at intermediate voltages. While the molecules in contact with the surface remain tilted an angle very close to the pretilt angle, molecules at the center height of the cavity tend to align with the electric field. This is a known behaviour that can be correctly modelled.

However, in the unit cells introduced in this chapter, due to the presence of two different potentials in the same unit cell (one per each dipole), not only the z inhomogeneity must be accounted for, but also the $x-y$ transversal inhomogeneity. In general, the LC unit cells do not have a considerable $x-y$ variation to account for in the RF response, which made the transversal inhomogeneity to not be properly examined, or at least a specific model has not been proposed to tackle it. In fact, most of the cells in the literature do have an $x-y$ variation, since the electrodes include resonant elements with certain geometries which do not cover the entire period [40]. However, unit cells with a single functionality (single bias applied per unit cell) can be efficiently modelled by assuming that the whole cavity is biased equally. Since the most weight of the RF response is typically confined in the regions below the metallic elements, small errors are made when the biasing assumption outside these is wrong. However, in the unit cell proposed in this work, there exists a strong RF relevance underneath each of the resonant element of each polarization, and both can in general be biased differently. Therefore, this $x-y$ variation takes importance, and is in fact the key of the cell functionality.

3.4.1 LC block partitioning

Using exhaustive volumetric models for the LC cavity, which can result very accurate since the LC director (i.e. the unit vector indicating the LC molecules orientation) is precisely determined in the whole cavity, results prohibitive in a design stage due to their computation cost. To tackle the z inhomogeneity efficiently (see Figure 1.6(b)), the community has successfully introduced an averaging strategy of the director tilt angle, which reduces tremendously the computation while assuming a very limited error [41]. An homogeneous permittivity tensor $\overline{\overline{\varepsilon}}$ is obtained that considers such inhomogeneity. However, there is no similar strategy for $x-y$ inhomogeneity. Here, a technique to account for this transversal inhomogeneity in an efficient way is first discussed, and then the model for the longitudinal inhomogeneity as a function of the molecule orientation will be detailed.

In the suggested single-resonant cell, the proposed solution to consider an accurate LC description through $x-y$ consists on splitting the LC region in two sub-volumes, one per each polarization element, and considering different permittivity tensors per each volume. This allows modeling two states independently in the same unit cell, while being compatible with the LC property of being locally biased. Similarly to the z inhomogeneity, the accuracy will be reasonable if the assumption about the LC permittivity tensors in the regions where most of the RF electric field is confined is valid. However, this requires a thoughtful placing of the boundaries between the sub-volumes. To do so, the AC electric field of the cavity in different biasing scenarios, especially where the interactions between the different LC states are greater, must be considered.

The methodology to determine these two LC sub-volumes is shown in Figure 3.4. The AC

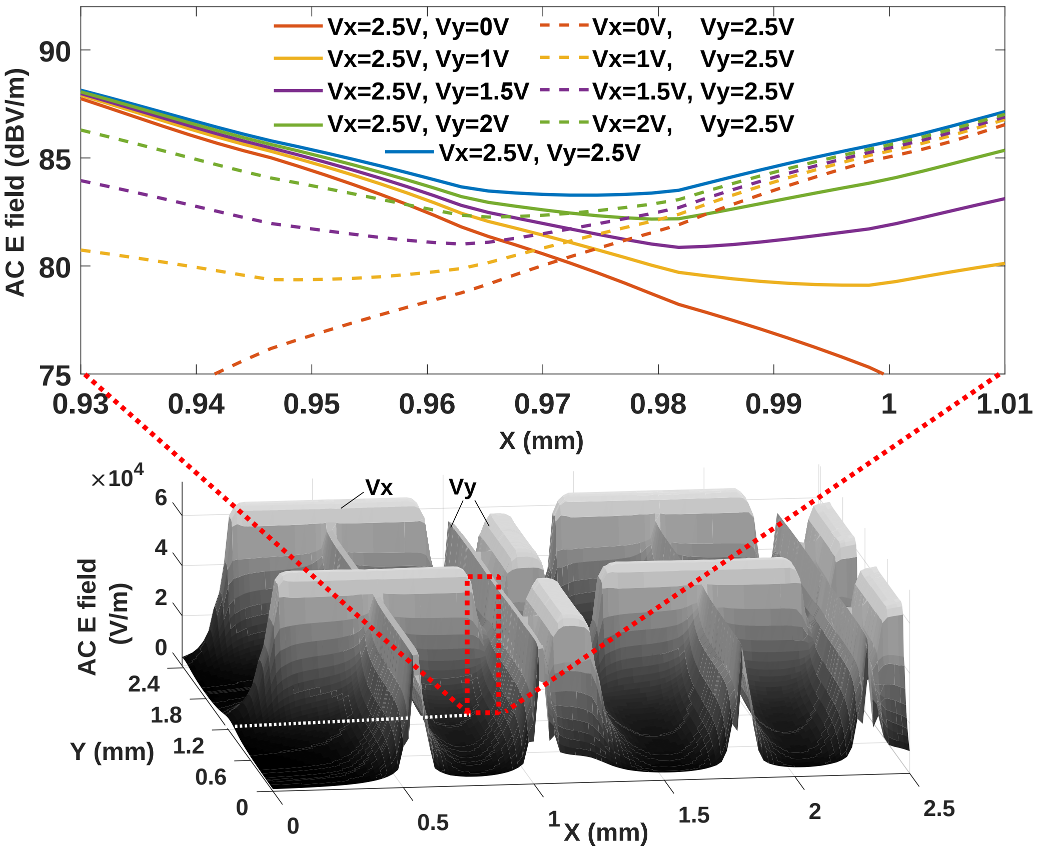

Figure 3.4: AC electric field in the unit cell region where the bias fields of the different polarizations interact the most (top). As indicated by the surface plot of the field (2x2 unit cells, bottom), the E field data is from the $y = 1.2mm$ cut (where the x bias and y bias metallization are the closest) and averaged across z.

electric field present in the region of interest, in which a boundary of the sub-volume must be defined, is shown in Figure 3.4 for several pairs of biasing voltages (bottom: surface plot; top: cut plane at $y = 1.2mm$). For the sake of brevity, only the AC field in one of the boundaries (red region of bottom Figure 3.4) is shown in the top part of the figure. Considering such AC electric field, the boundary is placed where the interaction between both metallizations is lowest ($x = 0.972mm$). Similarly, the other region where the interaction can be strong, between the x-oriented dipole and y-oriented dipole, is also analyzed, resulting in a boundary in $x = 0.085mm$, thus defining the X-polarization LC sub-volume block. The Y-polarization block is then defined as the subtraction between the defined block (X-pol) and the period. The resulting LC blocks are shown in Figure 3.5. The phase-shifts resulting from this partition strategy have been compared with a finer grained partitioning where only the regions below the metallic elements are switchable, with very little discrepancy between both but resulting in a lower computation time. Note that by independently controlling different LC volume regions within the same cavity and unit cell, not only it is possible to control two independent polarizations but it also opens the door to future unit cell designs in which local knowledge of the LC is needed, such as dual-band LC unit cells. This modelling strategy is experimentally validated in Section 3.6.

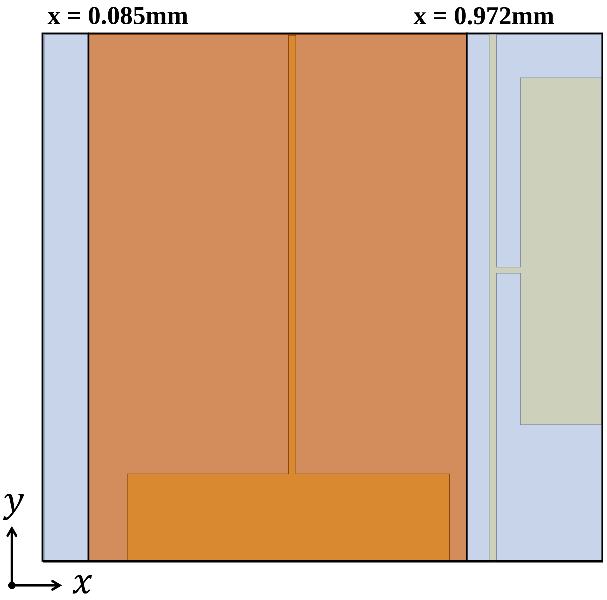

Figure 3.5: Resulting LC blocks after the partitioning for an accurate but efficient simulation. The blue region is homogeneously modelled considering the V_y biasing, while the orange region is homogeneously modelled considering V_x.

3.4.2 Steady-state characterization

In order to compute the unit cell responses in a full-wave electromagnetic simulator, the permittivity tensors of each sub-block must be found. Once the two blocks are defined, and therefore the transversal inhomogeneity is effectively considered, the different AC electric fields are used to compute the tilt angle of the molecules across z, which can be used to account for the longitudinal inhomogeneity of Figure 1.6.

The behaviour of the LC under an external excitation is found in the most general case by minimizing the free energy functional that relates how the electrostatic energy converts into elastic energy to rotate the molecules [29]. The Frank-Oseen LC elastic energy density for nematic LCs can be expressed as:

$$f_{elastic} = \frac{1}{2}K_{11}\left(\nabla \cdot \vec{n}\right)^2 + \frac{1}{2}K_{22}\left(\vec{n} \cdot \left(\nabla \times \vec{n}\right)\right)^2 + \frac{1}{2}K_{33}\left(\vec{n} \times \nabla \times \vec{n}\right)^2 \tag{3.1}$$

where the first term represents the splay deformation and K_{11} is the splay elastic constant, the second term represents the twist deformation and K_{22} is the twist elastic constant, and the third term represents the bend deformation and K_{33} is the bend elastic constant. Negligible elastic constants are omitted.

The electrostatic energy added by the external excitation to be considered is:

$$f_{electric} = \frac{1}{2}\varepsilon_0 \Delta\varepsilon_{AC}\left(\vec{E_{AC}} \cdot \vec{n}\right)^2 \tag{3.2}$$

where $\Delta\varepsilon_{AC}$ is the dielectric anisotropy at the frequency of the bias waveform, usually 1 kHz. It is important to note that the use of DC components when biasing the LC should be avoided, as it can have long-term damaging effects to the mixtures, and only pure AC biasing signals should be used [29].

Finding the elevation and azimuthal angles (θ, ϕ) that locally define the LC director vector requires minimizing the following total free energy in the cavity volume V:

$$F = \iiint_V \left(f_{elastic}(\theta,\phi) - f_{electric}(\theta,\phi)\right) dV \tag{3.3}$$

which can be solved through the Euler-Lagrange equations:

$$\frac{\partial f}{\partial \theta} - \frac{d}{dx}\left(\frac{\partial f}{\partial \theta_x}\right) - \frac{d}{dy}\left(\frac{\partial f}{\partial \theta_y}\right) - \frac{d}{dz}\left(\frac{\partial f}{\partial \theta_z}\right) = 0 \tag{3.4}$$

$$\frac{\partial f}{\partial \phi} - \frac{d}{dx}\left(\frac{\partial f}{\partial \phi_x}\right) - \frac{d}{dy}\left(\frac{\partial f}{\partial \phi_y}\right) - \frac{d}{dz}\left(\frac{\partial f}{\partial \phi_z}\right) = 0 \tag{3.5}$$

where $f = f_{elastic} - f_{electric}$, and the subscripts indicate derivation with respect to x, y or z.

Given the case that the anchorings were weak at the boundaries of the cavity (e.g. if photoalignment methods are used instead of polyimide), additional surface energy terms could be added to Equation (3.3), which can be different for polar and azimuthal anchoring strengths. Moreover, the previous angle representation of the director has dual expressions with a vector notation, which can simplify the notation in such cases [29].

This exhaustive representation of the LC director, including two angle dependencies and variation in the three spatial coordinates, and including the weak anchoring energies, allows a complete knowledge of the director in arbitrary volumetric shapes and boundary conditions. In our case, infinite anchoring can be assumed since the alignment method of rubbed polyimide provides a very strong anchoring. Moreover, since the $x - y$ inhomogeneity has already been considered through the LC region partitioning, the modeling can be done by assuming dependence with θ and z alone, which entails that the molecules only rotate in one plane. This greatly simplifies the previous director representation to:

$$n_x = 0; \quad n_y = cos(\theta(z)); \quad n_z = sin(\theta(z)); \tag{3.6}$$

and the Euler-Lagrange equation to:

$$\frac{\partial f}{\partial \theta} - \frac{d}{dz}\left(\frac{\partial f}{\partial \theta_z}\right) = 0 \tag{3.7}$$

which, after manipulating Equations (3.1) and (3.2), can be finally expanded into the following differential equation:

$$\begin{aligned}\Big(K_{11}cos^2\left(\theta(z)\right) + K_{33}sin^2\left(\theta(z)\right)\Big)\frac{d^2\theta(z)}{dz^2} + \left(K_{33} - K_{11}\right)\cdot \\ sin\left(\theta(z)\right)cos\left(\theta(z)\right)\left(\frac{d\theta(z)}{dz}\right)^2 + \varepsilon_0 \cdot E^2_{z,AC} \cdot \Delta\varepsilon_{AC} \cdot sin\left(\theta(z)\right)cos\left(\theta(z)\right) = 0\end{aligned} \tag{3.8}$$

Since this is too complex to be solved analytically, a commercial finite element methods solver (COMSOL Multiphysics [78]) is used. Boundary conditions for $\theta_{(z=0)}$ and $\theta_{(z=d)}$ must be applied, which are given by the pretilt conditions imposed by the polyimide (θ_{pre}). Therefore, a relation between the LC director and the AC electric field, and thus the applied voltages at the electrodes, is found. Figure 3.6 shows, for the case of a unit cell with a $40\mu m$ cavity filled with GT7-29001 and $\theta_{pre} = 4°$, the molecule orientation as a function of z.

It is relevant to note that, below a certain threshold voltage V_{TH}, the LC molecules do not react to the external excitation at all. This value depends only on the elastic constants and the dielectric anisotropy of the biasing signal:

$$V_{TH} = \pi\sqrt{\frac{K_{11}}{\Delta\varepsilon_{AC}}} \tag{3.9}$$

Moreover, when the voltage is above a saturation value $V_{SAT} >> V_{TH}$, most of the LC molecules except those strongly anchored at the surface are completely aligned with the AC electric field ($\theta \simeq 90°$) and further tunability cannot be achieved. Note also that in this case the cavity is much more homogeneous, and that in all cases $\theta(z = 0) = \theta_{pre}$ and $\theta(z = h_{LC}) = \theta_{pre}$.

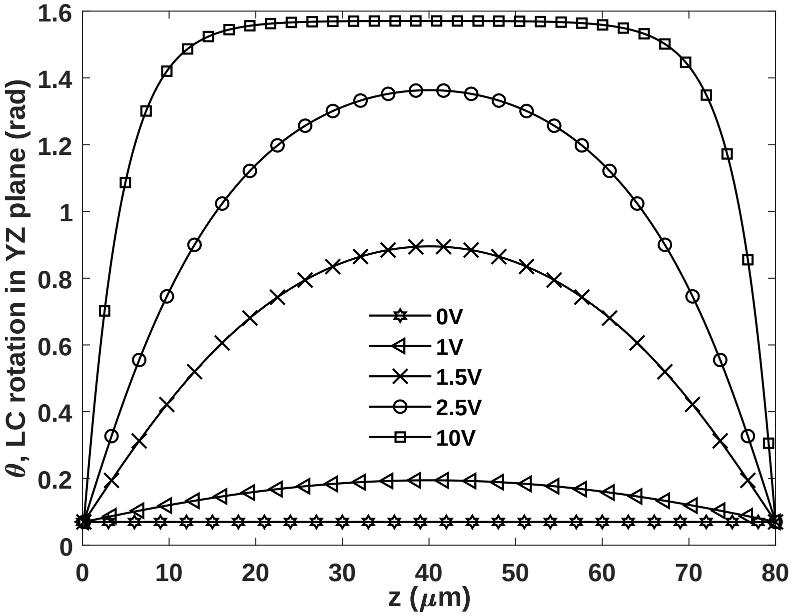

Figure 3.6: Longitudinal inhomogeneity in a $80\mu m$-thick cavity under different biasing voltages, with $\theta_{pre} = 4°$. LC mixture: GT7-29001.

The resulting molecule tilts, as those in Figure 3.6, entail a director orientation which depends on z, because of the longitudinal inhomogeneity. As mentioned in Section 3.4.1 it is a reasonable assumption to work with the averaged tilt angle across z. Therefore, for each electrode voltage, an average director angle can be found, which facilitates obtaining an homogeneous permittivity tensor by using Equation (1.2). That is, instead of working with the

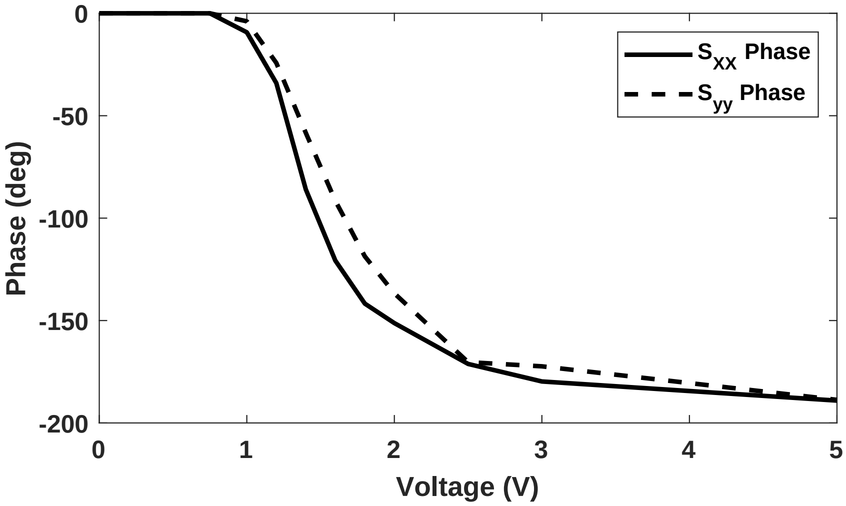

Figure 3.7: Simulated cell phase shifts at S_{XX} and S_{YY} (98 GHz) when varying V_x and V_y respectively, at an incidence angle of $\phi_{inc} = 0°, \theta_{inc} = 30°$.

$\overline{\overline{\varepsilon(z)}}$ tensor as described in Section 1.3 and Figure 1.6, an effective but accurate permittivity tensor can be used. This tensor partially encompasses the inhomogeneity, and is used so that the different LC sub-volumes are treated as anisotropic homogeneous materials.

Once the LC material can be completely described, and all the information about the unit cell is known, full-wave simulations using a commercial software (CST Studio) can be carried out to predict its behaviour under different electrode voltages and angles of incidence, such as in Figures 3.2 and 3.3. Contrary to exhaustively describing the LC director in both θ and ϕ and its dependence in three dimensions, and considering the actual AC electric fields in the cavity imposed by the two polarization electrodes of the unit cell, the modeling strategy presented here enables a fast but accurate simulation of the unit cells in all the voltage state pairs.

With this model, the phase-voltage relations of the co-polar S-parameters (S_{XX} and S_{YY}) can be obtained (Figure 3.7) for all incident angles, which as explained in the next subsections, are used to properly drive the unit cell electrodes for each beam configuration after a phase synthesis procedure. It is important to remark that, as the figure shows, the phase shift dependence with the voltages of both polarizations are very similar but not the same, so a specific characterization per each of them is required.

3.5 Reflectarray antenna design

With the previously proposed unit cell, an electrically large reflectarray antenna capable of beam steering in two orthogonal linear polarizations is designed (Figure 3.8). The array surface consists of 55×55 single-resonant unit cells and the focal points for the two polarizations are chosen to be at $(x_f, y_f, z_f) = (-31.3, 0, 136)mm$. This is done to simplify the measurement setup, since the coincident focal points allow measuring the radiation pattern of each polarization independently by conveniently rotating a single polarization 20dBi horn antenna. The corresponding f/D ratio is 1.98, which is relatively large as this reduces the impact of a limited phase range. However, the illumination taper is kept at -10dB, with minimum differences between polarizations.

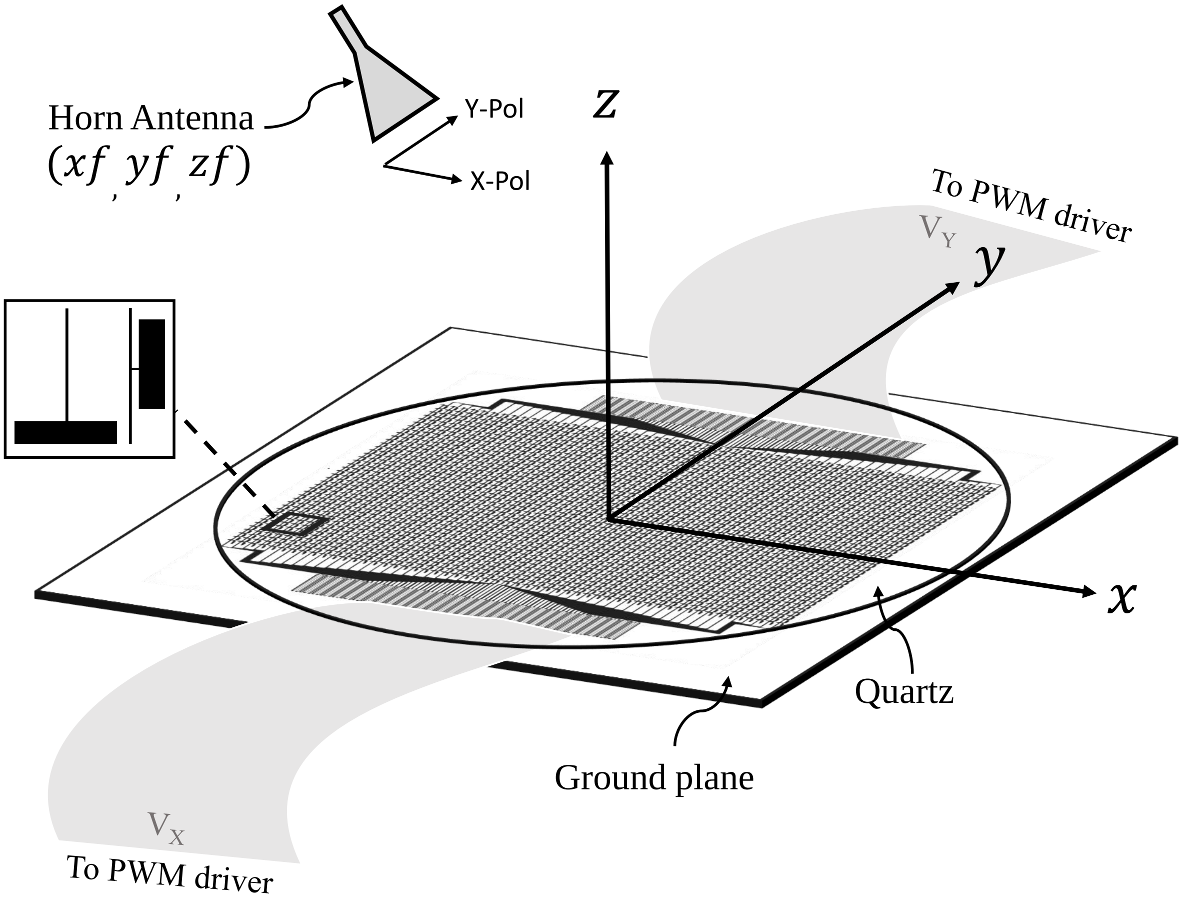

Figure 3.8: Sketch of the proposed LC reflectarray antenna, including the horn antenna feed and the flex connectors.

In order to compute the complete behaviour of the antenna, a full-wave simulation of the entire structure would be computationally prohibitive. Alternatively, a cell-by-cell analysis in conjunction with the assumption of local periodicity at the unit cells, allows an efficient evaluation of such electrically-large device, as usual in this kind of structures [5]. To do so, the unit cells under study are simulated in a periodic environment using CST Studio, which takes ∼5min per simulation. This considers, as mentioned in Chapter 2, the incidence of a plane wave into an infinitely large periodic surface of the single-resonant unit cells. By using this local periodic approach, a negligible error is made (the surface is, in reality, finite and quasi-periodic), but allows considering the mutual couplings of the periodic array. A simulation is carried out for each of the different incident angles and pairs of biasing voltages, in order to obtain the S-parameter matrix in each case, which provides information of both co-polarization (S_{XX} and S_{YY}) and cross-polarization (S_{YX} and S_{XY}) terms. Then, considering the impinging electric field from the feed (E^i), and the desired S-parameters for a specific radiation pattern, the reflected field on the aperture (E^r) is computed in each unit cell as shown in Equation (3.10). This way, the different configurations can be computed just by choosing the convenient S-parameter in each element and performing simple matrix multiplications, instead of having to perform all simulations in the entire surface (several hours per simulation) per each pair of states in each cell. Figure 3.9 shows the impinging electric field at the reflectarray surface, which has been computed with the commercial software TICRA GRASP [79] using a real horn antenna model.

$$\begin{pmatrix} E_x^r \\ E_y^r \end{pmatrix} = \begin{pmatrix} S_{XX} & S_{XY} \\ S_{YX} & S_{YY} \end{pmatrix} \begin{pmatrix} E_x^i \\ E_y^i \end{pmatrix} \tag{3.10}$$

The S-parameters required for each beam configuration have been obtained, initially, by synthesizing the radiation patterns with a phase-only algorithm, considering:

$$\phi_c(x_i, y_i) = -k_0 sin(\theta_t) cos(\phi_t) x_i - \phi_i(x_i, y_i) \tag{3.11}$$

where ϕ_c is the phase shift introduced by the cell, ϕ_i is the phase of the impinging electric field, and θ_t and ϕ_t define the target beam direction.

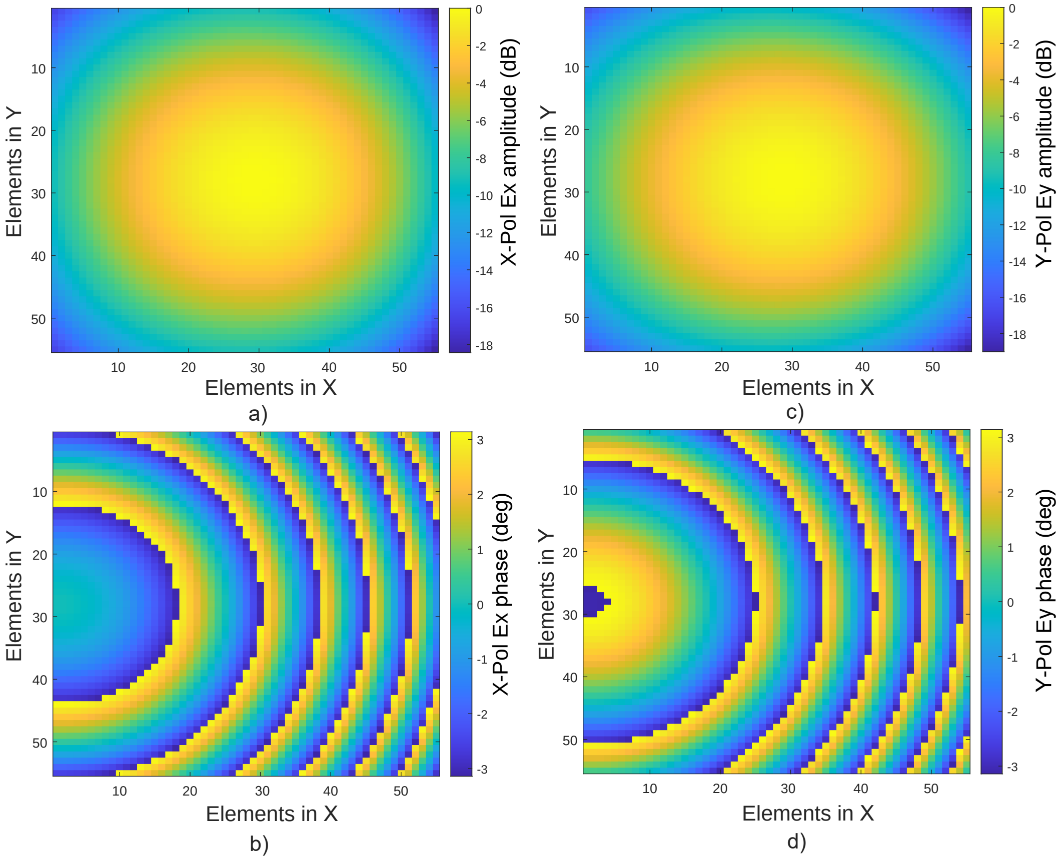

Figure 3.9: Impinging electric field at the reflectarray surface (98 GHz). a) X-Pol Ex amplitude (normalized). b) X-Pol Ex phase. c) Y-Pol Ey amplitude (normalized). d) Y-Pol Ey phase.

Since the electrode voltages around the surface can only be modified by columns, the reflectarray is treated as a 1D structure and only the electric field impinging at the central row of the array ($y_i = 0$) is considered to compute the cell phases across such row. This information is used to choose the voltages of each column per each beam configuration, independently in both polarizations, considering the incident angle in each of the cells.

Even though the modeling strategy reduced substantially the computation time of the unit cell response, a further simplification can be made to not having to obtain all the responses for all the incident angles. Specifically, an array segmentation has been used, only at the analysis step after designing the voltages, to obtain a very accurate but faster knowledge of the radiation pattern of the chosen configuration. The utilized angle segmentation, which can be seen in Figure 3.10, reuses the design responses of the central row and groups the other cells in 12 segments with different density, requiring only 67 angle computations in total. The mean incident angle of each segment is used as a single incident angle for all the cells in that region, substantially alleviating the total number of considered S-parameters. For a single case, this segmentation has been compared with a non-segmented analysis of the radiation pattern (considering all the $55 \times 55 = 3025$ incident angles), resulting in very little discrepancies due to the small angle sensibility of the cell.

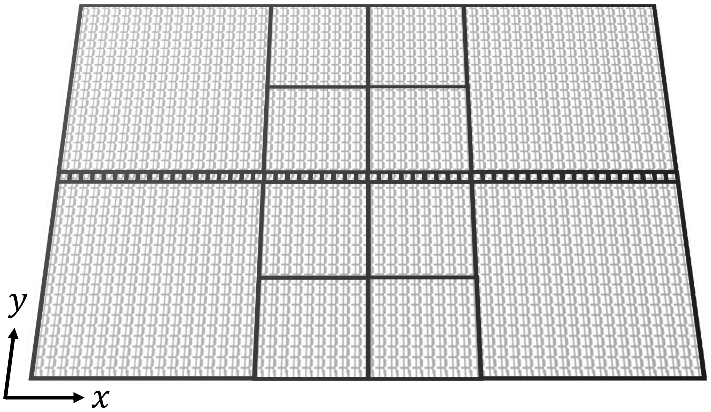

Figure 3.10: Array segmentation used for the incidence angles in the radiation pattern analysis.

However, given that the amplitude of the reflection coefficients is not negligible due to the lossy nature of LC, the chosen voltages considering only the phases might not be the optimal ones, and a significant amplitude ripple can appear at the surface. Moreover, considering that the single-resonant unit cell does not have a complete 360° phase cycle (the phase range is 200° but continuous), an additional strategy is performed to obtain the best radiation pattern of each configuration. Specifically, several phase constants (ϕ_k) are added to the initially chosen cell phase-shifts (ϕ_c) at the entire surface, which gives an equivalent set of phase profiles compliant with the desired radiation pattern beam direction. However, each phase profile will entail different amplitude profiles and phase cycles throughout the surface, which can lead to important changes in the final radiation. In fact, it has been observed that, as expected, the best resulting phase constants in terms of directivity and SLL are the ones that leave most of the lossy states and phase discontinuities out of the array center. These differences can be observed in the radiation patterns of Figure 3.11, where the only changing parameter in the phase synthesis procedure is ϕ_k. Note that, in the figure, apart from the SLL, the gain also changes with each ϕ_k, although the patterns of the figure are normalized. Therefore, choosing an optimal phase constant is very important for obtaining the expected performance. Given the independence of the unit cell response to each polarization, the whole phase synthesis procedure only has to be repeated twice, which greatly simplifies the problem as compared as having to compute all the crossed combinations.

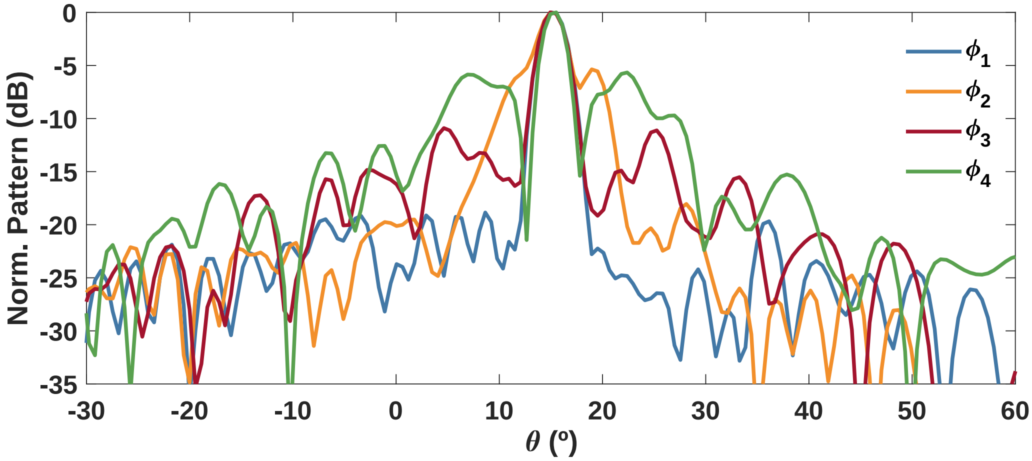

Figure 3.11: Normalized Y-Pol radiation pattern (simulated) of the antenna after considering different ϕ_k values during the phase synthesis procedure (98 GHz). In this case, ϕ_1 would be chosen for the best performance at $\phi_t = 15°$.

Finally, the reflection coefficients of the entire 55×55 array, with the designated voltages in each column and the correct incidence angle, are used in conjunction with the impinging fields to analyze the far-field radiation patterns. These, which will be focused only at the elevation plane, can be computed using the angular spectrum of plane waves.

After applying the aforementioned synthesis procedure, and considering the previous E^i, the resulting electric fields at the reflectarray surface for an example beam configuration of $\phi_t = 0°, \theta_t = 20°$ in both X-Pol and Y-Pol are shown in Figure 3.12, where it can be observed that an amplitude ripple is generated.

The corresponding electrode voltages can then be applied to the 110 columns of the antenna by using the phase-voltage relations of Figure 3.7, which are known for all the 55 elevation angles of incidence of the central row. For each beam configuration of each polarization, this procedure can be repeated, and the different electrode voltages can be obtained.

3.6 Experimental results

3.6.1 Antenna manufacturing

The antenna is manufactured in the CEMDATIC clean room facilities at UPM, according to the procedures described in Chapter 2. A $15nm$-thick chromium layer is sputtered on a $400\mu m$ 4-inch quartz for high-quality gold adhesion. Then, $1\mu m$-thick gold layer is deposited on top.

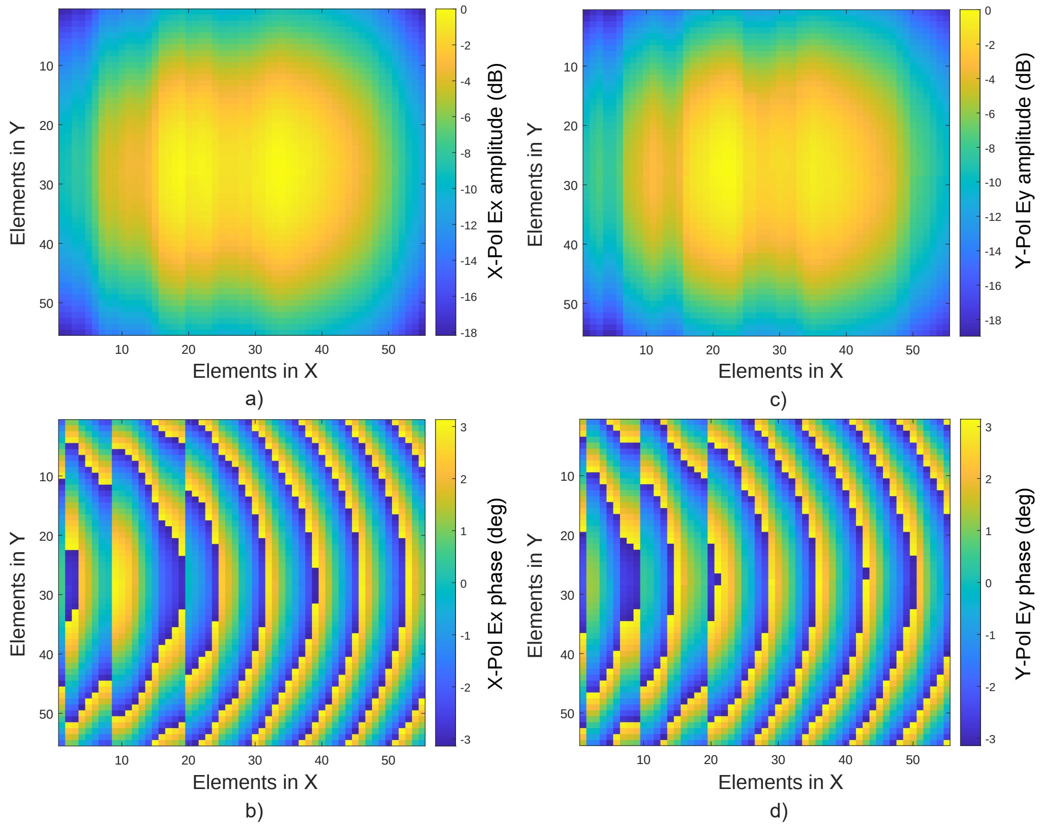

Figure 3.12: Reflected electric field at the reflectarray surface with $\phi_t = 0°, \theta_t = 20°$ beam configurations in both polarizations (98 GHz). a) X-Pol Ex amplitude (normalized). b) X-Pol Ex phase. c) Y-Pol Ey amplitude (normalized). d) Y-Pol Ey phase.

The next step is to pattern these metallic layers through photolithography and wet etching in order to obtain a clean quartz substrate with the gold resonant elements and connectors.

As can be seen in Figure 3.13, the mask contains two connector regions where the 55 voltages of each polarization can be coupled to external flex connectors. It also contains three alignment marks, which will be used at the assembly step.

Obtaining a perfect patterning through the photolithography process resulted challenging, mainly due to the aggressive ratio between the desired minimum feature size ($20\mu m$) and total area (4-inch quartz). Moreover, performing gold deposition via sputtering in such a large area leads to a significant thickness inhomogeneity, resulting in a thicker center and thinner edges. Inhomogeneity assessments, carried out by placing small test glasses covering different substrate regions, and measuring the resulting material gap with a surface profiler, confirm that this inhomogeneity corresponds to up to $\pm 300nm$. Then, at the patterning stage, the metal requires different etching times, which leads to either over-etching thin regions or under-etching thick regions (Figure 3.14).

In order to address this, two modifications are made. Firstly, the substrate is rotated while the sputtering is taking place. This partially reduces the gold inhomogeneity in the quartz. Secondly, in order to control the etching speed, this step is discretized in several phases.

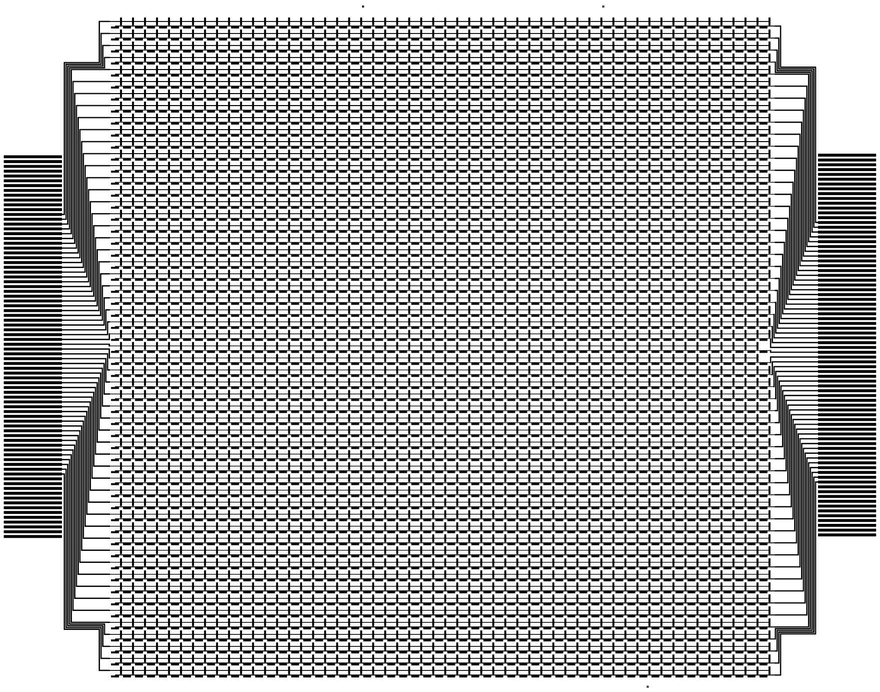

(a)

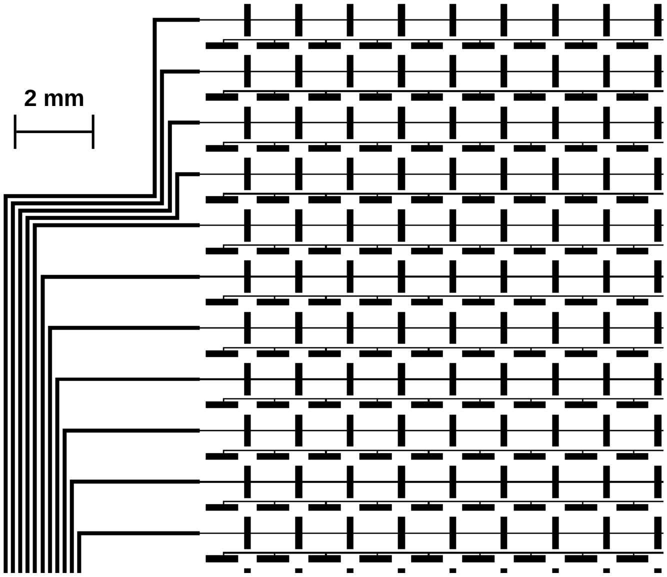

(b)

Figure 3.13: a) Antenna mask of the top substrate electrode. b) Zoomed in detail of the top electrode mask.

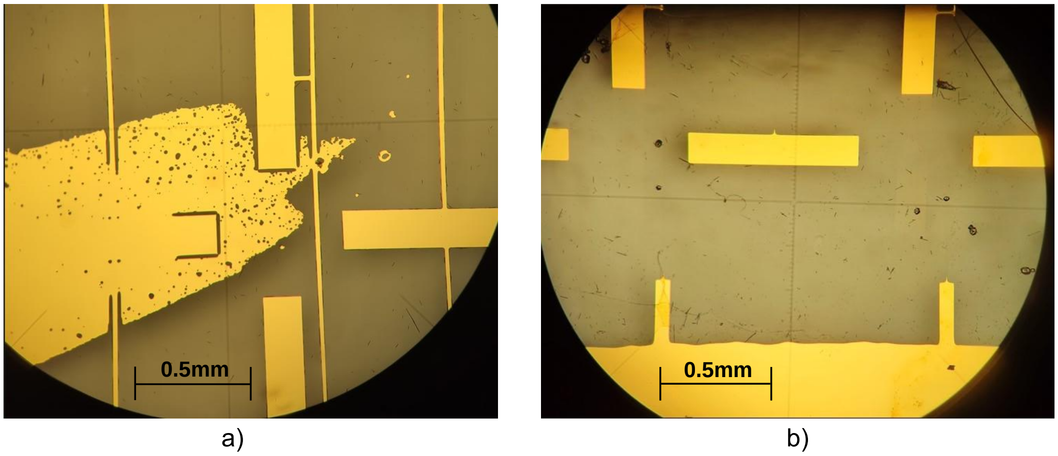

Figure 3.14: a) Under-etching in a central region. b) Over-etching in an edge region.

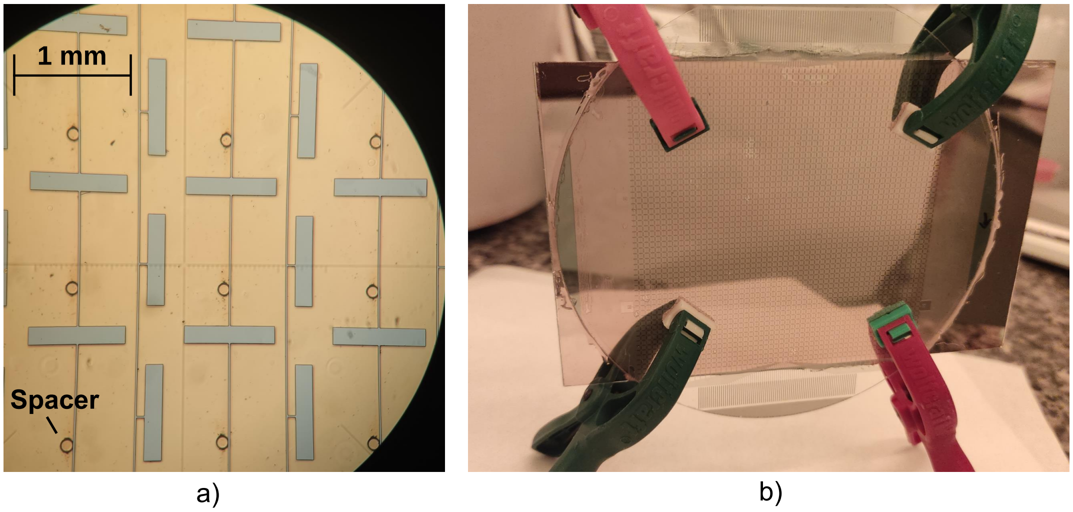

Figure 3.15: Pictures of the finished antenna. a) Detail of the unit cells. b) Antenna assembly.

Specifically, in each phase, the thinner outermost regions, which are etched faster, are manually coated in photoresist. This stops their etching, while it continues in the central regions. This resulted in an almost perfect gold patterning despite the thickness inhomogeneities.

Continuing with the manufacturing, the bottom electrode is made by covering glass in continuous gold, and polyimide is deposited and rubbed in both top and bottom electrodes to define the rotation plane of the LC molecules. On top of the polyimide layer of the bottom substrate, a SU8 photoresist deposition and posterior patterning is performed to grow the LC cavity spacers. The SU8 mask is completely dark except for a periodic 2D array of circles of 100nm diameter (same period P_1 as the unit cell), which will result in the cylindrical spacers. The mask also contains alignment marks, complementary to those at the top electrode, which ensure that the spacers are placed far from the dipoles to diminish their effect in RF (see Figure 3.15(a)).

Finally, the cavity is closed, filled with the LC, and sealed with adhesive (Figure 3.15(b)), and the entire antenna is mounted on a methacrylate plate to provide robustness. A ground

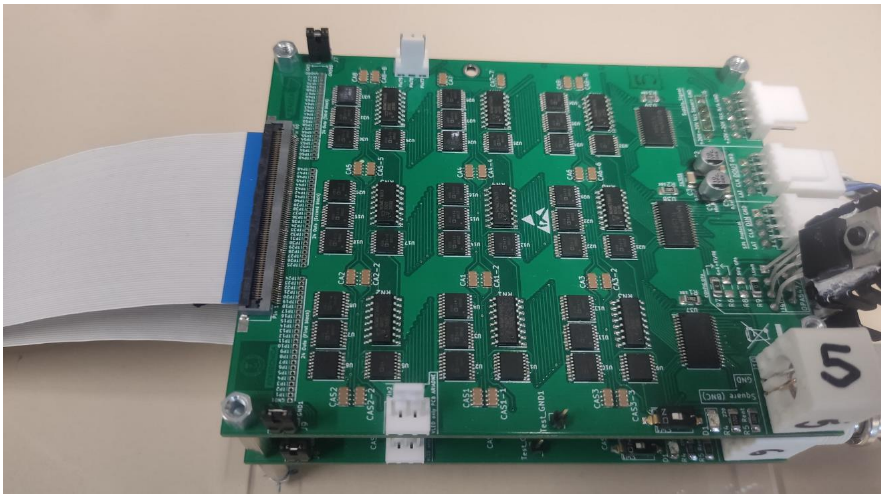

Figure 3.16: PWM drivers for the addressing of the LC antenna. Further details about the circuitry can be found in [80, 81].

connector and a couple of flex cables interconnect the electrodes with pulse-width-modulation (PWM) drivers, shown in Figure 3.16, which are capable of controlling the 110 bias lines simultaneously with the desired root mean square voltage.

3.6.2 Unit cell measurement

Once the reflectarray surface is manufactured, a macroscopic unit cell measurement in periodic environment is necessary to validate the cell-level simulations. Taking the considerations from the discussion in Chapter 2, a free-space reflection measurement is carried out. A VNA (Anritsu MS4647B) connected to a pair of horn antennas is first calibrated by means of a thru calibration procedure, using a metallic plate of the same size as the antenna as a reference. Then, the antenna surface is placed at the same plane, and the reflection coefficient is measured at a certain incidence angle ($\phi_{inc} = 0°, \theta_{inc} = 30°$). The measurement setup can be seen in Figure 3.17. The used horn antennas (Anteral LHA-30-WR10) have lenses embedded, which contributes generating a plane wave front to illuminate the sample. The distance from the antennas aperture to the reflectarray surface is 6cm.

In order to obtain a macroscopic measurement of the unit cell reflection coefficient, the surface must be periodic. To do so, all unit cells are short-circuited to the same voltage (1 kHz AC square waveform). This way, the LC is equally excited in each unit cell along the surface, obtaining a periodical surface with specular reflection. Note that the voltages of X-polarization (V_x) and Y-polarization (V_y) can still be different, as long as the unit cells are periodic.

The simulated and measured reflection coefficients are shown in Figure 3.18, where both polarizations are depicted. The response for each polarization has been measured while keeping the voltage of the resonant elements of the other polarization at 0V, although as will be seen this has a very reduced effect. Specifically, Figure 3.18(a) shows S_{XX} when varying the voltage for the x-oriented dipole, V_x, and keeping $V_y = 0$. Similarly, Figure 3.18(b) shows

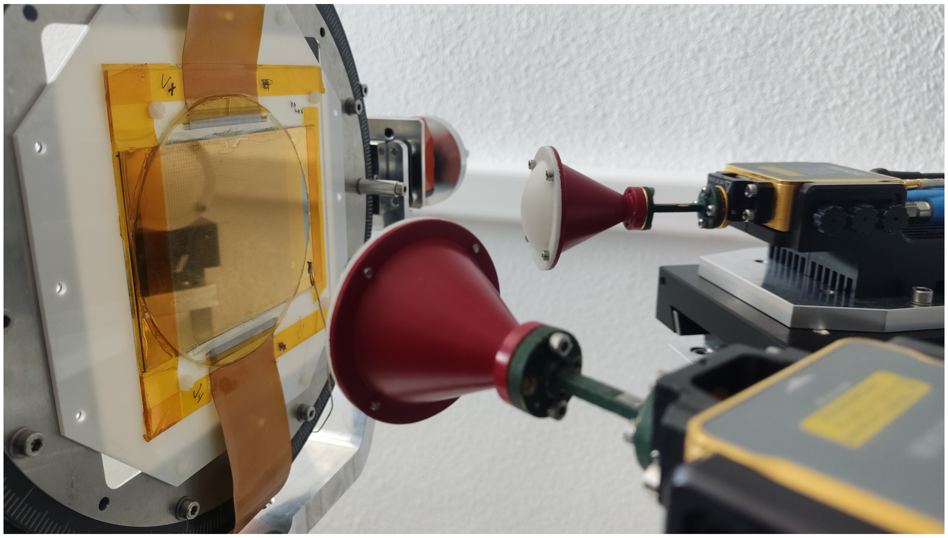

Figure 3.17: Manufactured reflectarray surface and unit cell measurement setup.

S_{YY} when varying the voltage for the y-oriented dipole, V_y, and keeping $V_x = 0$. Due to the model proposed in Section 3.4, there is an adequate prediction of the reflection coefficient in each state, both in amplitude and phase. Moreover, thanks to the final dimensional fine tuning in the unit cell design, the maximum cross-polarization levels of the unit cell reflection coefficient (S_{XY} and S_{YX}) across all the bias states is -12dB.

The biasing independence of each polarization has been tested next. To do so, the reflection coefficients have also been measured while varying the LC states of the opposite polarization. In Figure 3.19, S_{YY} remains almost unchanged when varying V_x from 0V to 5V, both in simulation and measurement. This can be explained by the local biasing of the LC, and validates the previous LC block partitioning strategy during the unit cell modeling. Moreover, this greatly facilitates the synthesis of the voltages since each polarization can be designed completely independently without considering the LC states of the other polarization in each unit cell.

The unit cell tolerance to different incidence angles is also measured (Figure 3.20). As expected, due to the small period and high symmetry of the unit cell, changing the incidence angle has very limited effect on the reflection coefficient. In the figure, the measured and simulated S_{YY} is shown for $V_y = 0V$ and $V_y = 5V$ ($V_x = 0$) under different incidence angles.

3.6.3 Antenna measurement

The different radiation configurations for each polarization of the antenna have been measured in an anechoic chamber. To facilitate a simpler setup, each polarization has been measured individually, using as feed a single polarization horn antenna (Flann 27240) and rotating it 90 degrees. This is possible due to the previous design of the focal point, which is the same for both polarizations. Due to the electric field superposition principle, the results are equivalent to using a dual-polarization feed. Figure 3.21 shows the antenna measurement setup in the anechoic chamber. As can be seen, a 3D-printed plastic holder helps setting the feed in place.

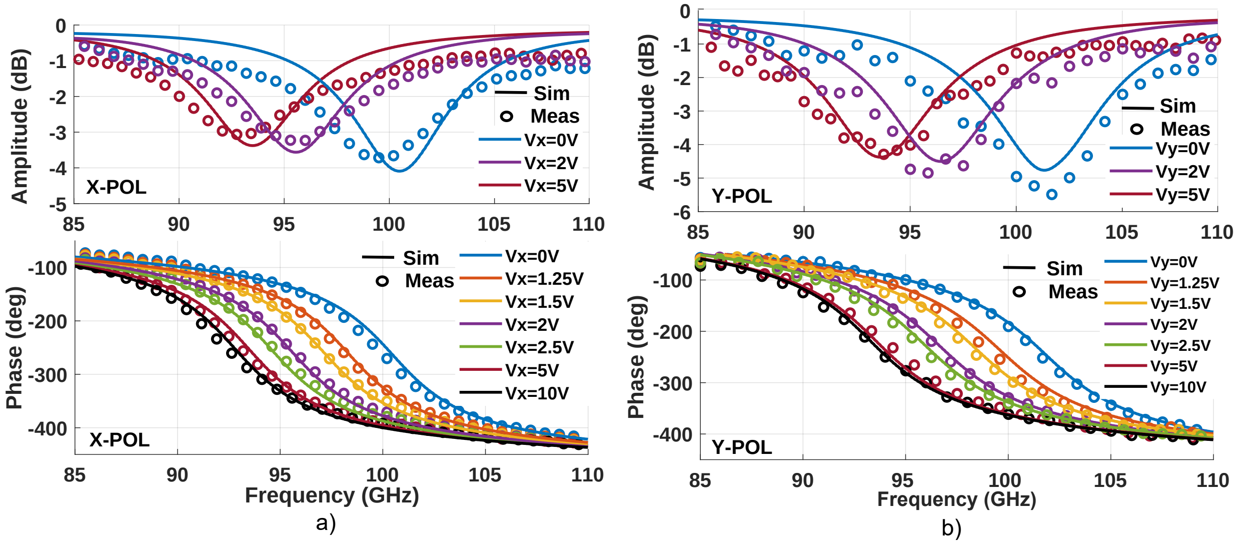

Figure 3.18: Measured (Meas) and Simulated (Sim) reflection coefficients (incidence angle $\phi_{inc} = 0°, \theta_{inc} = 30°$) as a function of the frequency. a) S_{XX} with $V_y = 0$. b) S_{YY} with $V_x = 0$.

Although the antenna is capable of scanning continuously, a total of twelve beam configurations, six per polarization between 5º and 40º, have been measured. The simulated and measured cuts of the gain radiation patterns in the scanning plane are shown in Figure 3.22. Moreover, the cross-polar patterns are depicted in Figure 3.23. As can be seen, each polarization behaves very similarly when pointing towards different directions. The achieved gain is 25 dBi and the corresponding efficiency is 24%. The gain is consistent with this kind of antenna, considering that an ideal reflectarray aperture would provide 36dB gain (including spillover and illumination efficiency), and that the ohmic losses, one-plane focusing, limited phase range (continuous 200º), and phase errors have been estimated to approximately represent 1.5dB, 6dB, 1.4dB and 2.1dB gain reduction respectively (See Table 3.1).

These estimated gain losses are obtained for the maximum beam direction. For other directions, not only these gain losses should be considered, but also the additional scanning losses. Moreover, it is worth noting that the losses in other pointing directions can fluctuate due to the lossy nature of the array. That is, even after considering the aforementioned optimization of the voltage synthesis through the phase constants, certain beam directions can be lossier than others, impacting on the final gain. However, these differences have proven to be minimum in practice. The minimum SLL is of 9dB in the entire scanning range and for both polarizations. Close to the specular direction, this SLL is improved to 13.5dB, and it worsens with increasing scanning angle due to the abrupt phase variations leading to greater phase errors.

The set of measured beam configurations (from 5º to 60º) are chosen considering the blockage of the feeding chain and the holder for the horn antenna. However, if the distortion and gain reduction due to the scattering on these elements are assumed, the scanning range could be drastically increased to negative angles as well. Moreover, additional simulations show that the antenna can further beam-steer to ±60° at the expense of assuming the inherent scanning

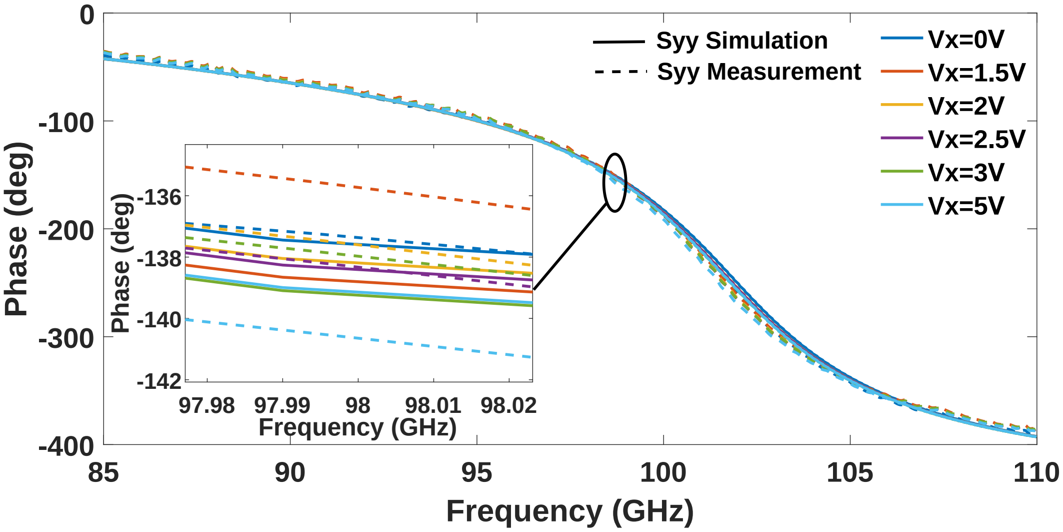

Figure 3.19: Measured and simulated S_{YY} phase for different X-polarization biasing states (V_x), keeping $V_y = 0$.

Ideal Reflectarray Gain	**36dBi**
Ohmic Losses	**1.5 dB**
LC Loss	1.1dB
Quartz Loss	0.2dB
Metal Loss	0.2dB
Other Losses	**9.5 dB**
One-plane focusing	6dB
Limited phase range	1.4dB
Phase errors	2.1dB
Cross-Polarization	<0.1dB
Achieved Gain	**25dBi**

Table 3.1: Breakdown of estimated gain losses.

losses, although no experimental data is available.

Even though the agreement is excellent, there exist small mismatches between measurements and simulations (for instance, 40º beam at X-polarization), which are due to different sources of errors. First, inevitable manufacturing tolerances are present ($\sim 5\mu m$ in gold photolithography, $\sim 3\mu m$ in SU8 spacers, $\pm 20\mu m$ in quartz thickness, and so on). During the final checks, it was detected that one bias line was cut due to the photolithography process, introducing a small error. Second, there might be a small inaccuracy on the feed location, due to the 3D-printed plastic holder. It is worth noting that, close to 100 GHz, any mismatch can result in several wavelengths displacement. Third, the fact that the cell is limited to a 200º quantization. Fourth, inherent measurement errors such as alignment (near-field measurement in planar range), and unwanted reflections on the flex connectors, are also present. In order to better quantify the impact of those factors, a tolerance analysis has been carried out, which consisted on computing the cell response considering all the different sources of errors.

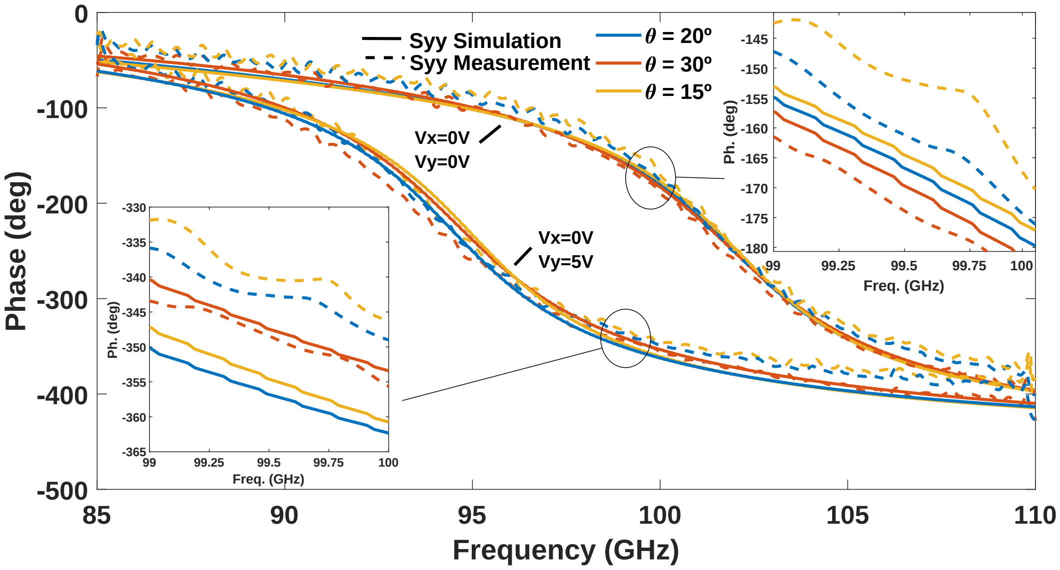

Figure 3.20: Measured and simulated S_{YY} phase under different incidence angles for two LC biasing states.

The worst-case scenarios for the phase deviation have been used to re-compute the far-field radiation patterns. The results indicate that the measured mismatches are consistent with the tolerances. Moreover, the tolerance analysis for the scanning angle of 40º also shows that the X-polarization is more sensitive to tolerances than the Y-polarization. However, even so, the differences between simulations and measurements for 40º X-polarization are not completely explained by the tolerances. Thus, this is attributed to a misalignment of the feeder that was detected when measuring this particular scanning angle, which could degrade the illumination to the reflectarray surface.

To experimentally assess the independence between polarizations, the radiation pattern in one polarization has been measured in the anechoic chamber for different biasing voltages of the other polarization. Leveraging the independence between polarizations, the voltages of each polarization have been chosen by considering the target unit cell phase of that polarization and assuming unbiased the other resonant element. Figure 3.24 shows the measured U-V radiation pattern for two different beam directions in X-polarization. As can be observed, when varying V_y to point the Y-polarization beam towards other directions, the X-polarization remains unchanged. Note that, due to the 1D scanning (LC bias addressing made by columns), as expected only one plane is collimated.

To this point, the radiation patterns have been obtained by illuminating the surface with a single linear polarization horn antenna, and rotating it to measure each polarization. However, the far-field radiation patterns have also been simulated under a simultaneous illumination of both modes assuming a dual-polarized antenna, which can be seen in Figure 3.25. The voltages configuration have been computed so that the X-polarization is reflected towards $\theta_t = 30°$ and the Y-polarization is reflected towards $\theta_t = 20°$. Then, the unit cell reflection coefficient is computed with the required pairs of voltages, which are in general different between them and both different than zero.

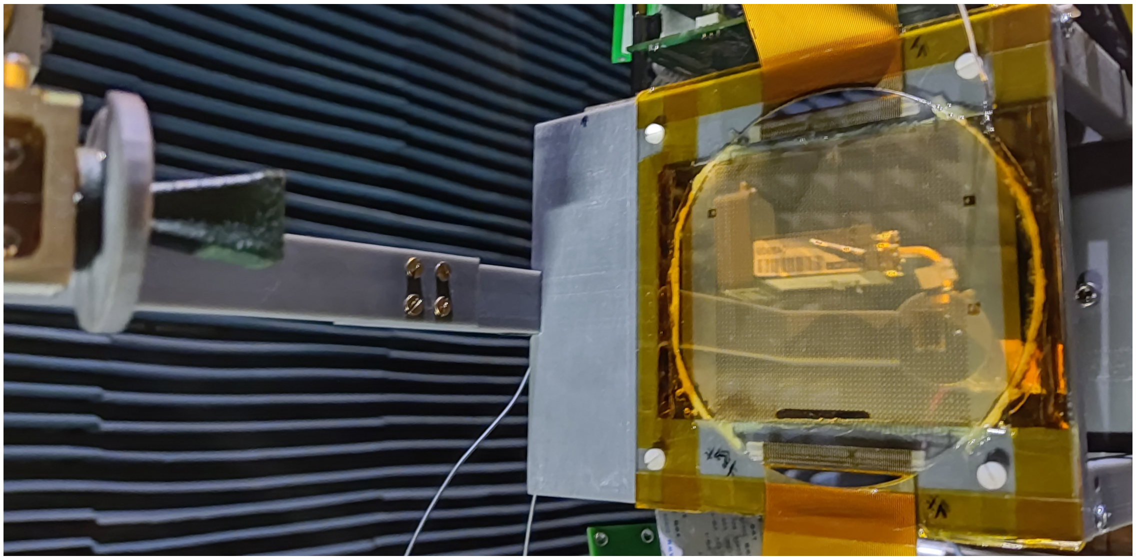

Figure 3.21: Antenna measurement setup in the anechoic chamber.

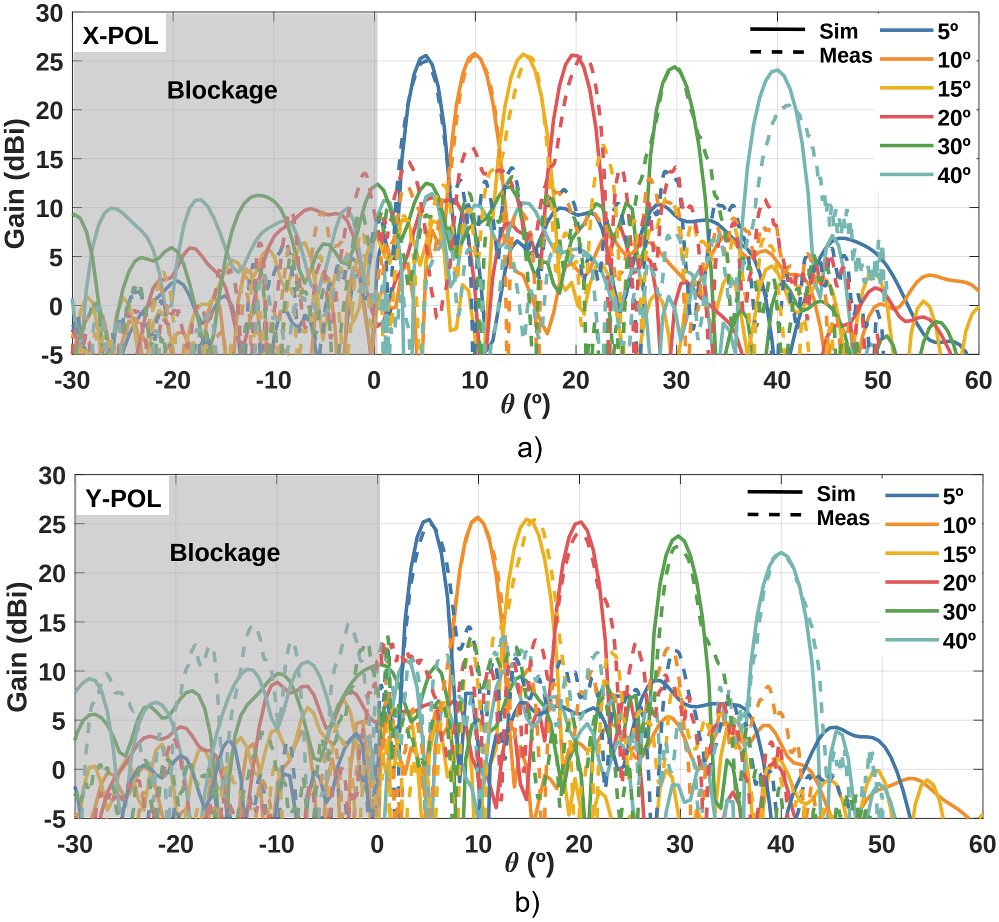

Figure 3.22: Measured (Meas) and Simulated (Sim) radiation patterns (98GHz) of the a) X-Polarization and b) Y-Polarization.

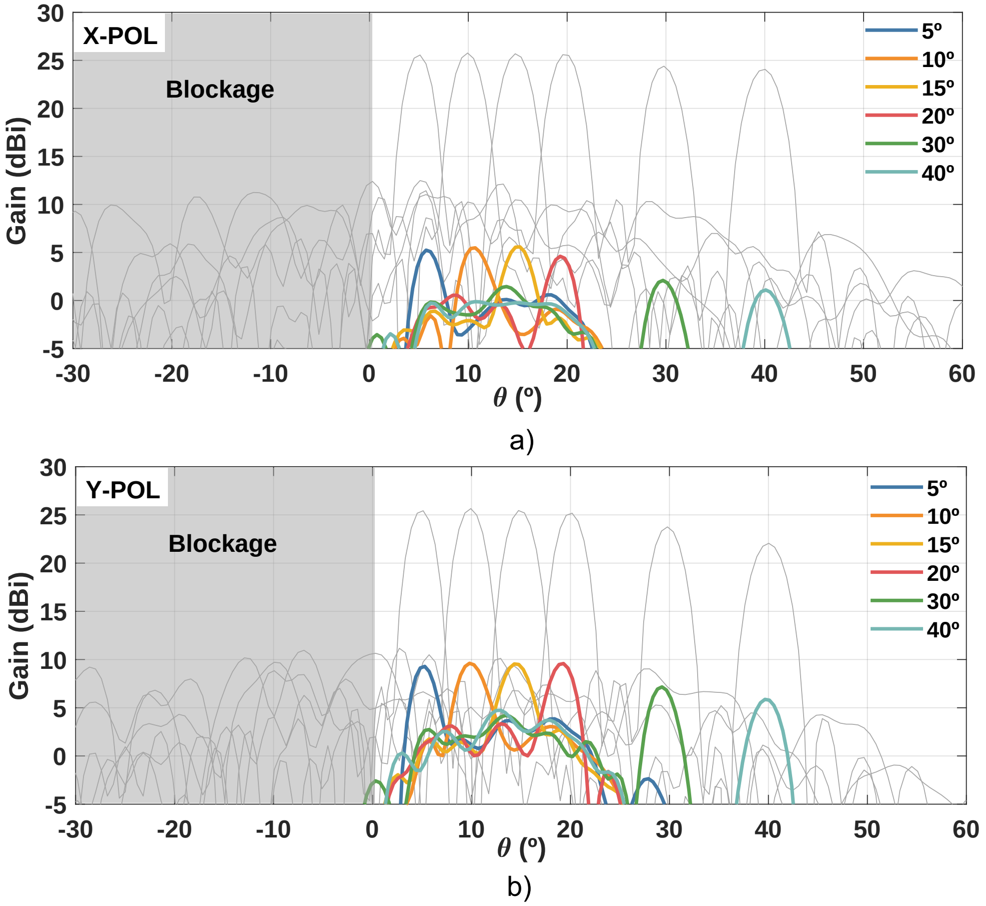

a)

b)

Figure 3.23: Simulated cross-polar radiation patterns (98GHz) of the a) X-Polarization and b) Y-Polarization. The co-polar patterns are shown in light grey color.

Finally, the reconfiguration time of the antenna, that is, the temporal transition between a certain configuration voltage is applied and the corresponding radiation pattern is achieved in a steady state, has been estimated to be around 20s, due to the large cavity thickness. The design of this antenna has not considered the response time, and therefore it is long. In Chapter 4, different techniques to improve this reconfiguration time are investigated.

Considering the obtained results, it is proven that multi-functional unit cells can be designed in LC technology. The proposed modeling strategy significantly alleviates the computation while being accurate, and the antenna is capable of steering both polarizations in a completely independent manner.

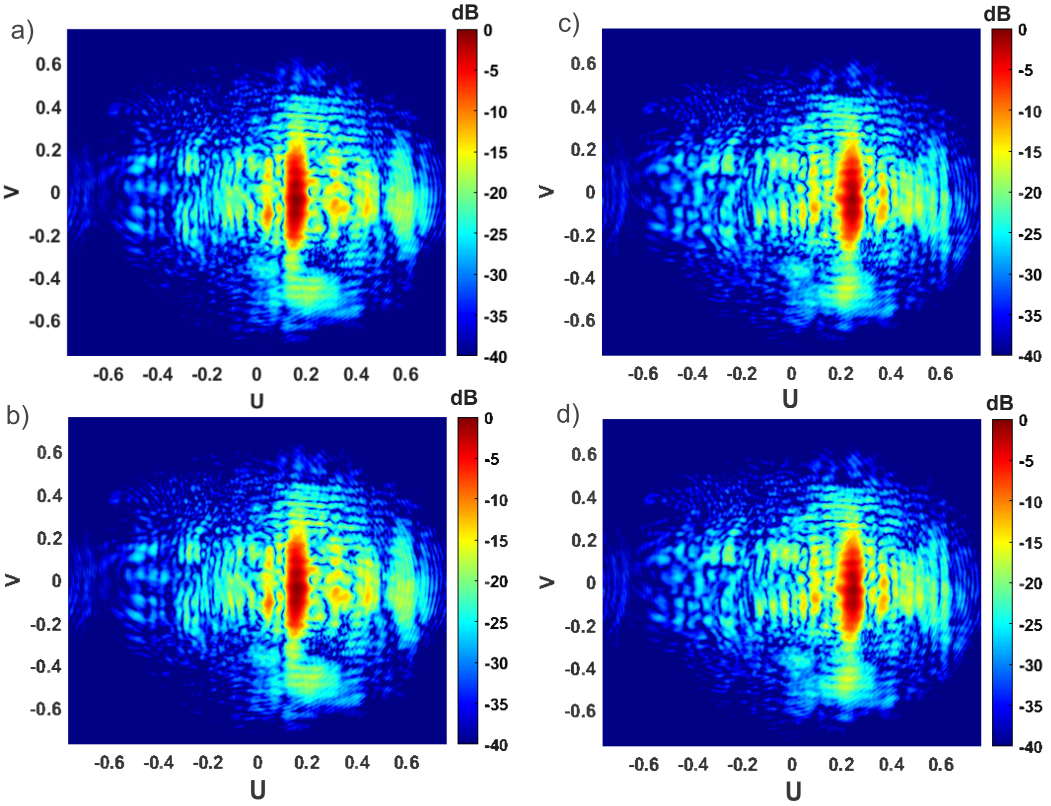

Figure 3.24: Measured X-polarization radiation pattern (normalized U-V diagram) when also varying the Y-polarization pattern. a) $\theta_{t,X-Pol} = 10^\circ$ when $\theta_{t,Y-Pol} = 20^\circ$ b) $\theta_{t,X-Pol} = 10^\circ$ when $\theta_{t,Y-Pol} = 10^\circ$ c) $\theta_{t,X-Pol} = 20^\circ$ when $\theta_{t,Y-Pol} = 20^\circ$ d) $\theta_{t,X-Pol} = 20^\circ$ when $\theta_t, Y - Pol = 10^\circ$.

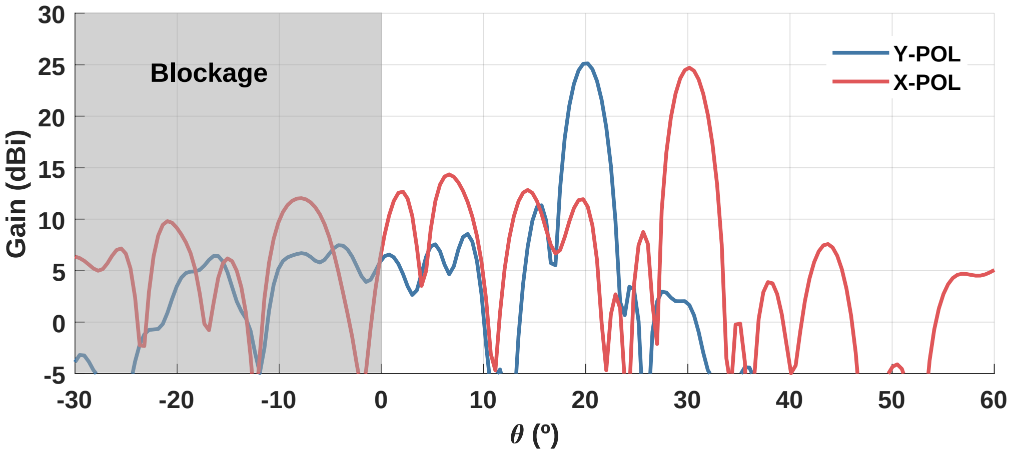

Figure 3.25: Simulated antenna radiation pattern when illuminated with a dual-polarized antenna, and simultaneously focusing each beam independently. The beam directions are $\theta_{t,X-Pol} = 30^\circ$ and $\theta_{t,Y-Pol} = 20^\circ$.

Chapter 4

Temporal Response Reduction of Liquid Crystal mm-Wave Devices

4.1 Introduction

The slow reconfigurability of LC mm-wave devices is one of the main drawbacks of such technology, and for some applications represents an important obstacle to overcome before it can be used in a real-world environment. While switching between states in optical devices takes from hundreds of microseconds to few milliseconds, the large thickness of the LC cavities in mm-wave devices yields much slower responses, typically in the order of several seconds or even minutes. Therefore, to become a competitive technology, reconfigurability times must be drastically reduced. In future ultra-reliable low-latency communication networks, improving these times until they are at least comparable to the channel coherence time is of utmost importance due to the stringent dynamic requirements of upcoming communication protocols.

As seen in Section 3.4.2, in nematic LC the molecules can be actively aligned with the appearance of an AC electric field across the cavity. Such transition is driven by a conversion of electric energy into elastic energy, which can be accelerated by increasing the magnitude of the driving voltage. However, when this AC electric field is removed to rotate back the molecules to their original relaxed state, the only force moving them is due to the surface anchoring and it is not controlled by any external force. Since this decay time usually is quadratically proportional to the cavity thickness, the fact that these cavities are 10-50X larger in mm-wave devices than in optic devices makes them excessively slow. Reducing the thickness could be an initial strategy to reduce reconfigurability times. However, by doing so one of the main design variables is no longer available for optimization, and for instance, in resonant devices such as reflectarrays, the risk of getting undesired critically coupled resonances greatly increases [82]. Using a mixture with reduced rotational viscosity parameters can also help improving the response times. However, this generates a trade-off in the mixture design itself, usually leading to high absorption or low tunability. Therefore, in RF, novel strategies are required for this technology to overcome the temporal constraints.

In this chapter, a dynamic model to predict the temporal response of the LC in mm-wave devices is introduced, and three different techniques that use such model to accelerate the reconfigurability of these devices are proposed. Finally, the dynamic far-field radiation is studied, as well as the impact of the different LC addressing waveforms into the transition dynamics.

4.2 Dynamic model of the Liquid Crystal response

In the previous chapter, a LC model has been presented, which provides the static relation between the quasi-static electric field in the cavity and the tilt angle of the molecules in the volume. Then, the tilt angle can be related to the volumetric permittivity that describes the LC material in electromagnetic terms. This model, however, only provided information in stationary states and, as such, is only valid when enough time has passed after an external excitation has been applied. It allows predicting the tilt angle of the molecules when they already lie in a stationary state, but not the real-time rotation during the transition of a changing quasi-static electric field, also known as the Fréedericksz transition.

Therefore, in order to study the temporal responses of different materials and under different excitations, a dynamic model that considers the transitions must be used.

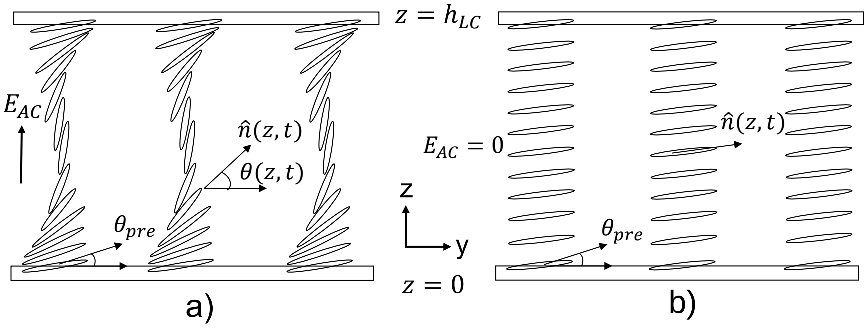

Figure 4.1: Time-dependent behaviour of LC molecules in a cavity. a) LC cavity with applied electric field b) LC cavity without excitation.

4.2.1 Modeling approach of the LC dynamics

Assuming that the applied quasi-static electric field is homogeneous across the cell, which as previously noted is feasible if the effects of transverse inhomogeneity are negligible, the dynamic behaviour of the LC under a such external excitation is described by the Ericksen–Leslie equation [83, 84, 29]:

$$(K_{11}cos^2\theta + K_{33}sin^2\theta)\frac{\partial^2\theta}{\partial z^2} + (K_{33} - K_{11}) \cdot sin\theta \cdot cos\theta(\frac{\partial\theta}{\partial z})^2 + \\ (\alpha_2 sin^2\theta - \alpha_3 cos^2\theta)\frac{\partial v}{\partial z} + \varepsilon_0 E_{z,AC}^2 \Delta\varepsilon_{AC} \cdot sin\theta \cdot cos\theta = \gamma_1\frac{\partial\theta}{\partial t} + I\frac{\partial^2\theta}{\partial t^2}, \quad (4.1)$$

where α_i are the Leslie viscosity coefficients, v is the flow velocity, $E_{z,AC} = V/d$ is the applied AC electric field, $\Delta\varepsilon_{AC}$ is the low-frequency dielectric anisotropy, γ_1 is the rotational viscosity and I represents the inertia. As can be seen, this equation is practically the same as Equation (3.8) but introducing additional terms related to the LC rotation dynamics. Note that, contrary to the stationary case, here $\theta(z,t)$ depends both on the molecule position and the time, as can be seen in Figure 4.1 for two states.

From Equation (4.1), two modifications can be safely made to simplify it. First, the inertia term is typically neglected as it has a very small weight [85]. Second, the Leslie coefficients terms can be disregarded, as they also play a minor role and obtaining them requires experimental measurements [86, 29]. Their impact will be seen later on in relation to backflow effects. Therefore, the previous equation reduces to [87, 88]:

$$(K_{11} cos^2\theta + K_{33} sin^2\theta)\frac{\partial^2\theta}{\partial z^2} + (K_{33} - K_{11}) \cdot sin\theta \cdot cos\theta(\frac{\partial\theta}{\partial z})^2 + \varepsilon_0 E_{z,AC}^2 \Delta\varepsilon_{AC} \cdot sin\theta \cdot cos\theta = \gamma_1 \frac{\partial\theta}{\partial t}, \quad (4.2)$$

which allows the time-varying director to be found.

Similarly to the equation in statics, Equation (4.2) is too complex to be solved analytically. As a consequence, oftentimes assumptions that allow obtaining approximate analytical solutions are made. One of the most common simplifications, also known as one constant approximation, consists on assuming that the bend, splay, and twist constants are equal ($K_{11} = K_{33}$), as this greatly reduces the previous expression. Depending on the mixture, this assumption holds relatively well. A second habitual simplification consists on considering that the LC is biased with a low voltage source, which allows modelling the $\theta(z,t)$ curve with a sinusoidal function, so that $sin(\theta) \sim \theta$. Considering these two premises, Equation (4.2) can be rewritten as:

$$K_{11}\frac{\partial^2\theta}{\partial z^2} + \varepsilon_0 E_{z,AC}^2 \Delta\varepsilon_{AC}\theta = \gamma_1 \frac{\partial\theta}{\partial t} \quad (4.3)$$

In this case, there exists a closed solution for the time-dependent tilt angle along z, which takes an exponential form with the following decay and rise time constants:

$$\tau_d = \gamma_1 \frac{d^2}{k_{11}\pi^2}, \quad (4.4)$$

$$\tau_r = \frac{\tau_d}{\left|\left(\frac{V}{V_{TH}}\right)^2 - 1\right|}, \quad (4.5)$$

where it can be observed that, as expected, the decay response of Equation (4.4) depends only on the cavity thickness and the material properties, while the rise response of Equation (4.5) is driven by the quasi-static electric field voltage.

Nevertheless, these expressions oversimplify the dynamic problem, since zero pretilt is also assumed, which is not realistic [89]. Moreover, they are restricted to small voltage excitations only, as this is where the tilt angle approximation by a sine function holds. This leads to another impediment, which is that a driving voltage greater than V_{TH} will result in large errors, but as will be seen later on, in practice much greater voltages are needed to operate a fast LC mm-wave device. Although more elaborated expressions have been introduced in [88] to include pretilt effects, small angle approximations and single elastic constants ($K = K_{11} = K_{33}$ or $K = (K_{11} + K_{33})/2$) are still assumed.

Most of these models are good enough to model the LC in optic devices. In those, the phase change that occurs from these tilt dynamics can be well modelled, and the optical intensity change can be well predicted, since for such a short wavelength the LC is simply a medium in which several π-times phase changes happen [89]. The input light polarization is generally kept within the cavity, and an isotropic material considering the permittivity of that polarization provides very accurate results. However, in mm-wave devices, where resonant metallizations are required at the unit cells to achieve a sufficient phase range up to a few π-times, the RF electric field becomes more complex. The introduced higher-order modes generate relevant field components in all directions, and the material anisotropy must be considered. Therefore, the phase changes originated from the tilt angle dynamics are much more intricate to predict. That is, since the phase change is produced by the resonant elements, such as printed dipoles, the cavity can not be modelled with a medium constant anymore. Furthermore, in optics, the cavities are typically much narrower ($\sim 10um$) than in microwave devices ($\sim 100um$), being such thick cavities quite unexplored and not modelled. In [41], the static voltage dependence of LC is studied and accurately predicted in reflecting surfaces, but the dynamics are not tackled. In [90], the LC temporal behaviour is experimentally measured for different commercially available materials, but a model is not provided. Therefore, it is necessary to solve Equation (4.2) for resonant cells without any of these limitations, so that an appropriate model is achieved considering the number of layers and the inhomogeneity to consider, and to be validated with measurement data.

The followed approach will consist on (i) solving the dynamic LC director for different state transitions; (ii) obtaining the permittivity tensor associated to each timestamp; (iii) computing the reflection coefficient of the unit cells at each timestamp. Additionally, a comparison between different simulation techniques will be carried out, together with an experimental validation of the results.

4.2.2 Model results in mm-wave cells

Dynamic LC director

In order to accurately model the tilt angle dynamics of the LC when an excitation change occurs, Equation (4.2) is computationally solved along z and t using a finite elements method in COMSOL Multiphysics. This avoids several error sources as we specifically consider the pretilt effects and a more complete set of elastic constants, obtaining a more precise data for the $\theta(z)$ curves at any timestamp and LC driving voltage. Moreover, this allows to model any kind of excitation beyond step-like functions, although if the excitation signal has a frequency high enough so that its period is much smaller than the relaxation time of the LC, it can be substituted by its root mean square (RMS) value in Equation (4.2).

Figure 4.2 shows the molecules tilt angle (θ) as a function of the cavity height (z) for different timestamps in three different rise excitation scenarios, in a $75\mu m$-thick cavity filled with the

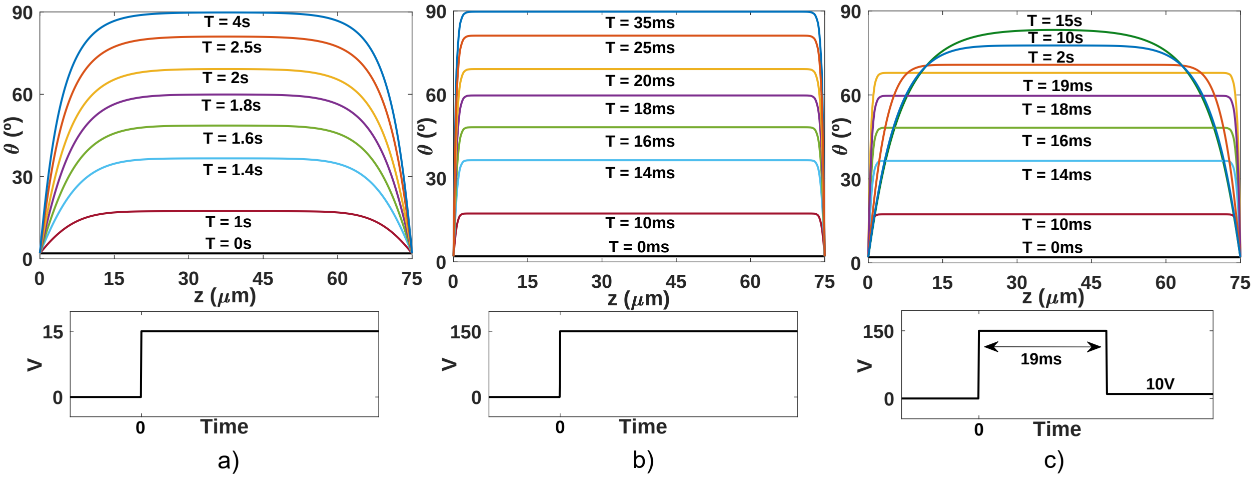

Figure 4.2: Tilt angle dynamics during rise transitions in a $75\mu m$-thick cavity filled with GT3-23001 LC. a) Step transition from 0V to 15V b) Step transition from 0V to 150V c) Transition from 150V to 10V after 19ms. The electric signal of each transition is shown at the bottom.

GT3-23001 LC mixture. It can be observed how, as compared to small voltage excitations (Figure 4.2(a)), large excitations result in faster transitions. Moreover, the tilting is much more homogeneous throughout the entire cavity (Figure 4.2(b)). Similarly, Figure 4.3 shows the evolution of the molecules tilt angle after two different decay transitions, that is, after removing the electric field from the cavity.

As can be observed, the tilt solutions differ substantially from a sine function, especially for large voltages. Moreover, the solutions show how the timings of the rising transitions depend on the voltage, whereas in the decay transitions the initial voltage is practically irrelevant.

By using the proposed method, Figure 4.4 shows the error on the computed rise time (10% to 90%) when the sine approximation and Equations (4.4) and (4.5) are used with respect to the real solution of Equation (4.2) for the same cavity. As expected, the results show that is necessary to rigorously model the cell, especially in the high voltage regime, given that errors larger than 10% could be made when predicting the LC temporal behaviour, which in turn induces large errors in the cell RF reflected phase as a function of time.

Dynamic RF response

Once the different tilt angles along z are obtained for each timestamp of a certain transition, and therefore $\vec{n}(z,t)$ is known, it is necessary to compute the permittivity tensors in accordance with the formulation of Equation (1.2).

After the permittivity model has been calculated using COMSOL Multiphysics, this is used in an electromagnetic simulator (CST Studio) with the aim of obtaining the electrical parameters of a periodical reflective cell in RF. Similarly to the case of the unit cell studied in Chapter 3, the simulation scenario corresponds to an infinitely large planar surface of periodic unit cells with an impinging plane wave.

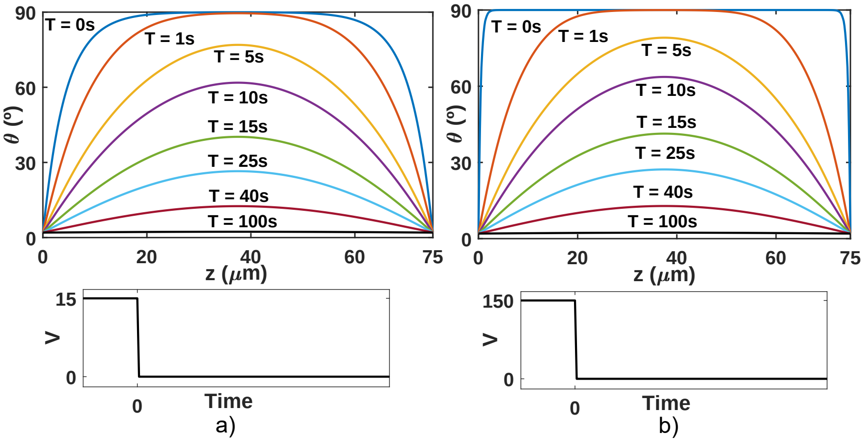

Figure 4.3: Tilt angle dynamics during decay transitions in a $75\mu m$-thick cavity filled with GT3-23001 LC. a) Step transition from 15V to 0V b) Step transition from 150V to 0V. The electric signal of each transition is shown at the bottom.

To accurately model the LC inhomogeneity along z and during the transitions, a comparison between two alternative strategies has been performed, as depicted in Figure 4.5. The first strategy stratifies the LC cavity in N uniform layers, in a similar way to [41]. In each layer, an average director tilt angle of the corresponding volume is assumed, so that the inhomogeneity along z is considered. Therefore, the larger the number of layers N, the more realistic and accurate this assumption will be, but the computation becomes more expensive. In fact, the computation becomes exponentially inefficient with increasing N, even more than in [41] due to the multiple simulations needed for a dynamics study.

On the other hand, an average of the tilt angle across the entire cavity has been considered in order to work with a single-layer material encompassing the permittivity inhomogeneity across z. The purpose of doing so is to find a trade-off between accuracy and efficiency given that a multi-layer electromagnetic analysis is very costly. Note that this is more precise than directly averaging the permittivity across z, as the molecule tilt angle is being taken into account. By doing so, a certain error is added to the model, which will result in small RF phase errors. However, this comes with a great benefit in simulation efficiency terms. Specifically, this latter approach is more reliable with extreme biasing voltages, when most of the molecules are either fully relaxed or fully rotated, since the $\theta(z)$ curve is either zero or saturated. This translates to a better match between the averaged tilt and the local tilt values across all z, and to a negligible difference with the exhaustive stratified method. This can be noticed in the top curves of Figure 4.2, where the 150V excitation makes almost all molecules along z to be rotated 90º at $T = 35ms$, in contrast with the 15V excitation at $T = 4s$.

As a consequence, when using intermediate voltages, the stratified procedure will perform slightly better but its complexity will increase abruptly. Figure 4.6 compares the phase evolution over time of such layered models by considering different rise transitions in a 1, 3, 5 and 20-layered unit cell. It can be observed how there are small differences in phase, thus denoting how the single layer (average) method is really precise, especially at large voltage excitations, as opposed to the analytical approximations. When comparing the homogeneous

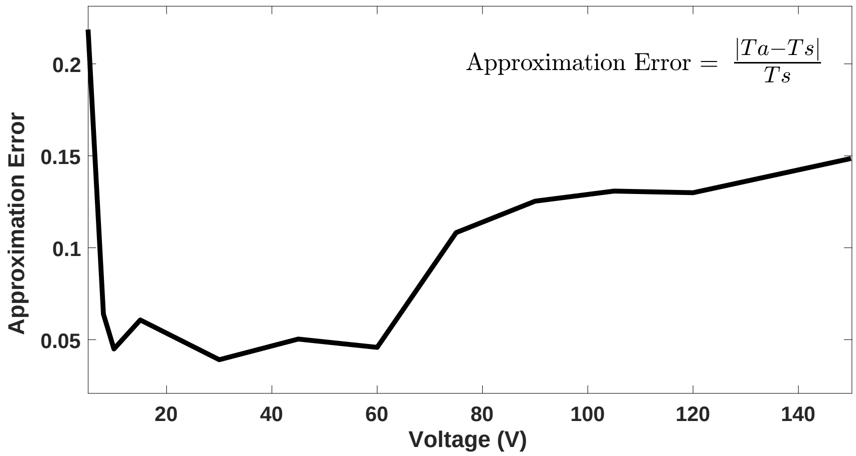

Figure 4.4: 10%-90% rise time approximation error compared to the solver solution in a 75μm thick cavity. Ta refers to the approximated time from the closed expressions and Ts refers to the simulated time from Equation (4.2). It can be observed how the closed expressions fail for large voltages, as the sinusoidal approximation becomes invalid, as well as the Vth effect.

case with the stratified model, these differences are observed to be reduced, of around 20º in the worst case, and tolerable considering that the corresponding degradation of the radiation pattern for such phase deviation is negligible [91, 5].

Moreover, it is observed that for large voltage excitations the difference between both methods disappears (20º and 0.5º difference in 5V and 150V excitation respectively). The error is similar to that found in [41] for statics, but it is generalized here for dynamics. Therefore, for the rest of the Chapter, single-layer modelling is carried out with the aim of increasing computation efficiency at a reduced accuracy loss, especially at high voltages. As will be seen later on, high-voltage excitations are of special interest for overdrive technique to reduce reconfigurability times. However, the stratified approach could be followed for a perfectionist modelling at higher computational cost. For mid-range problems, increasing the number of layers until the accuracy converges is a reasonable procedure.

Experimental validation

In order to validate the simulated dynamic results, the transient phase-curves at a certain frequency are compared against experimental data, captured from a reflectarray antenna whose unit cell is shown in Figure 4.7, containing a LC cavity filled with GT3-23001 from Merck ($K_{33} = 34.5pN; K_{11} = 24pN; \gamma_1 = 746mPas; \varepsilon_{||} = 3.27; \varepsilon_{\perp} = 2.47; \Delta\varepsilon_{AC} = 4.6$) sandwiched below a quartz superstrate ($\varepsilon_r = 3.78, tan\delta = 0.002$). The complete antenna consists on 60 x 60 identical cells (see Figure 4.8(a)), and its phase response is shown in Figure 4.9 for extreme excitations (OFF state corresponds to $V = 0$ and ON state corresponds to $V >> V_{TH}$) in stationary regime. Note that the resonant element dimensions of the cells are the same as those in Section 2.2.1.

The reflective measurement setup is similar to the one discussed in Chapters 2 and 3, but with slight modifications that allow acquiring the dynamic cell phase curves at each timestamp

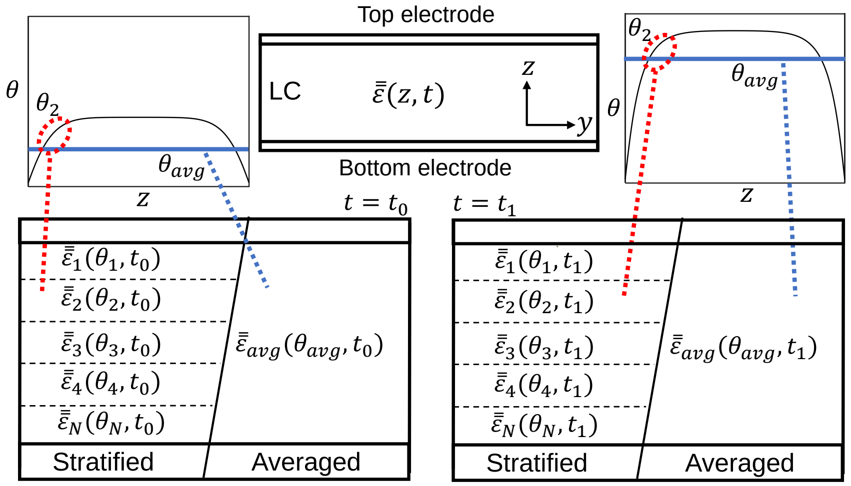

Figure 4.5: Stratified and averaged LC cavity dynamic modelling strategies. In the stratified strategy, $\bar{\bar{\varepsilon}}_i(\theta_i, t)$ is computed with Equation (1.2) and considering as θ_i the average tilt within the layer i. In the averaged strategy, $\bar{\bar{\varepsilon}}_{avg}(\theta_{avg}, t)$ is computed considering as θ_i the average tilt across the entire cavity.

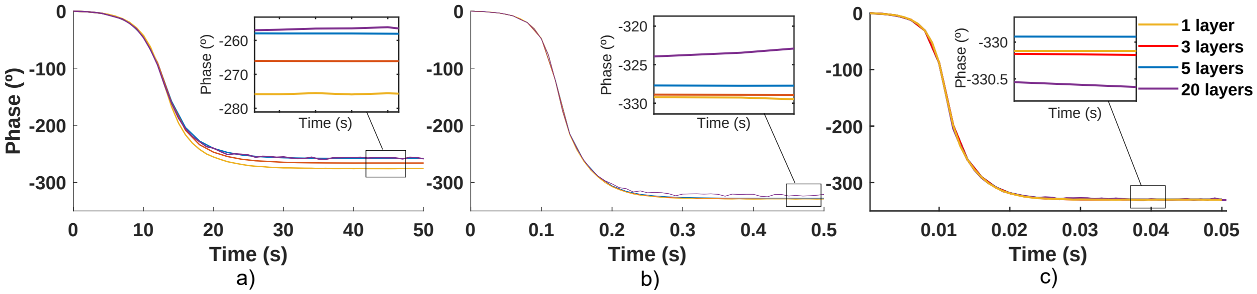

a)

b)

c)

Figure 4.6: Stratified simulation convergence study at 97 GHz a) from 0V to 5V b) from 0V to 45V c) from 0V to 150V.

for a specified frequency, incidence angle and bias signal. A diagram and a picture of the implemented setup can be seen in Figure 4.8(b) and 4.8(c). An arbitrary waveform generator (Keysight 33611A), programmed to output different bias signals, drives the LC of the reflectarray antenna through a x15 voltage multiplier. All unit cells of the antenna are short-circuited so that the LC is excited equally along the entire array, ensuring specular reflection. To synchronize the different biasing changes with the VNA captures, the waveform generator sends a SYNC signal to the VNA, which guarantees a timely capture of the transition. The VNA has been previously calibrated with a metallic plane reference and equipped with a pair of horn antennas, as explained in Chapter 2, and captures the evolution of the transmission scattering parameters at 97 GHz and 102 GHz when the bias signal sequence starts. The selection of those frequencies is based on the available phase range, as this is where the cells show the maximum phase course within the band of operation of the 360º cell, thus allowing the detection of the maximum phase errors. Both the experiments and the electromagnetic simulations have been carried out considering an impinging angle of 30º with respect to the normal of the reflectarray plane ($\phi_{inc} = 0º$, $\theta_{inc} = 30º$).

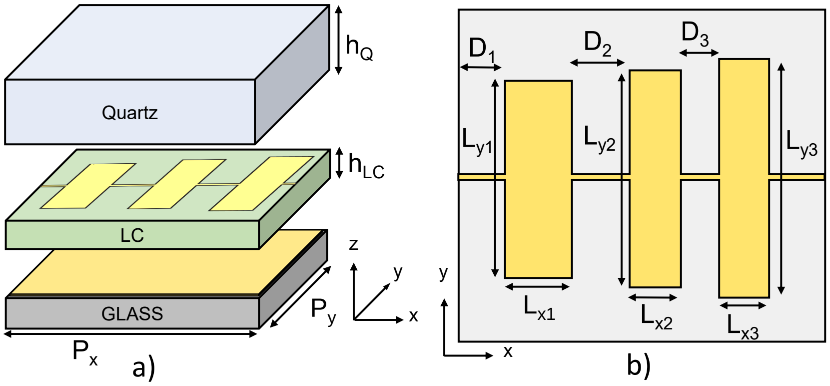

Figure 4.7: a) LC cavity with applied electric field b) LC cavity without excitation c) Layered view of the reflectarray unit cell d) Top-view of the reflectarray unit cell. Dimensions (mm): $D_1 = 0.171$, $D_2 = 0.096$, $D_3 = 0.042$, $L_{y1} = 0.707$, $L_{y2} = 0.748$, $L_{y3} = 0.792$, $L_{x1} = 0.2$, $L_{x2} = 0.211$, $L_{x3} = 0.2$, $P_x = 1.145$, $P_y = 1.093$, $h_Q = 0.55$, $h_{LC} = 0.075$.

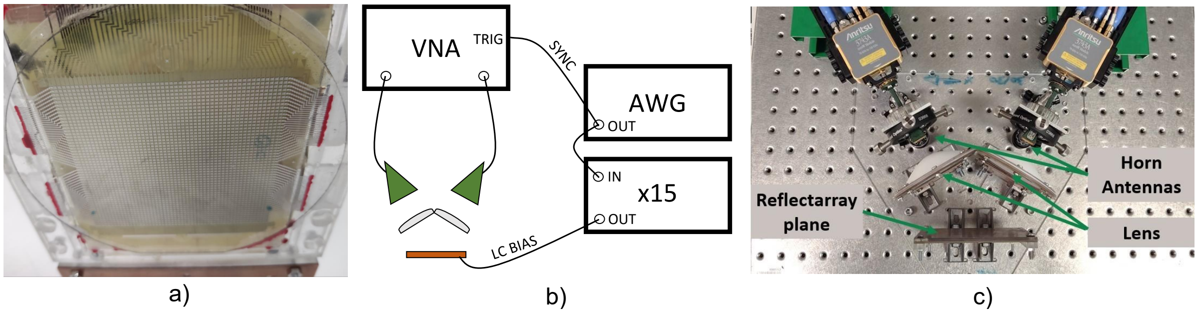

Figure 4.8: Measurement setup. a) Reflectarray picture b) Block diagram of the setup c) Quasi-optical bench picture

Figure 4.10(b) compares simulations and measurements of the transient reflected field phase at 102 GHz as a function of time for different voltage rise transitions starting from a steady state, verifying that the method can predict the actual cell behaviour relatively well. The model has been validated with relaxation measurements as well. Figure 4.10(c) shows simulation and measurement data of the reflected field phase evolution at 102 GHz for different decay transitions parting from varying voltages. During the modeling, the applied 1 kHz square signal allows to assume an amplitude equal to its RMS value in Equation (4.2). The corresponding biasing signals are shown in Figure 4.10(a).

Thus, the transitions obtained with such model match the experimental data both in rise and decay time, as well as in phase range. It can be seen how, as expected, differences in the applied voltages generate important differences in the temporal behaviour of rise transitions, from several seconds to milliseconds, while on the contrary the decay transitions are not so dependent of the biasing, showing similar evolution regardless of the driving amplitude at $T = 0$. There exist small discrepancies ($<30^{\circ}$) between the expected and measured phase range in the permanent regime, which can be explained by the phase curve in Figure 4.9, where the phase difference between both states slightly differs. It is worth noting that this range of errors is tolerable when designing the phases of a radiation pattern, and is comparable to a 3-bit

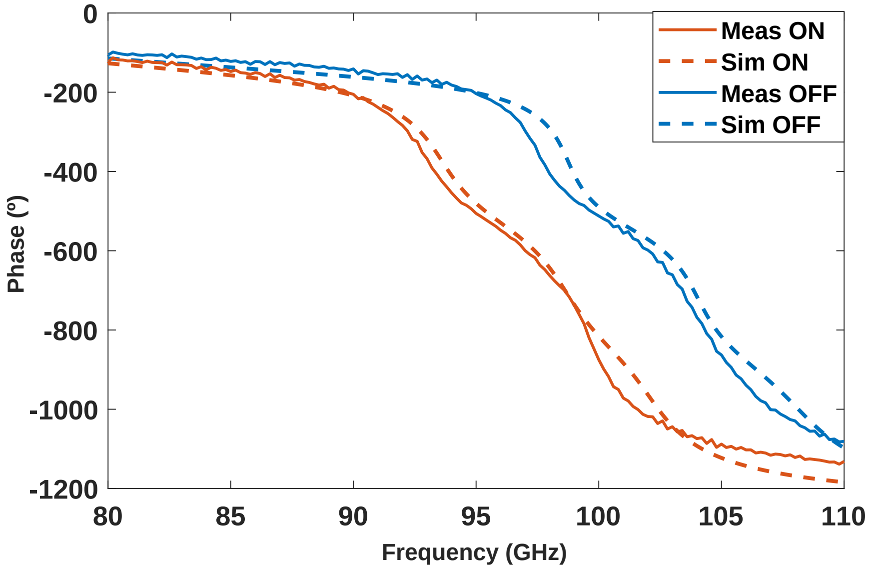

Figure 4.9: Phase of the reflection coefficient at steady state ($t \to \infty$). Dashed lines indicate simulation data and flat lines indicate experimental measurements.

phase quantization, which is not an impediment to perfectly synthesize a collimated beam and only deteriorates gain by 0.2 dB and SLL by 0.8 dB [91]. Apart from the phase range errors, transient regime errors up to 200º in the worst case of $V1 = 8V$, are also identified. These can be associated to different sources, including the single-layer assumption and especially the pretilt angle estimation and LC RF characterization, which plays an important role in the temporal response of these devices. In order to reduce this error, a denser layer stratification could be chosen by assuming a lower computational efficiency, considering their trade-off. Additionally, it should be mentioned that different error sources could be compensated in the model by performing, a posteriori, an effective parameter tuning for each voltage curve using measurement data.

4.3 Overdrive and underdrive

The dynamic modelling of LC multi-resonant cells, obtained and experimentally validated in Section 4.2, enables the development of bias voltage design techniques through simulations, which allow an improvement on the antenna reconfigurability times. To this point, only simple monotonous waveforms have been used, which represents the nominal driving technique. However, there is complete freedom in the waveform biasing, including the engineering of those considering the dynamic knowledge of the LC to accelerate the response. These methods can therefore be used to reduce both the relaxation times, through underdrive, and the rising times, through overdrive. As will be seen next, the main improvement occurs in the rising transitions.

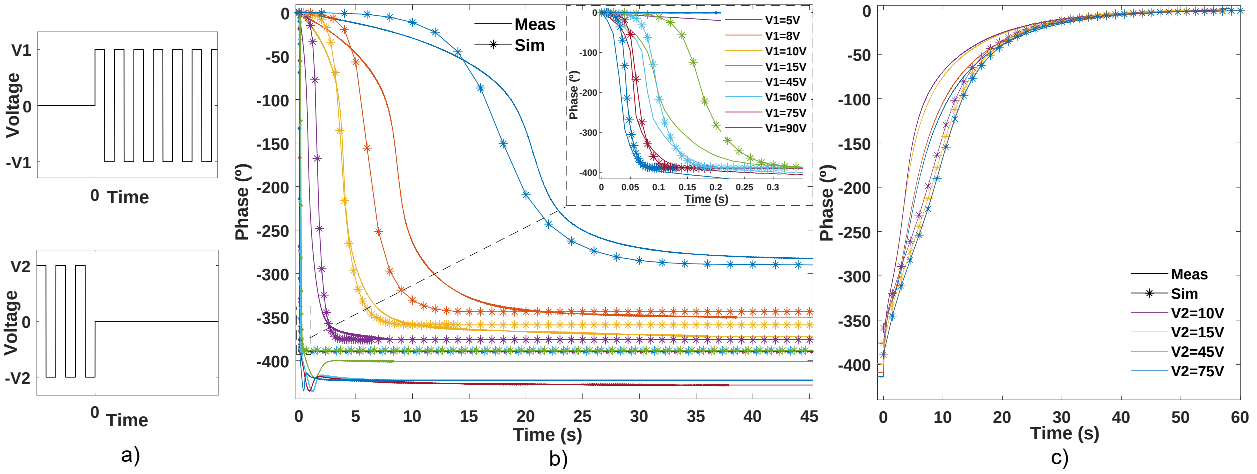

Figure 4.10: GT3-23001 phase transition dynamics at 102 GHz. a) 1 kHz biasing signal for excitation (top) and relaxation (bottom) dynamics. b) Excitation transient phase for different V1 values. c) Relaxation transient phase for different V2 values. The asterisk marker indicates simulation data and flat lines indicate experimental measurements.

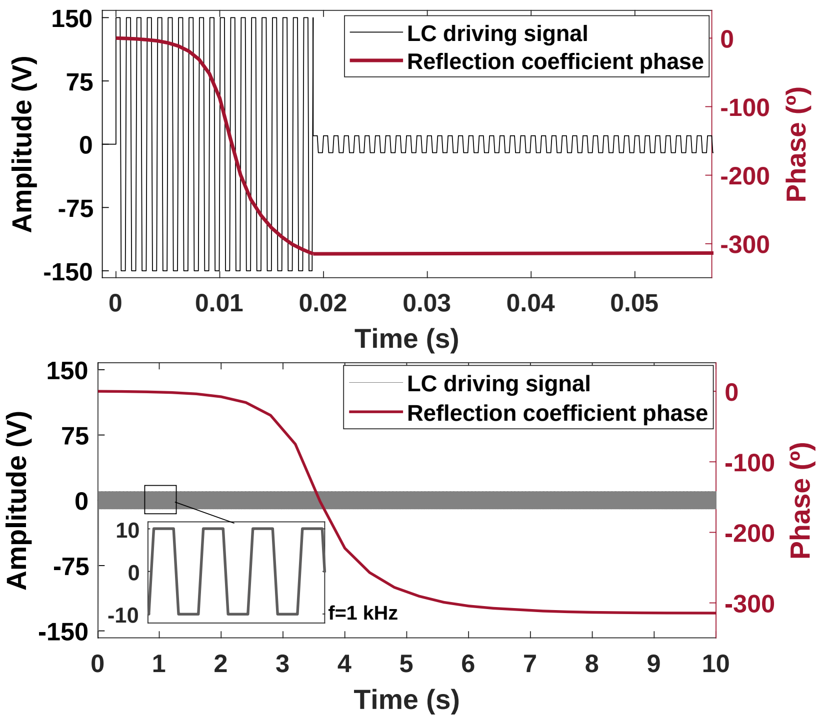

Figure 4.11: Examples of overdrive biasing technique (top) and nominal biasing (bottom).

4.3.1 Biasing synthesis

By leveraging an accurate temporal control of the LC, a timely driving of the LC cells can be used to accelerate the transition times between phase states. When the target voltage of the transition is above the initial state (i.e. the molecules rotate towards the z axis), the rise transition can be accelerated through overdriving. The biasing waveform is modified by using during a short period of time a larger voltage than the nominal biasing voltage (i.e. the voltage in which the cell presents the desired phase shift in permanent regime, after the molecules stopped rotating). An example of such biasing and its effect in the phase can be seen in Figure 4.11, where the overdrive LC driving signal amplitude is increased to 150V until the 10V objective reflection coefficient phase is achieved, instant in which the excitation is switched to the nominal 10V signal amplitude. As can be observed, in the example the overdrive technique improves by more than 5 seconds the nominal LC rise response.

When the target state of the transition is below the initial voltage (i.e. the molecules rotate towards perpendicular to z), a quicker reconfiguration is possible by means of underdrive, sometimes referred to as undershoot in optics literature. In this case, the LC is briefly driven at a lower voltage than the nominal one, for instance 0V.

The overdrive technique has been used in optic devices in the past [92], but by using approximations instead of an accurate profiling, and not in the mm-wave regime where the cell thickness and modelling become problematic.

In the case of aperture antennas where the objective parameter is the pixel phase, the design procedure of the LC overdriving signal for quickly achieving the desired phase of an array cell, defined by its dimensions and incidence angle, is the following:

1. Identify the nominal voltage that achieves the desired phase shift in stationary state.
2. Compute $\theta(z,t)$ for the rise transition towards the nominal voltage, by solving Equation (4.2).
3. Find the phase-time curve of such transition by solving the structure electromagnetically, for each timestamp, after finding $\overline{\overline{\varepsilon}}$ from Equation (1.2).
4. Repeat steps 2 and 3 for the rise transition towards the maximum voltage.
5. Pick, from the rise transition towards the maximum voltage, the timestamp in which the instantaneous phase matches the converged phase of the nominal transition.

Then, the driving signal consists on modifying the amplitude of the nominal biasing signal to the maximum voltage between $t = 0$ and the obtained timestamp. Regarding the underdriving signal design, the procedure is dual by using a drop transition towards a zero voltage. Given that implementing these strategies properly requires a very precise knowledge of the LC dynamics in the cells, and given that it is unfeasible to experimentally obtain such curves for each cell and incidence angle, it is necessary an accurate enough model, like the one previously proposed, that provides such information through simulations.

4.3.2 Experimental results

To validate the underdrive and overdrive methods, a set of transitions are accelerated by designing the proper biasing waveforms, and these have been used in the reflectarray surface of Figure 4.8(a) to measure, through the same setup, the corresponding phase responses.

In Figure 4.12, the results demonstrate that applying overdrive techniques to drive a reflectarray cell can significantly accelerate the rise time, achieving a 100-fold improvement. In Figure 4.13,

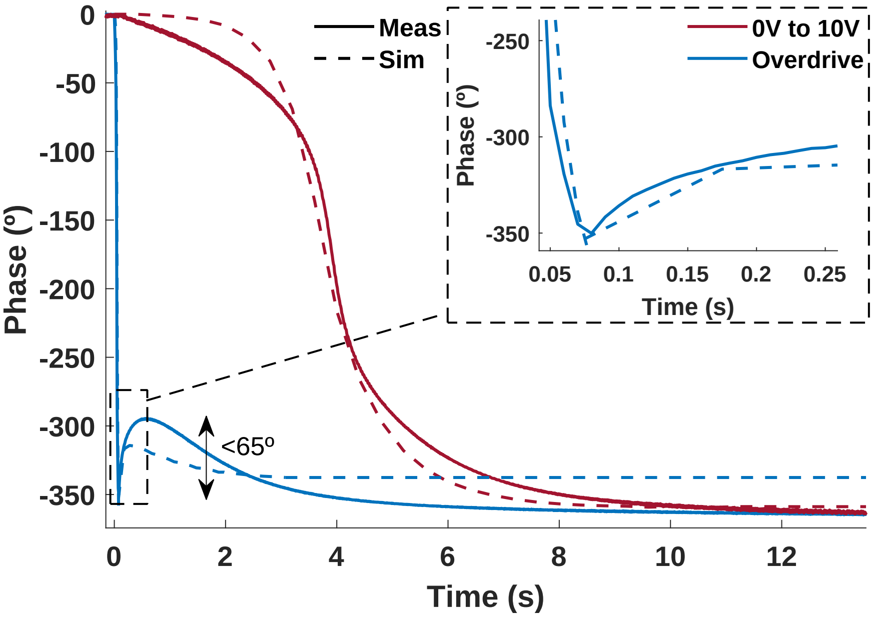

Figure 4.12: Measured and simulated phase of reflection coefficient at 102 GHz during a 0V to 10V transition. To quickly achieve the 10V state phase, we overdrive the LC to 75V during 75ms and then switch to the nominal 10V excitation.

measurements and simulations for both overdrive and underdrive techniques are compared against a normal biasing operation for different phase transitions at two representative frequencies in the band of design, and the corresponding bias signals are shown. It can be observed how overdriving allows a significantly quicker phase drop than the normal operation, reducing in several orders of magnitude the switching times. Although the underdrive technique also shows some time reduction (Figure 4.13(d)), its effect is not so pronounced, as the decay transition is less dependent on the excitation.

Interestingly, there is a rebound effect captured in some of the phase transitions just after reaching the objective phase under the overdrive excitation, as shown in Figure 4.12 and the middle row of Figure 4.13. This bounce is the manifestation of both the bias signal commutation (which causes the molecular reorientation of Figure 4.2(c)) and the backflow effect [93, 88, 94, 95], which appears as a consequence of working in the high-voltage regime in thick cells and that our model did not completely capture. This is a well known phenomenon that could be included in the problem derivation if details about the LC Leslie coefficients were available, either through manufacturer data or through experimental estimation [96, 86]. This would make the model more accurate but more computationally costly. Even though this effect deteriorates the experimental measurements as the phase oscillates slightly (<65º in Figure 4.12) until reaching the final value, the objective phase state can still be achieved much faster than under a nominal excitation, being the instantaneous phase during such transient effect only deviated ±20%.

The maximum voltage used in the designed waveforms is 150V. However, since the behaviour of the LC during the rise transitions depends directly on the driving amplitude, larger applied voltages could theoretically reduce the rising times. In practice, this is limited by the

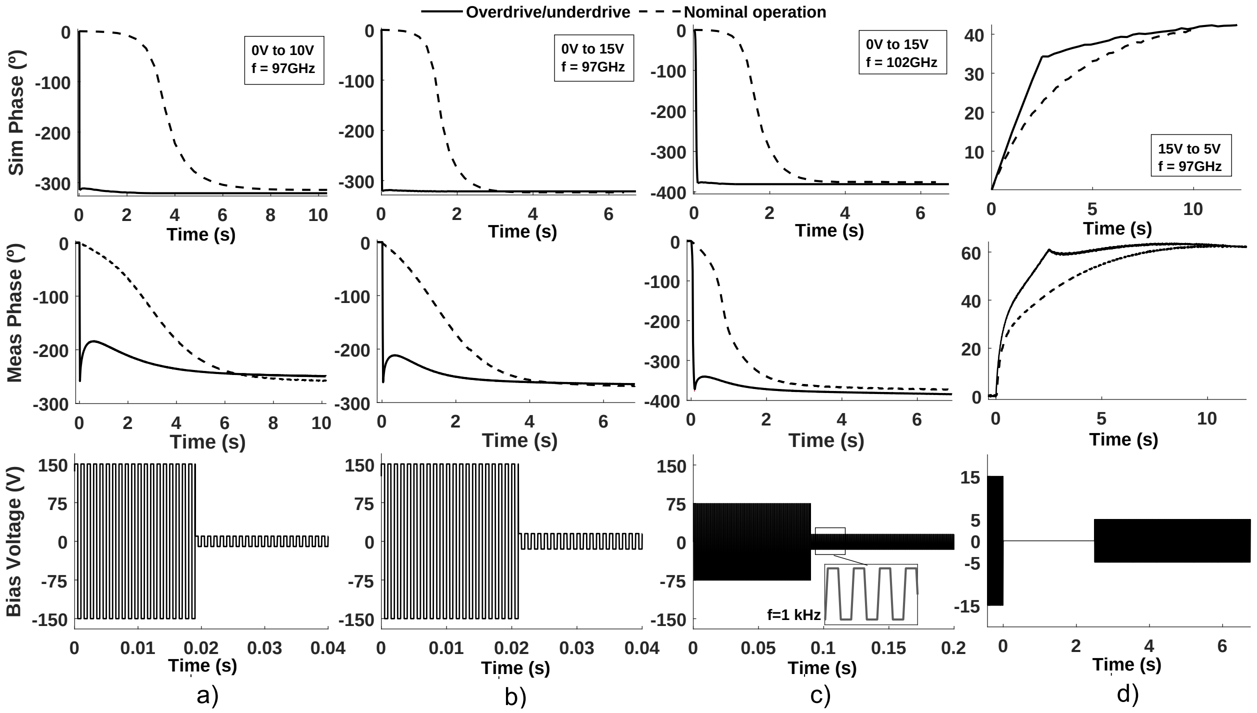

Figure 4.13: Phase transition between states using overdrive/underdrive and nominal excitations. Top row shows Simulations and middle row shows Measurements of a) 0V to 10V at 97 GHz, using a 150V overdrive for 19ms; b) 0V to 15V at 97 GHz, using a 150V overdrive for 21ms; c) 0V to 15V at 102 GHz, using a 75V overdrive for 90ms; d) 15V to 5V at 97 GHz, using 0V underdrive for 2.5s. Bottom row shows the applied overdrive/underdrive bias signal.

equipment and the limited cavity impedance, which is not infinite. In the underdrive case, however, the voltage cannot be reduced beyond 0V since it is the absolute magnitude of E_{AC} what makes the LC molecules to rotate. Notwithstanding, there exists the possibility of further reducing the decay times by choosing a less viscous LC. Moreover, given the large cavity impedance, it should be mentioned that the large applied voltages during these transitions do not imply large power consumptions, given that the LC cell hardly consumes any current.

Overall, the predicted and measured reflectarray cells transitioned a maximum of 250X and an average of 100X faster between phase shift states when using overdrive techniques, as compared to using nominal excitations. On the contrary, the applied underdrive technique consisting on removing the biasing voltage temporarily, only shortened in average a 2X factor the time it took to achieve 90% of the objective phase, as compared to the nominal excitations. Additionally, as will be seen next, these techniques can be used in combination of other acceleration techniques, for drastically reducing both the excitation and the relaxation times.

4.4 Polymer Network Liquid Crystals

Although the previous overdrive and underdrive techniques can substantially diminish the response time of the LC unit cells, their benefit is mostly at the rising transitions. That is, overdrive is much more effective than underdrive. Unfortunately, as the LC slowest reconfiguration occurs in decay transitions, the impact of designing those biasing waveforms on a complete nematic LC antenna is limited, and does not completely solve the speed problem.

Therefore, a different type of LC, namely Polymer Network Liquid Crystals (PNLC) are investigated as an alternative technology capable of accelerating the unit cell response to changing biases.

In order to obtain a PNLCs, a conventional LC is doped with a monomer, which upon polymerization yields a three-dimensional network that anchors the LC molecules in volume [97, 98, 99]. This network structure divides the entire cavity in domains. Since the anchoring energy of the molecules is much stronger in these small domains, which are all around the cavity, all molecules including the ones at the center relax at a much greater speed in the absence of an electric field, and the resulting relaxation time is substantially reduced. However, the strong anchoring given by the polymer network leads to a higher required excitation field, and a reduced range of the effective LC permittivity, which in practice could imply a reduction of the achievable phase range. The limited knowledge of the properties of many LC materials in the mm-wave range, coupled with the difficulties of developing an accurate electromagnetic model for the complex PNLC molecules to enable practical designs, has led to this approach being largely overlooked in RF applications above a few GHz, despite its known effectiveness in optics [100, 101, 102, 103]. Some works reported its usage in low-frequency transmission line phase shifters [104, 105], but without providing an electromagnetic model of the mixture that enables further design optimization.

There are examples of PNLC models, used in optics, that are based on effective scalar permittivities, assuming isotropy in the mixture. However, this is not suitable in resonant structures where there are higher order modes of electromagnetic fields. Thus, a more sophisticated characterization is needed to include the boundary conditions imposed by these devices. However, a model like the one previously used for conventional LC in mm-wave devices is not enough to represent PNLC. These models, which can accurately describe both steady and dynamic states, assume uniaxiality, but the molecular structure of the LC after polymerization is more complex and extremely difficult to predict (sometimes could be assumed as biaxial). Moreover, the elastic constants of the new mixture are unknown. Currently, no model of PNLC mixtures allows for predicting the response of resonant devices, and consequently, an accurate design of a device to meet specifications in mm-wave bands is not possible.

In this Section, a PNLC mixture which allows for the polymerization of the LC polymer dopant and works at 100 GHz is presented. This mixture is the first of its kind to show operability in mm-wave bands. Together with the mixture, a PNLC effective permittivity model for SFPS is obtained, enabling the design of devices with relaxation times reduced orders of magnitude with respect to using a conventional LC. To validate it, a reflectarray cell including such PNLC mixture is designed with enough phase range to allow beam scanning, and its temporal response is measured and compared to the improvements of the same mixture in optics.

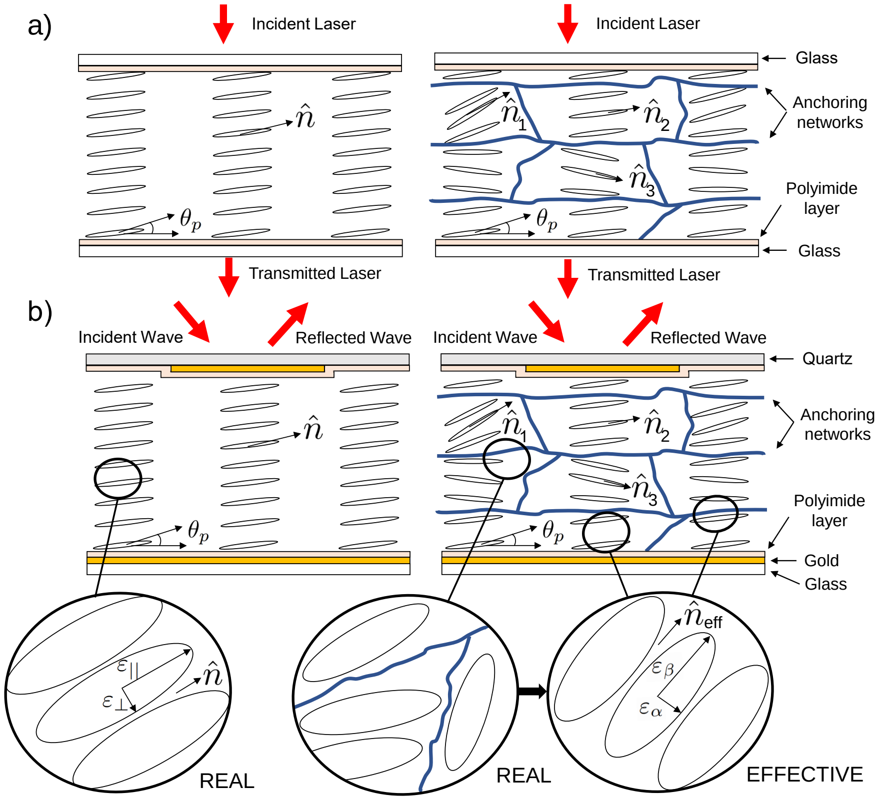

Figure 4.14: Sketch of a) transmissive (optics) and b) reflective (RF) LC cavities in repose state. Both conventional LC and PNLC cavities are shown on left and right, and the respective LC and PNLC molecular models are shown for the RF case.

4.4.1 PNLC background

As mentioned above, a PNLC consists of a conventional nematic LC doped with a reactive mesogen (RM), which is polymerized in situ inside the cavity. Upon polymerization the RM becomes an aligned polymer, which will act as an alignment agent in the volume of the LC. This polymerization can be performed at any state of the LC, including intermediate biasing states, and the anchoring will hold the molecules at that state even after removing the excitation. If the polymer is cured while the mixture is in a relaxed state, the polymer network will promote the relaxed alignment of the conventional LC in the whole volume of the cavity (see Figure 4.14), which is the case of interest to allow a fast transition towards the repose state.

Consequently, as compared to pure nematic LCs, higher bias fields must be applied to switch the mixtures, which are in the order of 1-10 V/μm depending on the cavity thickness and the dopant content, and a much reduced relaxation time is achieved. In fact, the response time depends on the domain size (i.e. the monomer concentration) rather than on the cavity thickness, and therefore could be advantageously used in larger cavity LC devices (i.e. lower frequencies) whose temporal response would be degraded using conventional LCs.

Apart from this, a second consequence of the polymerization is that the effective tuning of the device is partially hindered, as only the percentage of LC present in the whole volume will switch with the applied voltage. Moreover, the strong anchoring of the conventional LC into the rigid polymer network will make part of this LC to also not realign with any applied field of a reasonable magnitude. Therefore, while PNLCs accelerate how fast $\vec{n}(\bar{r}, t)$ relaxes, it also comes with a reduction in permittivity tuning range.

4.4.2 PNLC mixture and characterization procedure

As mentioned above, when compared to pure LCs, whose elastic constants and other material properties allow for modelling both in statics and dynamics, PNLCs are harder to model given the complex resulting mixture and that the RM material, whose concentration is typically between 1% and 20%, is not switchable once polymerized. Therefore, computing $\hat{n}(\bar{r}, t)$ as in the regular LC of the previous Section is not feasible. As a consequence, some works tried to approximate the PNLC dynamics by adding an auxiliary term to the Ericksen-Leslie equation using an effective electric field for the relaxation stage [106], which is valid only for small excitations and reorientation angles. In [107], correcting terms were directly added to the permittivities.

Alternatively, the response of the LC in statics could be approximately predicted by using a range of effective scalar permittivities, $\varepsilon_{eff,max}$ and $\varepsilon_{eff,min}$, which has shown reasonable results in phase-shifting optic devices under the isotropic assumption ($\Delta\varepsilon_{eff} = \varepsilon_{eff,max} - \varepsilon_{eff,min}$). However, in the case of SFPS with resonators, higher-order modes exist in the LC cavity, and the electric fields in it are more complex and challenging to predict. Then, the anisotropy has considerable effects on the resulting phase and the effective permittivity model must include it to properly generalize. Therefore, to design a structure requires obtaining $\vec{n}(\bar{r}, t)$ from measurement data, at least for some steady states.

In this thesis, the dielectric permittivity is modelled using an uniaxial effective anisotropic model deduced from measurements at the relaxed ($V = 0$) and maximum ($V = V_{SAT}$) excitation states. Since both steady states are approximately homogeneous for conventional LC, the effective permittivity is also assumed to be homogeneous for both cases in the PNLC model. While the full LC elastic model cannot be applied to PNLCs, the proposed model is expected to effectively represent the static behavior of the mixture when effective values are used. This capability allows for the design of different structures and accurate prediction of their behavior.

As introduced, the PNLC is going to be electromagnetically characterized by finding appropriate effective permittivity values ($\varepsilon_\beta, \varepsilon_\alpha$ in Figure 4.14), that can later be used in a design procedure using this specific mixture. This effective model is derived from measurements of experimental cells in RF. To do so, a monomer (RMM34C provided by Merck) 20 wt% is mixed with a LC host that allows polymerization and that provides dielectric anisotropy at mm-wave bands (MDA-98-1602 by Merck). It is worth noting that not all LCs can be mixed with the monomer, and a previous study must be done. In this case, the RM is in itself a LC, which will align with the conventional LC. In PNLCs, relaxation times reduce as the monomer concentration increases, at the expense of a reduced tunability and increased saturation bias voltage (V_{SAT}) [108]. Therefore, the concentration of 20% is chosen considering this trade-off.

The complete process of obtaining a valid mixture, its modelling at mm-wave bands, and using it to design new structures is detailed and explained in Figure 4.15. In order to confirm the appropriate PNLC mixture, first optical (transmissive) cells are manufactured and measured. Once the mixture is chosen, RF (reflecting) samples are manufactured and used to extract the electromagnetic model, which will finally enable a unit cell design with enough phase range to be used as reflectarray cell.

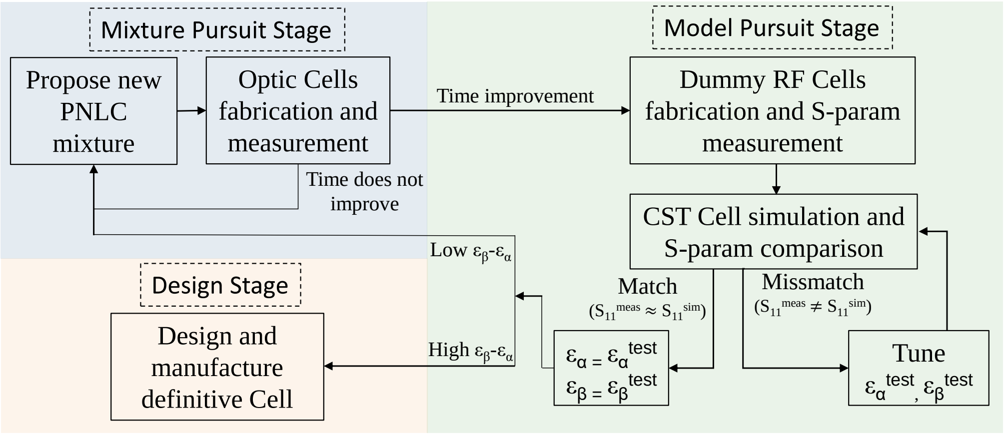

Figure 4.15: Process followed to obtain a PNLC-based cell design. First, in a mixture pursuit stage, the new PNLC mixture is proposed and its performance is first measured in optics. If the time response improvement is satisfactory, in the model pursuit stage the mixture is iteratively modelled from a mm-wave S-parameters measurement and by comparing it with CST simulations. Finally, if the mixture tunability is enough at mm-wave, the model can be used to design and manufacture a definitive cell.

4.4.3 Optical cells: MDA (cell 1), MDA+PN (cell 2)

The mixture has been initially used for the manufacturing of optical cells, to carry out a first check of the mixture capabilities to improve the temporal response of the LC molecules, and to compare the temporal performance of the doped and the undoped cases. Moreover, this will allow a comparison between the optical and mm-wave cells performance. Thus, these cells have been first manufactured and measured in optical frequencies. Given that the time reduction comes from a faster mechanical response of the LC molecules, an improvement measured in the optical regime will translate into an improvement in RF as well.

The transmissive sample cells are manufactured with transparent glass electrodes, which are covered with an indium tin oxide (ITO) conductive coating at their inner surfaces, and treated with polyimide. Note that the electrodes of these cells lacks resonators, because in optics the simple transmission allows to have enough phase shift (several 360º cycles). The formed LC cavity is $75\mu m$-thick and is sandwiched between the two glass plates. The edges of the cavities of these samples are sealed using a NOA 81 UV-curing adhesive. In the doped case, the cells are first filled with the MDA+PN mixture, and afterwards UV-cured to create the anchoring networks. This can be seen in the cells of Figure 4.16(b), where the PNLC sample is visibly opaquer than the undoped sample. It is important to note that the additional manufacturing step required to produce PNLC from conventional LC does not limit mass production, as it involves a straightforward material mixing process only.

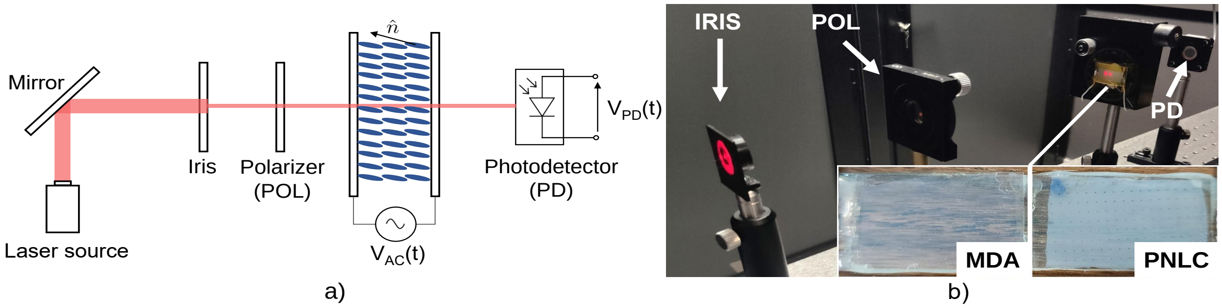

Figure 4.16: a) Schematic of the optical setup b) Picture of the setup. The inset shows the manufactured MDA and PNLC transmissive cells.

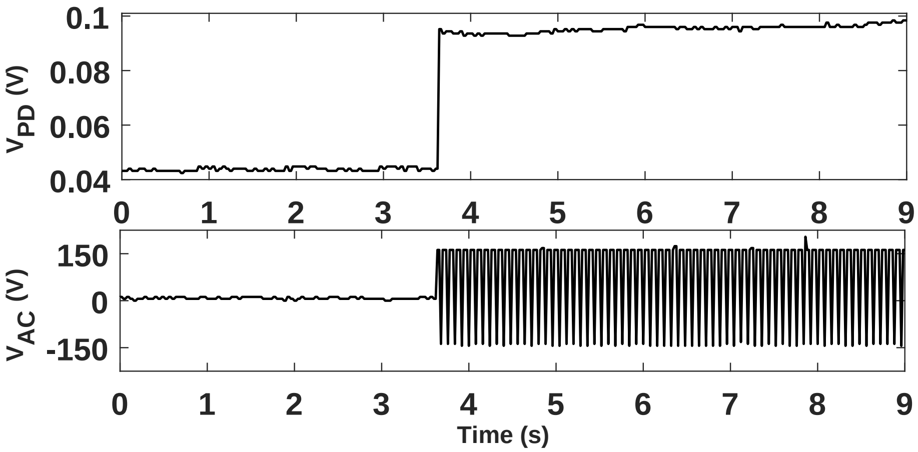

Figure 4.17: Measured excitation transition of MDA transmissive cell 1.

After both the pure MDA and the PNLC cells are fabricated, their temporal behaviour is measured in the optical setup of Figure 4.16. The cells are placed between a 632nm (474.7 THz) laser source and a photodetector, whose output $V_{PD}(t)$ is proportional to the incident radiant power and is captured using an oscilloscope.

The process to evaluate the OFF-ON and ON-OFF transitions is as follows. A square excitation signal $V_{AC}(t)$ is applied to the cell, with amplitude voltages of either 0V or 150V. For recording the OFF-ON transition, the signal starts at 0V and switches to 150V, and vice-versa for the ON-OFF case. Figures 4.17 and 4.18 respectively show the measured ON and OFF transitions of the undoped cell 1 (MDA). Both the LC biasing voltage $V_{AC}(t)$ and the photodetector output $V_{PD}(t)$ are shown. Figure 4.19 depicts the photodetector output signal and the applied LC control signal for both a rise and decay transitions of the doped cell 2 (MDA+PN). It can be seen how, as compared to the MDA case, the relaxation time of the polymeric mixture is improved significantly, as it took 11ms to relax as compared to 32s in the MDA case (90%-10% in number of 2π optical oscillations). The rising transition is similar in both cases (<20ms from 10% to 90%), due to the large voltages used. It is worth noting that these voltages (150V in this case) are used for characterization only (LC director at 90º), although a real device under normal operation would mostly apply lower voltages to work in intermediate states. Moreover, this voltage could be reduced by using a host LC that

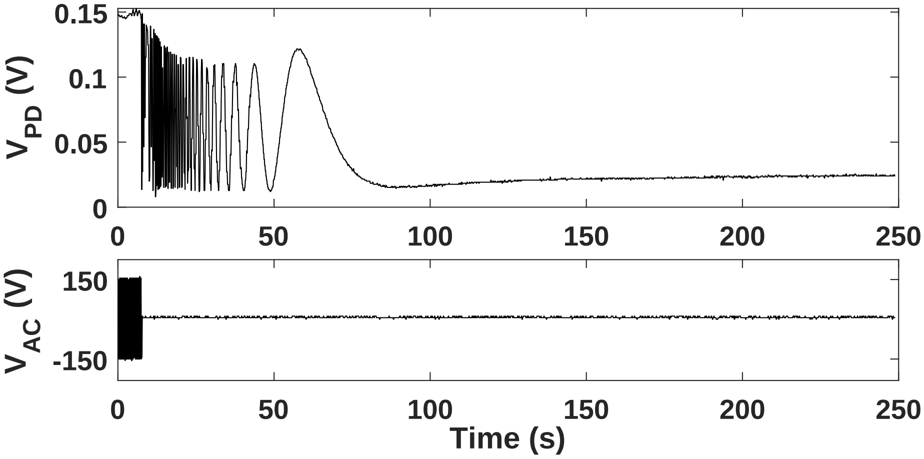

Figure 4.18: Measured relaxation transition of MDA transmissive cell 1.

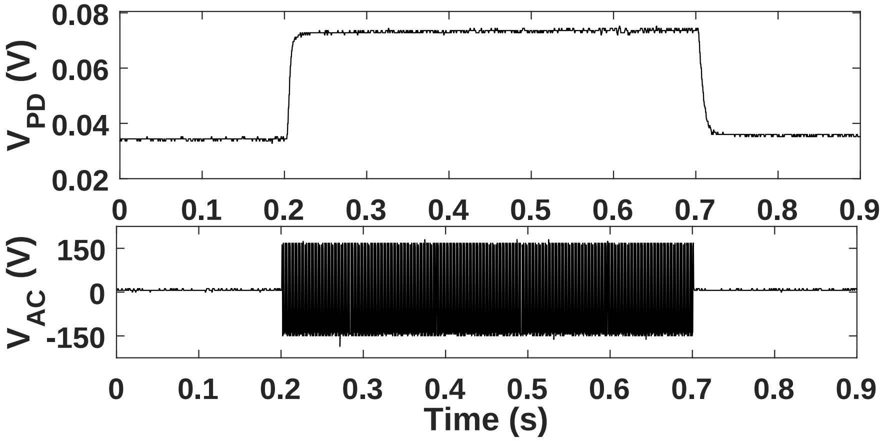

Figure 4.19: Measured temporal transitions of PNLC transmissive cell 2.

shows higher anisotropy and lower viscosity. Additionally, depending on the application, a lower polymer concentration can be used, which reduces V_{SAT}.

4.4.4 mm-Wave cells: MDA (cell 3), MDA+PN (cell 4)

Since the previous temporal results obtained with the optical cells show a significant improvement, and considering that the host LC is anisotropic enough in mm-wave bands, a characterization for both MDA and PNLC is performed to study their dielectric tunability and losses. Consequently, undoped (cell 3) and doped (cell 4) mm-wave sample cells are manufactured and measured to characterize the electromagnetic properties of the materials and to measure their temporal response. In this case, the mm-wave cells with resonators are reflective since it facilitates the measurement with a VNA.

Given that cells 3 and 4 are reflective resonant surfaces, their manufacturing is similar to the one described in Chapters 2 and 3. Gold resonators are grown on the inside of the superstrate using photolithography, as shown in Figure 4.20. The manufactured devices consist of a $75\mu m$ thick LC cavity sandwiched between a top $1.25mm$ thick quartz superstrate and a bottom

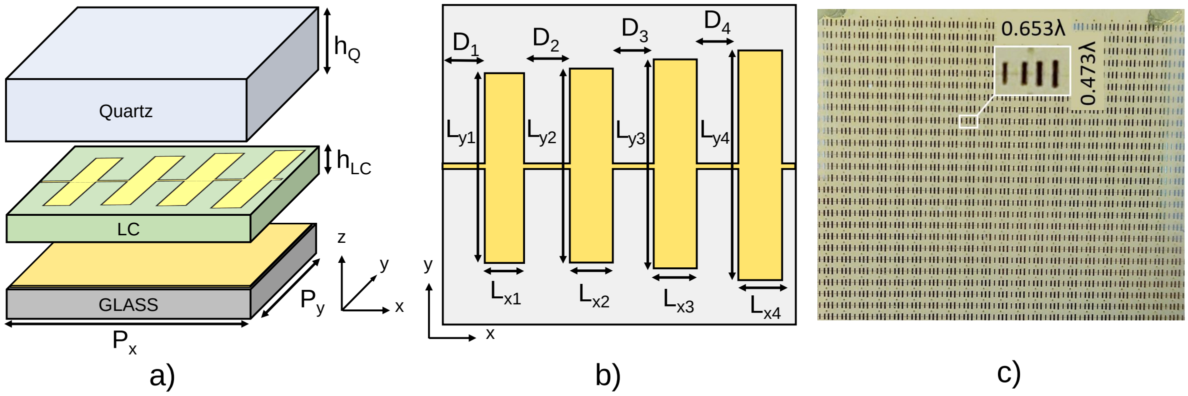

Figure 4.20: Unit cell structure of the reflective manufactured cells. The specific dimensions for cells 3, 4 and 5 are detailed in Table 4.1. a) 3D view. b) Top view. c) Picture of the manufactured cell 3.

Param.	**Cells 3&4**	**Cell 5**	**Param.**	**Cells 3&4**	**Cell 5**
P_x	1.96	1.4	L_{x3}	0.19	0.19
P_y	1.42	1.4	L_{x4}	0.18	0.17
D_1	0.1857	0.125	L_{y1}	0.6322	0.68
D_2	0.3884	0.195	L_{y2}	0.6765	0.75
D_3	0.1448	0.12	L_{y3}	0.738	0.81
D_4	0.2586	0.125	L_{y4}	0.7995	0.86
L_{x1}	0.133	0.17	h_{LC}	0.075	0.045
L_{x2}	0.18	0.18	h_Q	1.25	0.43

Table 4.1: Dimensions (mm) of the manufactured sample reflective cells 3&4 and PNLC reflectarray cell 5.

ground plane made of $1\mu m$ thick gold, treated with polyimide. Based on this structure, two identical dummy cells are manufactured, one filled with MDA (cell 3) and another filled with the MDA+PN mixture (cell 4). The sample dimensions of these cells can be found in Table 4.1, whereas Figure 4.20(c) shows a picture of the manufactured cell 3.

As explained, the model consists on assuming effective values for the extreme cases of the permittivity. From Equation (1.4), the effective uniaxial permittivity matrices in the extreme states of LC molecules can be written as:

$$\bar{\bar{\varepsilon}}_{OFF} = \begin{pmatrix} \varepsilon_\alpha & 0 & 0 \\ 0 & \varepsilon_\beta & 0 \\ 0 & 0 & \varepsilon_\alpha \end{pmatrix}; \qquad \bar{\bar{\varepsilon}}_{ON} = \begin{pmatrix} \varepsilon_\alpha & 0 & 0 \\ 0 & \varepsilon_\alpha & 0 \\ 0 & 0 & \varepsilon_\beta \end{pmatrix} \tag{4.6}$$

This general expressions can be used for both doped and undoped cells. In cell 3, which contains conventional LC, the parameter extraction process provides the conventional values of $\varepsilon_\beta = \varepsilon_{||}$ and $\varepsilon_\alpha = \varepsilon_\perp$. In PNLCs (cell 4) these will be effective values, given that they actually are not composed by a pure uniaxial structure (see Figure 4.14), as aforementioned. The model consists on obtaining these values from measuring the S-parameter of the cells. To do so, an iterative simulation process is conducted to match the simulated response, using test ε_α, ε_β values, with the measured data across the entire frequency band. This is a similar procedure to the one used for characterizing the GT7-29001 mixture in Chapter 2. In that case, as in MDA, ε_β and ε_α provided the true parallel and perpendicular permittivity values.

It is also important to note that in PNLCs these effective ε_α, ε_β differ from effective scalar permittivities $\varepsilon_{eff,max}$, $\varepsilon_{eff,min}$ of the isotropic model used for in optical devices. Note also that given that for cell 3 (undoped) both $\varepsilon_{||}$ and $\varepsilon_\perp$ are known for the conventional MDA, together with its elastic constants and viscosity, the phase-voltages curves and the dynamics can be computed solving Equations (1.2) and (3.8). In the case of cell 4 (doped), however, the effective ε_α and ε_β do not allow such realistic predictions for PNLCs, as the elastic constants and viscosity of the new mixture can not be properly defined. Thus, the effective permittivity matrices obtained through the PNLC model are specific for the steady extreme states, and therefore, a complete phase-voltage and dynamic characterization of the PNLC would require a measurement for each bias of interest. Moreover, the extraction is linked to a specific unit cell structure. However, the model is general enough to enable accurate designs of any similar planar structure, cavity thickness and incidence angle suitable for phase manipulation of mm-waves, as will be seen in the following section.

The S_{11} parameter of both manufactured cells has been measured in periodical environment with the same $V_{AC}(t)$ by means of a quasi-optical free space measurement setup and a VNA connected to a pair of horn antennas (Flann 27240-20 WR10), as detailed in Chapter 2. A sketch of such setup can be seen in Figure 4.21, where an arbitrary waveform generator, together with a x15 voltage amplifier, is used to bias the LC cells. To obtain a macroscopic S_{11} measurement of the unit cell, all the unit cells are short-circuited and connected to $V_{AC}(t)$, in the same way as in Chapter 3. Finally, the S_{11} has been used to derive the values of the permittivity matrix using an iterative process that compares the measured and modelled S_{11} parameters, as shown in Figure 4.15.

That is, to extract a model that allows obtaining the effective dielectric permittivity components and the losses for any applied AC electric field, for both the MDA and PNLC materials, the measured reflection coefficients and those resulting from full-wave electromagnetic simulation (CST Studio) are fitted, along the entire frequency band, by iteratively modifying the simulation parameters. This requires a careful adjustment of the complex dielectric permittivity components of the uniaxial model in each iteration. Similar to the modelling procedure carried out in the previous chapters to account for the longitudinal inhomogeneity, the local director angle is averaged across z to reduce the compute cost while assuming a low accuracy degradation. As aforementioned in Sections 3.4.2 and 4.2.2, this is more precise in the extreme biasing states of conventional LCs, where the molecules are either fully rotated or fully relaxed across almost the entire cell, as previously observed .

4.4.5 Characterization results

The permittivity characterization results of both MDA (cell 3) and MDA+PN (cell 4) mixtures, obtained after the model derivation of the previous subsection, are shown in Table 4.2. To confirm that the obtained results are correct, Figure 4.22 shows the measured and the

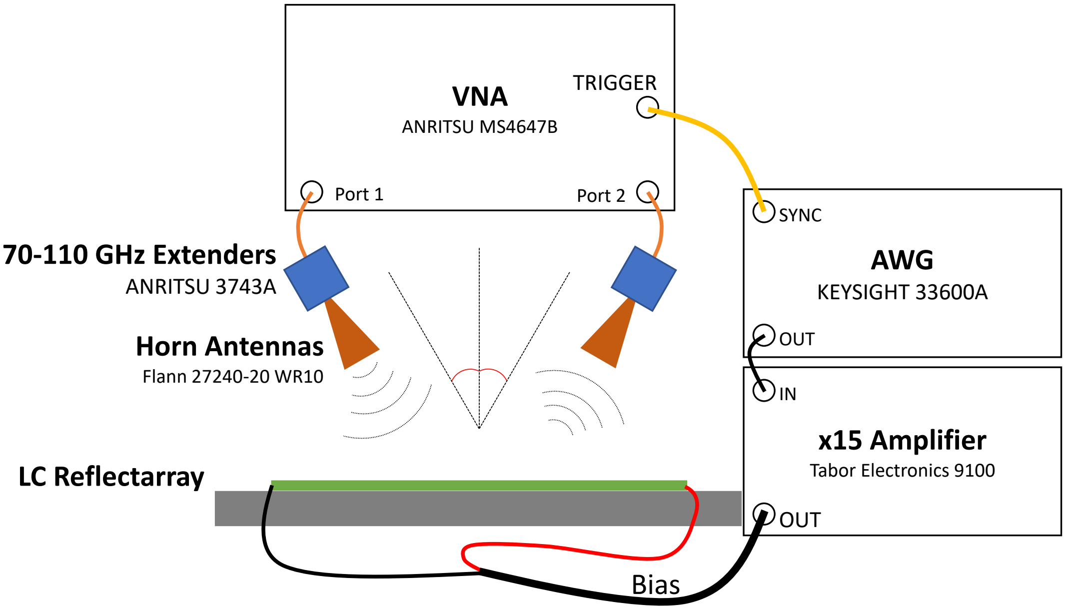

Figure 4.21: Top-view scheme of the experimental setup to electromagnetically characterize the PNLC mixture.

simulated amplitude of the reflection coefficient (S_{11}) for both cells after sufficient time has passed (stationary regime), for zero and high amplitudes of V_{AC} (OFF and ON states), and at an incidence angle of 45º. The simulation results have been obtained using the matrices of Equation (1.4), considering the derived parameters reported in Table 4.2.

As can be seen, the simulation matches the measurements of cells 3 and 4. For the PNLCs, around 3X reduction in the dielectric tunability ($\Delta\varepsilon = \varepsilon_{||} - \varepsilon_{\perp} = 0.59$ in MDA and $\Delta\varepsilon = 0.19$ in PNLC) and increased cell losses (around -3dB in measurement data) as expected is observed.

Apart from the material characterization, the temporal transitions of both MDA and PNLC structures are also studied. The reflection coefficient phases are recorded in the quasi-optical bench, by externally triggering VNA captures in sync with the LC driving transitions. The measurement is performed at 97GHz, where the phase range is maximum, and at an incidence angle of 45º. In this case, the S_{11} phase is measured, instead of amplitude, since it is a

Param.	**GT3-23001**	**GT3+PN**	**MDA-98-1602**	**MDA+PN**
$\varepsilon_{\|\|}$	3.27	N/A	3.28	2.69^{*}
$\varepsilon_{\perp}$	2.47	N/A	2.7	2.5^{**}
$tan\delta_{\|\|}$	0.015	N/A	0.015	0.02^{*}
$tan\delta_{\perp}$	0.02	N/A	0.02	0.021^{**}
V_{sat}^{***}	15V	N/A	$\sim 15V$	$\sim 150V$

* Effective ε_{β} ** Effective ε_{α} ***In $75\mu m$-thick cells

Table 4.2: LC parameters and Characterization results at 100 GHz.

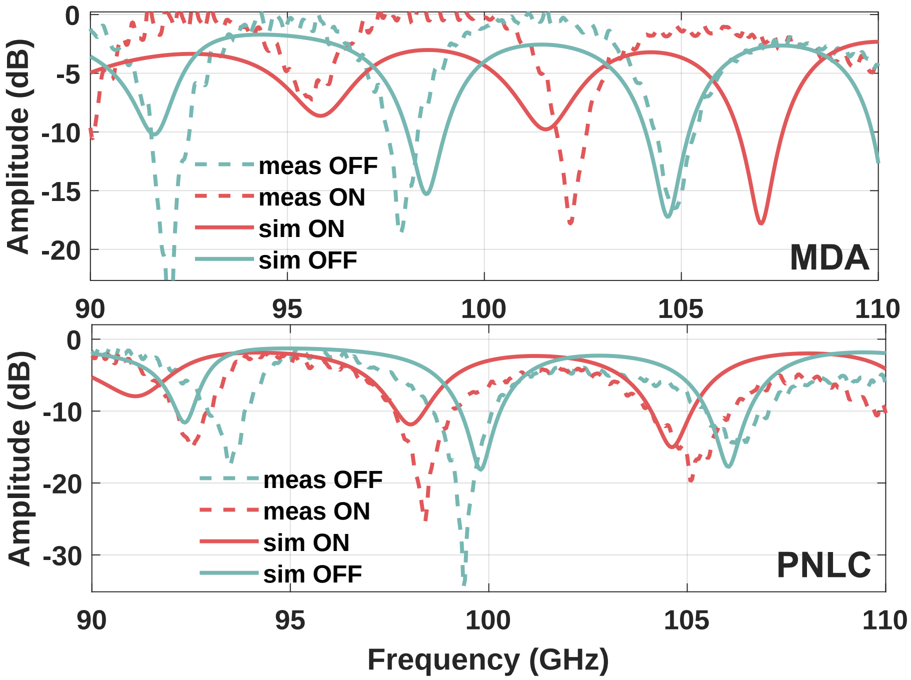

Figure 4.22: Measured S_{11} amplitude of MDA (top) and PNLC (bottom) cells 3 and 4 as a function of frequency for a permittivity matrix characterization, from which the data of Table 4.2 is obtained. The reconstructed (simulated) S_{11} amplitude according to this extracted data (iterative process solution) is also shown. Extreme states in permanent regime are shown, with 150V (ON) and 0V (OFF) V_{AC} amplitudes, for a 45º incidence angle.

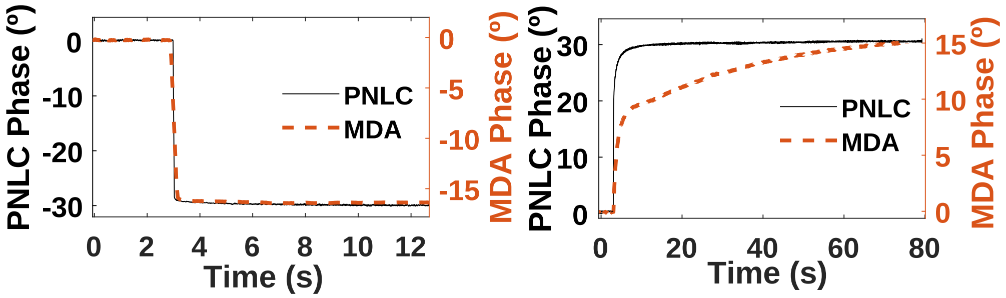

Figure 4.23: Measured MDA and PNLC excitation (left) and relaxation (right) S_{11} phase transitions in reflective cell samples at 97GHz.

more appropriate magnitude to measure temporal responses. As shown in Figure 4.23, the excitation transition is relatively quick in both MDA and PNLC cases (<40ms), while the 90%-10% relaxation time is reduced by a factor 50X in the PNLC sample, from 42s to 800ms. A direct comparison between the phase ranges is not possible, since the lack of electromagnetic knowledge for the permittivities of the MDA and the PNLC prevented an optimized design of these devices. Therefore, very reduced phase shifts are observed and each device has a completely different resonant behaviour in the band. However, it is worth highlighting how, while their phase evolution is identical in the excitation stage, the PNLC device is much faster in returning to the relaxed state. The improvement in switching time is therefore significant when the LC is doped with polymer.

The temporal performance of the manufactured and tested cells, in terms of decay times, is summarized in Table 4.3, where the cavity thickness is also included. It can be noted that the cells 1 and 3, which contain conventional MDA and are designed for optics and RF respectively, exhibit different decay times although both have the same thickness. This can be attributed to different sources: (i) The manufacturing tolerances of $\pm 2\mu m$ for the LC thickness, which only relates to a time variation of a 5%. (ii) The different magnitude being measured, i.e. optical intensity and S_{11} phase, whose convergence can not be directly compared even if the LC molecular structure is the same. In other words, the 90% convergence of one magnitude can be achieved earlier than the other for the same LC state. Note that the electromagnetic field in the LC layer of RF resonant cells is a combination of multitude of modes, whose propagation constants depend on the cell dimensions and the permittivity matrix components, which in turn are very dispersive. Therefore, the reflection of these cells exhibits a different and much more complex dependence with the permittivity than that showed by the optical cells used here, where a single plane wave is propagated.

There is also an important discrepancy in the response times of cells 2 and 4, as seen in Table 4.3, which correspond to the doped case for optics and RF configurations. Although the previously mentioned differences can also be extended here, in this case these variations can be almost entirely assigned to (iii) the different irradiation conditions in the UV curation process [104]. Since the top electrode of the resonant RF cells contains metallic dipoles, there is a certain inhomogeneity in the polymerization. That is, the volume underneath the metallic areas is not completely polymerized, as opposed to the transmissive optical cells whose mixture is completely polymerized throughout the whole volume. This results in certain LC molecules within the PNLC RF cells rotating slower compared to those in cells without metallic resonators. Despite this, the relaxation time showed great improvement as compared to conventional LC. To further enhance the 50X factor, it may be possible to intensify the irradiation conditions or optimize the resonator design to occupy a smaller superstrate area while maintaining their RF purpose.

Table 4.2 includes the results of two additional cells, manufactured to evaluate the performance of the polymer network mixed with another LC typically used in microwaves (GT3-23001 by Merck). However, the dopant was not polymerizable in the presence of GT3, which is is likely to be caused by radical scavengers in the GT3 mixture, or due to UV-induced decomposition of one or several components of GT3, inhibiting the polymerization.

4.4.6 PNLC-based reflectarray design

Once the mixture electromagnetic model is known, as well as its temporal capabilities, a PNLC reflectarray cell (cell 5) is designed in order to validate them and to test the model generalization. The device is designed using the data of Table 4.2, and further manufactured and tested using the same procedures of the reflective mm-wave samples. In this case, the cell is designed targeting a fast device that can exhibit a phase range of at least 180º, to show its applicability. Figure 4.24 shows a picture of the manufactured surface, whose dimensions can be found in Table 4.1.

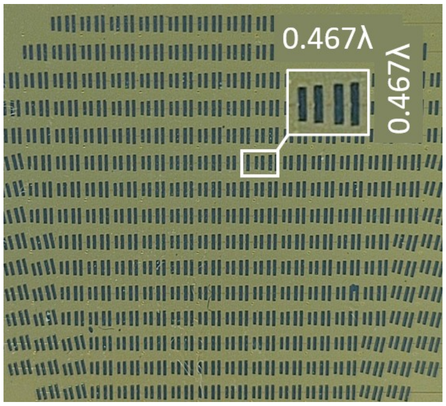

Figure 4.24: Picture of the manufactured final PNLC-based reflectarray cell 5.

Sample	**Material**	**Thickness**	**Relax. Time**	**Improv.**
Optical Cell 1	MDA	75μm	32s	∼3000X
Optical Cell 2	MDA+PN	75μm	11ms	
RF Cell 3	MDA	75μm	42s	∼50X
RF Cell 4	MDA+PN	75μm	800ms	
RF Cell 5	MDA+PN	45μm	210ms*	

* Measured 90%-10% to the target 180º phase shift

Table 4.3: Measured temporal performance of LC and PNLC cells.

The manufactured reflectarray cell has been measured at an incidence angle of 30º. This angle was deliberately changed from the previously used one, during the parameter derivation (45º), to validate the generality of the permittivity model. The measurement results, presented in Figure 4.25, show the amplitude and phase of the reflection coefficient. As can be seen, the effective uniaxial model allows the prediction of the cell behavior even in a different structure and incident angle, showing geometry-independence.

Because of the reduced dielectric tunability of the PNLC mixture, the achieved phase range is reduced but still sufficient to obtain the desired 180º in three different bands (94 GHz, 98.5 GHz and 106 GHz), being the 97.1 GHz-100.3 GHz the most relevant one as shown in Figure 4.25. This phase range allows for a 1-bit quantization reflectarray design. In terms of antenna performance, this compromises the gain and sidelobe level when compared to a 360º cell [91] but still allows for a continuous scanning. Achieving a larger phase range with such a reduced dielectric anisotropy imposed by the PNLC is challenging. One possibility is to reduce the cavity thickness, which would in turn increase losses and coupling problems [82]. A potential alternative is doping LC materials whose dielectric anisotropy $\Delta\varepsilon$ is very large at mm-wave frequencies, so that when mixed with the polymer the effective tunable anisotropy $\Delta\varepsilon_{eff}$ results sufficient to achieve 360º. One potential candidate is the LC GT7-29001, that in preliminary experiments shows to be compatible with polymerization.

The temporal behaviour of the reflectarray has also been measured, at the frequency of greatest phase range, as shown in Figure 4.26. The 180º 10%-90% OFF-ON transition takes 12ms while the 90%-10% ON-OFF transition takes 210ms. The temporal response could be further decreased by using a PNLC mixture with a higher polymer network concentration,

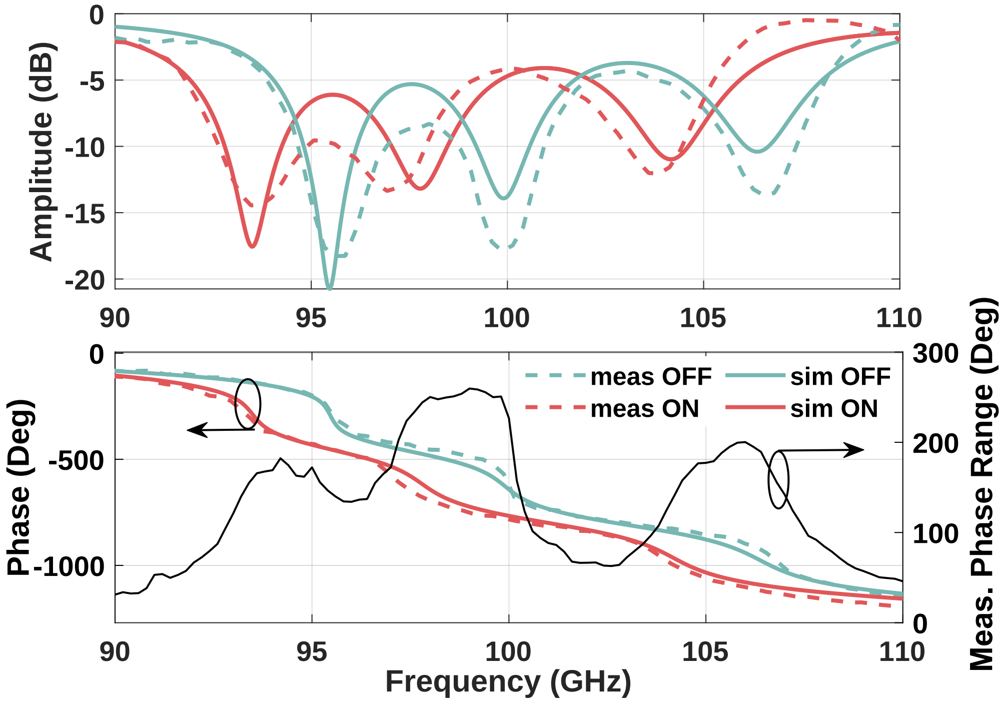

Figure 4.25: Reflection coefficient amplitude (top) and phase (bottom) of the PNLC-based reflectarray cell 5.

although this would come at the cost of a lower effective dielectric tuning range and of an increase of the required voltages for driving the cells. Additionally, adopting new generations of LC which show greater dielectric anisotropy in mm-wave bands, that may be capable of polymerizing, and that feature low saturation voltages, could enable relaxation times in the tenths of milliseconds using only a few volts of bias excitation with similar cavity thicknesses.

The analyzed results have been performed at the cell level. In regards to a complete system capable to provide beam-scanning, the surface implemented here is identical to the one required one. However, the external driving circuitry will require proper addressing and the handling of high-voltages due to the PNLC.

As it has been shown, the PNLC mixture and its model allowed for a significant response time reduction. However, the improvement is not the same as in the optic cells due to the different convergence of the magnitudes being measured (optical intensity and RF phase), and other fabrication matters such as the polymerization conditions. The results demonstrate that an uniaxial model can be used to emulate the complex behaviour of PNLCs in multi-resonant cells with enough accuracy, only by considering effective values of dielectric anisotropy. The model should be obtained from measurements for each PNLC mixture, dopant concentration, cell geometry and angle of incidence, as it tries to describe a more complex molecule than the uniaxial. However, it is shown that once the model is obtained, it is general enough so that it can be used under different incidence angles, cell thickness and slight cell geometry variations, contrary to the isotropic effective model.

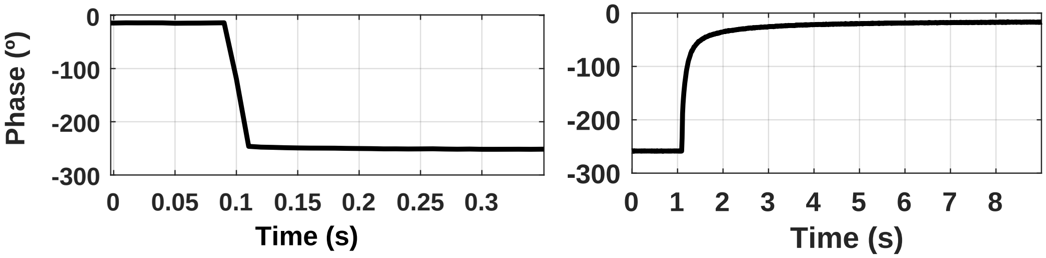

Figure 4.26: Measured excitation (left) and relaxation (right) S_{11} phase transitions of the designed PNLC cell at 99GHz.

4.5 Dual Frequency Liquid Crystals

In the previous section, the use of PNLCs was presented as an alternative to the underdrive biasing to reduce the decay times of LCs in mm-wave devices. However, the dielectric anisotropy of PNLCs is dramatically reduced with respect to conventional LCs, given that the polymer network cannot be tuned, which in practice seriously diminishes the achievable phase range. Moreover, the required voltage to fully rotate the molecules rapidly increases with polymer concentration, which is undesired as the response acceleration also increases with polymer concentration.

A third possible solution is to use Dual Frequency LC (DFLC), a specific type of LC that shows a sign inversion of its dielectric anisotropy at few kHz of bias frequency. This characteristic feature of DFLC allows for a rotation of the molecules which is induced by the applied external electric field, both for the rise and decay transitions. At the positive dielectric anisotropy biasing range, molecules actively rotate parallelly to the electric field, which is the common case for nematic LCs as the ones previously used. However, at the negative dielectric anisotropy biasing range, they actively rotate perpendicular to the AC field, which allows a great reduction of the response time as compared to the viscous decaying transition to the repose state [109]. The operating principle of DFLC is completely different to the previous strategies, and it does not intrinsically entail a tunability reduction.

Similarly to the PNLC case, there exist use cases of these mixtures in optics [110, 111, 112, 113, 114]. However, its usage there is not widespread since the response time of optical devices is rarely a limiting factor. Recently, they have also been tested in microwave devices such as filters and phase shifters [115, 116, 117]. However, in such works the device is manufactured blindly, that is, without *a priori* information of the DFLC material.

Given that DFLC mixtures have been historically used in optic devices only, there is a general lack of electromagnetic knowledge in terms of permittivity and losses at RF frequencies. This is not only problematic at the design stage, where the only possibility for the engineer is to guess the possible behaviour of the mixture, but also at the testing stage since the different LC states are not predictable and thus a device control can only be based on experimental measurements, which does not guarantee proper operation or repeatability. Moreover, this complicates the extrapolation of the technology to other devices, since the only true characterization in LCs comes from the permittivity tensor. For instance, in [118], the usage of DFLC is disregarded assuming that their dielectric anisotropy is too small, whereas through this work it will be shown that there exist specific mixtures with enough dielectric anisotropy.

Therefore, a rigorous electromagnetic and temporal characterization of these mixtures in mm-wave bands is necessary before they can be properly used. In the case of resonant planar structures such as RIS and reflectarray antennas, DFLCs have not been implemented yet, and it is unknown whether their tunability is sufficient to achieve enough phase range (e.g. 360º). In some applications, these devices require reconfigurability times of few milliseconds [119], which have not been achieved with current technologies, as it has been previously introduced. Moreover, in those structures, DFLCs could even help reduce the losses, since one of their main causes is the small thickness of the LC cavities necessary to reduce reconfiguration times. By using DFLCs, the trade-off between thicker cavities and increased response time can be relaxes, so that thicker devices with reduced losses could be designed.

In this Section, the use of DFLC to reduce the reconfigurability time of planar cells for spatially fed antennas is proven for the first time in mm-wave resonant SFPS. Here, a sample of DFLC, which was characterized in [120], is used to design a LC cell exhibiting enough phase range and fast response time. The reflectarray cell is manufactured and measured thus demonstrating the capabilities of these mixtures in mm-wave.

4.5.1 DFLC background

DFLC are designed and obtained by mixing two types of LC. The first type consists of a LC that shows a positive dielectric anisotropy at low AC frequencies which decreases with frequency. The second type shows negative dielectric anisotropy in the whole AC biasing band [121]. Consequently, a LC with positive anisotropy at low frequencies and negative anisotropy at higher frequencies, typically within the kHz range, is obtained. The frequency at which $\Delta\varepsilon_{AC} = 0$ is called the crossover frequency f_c. This can be seen in Figure 4.27.

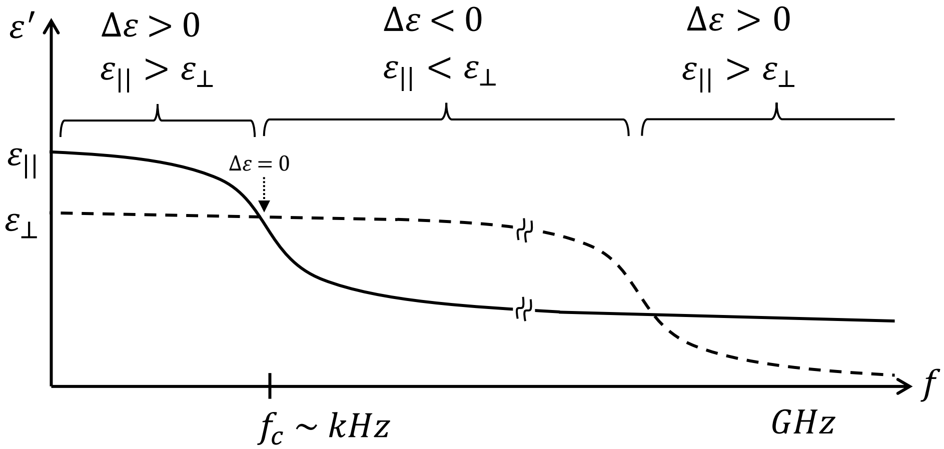

Figure 4.27: Typical DFLC permittivity dependence with frequency of biasing signal. Three distinct sections can be observed where $\Delta\varepsilon$ shows different module and sign.

This change in the sign of the dielectric anisotropy is exploited to make the LC molecules react differently to the bias electric field. When parallel orientation of the molecules towards the field is desired, a low AC frequency bias below f_c is chosen, where the mixture exhibits

Mixture	$\varepsilon_{\parallel}$	$\varepsilon_{\perp}$	$\Delta\varepsilon$	$tan\delta_{\parallel}$	$tan\delta_{\perp}$	**Manufacturer**
MLC2048	3.1	2.65	0.45	0.035	0.04	Merck [56]
MLC2177	3.0	2.5	0.5	0.03	0.035	Merck [56]
W1978C	2.43	2.27	0.16	0.02	0.025	MUT [122]
P00-026	3.05	2.42	0.63	0.03	0.05	HCCH [123]

Table 4.4: Electromagnetic properties of various DFLC mixtures at W-band [120].

positive anisotropy. When perpendicular orientation of the molecules towards the field is desired, a higher AC frequency bias above f_c is chosen, where the mixture exhibits negative anisotropy. This can be understood by looking at the electric energy density of Equation (3.2) and Equation (3.3). In those, the functional is minimized for $\vec{E}_{AC} \parallel \vec{n}$ when $\Delta\varepsilon_{AC} > 0$, and for $\vec{E}_{AC} \perp \vec{n}$ when $\Delta\varepsilon_{AC} < 0$. Since both excitations are independent, the different transitions can be controlled to obtain the desired response times.

It is then clear that DFLC is a promising solution to reduce the slow decay time of thick mm-wave devices, since an external control for both transitions is achieved. As compared to underdriving a conventional LC, which only reduces decay reconfigurability times by 2x, DFLC can theoretically reduce this time by several orders of magnitude. As compared to PNLC, DFLC does not necessarily imply tunability reduction, and it does not require large biasing voltages. Nevertheless, few DFLC at 100 GHz have been properly characterized [120], so their dielectric tunability and losses are mostly unknown, preventing proper design procedures.

The DFLC mixtures currently available, similarly to most of the LC mixtures, are developed for optics purpose. As such, they are expected to provide a reduced dielectric anisotropy range that in mm-wave bands. This leads to much more sensible devices, where the operating frequency or performance could be deviated significantly if the mixture characteristics are not know. The different design variables, such as cavity thickness, biasing voltages or resonant element dimensions, are therefore at the edge of viability, considering the tight trade-offs between losses, operating voltage, and reconfigurability capabilities and speed. Therefore, in the case of using a novel mixture, a proper characterization is critical, and an audition of whether it provides a set of favorable design points to tune the different trade-offs must be done.

4.5.2 Mixture analysis

The complex permittivities of four different mixtures, obtained through an iterative fitting process [120] are shown in Table 4.4. As can be seen, the dielectric anisotropy of the studied mixtures is in general low, as compared to mm-wave optimized mixtures (e.g. GT7-29001), and there is one mixture whose dielectric anisotropy is especially limited. However, the highest tunable mixtures can suffice to design devices with the required phase range (360º). Note that P00-026 shows the greatest dielectric permittivity ($\Delta\varepsilon$=0.63). In terms of losses, the four mixtures are very lossy, even more than PNLC, given that they were not optimized to be used in this band. This is similar to early LC-based reflectarray works [34, 36, 37], which used mixtures optimized for optical devices such as K15, BL006 and BL037 (see Table 2.1).

Therefore, as the technology advances, it is expected that the LC manufacturers will develop mixtures whose dielectric permittivity, and especially the losses, are further optimized at the mm-wave bands.

Apart from the static electromagnetic knowledge of the mixtures, accurate information about the temporal behaviour of each material is also required for estimating the device response, as different parameters (viscosity, elastic constants, $\Delta\varepsilon_{AC}$, and so on) can influence the resulting times. In [120], a temporal analysis has been carried out by measuring the temporal evolution of the S_{11} phase after changing the LC biasing electric field, similar to Section 4.2.2. This provides the temporal behaviour to be expected for DFLC cells that are filled with the different mixtures, when applying different biasing signals as shown in Figure 4.28. In the figure, a qualitative phase evolution is also shown for each state switching.

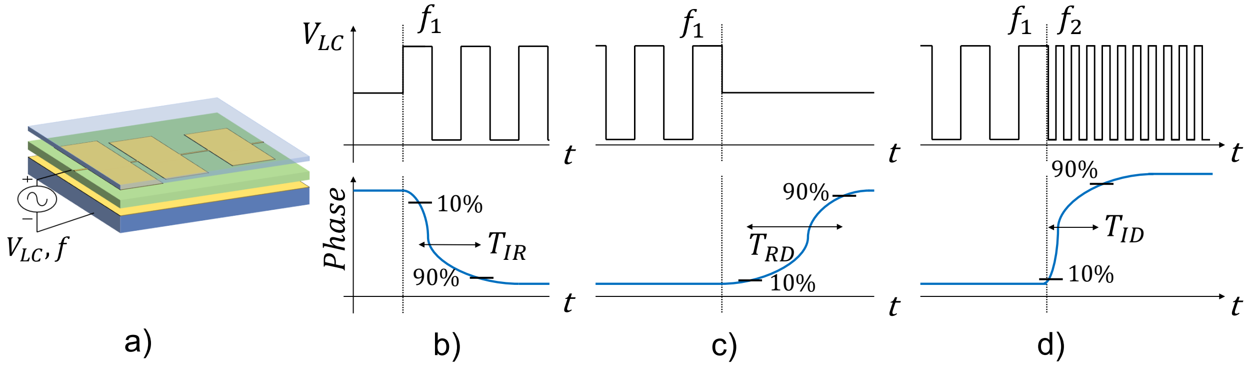

Figure 4.28: Description of basic biasing signals for DFLC mixtures. The qualitative phase evolution of the different transitions is also shown. a) Sketch of the applied bias at the cell. b) Induced rise transition c) Relaxation decay transition d) Induced decay transition.

The waveform sequence of Figure 4.28(b) defines the induced rise transition, from OFF to ON states, and the time it takes for the phase to reach the new steady state (T_{IR}). This time is defined considering a 10%-90% phase change. Similarly, the sequence of Figure 4.28(c) defines the time of a relaxation decay transition (T_{RD}) from ON to OFF. These are the same excitations occurring in conventional LC for an increase an decrease of the cell voltage. The sequence of Figure 4.28(d), which is specific for DFLC, defines the time of an induced decay transition (T_{ID}) from ON to OFF, leveraging the negative anisotropy at the bias frequency.

The details of each switching transition and possible states are further summarized in Table 4.5. In short, rising transitions occur from a lower voltage state to a higher state, and are induced as in conventional LC. Decay transitions occur from a higher to lower state, and can be either through relaxation, as in conventional LC, or induced, which is exclusive to DFLC. Intermediate molecule rotation, in-between extreme states, can be reached by any of the previous three transitions, depending on the initial and final voltage. Note that rise and decay transitions refer to the molecule variation rather than the phase variation.

These biasing waveforms are the simplest ones that allow the necessary transitions to demonstrate that both rise and decay times can be controlled independently, while in the following

Sections more complex waveforms will be proposed and evaluated in order to leverage DFLC properties and engineer a reduction of the LC temporal response.

The temporal characterization of each DFLC mixture are summarized in Table 4.6, where transition times are measured considering the 10%-90% phase change, extracted from [120]. As expected, induced decay transitions are significantly faster than relaxation decay transitions, since the extra torque induced by the biasing field accelerates the rotation of the molecules towards the relaxed state, contrary to a relaxation driven only by viscosity. Note that while T_{ID} is very voltage-dependent, and it can be decreased with this information, T_{RD} values are consistently high for all mixtures and do not show significant changes with the voltage.

In this case, the chosen frequencies f_1 and f_2 are recommended in the manufacturer datasheet. As can be seen in Figure 4.27, each biasing frequency entails a different $\Delta\varepsilon_{AC}$, which is the ultimate parameter by which the response time is determined. Note that, in Equation (4.2), a larger $\Delta\varepsilon_{AC}$ value has a similar repercussion as a larger voltage. Therefore, the responses can be optimized by defining f_1 and f_2 at the frequencies where $|\Delta\varepsilon_{AC}|$ are largest, since the force induced by the biasing field would increase. To do so, a fine sweeping of frequencies would reveal the ones for which the mixture works best. This effect can be seen in Table 4.6, for columns T_{IR} and T_{ID}, where the reconfigurability times differ for the same applied voltage, as this represents different values of $|\Delta\varepsilon_{AC}|$, between f_1 and f_2, being used. Since the times are measured for $45\mu m$ thick LC layers, which is within the typical range of thicknesses of mm-wave planar cells, these times can be used as a reference to know what to expect for these devices.

The f_c frequency, although typically provided by the manufacturer, can also be measured experimentally. To do so, a reflection coefficient at the unbiased state must be first acquired. Then, a bias waveform similar to the one in Figure 4.28(b), of a high voltage and the test frequency $f_1 = f_{c,test}$, must be applied. The resulting reflection coefficient which is most similar to the unbiased one determines f_c.

Transition	**Initial state**	**Final state**	**Biasing**
Induced rising	Lower state	Higher state	$\{V, f_1\}$
Induced decaying	Higher state	Lower state	$\{V, f_2\}$
Relaxation decaying	Higher state	Lower state	{0,-}

State	**Rise to by**	**Decay to by**	**Rotation**
OFF	-	Induced decay or relaxation	Parallel
ON	Induced rise with $\{V_2, f_1\}$	-	Orthogonal
Intermediate	Induced rise with $\{V_1, f_1\}$	Induced decay or relaxation	In-between

Table 4.5: DFLC transitions and state nomenclature

Since DFLC do have the same uniaxial structure of the molecules as conventional nematic LCs, it is possible to model the dynamics of their state switching, that is, predicting the permittivity tensor $\overline{\overline{\varepsilon}}(\vec{r}, t)$ even during transitions, by using the procedure of Section 4.2.

Mixture	f_c	f_1	f_2	V	T_{IR}	T_{RD}	T_{ID}
MLC2048	18kHz	1kHz	50kHz	5	5.6s	3.9s	1s
				10	1s	3.5s	0.3s
				15	0.5s	3.6s	0.1s
				45	0.2s	4.9s	15ms
				90	0.1s	4.2s	5ms
MLC2177	18kHz	1kHz	50kHz	5	3.4s	3s	0.9s
				10	0.55s	4.3s	0.6s
				15	0.28s	3.7s	0.25s
				45	25ms	3.6s	25ms
				90	10ms	4.4s	5ms
W1978C	3kHz	100Hz	15kHz	5	4.9s	10.4s	5s
				10	0.95s	10.7s	1.2s
				15	0.45s	10.8s	0.64s
				45	45ms	11.3s	60ms
				90	15ms	11.6s	15ms
P00-026	17kHz	500Hz	50kHz	5	5.1s	3.1s	1.1s
				10	0.4s	3s	0.3s
				15	0.2s	3.3s	0.12s
				45	20ms	2.9s	10ms
				90	5ms	3s	<5ms

Table 4.6: Temporal behaviour of the studied DFLC mixtures in $h_{LC} = 45\mu m$ cells at 101 GHz [120].

However, that would require knowing both the elastic constants of the mixtures and their rotational viscosity. If only the elastic constants are known, the static permittivity tensor can be predicted, as in Section 3.4.2. In practice, this information is unknown in most LC mixtures, although it could be extracted by experimental measurements [124]. However, the relationship between the obtained phase shift through the different applied voltages, as well as the temporal response under different excitations, can be acquired directly from measurements in a manufactured device.

Although it is common for LC-based devices to only operate under the extreme states (ON and OFF) of the LC biasing, as in the application of 1-bit reflectarray antennas or RIS, in general other applications can require of a continuous tuning of the voltage to work with intermediate LC states. For those cases, the synthesis of the voltages requires a fine prediction of the molecule tilt angle from these voltages, and finally the relation to its related exact permittivity tensor. This is usually a required step previous to operate these kind of devices. For instance, in reflectarray antennas, this is the commonly followed process that provides the relation between the applied voltage and the phase shift introduced by each unit cell. Therefore, this highlights the importance of such model, which can even include the material dynamics.

Name	**Initial state**	**Step 1**	**Step 2**	**Step 3**	**Final state**
Overdriven induced transitions	Lower state	$\{\pm 45V, f_1\}^1$	$\{\pm V, f_1\}^2$	-	Higher state
	Higher state	$\{\pm 45V, f_2\}^3$	$\{\pm V, f_1\}^2$	-	Lower state
Overdriven rise + reset	Any	$\{\pm 45V, f_2\}^4$	$\{\pm 45V, f_1\}^1$	$\{\pm V, f_1\}^2$	Any

[1] Overdriven rising transition to any state.
[2] Sustaining intermediate state.
[3] Overdriven decay transition to any state.
[4] Reset transition (overdriven decay to OFF state).

Table 4.7: Overdriving Biasing Techniques for DFLCs

4.5.3 Designing the bias of DFLC reflectarrays

In this Section, the previous DFLC information, obtained from simple bias signal transitions, is used to design waveforms that reduce the reconfigurability times, which can be finally used to operate devices at intermediate states.

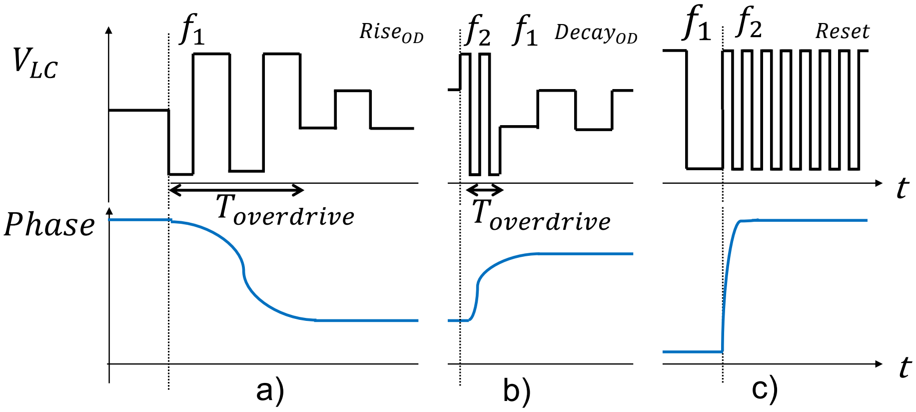

Figure 4.29: a) Overdriven rise bias signal. b) Overdriven decay bias signal. c) Reset decay bias signal.

As already mentioned, the transitions induced by the biasing field are significantly faster than the relaxation transitions occurring without any biasing field. Moreover, to sustain an intermediate step for a long period of time, the biasing waveform has to be kept at the desired amplitude voltage and at a frequency of positive anisotropy (e.g. f_1), since it is the only way in which the induced elastic forces oppose the anchoring torque. That is, if an intermediate state is reached by an induced decay transition, it can only be maintained by modifying the biasing waveform such that $|\Delta\varepsilon_{AC}| > 0$.

It has been seen how, when using DFLC, induced transitions are possible for both rise and decay (Figure 4.28(b) and Figure 4.28(d)), and thus achieve the time reduction, although the decay relaxation can still be used as with conventional LCs (Figure 4.28(c)). Since it is possible to actively drive both transitions, the dynamics can be controlled through the waveforms, similarly to the the process carried out in Section 4.3. Therefore, it is possible to speed up the reconfiguration between states not only by the induced decay but also by using overdrive biasing techniques. However, this requires applying more complex addressing waveforms, due to the required engineering of the signals.

With this in mind, two biasing techniques that can reduce the switching time between intermediate states are proposed, as detailed in Table 4.7. The first one consists of using, for both a rising transition and a decay transition, a precise design of the waveforms and overdrive, which monotonously modifies the phase from the initial state towards the final state. That is, the applied overdrive tries, for both transitions, to achieve the final phase as fast as possible. In the case of overdriven rise transitions to an intermediate state, a short high-voltage pulse with f_1 (e.g.: $\{\pm 45V, f_1\}$), followed by a lower voltage signal with f_1 (e.g.: $\{\pm 5V, f_1\}$) has to be applied as shown in Figure 4.29(a) under the label $Rise_{OD}$. In the case of overdriven decay transitions to an intermediate state, a short high-voltage pulse with f_2 (e.g.: $\{\pm 45V, f_2\}$), followed by a lower voltage signal with f_1 (e.g.: $\{\pm 5V, f_1\}$) has to be applied as shown in Figure 4.29(b) under the label of $Decay_{OD}$. This, as previously mentioned, is the result of the torques at play, since signals with f_2 induce an elastic force in the same direction of the anchoring torque, and thus an intermediate state cannot be sustained with such frequency.

By applying this bias technique, the best temporal behaviour is achieved, since the molecules directly rotate between the desired states, and it is accelerated through overdriving. However, the required circuitry to drive a SFPS device through this technique results complex, since each unit cell has to be driven independently at all times (as opposed to the second technique) and each cell must work both with low and high frequencies of the biasing signal (f_1 and f_2). An implementation of this strategy will be discussed in the next section for a prototype sample, where all the unit cells will be short-circuited, thus avoiding the biasing of independent unit cells.

The secondly proposed strategy applies a different approach for accelerating the transitions, where overdrive is also used. This consists of first applying an overdriven decay transition to the OFF state, termed as reset, to all the cells that must be reconfigured, as outlined in the last row of Table 4.7. Once the molecules have been quickly rotated towards their relaxed state, an additional overdriven induced rise transition is applied to reach the desired intermediate state. As it will be explained next, this second method comes with the advantage of a reduced circuitry complexity, because the reset can be easily applied to all unit cells simultaneously, but at the expense of a slightly increased reconfigurability time at the decay transition. Note that, even though for each state reconfiguration the molecules rotate to the OFF state before reaching the desired state, this is a much smaller time interval than the conventional decay transition.

As explained in Section 4.3, an accurate design of the biasing waveforms is required to make the most of the overdrive techniques. This means that the dynamics of the rotation of the LC molecules, and its effect in the phase, must be known for each transition. This allows to properly choose the duration of the high voltage pulses (labeled $T_{overdrive}$ in Figure 4.29), of both the induced rising and decaying transitions. It is important to highlight than, as in conventional LCs, the power consumption of the LC cells is kept very low even though high voltages are used while overdriving them, as the AC current flow through the cavity is very small.

In order to better understand the benefits of the secondly proposed biasing technique (reset between states), Figure 4.30 shows an example of a complete antenna implementation with independent unit cell addressing (2D). Rise transitions can be achieved by applying the signal ($\{V_i, f_1\}$) to each pixel of the bottom electrode (or by overdriving), and using the top electrode as ground for the biasing field, as shown in Figure 4.30. At $t > T$, the reset is easily achieved for all unit cells simultaneously by applying the signal ($\{V_{TOP}, f_2\}$) to the short-circuited top electrode. The resulting voltage across each unit cell of the cavity is $V_{LC} = V_{TOP} - V_i$.

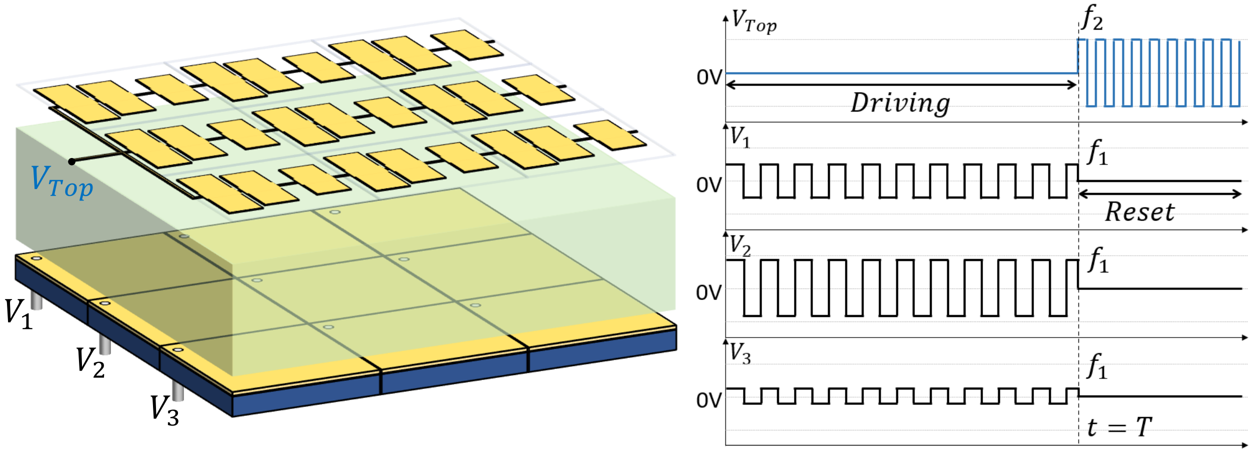

a) b)

Figure 4.30: Example of a 2D addressing reflectarray antenna implementation using the DFLC overdriven + reset biasing technique. a) 3D view of the antenna (3x3 portion shown for simplicity). The top AC electrode is short-circuited and connected to V_{TOP} whereas the bottom AC electrode is segmented in independent (V_i) unit cells. b) Bias signals to be applied. For $t < T$, the LC in each unit cell is being driven in an intermediate state. For $t > T$, a reset procedure quickly relaxes all the molecules simultaneously.

To exemplify this in a specific circuitry, a foreseeable architecture that could be developed to drive LC-based SFPS is an active matrix (AM) controller similar to the ones used in LCD, which are capable addressing the bias of thousands of pixels. These controllers make use of transistors and capacitors, included in each pixel, to hold the required states. These elements should be capable of handle biasing signals of higher frequencies (e.g. 50kHz vs. 1kHz) in the first method than in the second method, as the reset can be done at the other plane in the second method. Therefore, the second technique would allow a fast reconfiguration (compared to conventional driving) with simpler circuitry.

4.5.4 Fast-switching LC reflectarray unit cell

Leveraging the previous electromagnetic study of DFLC mixtures, and their temporal capabilities, a reflectarray unit cell fulfilling phase range (>360º) and temporal response specifications ($<20ms$) has been designed, and a sample surface (50 × 50 elements) has been manufactured and tested. Considering the dielectric anisotropy and temporal response of the studied mixtures, the chosen commercial DFLC is P00-026. The unit cell is similar to the one used in Section 4.2, but patterned in a $400\mu m$-thick quartz superstrate, and having a DFLC cavity thickness of $50\mu m$, as shown in Figure 4.31. The ground plane is constituted by a glass substrate which has been continuously covered with gold through sputtering. The inner surfaces of both the substrate and superstrate are treated with a polyimide layer to anchor the LC molecules, and properly rubbed to define their rotation plane. Finally, the cavity is sealed at the edges using UV-curing adhesive (NOA 81).

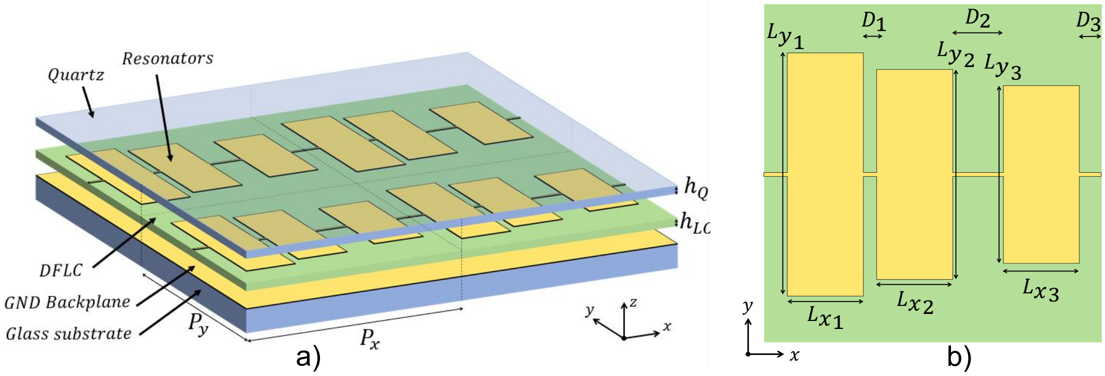

Figure 4.31: a) Layered view of the reflectarray with 4 unit cells (2x2 grid) b) Top-view of the reflectarray unit cell. Dimensions (mm): $D_1 = 0.042$, $D_2 = 0.096$, $D_3 = 0.171$, $L_{y1} = 0.792$, $L_{y2} = 0.748$, $L_{y3} = 0.707$, $L_{x1} = 0.2$, $L_{x2} = 0.211$, $L_{x3} = 0.2$, $P_x = 1.145$, $P_y = 1.093$, $h_S = 0.4$ and $h_{LC} = 0.05$.

The manufactured reflectarray cell, which can be seen in Figure 4.32(a), has been measured in the same setup as in the previous chapters in order to obtain the S_{11} parameter and temporal response. All the unit cells in the sample are short-circuited, since cell-level measurements are performed only, and periodicity is desired. Figure 4.32(b) shows, at the two extreme biasing states (ON and OFF) in stationary regime, the measured and simulated amplitude of the S_{11}, with an adequate agreement between both. This further validates the extracted permittivity values of Table 4.4, since the model allows a proper prediction of the measured behavior when manufacturing a different device (different LC cavity thickness and superstrate material). The device shows large losses, mainly determined by the mixture $tan\delta$ but also by the structure.

This manufactured reflectarray cell has been designed with the complete mixture knowledge, which allowed optimizing the structure to show enough phase range, at the expense of large losses. The reflectarray shows a reconfiguration bandwidth of 10% (>300º phase range), as shown in the measured S_{11} phase of Figure 4.33 for different biasing states. As can be seen, most of the phase change occurs between 2V and 5V, compatible with the mixture threshold voltage.

With the purpose of evaluating the temporal response of the device, the switchings between

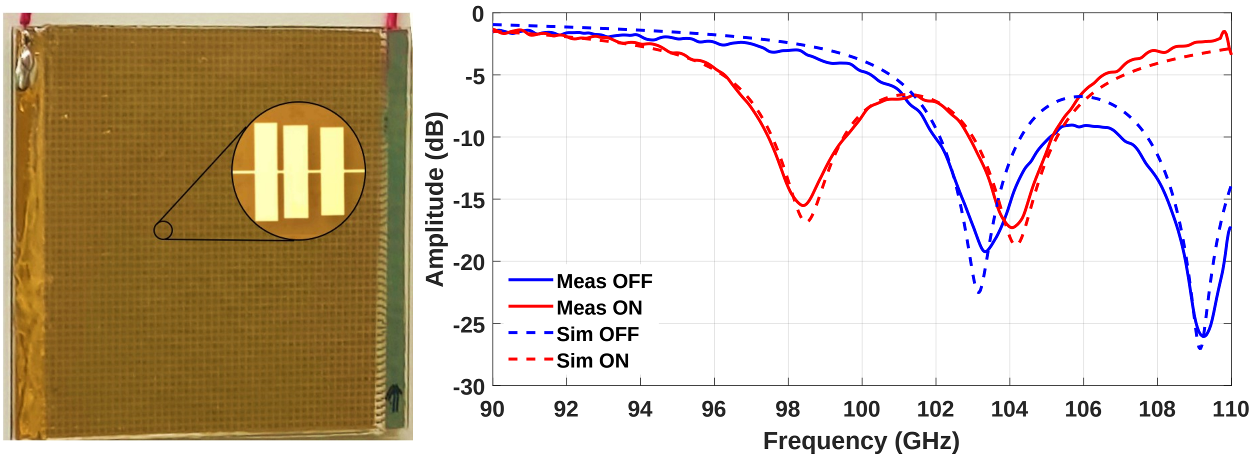

a)

b)

Figure 4.32: a) Picture of the manufactured DFLC reflectarray sample. A microscope image of the unit cell is included as inset. b) Measured and simulated S_{11} amplitude of the manufactured reflectarray unit cell using P00-026 DFLC.

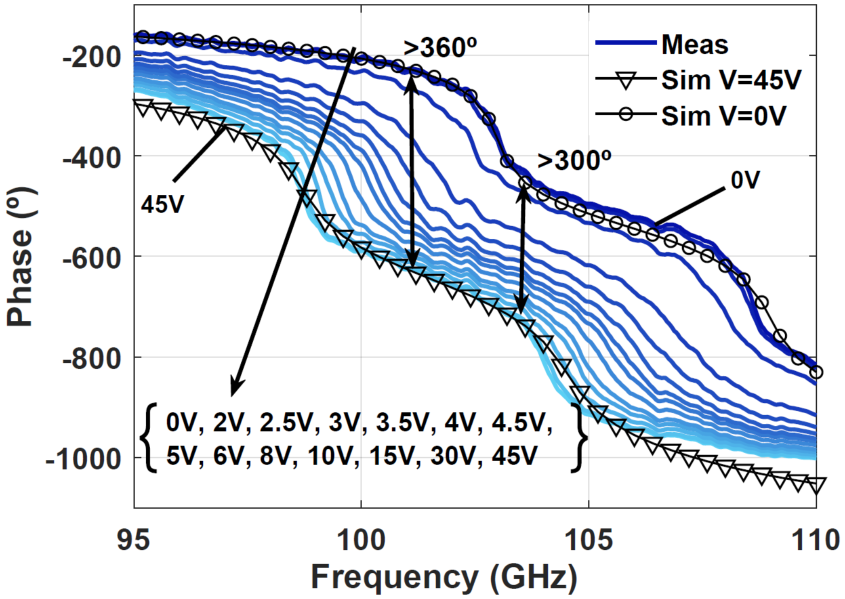

Figure 4.33: S_{11} phase of the manufactured reflectarray unit cell. Solid lines indicate measurements at different bias states, while triangle and circle markers indicate simulations at extreme biasing states.

extreme states (ON and OFF), and also in intermediate states, have been experimentally analyzed. By first considering the extreme state transitions, Figure 4.34 shows the measured behaviour of the device, in terms of the S_{11} phase evolution under four different transitions: induced decay through overdrive, relaxation decay, induced rise and induced rise through overdrive, where the actual corresponding signals for each transition are included. Note that, for clarity, the phase state at 0V has been normalized to 0º. Therefore, this figure represents the actual measurements of the previously sketched switchings of Figure 4.28. The conventional transitions, that is, induced rise (solid red) and relaxation decay (solid blue), which do not make use of overdrive, take more than 5s to converge to the final state. On the contrary, when using overdrive, the induced rise transition (dashed red) and the induced decay transition (dashed blue) take 20ms and 10ms to converge, respectively. It is interesting to note that the converged phase state of the overdriven induced transitions are not exactly the same as the ones reached by the non-overdriven states. In the case of the induced decay transition, the small difference comes from the fact that the final state of the molecules is different from the repose state, as there is a strong force pushing the molecules parallel to the reflectarray plane. This goes beyond the position of the unbiased case, where they are not perfectly parallel. In the rise transition, the difference is slightly larger and is caused by the different states under consideration (5V is applied for non-overdriven and 45V for overdriven). Given that these values are way beyond the LC threshold voltage, the reached states are quite similar, since most of the phase change occurs from 2V to 5V.

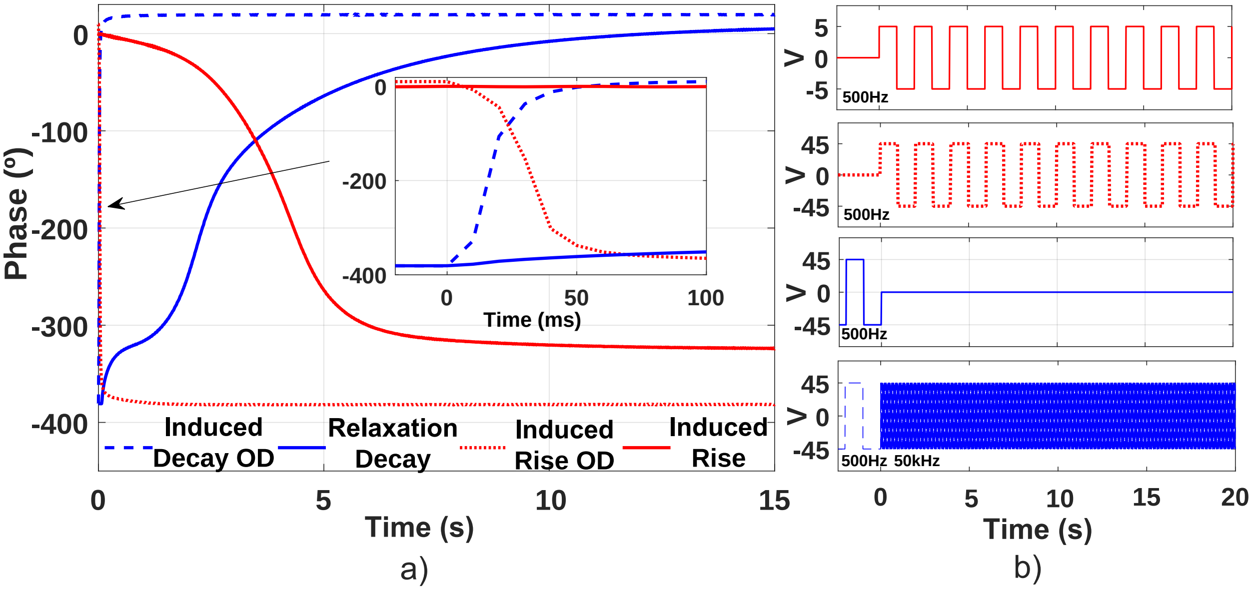

Figure 4.34: a) Comparison of measured DFLC phase transitions (S_{11} at 100 GHz) between extreme states (0V and 45V) with and without overdrive (OD). b) Biasing signals for the different transitions.

The switching between intermediate states has been analyzed next. First, the phase change is measured in an induced rise transition, from 0V to 5V, as shown in Figure 4.35(a). A transition without overdrive (black) and two overdriven transitions (red and blue) are shown. The overdriven transitions have been carried out using the induced transition technique rather than the reset technique (see Table 4.7), in order to minimize the response time. Therefore, the phase after a certain time of applying a high-voltage pulse determines the transition. Similarly to the previous case, using overdrive results in an important benefit in terms of temporal reduction, although in this case the objective of specifically reaching the 5V phase state reveals interesting effects on the resulting phase. The biasing of the first overdriven transition (red) consists of a 60ms 45V pulse preceding a 5V sustained state. This generates a rebound on the phase, attributable to backflow and inertia effects of the LC, similar to the one saw in Section 4.3. This rebound introduces a transient 70º phase error, although the agreement of the final phase state with the induced rise transition is excellent. Considering this transient error as tolerable, the resulting switching time is of 40ms, while the equivalent time through the induced rise transition (non-overdriven) is of 5s. Similarly, the second overdriven transition (blue), consisting of an 80ms 45V pulse preceding a 5V sustained state, reaches the desired state in 300ms considering a 20º transient phase error. Note that these times could be further reduced by employing voltages above 45V. These 70º and 20º errors, which are shaded in yellow and red in the figure, represent smaller errors than a 2-bit and 4-bit quantization errors, respectively, which in the case of a pencil beam only compromise the gain by 0.6dB and <0.2dB and slightly increase the SLL [91].

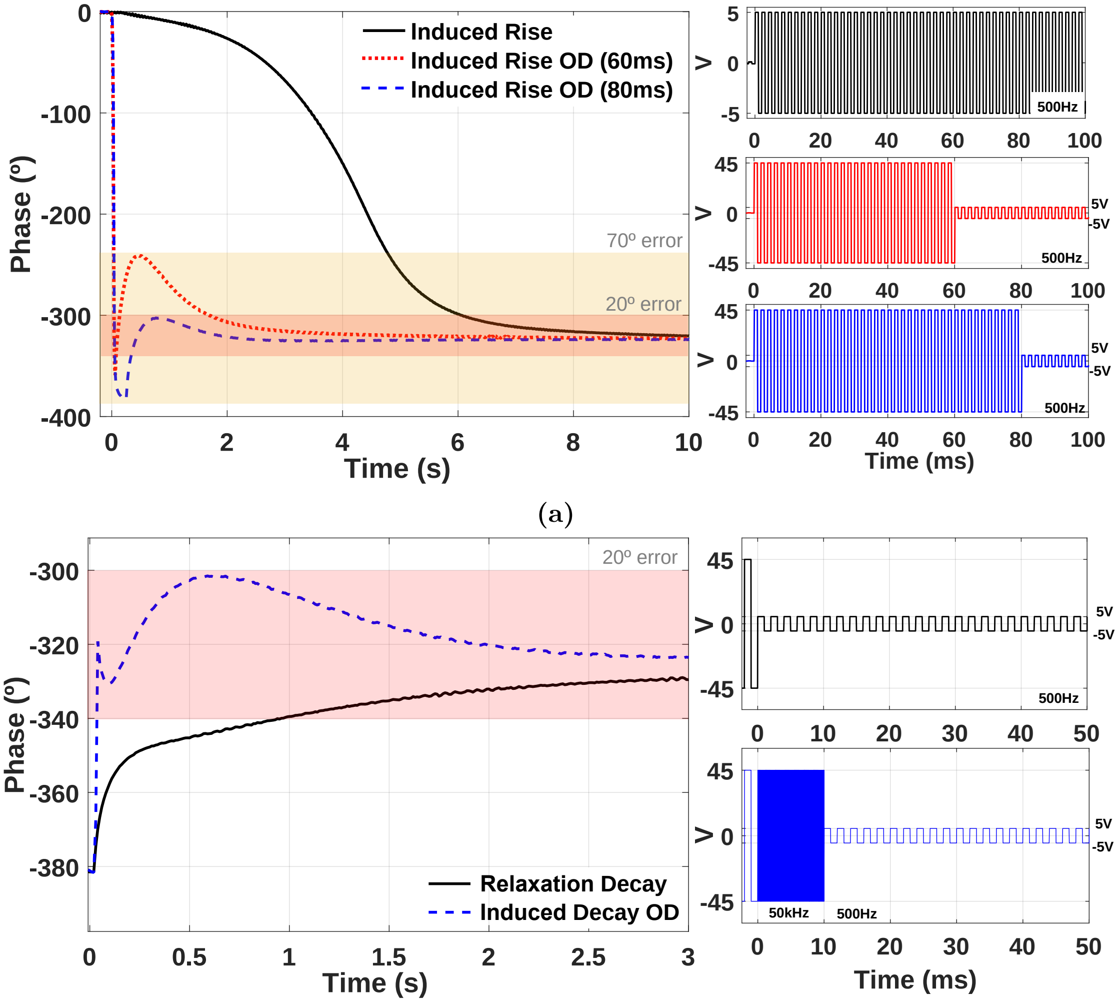

(a)

(b)

Figure 4.35: DFLC acceleration by means of overdriven induced transitions to intermediate states. The biasing signals for the different transitions are also shown. a) Measured rising transitions from a 0V state to a 5V state, b) Measured decaying transitions from a 45V state to a 5V state. The S_{11} phase at 100 GHz is shown.

Finally, Figure 4.35(b) shows the measurements in the S_{11} phase change of a decay transition from 45V to 5V, where both relaxation (black) and overdriven induced (blue) waveforms are shown. It can be observed how the relaxation (non-overdriven) decay transition takes around 1s to converge towards the final state, considering a 20º phase error. On the contrary, the overdriven induced transition converges in only $10ms$. In this case, the waveform includes a $10ms$ 45V pulse at 50kHz, which is not long enough to completely rotate the molecule (and, as such, the overdriven induced transition is used instead of the reset method), and the subsequent driving at 500Hz holds the molecule at the 5V state. It is worth mentioning that the intermediate state switchings shown in Figure 4.35 can be considered as the worst case scenarios, due to the presence of LC inertial effects, which are nonexistent in transitions to extreme states, and due to the small difference in bias voltage between states.

As has been observed, DFLC represents one of the best ways, if not the best, to reduce the response time of LC-based SFPS. The dielectric anisotropy of the studied mixtures are relatively low, but sufficient to design devices with enough phase range. However, they present large losses, given that they have not been optimized to be used in mm-wave. These aspects are expected to improve if specific mixtures are designed for mm-wave applications. Nevertheless, a reflectarray cell designed using one of the characterized commercial mixtures exhibits a complete phase range (360º), and temporal responses (rise and decay times) in the order of tenths of milliseconds, although at the expense of using overdriving techniques for both modes of operation of the DFLC. Therefore, the applied voltage must be in the order of tens of volts, and inertia effects must be also assumed, which produce transient rebound in the phase that makes necessary a previous definition of tolerable phase errors to define the transition times.

4.6 Far-field dynamic evolution

In the previous sections, different strategies to reduce the response time of LC devices have been studied. Even though the response to those techniques has been studied at the cell level, in many radiating devices, such as antennas or RIS, the final metric of interest is the far-field pattern. Therefore, expanding the previous results to their far-field effects is required.

During a configuration transition in a SFPS, the phases of all unit cells are changing simultaneously, and the ultimate effect on the radiation pattern is unknown. Depending on both the initial and final voltages, together with the specific LC mixture and cell dimensions, this transient process will take a different amount of time until the target phase state is reached in stationary regime, for each unit cell. Therefore, obtaining the reconfiguration time from the cell level to the antenna level is not trivial, given that the unit cells are transitioning from/to different states, which entails different switching times. As such, the repercussion for an entire array being reconfigured is missing in the literature. A study of these far-field radiation pattern transitions would be valuable to characterize and optimize the real behaviour between stationary states. For instance, in certain radar systems [125], information about the beam scanning transition could be used to improve the quality of the acquired data. In user beam scheduling schemes [126], a better prediction on the user throughput could be attained for the optimizations, and the corresponding scheduling algorithm could benefit from this information.

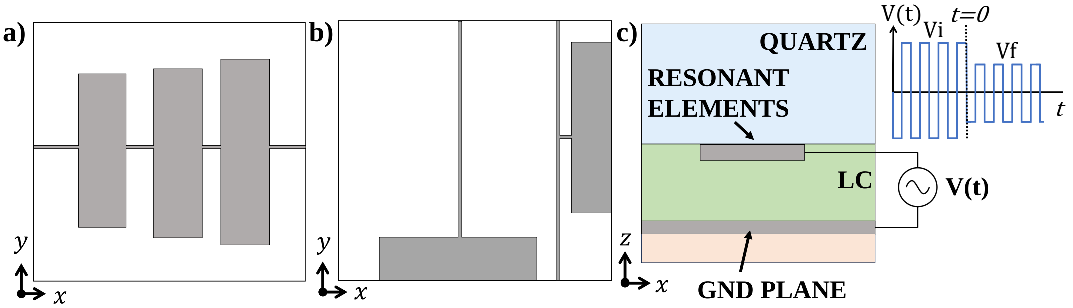

Figure 4.36: Unit cells used to evaluate the transient effect between states. a) Single-polarization (SP) unit cell (top view) from [41]. b) Dual-polarization (DP) unit cell (top view) from Chapter 3. c) Side view of the unit cells. The inset sketches the bias waveforms in each cell and the initial and final states.

4.6.1 Scenario considerations

The evolution of the radiation pattern is obtained for two different reflectarray antenna designs, considering the dynamics of the reflection coefficient of each individual unit cell from their initial to final bias voltages.

As introduced in Section 4.2, the dynamic reflection coefficients are first computed. For all the origin-target voltage pairs, the 1D Ericksen-Leslie Equation (4.2) is solved for 45 timestamps. The resulting data are the $\theta(z,t)$ curves of the LC director tilts, which are averaged across z to obtain an homogeneous material representation of a single layer $\theta(t)$. Then, as in Section 4.2, the permittivity tensor is computed from the averaged tilt angle, and a full-wave electromagnetic simulation (CST Studio) of the unit cells under those material conditions is carried out at each timestamp, to obtain the reflection coefficient evolution at 100 GHz.

The studied unit cells are the already introduced cells of Figure 3.1 (dual-polarization, single-resonant) and Figure 4.7 (single polarization), as their behaviour is well-known. The chosen LC mixture is GT7-29001 for both cells. A sketch including the biasing waveforms is shown in Figure 4.36.

The resulting cell-level transitions are shown in Figure 4.37 for both the single polarization cell (top) and dual polarization cells (bottom). Note that, as the single polarization cell has multiple resonances, its phase range is larger.

The SP antenna consists of 20×20 elements, and its unit cell is shown in Figure 4.36(a). On the other hand, the DP antenna consists of 55×55 elements, and its unit cell is shown in Figure 4.36(b). Even though this cell is sensible to both TE and TM polarizations, only the TE radiation is analyzed due to the great symmetry between both. The corresponding focal points of the horn antenna feeds for the SP and DP cases are located at $(x, y, z) = (0, 0, 45)mm$, and $(x, y, z) = (31.3, 0, 136)mm$ from the surface center.

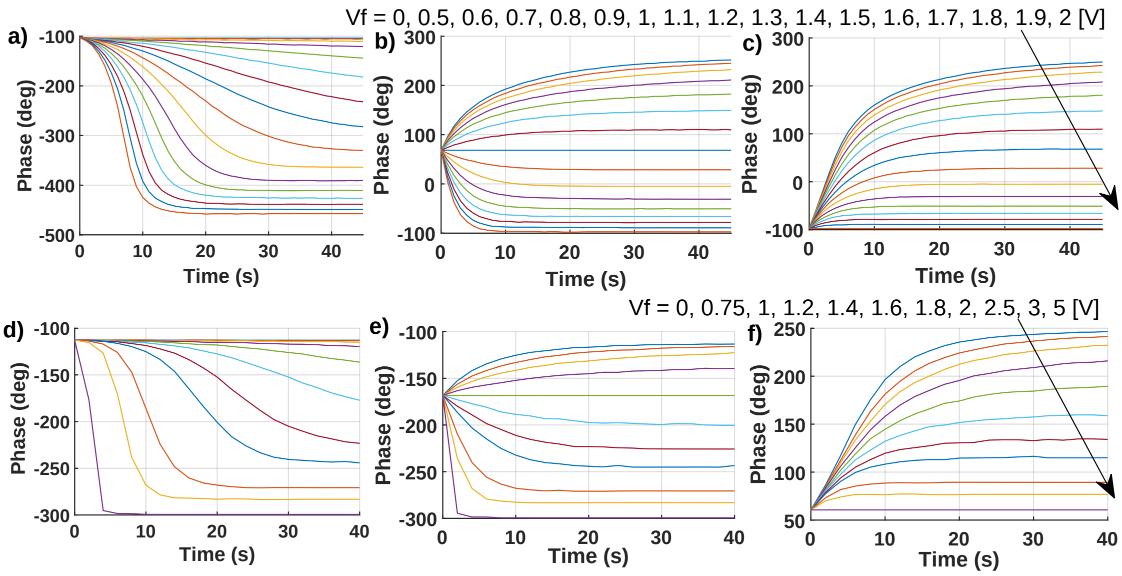

Figure 4.37: Evolution of S_{11} phase in different cell state transitions. a) From V_i=0V to V_f in the SP cell. b) From V_i=1.5V to V_f in the SP cell. c) From V_i=2V to V_f in the SP cell. d) From V_i=0V to V_f in the DP cell. e) From V_i=1.5V to V_f in the DP cell. f) From V_i=5V to V_f in the DP cell.

4.6.2 Far-field results

Once the unit cell behaviour is known for all incident angles and pairs of initial-final states, different beam configurations can be computed, and their transitions can be evaluated. Considering each reflectarray surface size and their focal points, the impinging fields are obtained. Then, by considering computed time-dependant reflection coefficients of all the unit cell elements, the reflected electric field is computed. Finally, the radiated far-fields are obtained using the angular spectrum of plane waves. This is done for different beam configuration transitions.

The resulting evolution of the radiation patterns between pairs of beam directions for both antennas can be seen in Figure 4.38. As can be observed, the target beam appears relatively soon during the transition, while the original beam gradually disappears. The radiation pattern responses are proportional to the response time of the unit cells, but considering an averaging effect among all the different cell state transitions occurring in each beam transition. The average unit cell response time (10%-90%) for the transitions in Figure 4.38(a-d) are 10.6s, 9.1s, 15.9s and 17.6s respectively, although as can be observed the target beam is generally formed much sooner.

Since the response time of the entire radiation pattern depends on the individual response times of each unit cells, there is no clear relation between the similarity of the initial and final radiation pattern and the response time of the beam. That is, sweeping a beam sequentially, as in a radar system, is not necessarily faster than switching between very different beams. However, this tool opens the door to study initial and final phase profiles that can accelerate such response. For instance, one could choose specific initial and final phases such that most

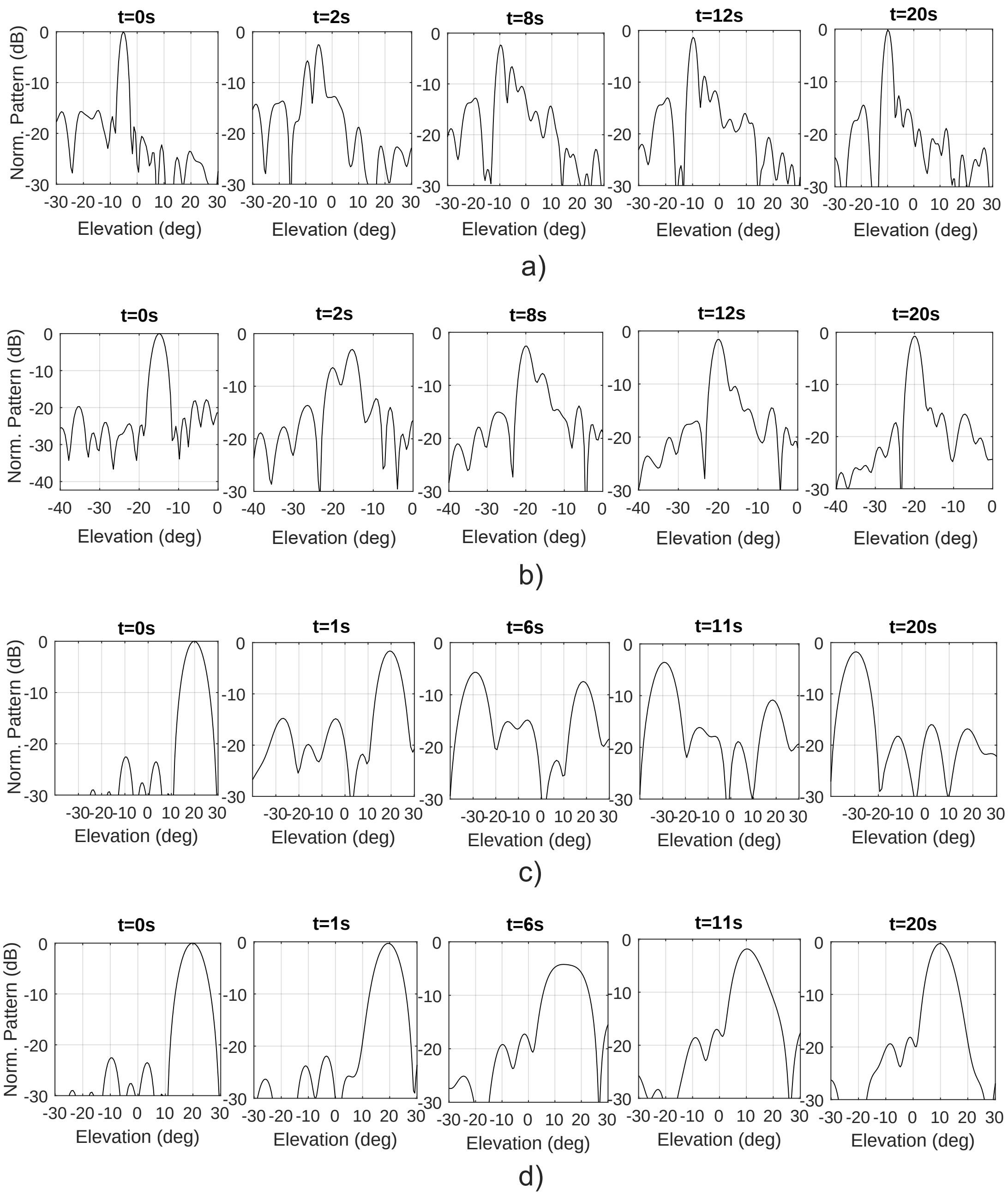

Figure 4.38: Evolution of the normalized radiation pattern. a) DP from -5º to -10º. b) DP from -15º to -20º. c) SP from 20º to -30º. d) SP from 20º to 10º.

of the unit cells suffer an increase of the voltage in a chosen set of critical beam transitions, which would result in a fast response. Moreover, since the center cells are expected to play a greater role, because their illumination power is higher, quick responses can be engineered by leaving the slowest transitions far from this area.

Note that the unit cells evaluated here do not make use of any of the LC acceleration techniques introduced in the previous sections, and therefore, the switching times are in the order of the seconds. However, this tool is also useful when considering LC antennas using acceleration techniques, since their dynamic permittivity tensor can be easily predicted. Therefore, much faster far-field transitions can also be predicted. Moreover, as in the originally presented antennas using these unit cells, the LC driving is by columns (1D). However, this analysis could be expanded to the different 2D driving techniques.

4.7 Dynamic effects of LC addressing techniques

To this point, the biasing waveforms have been considered ideal. That is, it has been assumed that the voltage driving the unit cells was exactly the same as the desired one, without any distortion or without considering the possible problematic related to it. In the antenna of Chapter 3, these issues were relatively limited because of the 1D biasing, which required only synthesising 110 simultaneous voltages. However, when 2D biasing is required, or when the number of simultaneous voltages increases, the connector handling starts to become complex, and proper strategies are required. For instance, if the same antenna was designed for 2D with the same biasing strategy, the required number of connectors would be 3025. For a M×N = 80×80 elements array, which is a reasonable size for a high-gain antenna, 6400 connectors would be needed.

Fortunately, there exist biasing techniques that ease this issue, but at the expense of signal distortions, such as leakage and crosstalk. Each of these techniques apply, in different ways, varying effective root mean square voltages to drive the LC. The Selection Ratio (SR) of the unit cell biasing signal is defined as the relation between the maximum and minimum effective cell voltage $SR = V_{ON}^{rms}/V_{OFF}^{rms}$. While in optics a small SR can be used in some cases, to do so in RF devices can lead to unusable devices that provide virtually no phase shift. Although these biasing techniques are widely studied in optics [29, 127, 128], their implications in multi-resonant RF devices are unexplored. Therefore, this study is a necessary step in the design process of such devices before the manufacturing takes place, since it allows for the validation of the driving controllers, the array dimensions, the biasing signals and the real achievable phase range of the cells. That is, even if the unit cell design is perfectly optimized to provide a great phase range and other performance metrics, an inadequate or poorly sized bias method that introduces unexpected effects on the LC excitation signals can greatly degrade the RF behaviour of the entire device.

In this Section, these are considered in the dynamics of a well-known unit cell [41] response, allowing a prediction of the reflection coefficients in a more realistic scenario. The procedure aims at helping design and validate the bias technique and its proper signals, as well as the sizing of the array according to the chosen strategy. As such, it can be used before manufacturing a final device to prevent errors with respect to the expected phase range and other RF performance metrics.

4.7.1 Direct addressing

In a direct addressing scheme, each pixel of the array is biased independently. That is, $M \times N$ different signals are required to drive all the elements with complete freedom if 2D scanning is desired, where M and N are the number of rows and columns respectively. This technique allows to provide true zero voltage to some cells and to completely activate other cells, which can theoretically produce an infinite SR. However, the number of required signals grows rapidly in large arrays and can become very complex to manufacture in practice, even prohibitive. Figure 4.39 shows an example of the bias signals required to drive the array using this strategy. As can be seen, each pixel directly receives the required voltage so that the LC is biased to the desired state.

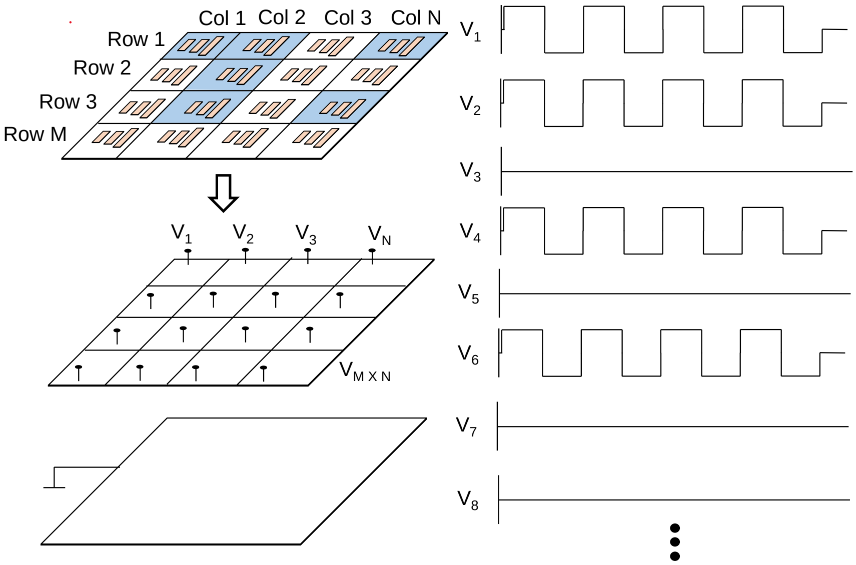

Figure 4.39: Direct addressing example. Blue/white pixels are active/inactive.

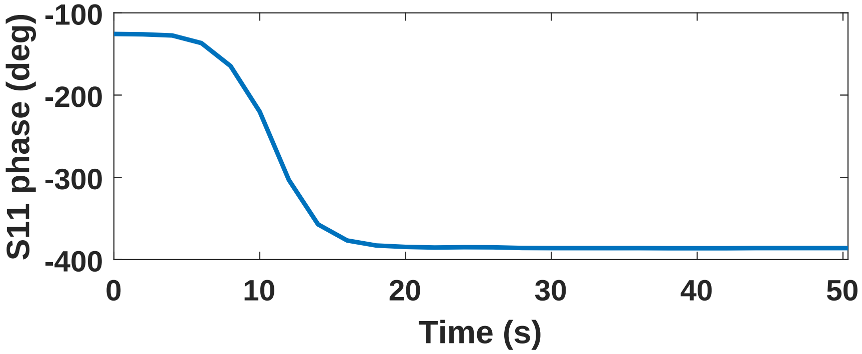

Figure 4.40: Reflection coefficient phase evolution under a 7V direct addressing signal of the cell of [41]. The cell is initially unbiased (LC relaxed state).

In terms of electromagnetic performance this is the most attractive biasing. To model its behaviour is straightforward by taking the dynamic model introduced in Section 4.2, as the cavity AC electric field is directly determined. Figure 4.40 shows how the phase of the evaluated unit cell evolves over time after when a direct addressing signal is used to bias the LC. As can be seen, the phase directly converges to the corresponding value, as this is the most ideal case of biasing. This is the case of the Dual-Polarization reflectarray antenna introduced in Chapter 3, although in that case the relaxed 1D scanning requirement reduces the required control signals to the columns only ($N = 2 \times 55$). [43] and [129] are examples of reflectarrays implementing 2-D direct addressing.

4.7.2 Active addressing

Active biasing consists on reducing the number of control signals to only $M + N$, but at the cost of placing active elements in each pixel [130]. In this strategy, the different cells are being periodically swept with the proper voltage to maintain the desired bias state. Consequently, the role of the active elements is to hold the voltage during the period of time in which the pixel is not being addressed. Moreover, this provides a certain pixel independence, which results in a large but not infinite SR, and reduced crosstalk between bias lines. These active elements typically consist on a transistor and a capacitor. For instance, in [42], a LC reflectarray that uses active addressing to scan the beam in 1D is presented.

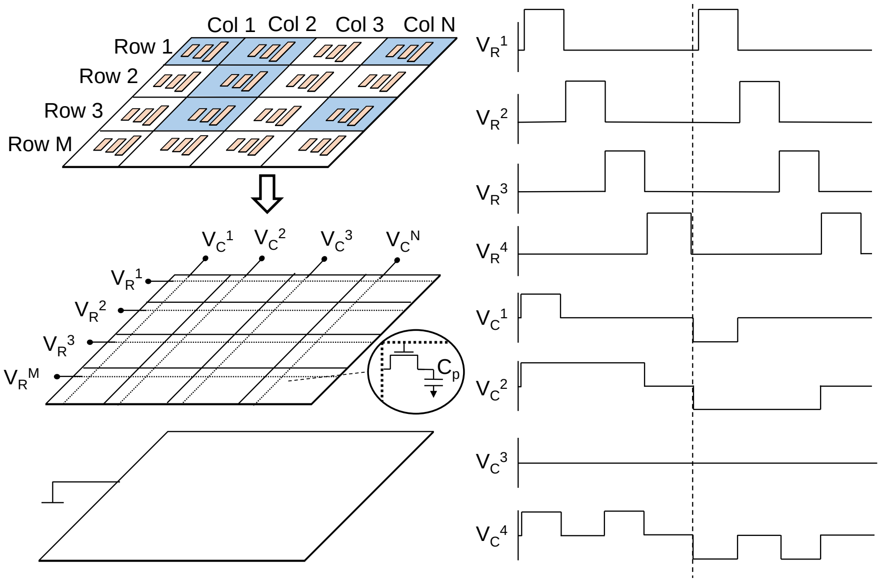

Figure 4.41: Active addressing example. Blue/white pixels are ON/OFF.

Figure 4.41 shows an example of bias signals required to drive the array using this strategy. In this case, the row signals are used to select an entire row, that is, to activate the transistors, and the column signals are the data voltages that will actually bias the LC. As can be seen, row signals periodically select the different rows, and while a row is selected all the column signals are used to update the bias state of such row.

Ideally, the transistor leakage together with the parasitic elements and the crosstalk between pixels are negligible. In that case, the voltage across the LC cavity is the same as in the direct addressing case. However, in practice these effects will co-exist and can modify the electromagnetic performance of the array. For instance, when leakage takes place, the root mean square voltage reduces and therefore the cell behaves differently, as seen in Figure 4.42(a).

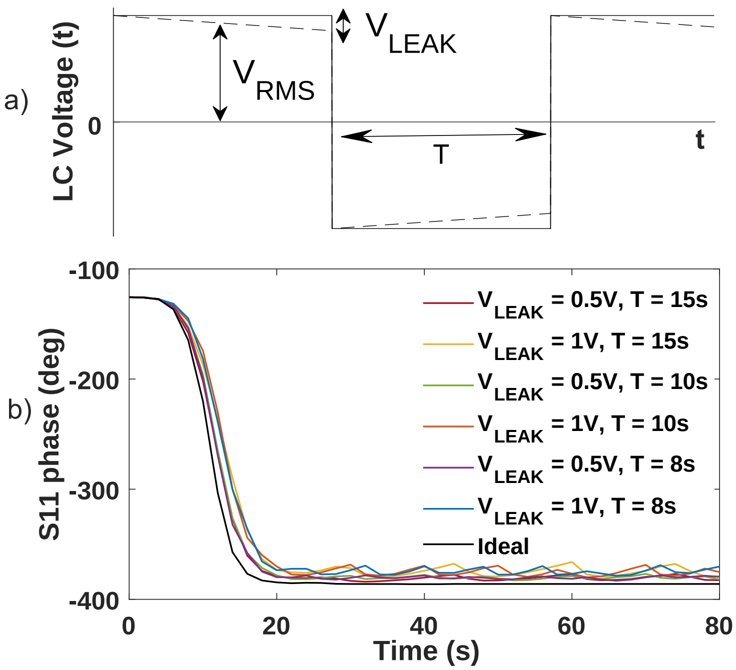

Figure 4.42: a) Ideal (solid) and leakage (dashed) cell voltage. b) Reflection coefficient phase evolution under different active addressing scenarios of the cell of [41]. The cell is initially unbiased.

The phase change evolution over the time, when a 7V active addressing signal suffering from leakage is used, can be observed in Figure 4.42(b), where different leakage scenarios and refreshing rates are analyzed. Although there is little difference with the previous direct addressing case, it can be seen how the leakage and the different refreshing rates result in a slight periodic phase relaxation. Moreover, the final achievable phase slightly varies as well. This indicates that the slower our refreshing rate, or the larger our array, the more leakage our cells will suffer and therefore the more unstable will be the phase. Even though the electromagnetic performance is barely degraded, this ultimately depends on each application of the SFPS. Consequently, performing this analysis allows to validate that the number of rows and columns in our array is properly designed, together with the bias voltage and refreshing rate of the cells, considering leakage effects. It is worth noting that other undesired effects, such as the kickback effect resulting from the transistor turn off, parasitic effects, or any actual waveform variation, can be easily included as well.

4.7.3 Passive addressing

Biasing the array by means of a passive addressing strategy allows, as in the active addressing case, to reduce the number of control signals to $M + N$. However, in this case, manufacturing complexity is reduced as no active elements are placed, at the cost of obtaining an electromagnetic response which is highly dependent on the LC dynamics. This is, therefore, the addressing technique in which this analysis is most useful.

Since the pixels are not isolated, the voltage across the cell must be designed such that the root mean square voltage is high enough (above the LC threshold voltage V_{TH}) for active pixels, but low enough (below V_{TH}) for inactive pixels. To do so, the row signals, $V_R^i(t)$, and the column signals, $V_C^j(t)$, are properly designed and connected to different planes (top and bottom electrodes respectively) as can be seen in Figure 4.43, where T is the refreshing period. Therefore, the voltage across the cell is $V_{LC,ij}(t) = V_R^i(t) - V_C^j(t)$.

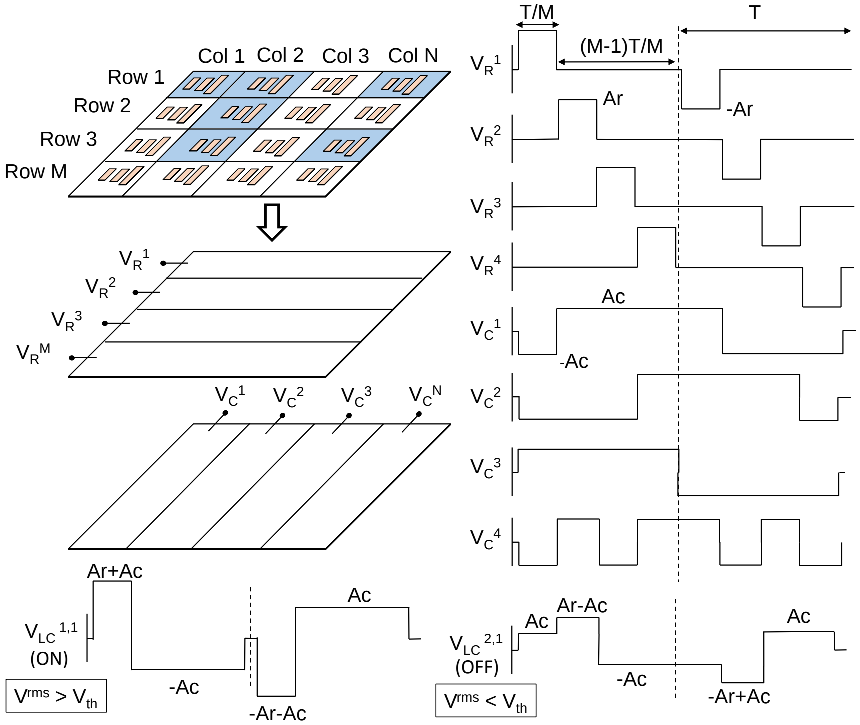

Figure 4.43: Passive addressing example. Blue/white pixels are ON/OFF (1-bit).

By following this scheme, when a pixel is active (ON) the applied voltage is $|Ar + Ac|$ during the row selection period, and $|Ac|$ the rest of the time. During this non-selection period, the passive addressing method relies on the slow relaxation time of LC to hold the LC molecules switched on during a certain amount of time. Similarly, when a pixel is inactive (OFF) the applied voltage is $|Ar - Ac|$ during the row selection period, and $|Ac|$ the rest of the time [131]. Therefore, an inactive pixel will never have a true zero voltage, and the resulting SR is very limited. Consequently, to achieve the desired root mean square voltage in each case requires a careful selection of Ac and Ar. An improper selection of those parameters can lead to accidental activation of inactive cells and vice-versa. For this analysis, the chosen Ac, Ar are the ones that maximize the SR ($Ar/Ac = \sqrt{M}$), and so that $V_{OFF}^{rms} = V_{TH}$, as suggested in [131]. Note that this last option is a design choice, and that choosing a V_{OFF}^{rms} such that the effective phase-voltage steepness of the cell is maximized, which depends on many geometric aspects of the cell, can lead to better results. In a reflectarray design process, M is usually fixed by the radiation requirements. Then, once Ac and Ar are chosen, T is the only free parameter left. Intuitively, the larger T is the slower our device will reconfigure. Moreover, when T is large, the non-selected period can be large enough so that the LC molecules completely relax and the phase returns to the relaxed state. Figure 4.45 shows the

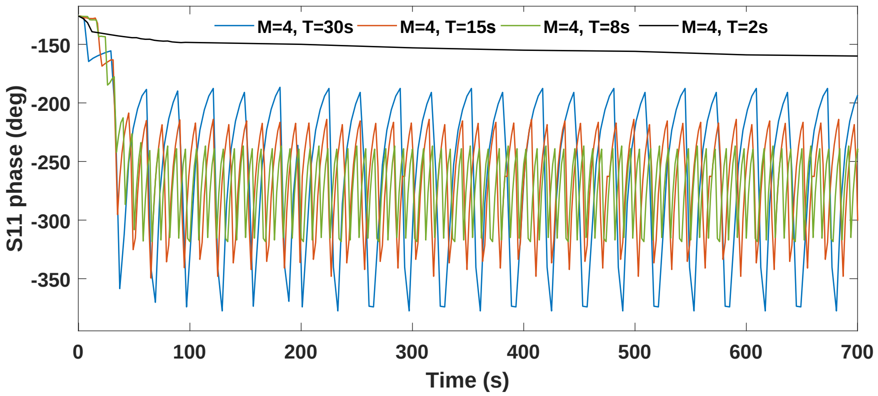

Figure 4.44: Reflection coefficient phase evolution under different passive addressing scenarios. The used cell is that presented in [41], and is initially unbiased.

selection ratio curve as a function of the number of rows in a passive addressing scheme. Since the SR increases with M, large arrays will present a deficient contrast and the applicability reduces. This is seen in Figure 4.45, where the SR gets asymptotically close to 1 (null phase range).

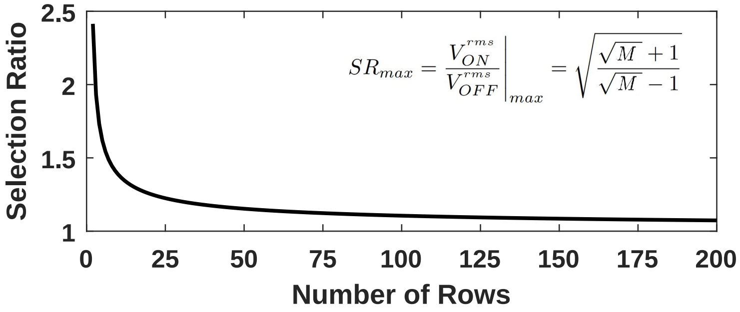

Figure 4.45: Maximum selection ratio as a function of M in passive addressing.

Figure 4.44 shows the temporal evolution of the reflection coefficient phase of the active cell, within an $M = 4$ array, under different signal conditions. This small value is chosen to give emphasis to the passive addressing effects. As can be observed, $T = 30s$ and $T = 15s$ conditions make the phase relax every T seconds, which reduces the effective achievable phase range of the cell and introduces a large error (up to 150º). $T = 8s$ also makes the phase to fluctuate but reduces such error. It should be noted that making the bias signal vary too fast, as in the $T = 2s$ case, can make the molecules to not have enough energy to be properly excited, resulting in a very poor phase shift. Therefore, choosing a proper value of T according to our array size and Ac, Ar values is essential.

To further consider a more realistic scenario, the electromagnetic behaviour of the cells suffering from crosstalk effects is analyzed. Crosstalk arises when certain parasitic capacitances and resistances appear in the biasing network circuitry. Therefore, these effects can be included by considering the independent RC charging effect of the row and column signals [131]. This allows to take under consideration the asymmetric effects of the row/column cables and the

LC cavity capacitance when evaluating the achievable phase of the cell, and therefore to validate the array capabilities in realistic or worst-case scenarios, before manufacturing. The effects of the crosstalk in the bias signals are depicted in the example of Figure 4.46, where the rows and column signals are affected by a symmetric crosstalk (same RC) for an entire row ($M = N = 4$ array). This is a different case from that in Figure 4.43. As can be seen, the first and the last cells will be switched off as the V^{rms} is below $V_{TH} = 2.4V$, while the second and third cells will be active, but significantly affected by the effects of crosstalk. Figure 4.47 shows the temporal evolution of the reflection coefficient phase under different crosstalk conditions (different and symmetric/asymmetric RC constants), where the last case corresponds to the biasing of Figure 4.46. It can be observed that the phase behaves as expected, but in some cases the cells are not be completely on/off due to the crosstalk. This allows designing and assessing a correct size of reflectarrays and other LC-based metasurfaces.

Even though the examples above show a binary activation of the pixels (1-bit), a partial activation with intermediate V^{rms} is also possible, usually referred to as greyscale in optics. There are several techniques to achieve a medium RMS voltage in the pixels rather than extreme values $V_{ON}^{rms} >> V_{TH}$ or $V_{OFF}^{rms} << V_{TH}$, being the use of pulse width modulation (PWM) the most extended one. Since this tool is general to any bias signal, it can also be used to pre-compute the PWM temporal signals to obtain the desired continuous phase values.

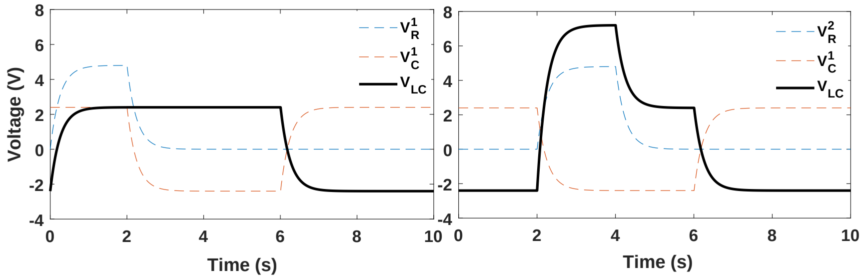

a) Column 1, Row 1

b) Column 1, Row 2

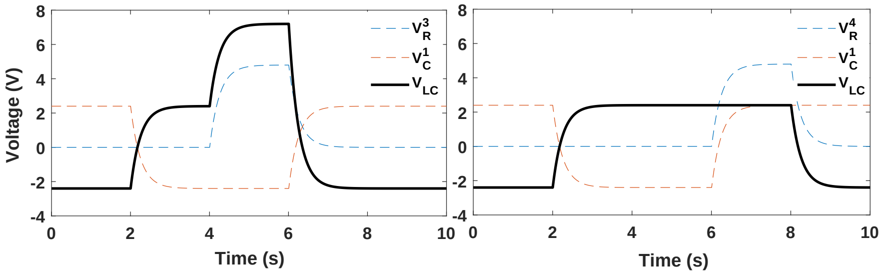

c) Column 1, Row 3

d) Column 1, Row 4

Figure 4.46: Bias signals example for a passive addressing scheme suffering from crosstalk (RC=0.25 symmetric, M=N=4, T=8s). 4.43

Finally, a comparison for different unit cells is carried out in terms of SR. Two sets of cells (A and B), with different cavity thicknesses ($45\mu m$ and $75\mu m$) are studied, so that they exhibit different phase ranges. Figure 4.48 shows how by designing unit cells with steeper curves, which are in general attainable by manufacturing thinner LC cavities, smaller SR can be tolerated, allowing addressing techniques with small SR that tend to be simpler (e.g. passive

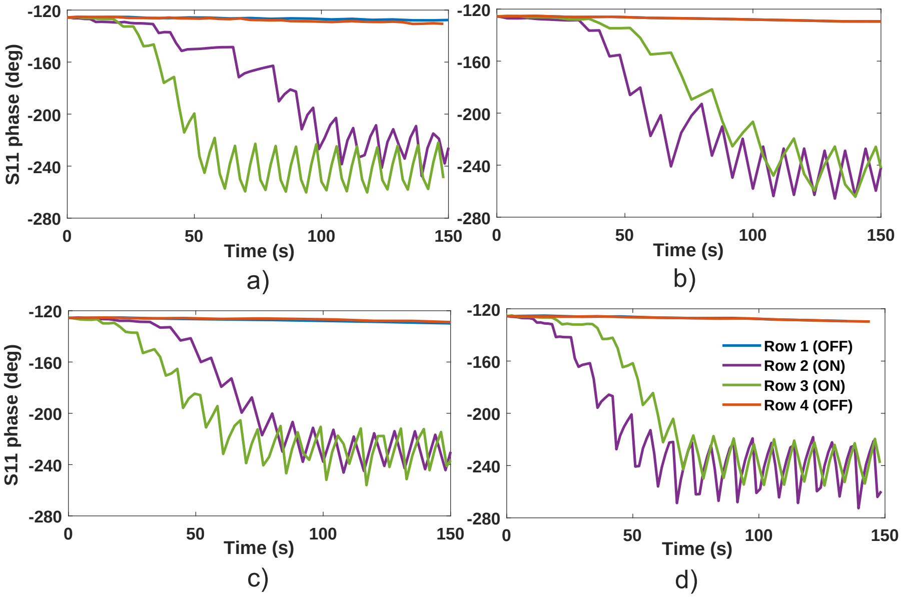

Figure 4.47: Reflection coefficient phase evolution under different passive addressing scenarios suffering crosstalk. a) Column RC=0.5, ideal Rows (asymmetric) b) Column RC=0.25, ideal Rows (asymmetric) c) Column RC=0.5, Row RC=0.5 (symmetric) d) Column RC=0.25, Row RC=0.25 (symmetric). The cell is initially unbiased (N=M=4, T=8s).

addressing). However, this comes at the cost of a higher sensitivity and, in general, higher losses. As can be seen, the direct addressing allows for the maximum phase range and the active one slightly reduces it, while the passive clearly deteriorates it.

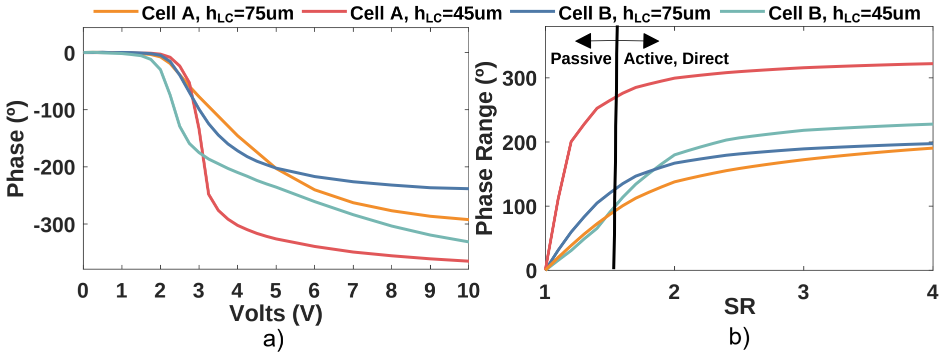

Figure 4.48: a) Phase-Volts b) Phase range-SR curve in different RA cell designs. Cell A is the same used for all the analysis [41], while the design of cell B corresponds to the cell 3 introduced in Figure 4.20, Table 4.1.

Overall, although the passive addressing scheme is the most simple to implement, it is impractical to implement for large array devices, due to the SR and crosstalk limitations. For medium-sized arrays, direct addressing provides the best performance results at a limited complexity cost, while for large array implementations the active addressing scheme should be chosen for a reasonable trade-off between SR and complexity. However, the cell design and its achievable phase range have great impact on the optimal addressing technique.

Given the SR limitations in RF, as well as the radically different way phase shifts are obtained as compared to photonics, an accurate dynamic LC characterization becomes relevant in the different addressing techniques, especially in passive and active addressing arrays with large M and N values. Amplitudes and timings of the biasing signals must be properly chosen considering the LC dynamics under such cells, so that the RMS is effective and the phase behaves as expected between refreshes.

Chapter 5

Development of a Reconfigurable Intelligent Surface based on Liquid Crystal

A fairly new concept of device, which can be categorized as SFPS, are reflecting electromagnetic surfaces that re-radiate impinging waves towards a specific direction or set of directions, in order to improve the network coverage. These are usually given the name of RIS [132, 133], although they are also denominated intelligent reflecting surfaces (IRS), metasurfaces [50, 134] or electromagnetic skins [135]. Since the purpose and application of these is very similar, in the last years there has been an attempt to unify all these nomenclatures [136].

RIS are an essential part of the concept of smart radio environment, in which dynamically controlling the electromagnetic medium is intended (see Figure 1.2(b)), rather than trying to adapt our devices to the existing one [137]. These concepts have not been needed for now, due to the high penetration of the bands currently deployed in base stations. However, this can make sense when thinking about the future networks operating at mm-wave bands, where even small objects can block or significantly degrade signals, and many communication systems could rely on line of sight. RIS devices aim at providing better reflection performance than the conventional metallic plate, providing enhanced communications to the specific environment (passive RIS). In the case of electronically reconfigurable RIS, the beam can be modified as desired through the control of the phases in the surface. These devices are thought to be useful not only outdoors, where they could provide cellular coverage to blind zones where signals cannot reach due to blocking elements, but also indoors, for demanding devices utilizing ultra high capacity links, such as AR/VR [138].

As previously mentioned, the main difference between a RIS and a reflectarray antenna is the application scenario, which leads to enlarged panels and a large distance to the feeder in the RIS case, but their operating principle is very similar. As a comparison, the incident electric field of the antenna developed in Chapter 3 comes from a closely placed horn antenna. Its position can be designed for an optimal illumination, and the impinging waves are spherical. Its purpose is to radiate the electromagnetic waves from the feed horn to the far-field while varying the radiation pattern. On the contrary, in the expected RIS applications, the illumination comes from a far-away base station, which does not leave much room for choosing a proper impinging field, and the purpose is only to partially improve the coverage in some region.

However, both the reflectarray antennas and RIS share a resonant behaviour to generate phase-shifts, which can be used to fulfill the radiation pattern requirements. In both cases, the radiation pattern can be reconfigurable (active) or not (passive), and the technologies to do so can work very similarly.

There exist few implementation cases of LC-based RIS [119]. In [139], 32×32 element RIS operating at 280 GHz is presented, but system-level measurements in realistic environment are not carried out. In [140], a moderated-size 30 GHz LC RIS device containing 12×12 cells is manufactured and tested with 1-bit beam-forming. A 15×15 surface resonating at 40 GHz is measured at the cell level in [141]. Similar examples include [142], [143], where measurements are done assuming electrically close illumination feeds. However, there is a lack of real electrically large prototypes that can successfully beam-steer, and not enough signal or system-level tests have been carried out. That is, there is very limited experimental literature about the impact of LC RIS in terms of SNR, error rates and other link metrics when transmitting modulated signals.

This is because of several difficulties. Current commercially available end-to-end transmission systems are focused on the deployed (5G) or soon-to-be deployed bands, which rarely go beyond 30 GHz. However, the LC technology is easier to be implemented at higher frequency bands, from 100 GHz above. Designing and fabricating SFPS LC devices operating below 30 GHz requires specific clean room technologies, increasingly dissimilar to the ones for optic devices, and the ones specified at Chapter 2. This becomes more complex if microwave substrate materials are used. This contradicts one of the key advantages of LC devices, which is their well-known and standardized manufacturing processes from the optics industry. Moreover, apart from the manufacturing itself, the RIS illumination conditions require large active array areas to radiate a relevant amount of power, which for low frequencies translates to very large physical dimensions. This enlarged area, added up to the increased wavelength of operation, can soar the overall costs, including the amount of mm-wave optimized LC material itself.

In this Chapter, a LC-based RIS is designed at 27 GHz. The large sizes required for the expected RIS operation are compensated by means of a modular design in which separate RIS panels can be mounted together to obtain a larger active area. A RIS panel is manufactured and tested, and system-level metrics using standardized 5G control signals are measured. Its performance is compared to the equivalent scenario with a metallic ground plane which only provides specular reflection.

5.1 Unit cell and panel design

The unit cell is based in a single-resonant dipole-shaped metallization element, as shown in Figure 5.1. It is chosen for its simplicity, since the objective of the device is not to provide any advanced capability, such as wideband or dual polarization, but to demonstrate the feasibility of a LC RIS with enough size at this operating frequency. The S_1 and S_2 distances are chosen such that the patch is centered. It has been designed for TM operation, that is, at $\phi_{inc} = 90°$, and for reduced sensitiveness to the angle of incidence. The bias lines are perpendicular to the patch resonant dimension axis, targeting 1D focusing and beam-steering in elevation.

An important feature of this unit cell is the superstrate material, which is chosen to be Rogers 4350B. This material is specifically designed for microwave designs, such as microstrip devices, and as such it features low losses ($\varepsilon_r = 3.65, tan\delta = 0.0035$). Contrary to using quartz, this material is not perfectly suitable to be used with LC, and therefore there are specific aspects to consider, such as its roughness, hardness, and its tolerance to the baking temperatures, for successful manufacturing. However, its cost is much more reduced, as printed circuit board machining and patterning technology can be used. The material of the ground plane (glass), and the rest of the unit cell elements are similar to the previously introduced ones. A microwave-optimized material is not considered for the ground plane as it does not have any benefit in RF performance (the metallic backplane completely masks it), and its properties are less adequate for manufacturing LC structures.

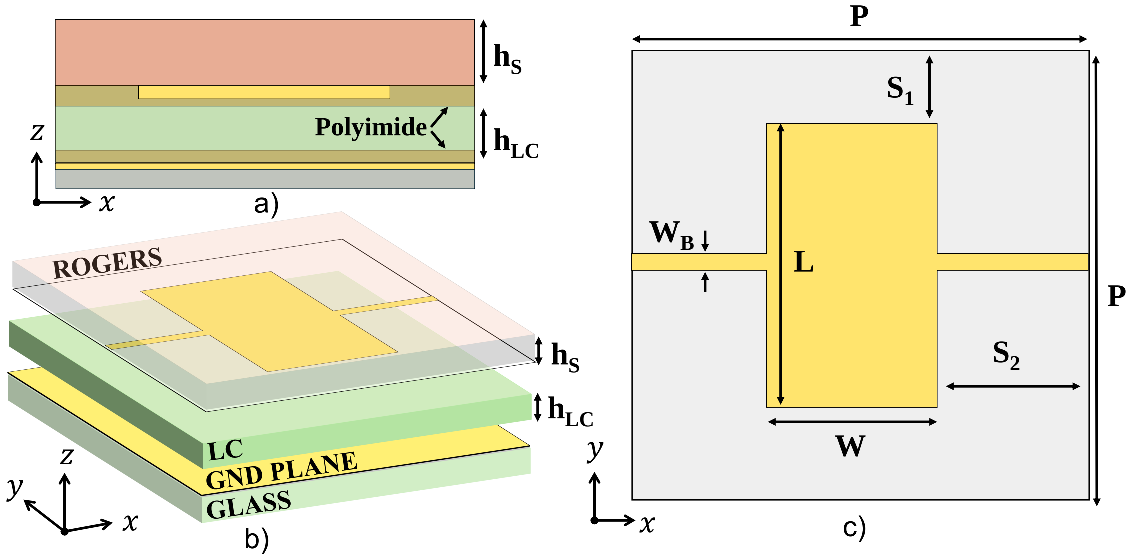

Figure 5.1: a) Side view of the RIS unit cell b) 3D view of the unit cell c) Top view of the unit cell. Dimensions (mm): $h_S = 1.524, h_{LC} = 0.11, h_G = 0.03, P = 4.9, L = 2.967, W = 1.932, W_B = 0.2, S_1 = 0.967, S_2 = 1.484$.

The size of the panel active area is 175×185 mm, which fits 36×38 elements per panel and already represents an electrically large surface on its own. This forced a few modifications to the manufacturing procedures at the clean room, specifically in the spin-coatings, alignment layer and sealing steps. The thickness of the metallic resonant elements is also to be considered. While in the quartz or glass the sputtered gold thickness is around 1 μm-thick, it is of 30 μm in these panels. This generates additional differences in the LC cavities, to be taken into account.

Note also that the thickness of the LC cavity is large. The reason for this is twofold: first, the scaled up dimensions, relative to the wavelength of operation, already leads to an increase thickness. Otherwise, keeping a very thin cavity leads to critically-coupled antiresonances [82]. Nevertheless, in the benefit of a reduced usage of LC volume and reduced response time, the cell is theoretically designed to work at $80\mu m$. However, because of the gold thickness of the superstrate, the resonant elements protrude significantly from it. This region beneath the resonant elements is where the RF fields are mainly confined, and thus the effective thickness of the cavity is reduced to approximately $h_{LC} - h_G$.

The complete RIS device will consist on mounting together several of these panels side-by-side, with a correct alignment and biasing voltages, such that it acts as a single device as shown in Figure 5.2(a). However, because of this modular approach, the panels can be added or subtracted, and the total RIS active area will correspond to the addition of all the panels active areas. Each of the panels, apart from the 36×38 resonant elements, contains the bias lines and the connectors interface to a flex cable. This allows an independent connection of each panel to the corresponding drivers.

It is important to note that, at the phase synthesis stage of the RIS, when the panel voltages are computed considering the relative phases of the impinging waves, the coherence of the phase shifts must be kept (using the same phase reference through all the panels) to avoid important aberrations in the reflected field phase, which could lead to a radiation pattern degradation. Additionally, it is possible that during the assembly of the different modules, small misalignment occurs, which leads to phase mismatches. However, in passive multi-faceted devices this has shown a reduced impact [3], and in this case it could even be corrected through the voltage synthesis of the panels. This is, in fact, one of the main advantages of reconfigurable surfaces, since phase errors can be corrected *a posteriori*.

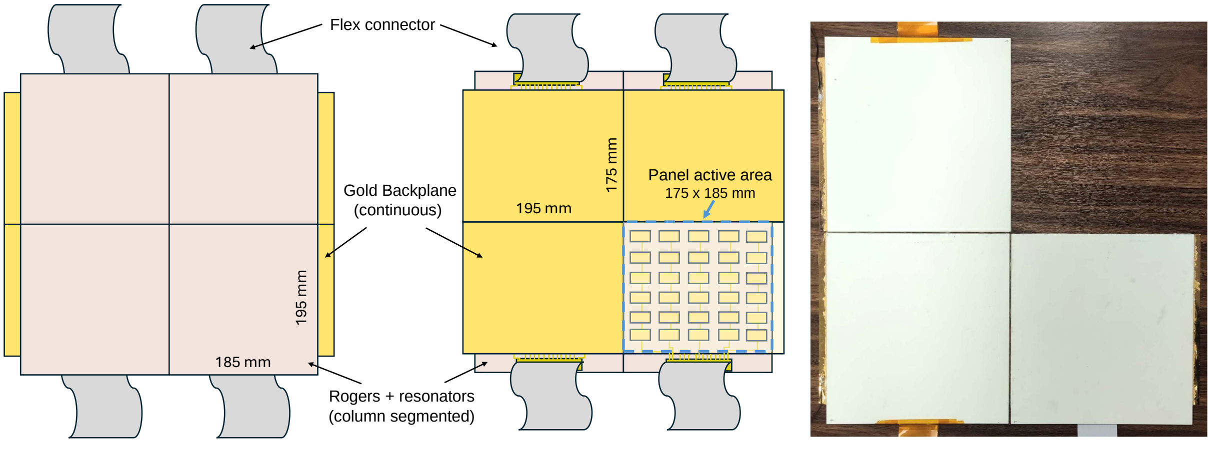

a) b)

Figure 5.2: a) Modular example (2×2) of the RIS device after mounting various panels together, obtaining a larger effective area for the RIS. Top and bottom views are shown. b) Picture of all the manufactured LC RIS panels, from which only one operates as expected.

5.2 Superstrate Panel measurement

The designed superstrate panel, including only the dielectric and the metallic resonators, is measured on its own first. Because of the presence of resonances in the band of interest, its measurement is helpful for verification purposes. A transmission setup measurement is compared to a transmission scenario simulation in an infinite periodic environment. To do so, a two-port calibration procedure is performed on a VNA equipped with two horn antennas, which allows to simultaneously acquire both reflection and transmission measurements, as explained in Chapter 2. The calibration consists on a short (metallic ground plane), through (no sample in between the horn antennas) and line ($\lambda_0/4$ relative displacement of the antennas). Then, the panel is placed between both horn antennas, whose relative distance is such as to correctly illuminate the sample.

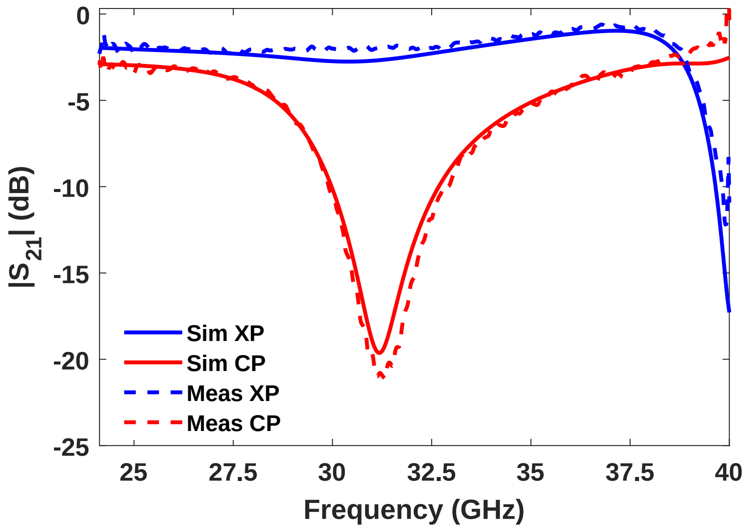

Figure 5.3: Measured (meas) and Simulated (sim) S_{21} transmission coefficient of the top substrate layer of the RIS.

The measured and simulated results can be observed in Figure 5.3, where both the $|S_{21}|$ co-polar and cross-polar components are shown, with great accordance. Finally, the union of a 2×2 superstrates have been mounted together and measured in the same setup, readjusting the antennas illumination into the sample, obtaining practically the same measurement results. This is because the infinite and periodical surface approach holds. Moreover, the unit cells at the edges of the panels have been positioned such that the union of the panels does not break such periodicity, keeping a consistent cell period even at the junctions of the panels.

5.3 Unit cell measurement

In order to obtain system quality metrics from a modulated signal, a single panel has been manufactured and measured, instead of the entire RIS. This is because of the manufacturing issues appearing when trying to assemble a large panel that operates at low frequencies

(27 GHz). These made that, from three manufactured panels, shown in Figure 5.2(b), only one resulted with the target thickness and with enough homogeneity through the cavity, which leads to different responses. These issues are related to the following points: (i) The cavity thickness is much larger than in optics or W-band devices. Apart from the longer time response, which could be tackled with the strategies reported in Chapter 4, achieving an homogeneous SU8 spacer layer along such a thick and large surface is problematic. By following a similar procedure as that detailed in Chapter 2, the thickness tolerances increase, and the homogeneity is not guaranteed; (ii) Large surfaces are more prone to deformation and bowing. When a constant micro-scale cavity thickness must be kept throughout the entire panel, these deformations can be of a significant impact, and periodicity can be broken. Since the superstrate material is not as hard as other materials previously used, such as quartz or glass, the surface can result bent after the assembly; (iii) The filling process is less intuitive, given the opaque nature of the superstate. While filling transparent surfaces enables the easy detection of air bubbles in the cavity, doing so in surfaces with microwave superstrates such as Rogers is not possible; (iv) Depositing materials in such large surfaces, both in spin-coating or sputtering processes, leads to large inhomogeneities. Because of all these points, a manufacturing procedure which is adapted to the new requirements that these structures demand, is required.

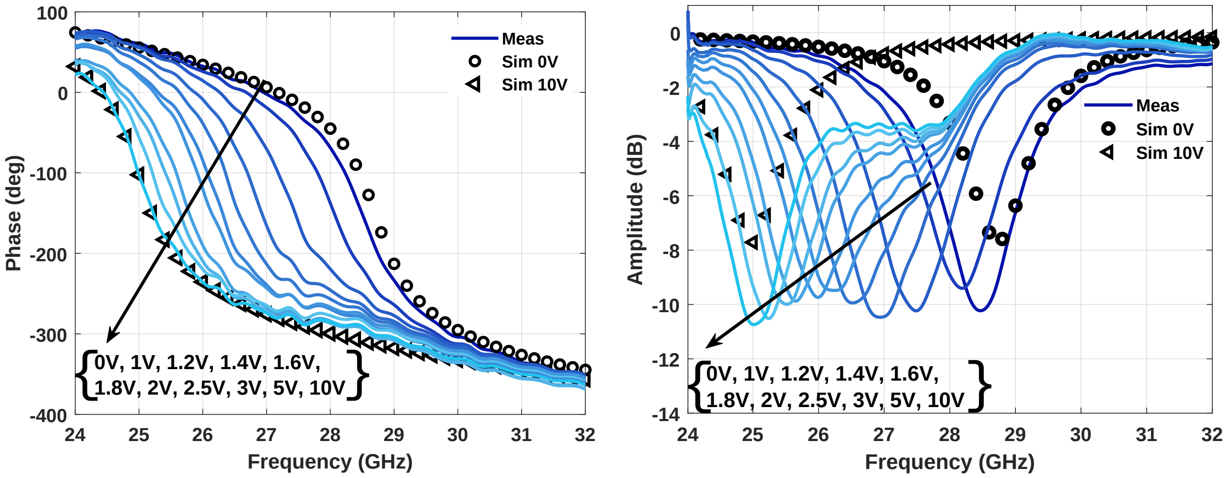

(a) **(b)**

Figure 5.4: Measured (Meas) and Simulated (Sim) reflection coefficient phase (a) and amplitude (b) of the RIS unit cell at $\phi_{inc} = 0°, \theta_{inc} = 15°$.

The single manufactured panel has been measured in a reflection setup in order to validate the unit cell behaviour. The measurement setup is similar to the one implemented in the previous chapters to obtain macroscopic unit cell measurements, with two horn antennas connected to a VNA, which acquires the S_{21} data, corresponding in this case to the S_{YY} unit cell parameter. The distance from the horn antennas to the surface is 35cm, for a proper illumination taper. Figure 5.4 shows the measured amplitude and phase of the reflection coefficient for different biasing voltages. The small mismatches between simulation and measurements are attributed to the unknown dispersive nature of the LC at this frequency range, as well as to the manufacturing difficulties previously described, mainly to the cavity thickness.

5.4 System-level measurements

Considering the real purpose of a RIS, system-level measurements have been carried out for this device. This will allow the assessment in performance and effectiveness of the prototype in real-world wireless communication deployments. The setup includes a transmitting (TX) antenna, which sends a modulated (4-QAM) 5G signal containing, among other data, the 5G Synchronization Signal Block information. This block includes the Physical Broadcast Channel (PBCH), which is used by base stations to broadcast (downlink) their parameters so that user equipments can initiate a communication [144]. The TX antenna is pointing towards the RIS, which can redirect the radiation to the receiving (RX) antenna. The RX antenna, in return, is connected to a spectrum and signal analyzer (Field Master Pro MS2090A) capable of demodulating the signal.

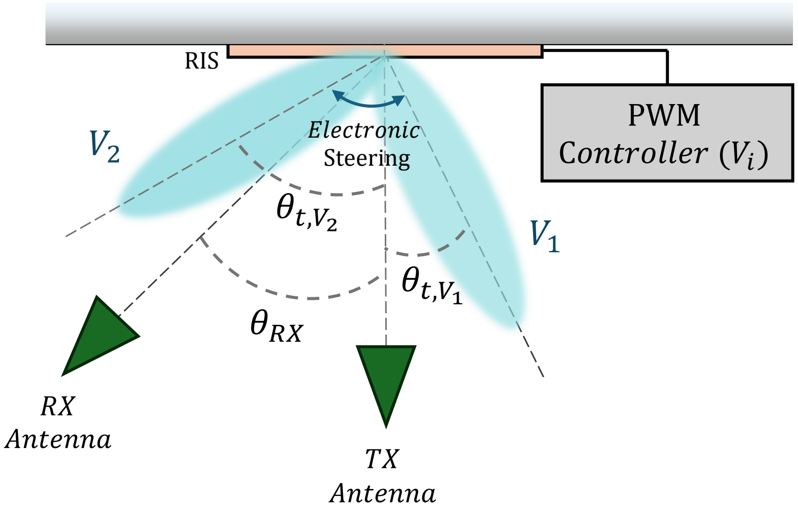

Figure 5.5: Schematic of the system-level measurements. The PWM Controller configures the direction of the desired beam configuration (θ_t) by using different column voltages V_i. For maximum signal reception, V_i can be chosen so that $\theta_t = \theta_{RX}$. Therefore, in a dynamic environment where θ_{RX} changes, the RIS can keep providing coverage over time.

The system has been evaluated in two different situations: a laboratory environment and a corridor environment. In each environment, the RX antenna is placed at different positions to evaluate the RIS steering performance (two for the laboratory case and four for the corridor case, resulting in 6 different measurement scenarios). In each scenario, the RIS is electronically reconfigured through a set of column voltages V_i to generate a pencil beam towards the corresponding direction, and the RX antenna is placed accordingly, emulating a user equipment. This can be observed in Figure 5.5. For each scenario, the performance is analyzed under two device conditions: when the RIS is radiating towards the RX antenna, and when it is replaced by a metallic plate (GND) of the same size. This allows measuring the real impact and benefit of the device.

Scenario	RX location	Electronic Beam Direction	Environment
A	$\theta_{RX} = 35°, \phi_{RX} = 180°$	$\theta_t = 35°, \phi_t = 180°$	Lab
B	$\theta_{RX} = 45°, \phi_{RX} = 0°$	$\theta_t = 45°, \phi_t = 0°$	Lab

Table 5.1: Description of the measurement scenarios and beam configurations at the lab environment. The coordinate system is centered at the array surface.

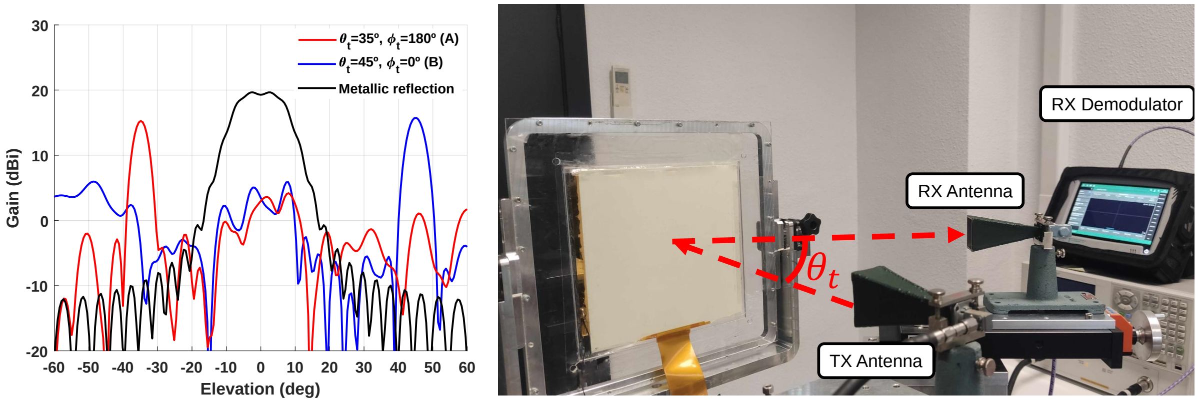

a) b)

Figure 5.6: a) Simulated radiation patterns of the RIS panel in the lab environment. Each beam is obtained by electronically reconfiguring the RIS towards the different directions of scenarios A and B. b) Picture of the RIS setup in the lab environment ($\theta_{inc} = 0°$). The RX antenna is connected to a commercial demodulator.

5.4.1 Lab environment

Figure 5.6 shows the measurement setup in the first evaluated environment, an indoor laboratory, where a close-range distance is chosen. This test focuses on the system integration and evaluating how the RIS operates alongside the transmitter and receiver, to verify the compatibility and performance of the entire mm-wave 5G wireless communication system under realistic deployment conditions. The TX antenna is illuminating the surface at 35cm with normal incidence ($\theta_{inc} = 0°$), and the RX antenna is also positioned at close-range, as can be seen in Figure 5.6. The behaviour of the RIS has been measured in two beam configurations (A and B, as outlined in Table 5.1, whose simulated radiation patterns can be seen in Figure 5.6(a)), and thus there are two RX antenna positions to consider. The setup of Figure 5.6(b) allows mounting the RX antenna in a radial structure, which can produce a rotation movement centered at the RIS, thus facilitating the measurement at the different scenarios.

The system-level results are shown in Figure 5.7, where both the RIS and the GND cases are detailed for the scenarios A and B. Different metrics have been measured under different transmitted power conditions, obtained from the PBCH channel. As can be seen in Figure 5.7(a), where the average Reference Signal Received Power (RSRP) metric is shown, the signal improvement when using the RIS is substantial. As expected, the RSRP grows proportionally to the transmitted power for both scenarios and device conditions, which serves as a first check for the entire system and device setup. Moreover, the metric is consistently improved by using

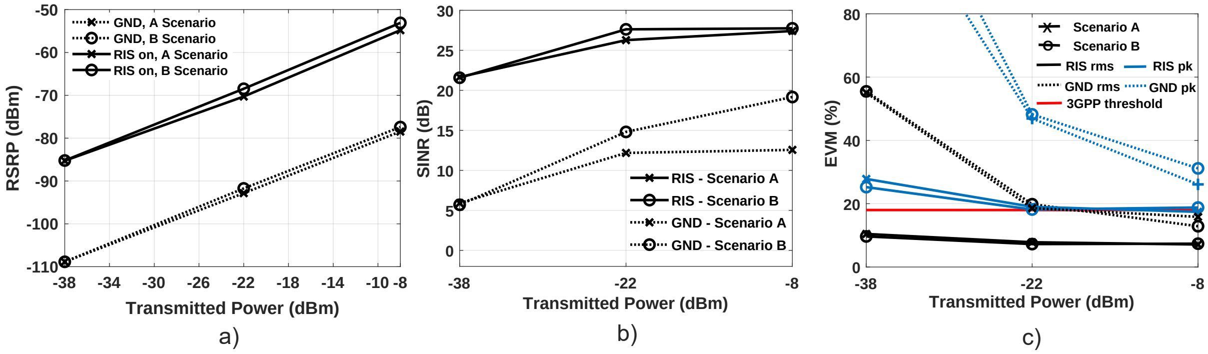

Figure 5.7: System-level measurements of the laboratory environment setup. a) RSRP vs. transmitted power. b) SINR vs. transmitted power. c) RMS EVM and peak EVM vs. transmitted power.

the RIS. When the transmitted power is not too large, the signal-to-noise-plus-interference ratio (SINR) is enhanced by more than 15dB (Figure 5.7(b)) and the RMS error vector magnitude (EVM) of the received symbols is reduced by 50 points in percentage (Figure 5.7(c)), as compared to using the GND. In the Figure, the 3GPP threshold (18%) is also shown (in red), which as can be seen is only guaranteed with the RIS. These metrics are measured following the standard definitions of 3GPP. When the power is high, the effect of a RIS is diminished as the multi-paths take more relevance and the receiver can demodulate the 5G signal, but its presence still improves the signal metrics significantly. This is because of the signal diversity effects taking place, which allows the receiver to demodulate correctly through the standard implemented error-correcting techniques.

In general, independently from the power, the RIS scheme always outperforms the GND deployment, which indicates the superiority of the device, which is capable of focusing the radiation in different directions while the GND can only reflect towards the specular direction. As can be observed in Figure 5.6(a), the expected gain difference between the RIS beam and the reflection from a metallic plate is between 15-20dB in the different RX positions. This is consistent with the RSRP and SINR measurements. It is worth noting that, due to the lossy behaviour of the device, there are significant gain level differences between the metallic reflection and the RIS beams. However, the key advantage of the RIS is its capability to beam-steer to directions where a passive device would never steer, providing a better dynamic coverage overall.

5.4.2 Corridor environment

As a second scenario, shown in Figure 5.8, the RIS is attached to a corridor wall, and the TX antenna illuminates it with normal incidence ($\theta_{inc} = 0°$) at a distance of 200cm. This setup generates large spillover, representing more realistic RIS illumination conditions than in the previous setup. The simulated radiation patterns under the different scenarios considered for the corridor environment are shown in Figure 5.8(a), and a picture of the setup can be seen in Figure 5.8(b). In this case, tripods and alignment laser tools are used to measure the respective rotations of the different scenarios.

Scenario	RX location	Electronic Beam Direction	Environment
C	$\theta_{RX} = 30°, \phi_{RX} = 0°$	$\theta_t = 30°, \phi_t = 0°$ $\theta_t = 30°, \phi_t = 180°$ (ot)	Corridor
D	$\theta_{RX} = 40°, \phi_{RX} = 0°$	$\theta_t = 40°, \phi_t = 0°$ $\theta_t = 40°, \phi_t = 180°$ (ot)	Corridor
E	$\theta_{RX} = 30°, \phi_{RX} = 180°$	$\theta_t = 30°, \phi_t = 180°$ $\theta_t = 30°, \phi_t = 0°$ (ot)	Corridor
F	$\theta_{RX} = 40°, \phi_{RX} = 180°$	$\theta_t = 40°, \phi_t = 180°$ $\theta_t = 40°, \phi_t = 0°$ (ot)	Corridor

Table 5.2: Description of the measurement scenarios and electronic beam configurations at the corridor environment. (ot) denotes off target.

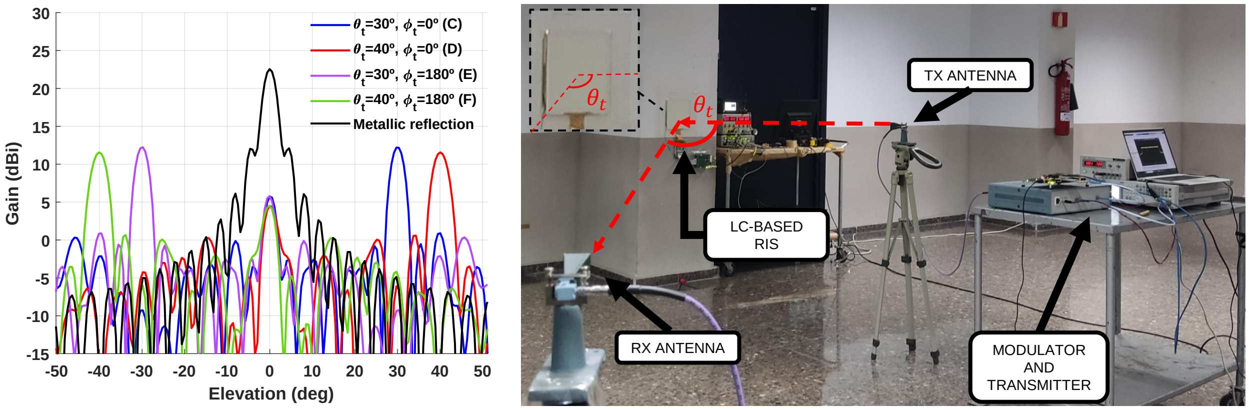

a) b)

Figure 5.8: a) Simulated radiation patterns of the RIS panel in the corridor environment. Each beam is obtained by electronically reconfiguring the RIS towards the different directions of scenarios C-F. b) Picture of the RIS setup in the corridor. The TX antenna is placed such that $\theta_{inc} = 0°$, at a distance of 200cm of the RIS, and is connected to the modulator.

As can be seen in Table 5.2, four different scenarios (C-F) are measured in this corridor environment. In this case, the transmitted power is fixed to -8 dBm to ensure a consistent baseline for performance comparison across all deployment configurations. Moreover, apart from the active RIS and GND device conditions, two additional device conditions are measured for each scenario. The first one consists of using the RIS to radiate off target, that is, towards a certain direction away from the RX antenna. The off target direction corresponds with the opposed azimuth angle ($\phi_t = 0° \leftrightarrow \phi_t = 180°$) of the corresponding scenario, as outlined in Table 5.2. Therefore, in these conditions, the position of the RX antenna does not match the direction of the RIS pencil beam. The second additional device condition is given by using the RIS unpowered (all unit cells with zero voltage applied), which should provide a similar behaviour as the metallic plate.

The measured results are detailed in Figure 5.9, where both the SINR and the EVM are shown for the scenarios C-F. When the device is not operating, the SNR values range from 6.16dB to

12.09dB, representing low SNR values. In this sense, the low values in all scenarios, specifically in Scenario E, emphasize the negative effects of fading, interference, and attenuation on mm-wave signal quality. As expected, the SINR improves by 10-15dB in all scenarios when the RIS is targeting the RX antenna (Figure 5.9(a)), which delivers consistently superior results, with SINR values between 21.91dB and 23.60dB. The measured EVM is drastically reduced when the RIS is operating (Figure 5.9(b)), and is the only device condition capable of achieving EVM values below the 3GPP threshold of 18%. It is also interesting to note that, in some scenarios, when the RIS is radiating off target, the EVM can be improved with respect to the GND or unpowered RIS conditions. This effect is attributed to the setup environment, which can lead to diverse multi-path conditions.

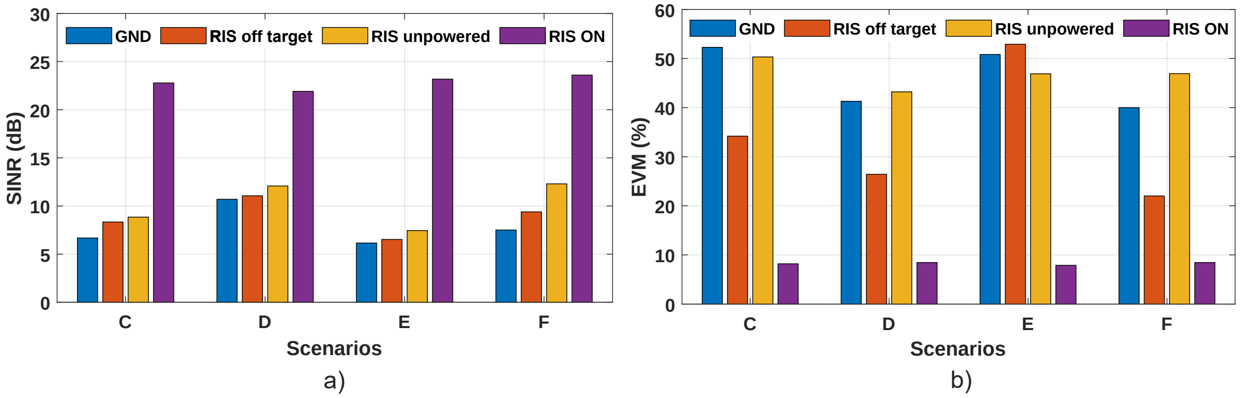

Figure 5.9: a) Measured SINR in the different corridor scenarios for -8 dBm transmitted power. b) Measured EVM in the different corridor scenarios for -8 dBm transmitted power.

Sc.	GND			RIS unpowered			RIS off target			RIS on		
	PSS	SSS	PBCH	PSS	SSS	PBCH	PSS	SSS	PBCH	PSS	SSS	PBCH
C	46.3	46.3	52.3	33.4	35.9	34.2	36.7	38.3	50.3	6.9	7.6	8.2
D	37.6	37.4	41.3	29.8	28.4	26.4	38.1	42.1	43.2	7.7	8.03	8.5
E	45.6	45.1	50.8	46.9	47.2	52.9	47.6	47.5	46.9	6.1	7.19	7.9
F	37.5	38.5	40.0	24.2	23.3	22.0	47.2	47.3	46.9	7.7	8.03	8.4

Table 5.3: Measured RMS EVM (%) of different synchronization signals (PSS and SSS) and PBCH in the corridor environment.

Additionally, it is worth noting that, although intuitively a higher SINR will lead to better EVM results, their relation is in fact much more intricate and this correlation does not always hold, as the EVM metric considers the implemented system-level error correction techniques, which takes into account phase errors and other channel aberrations, while the SINR is a pure power metric. Moreover, such high EVM values, way above the 3GPP threshold, result from detecting very weak signals providing less accurate measurements.

Further measurement data captured not only from the PBCH channel, but also from the Primary Synchronization Signal (PSS) and the Secondary Synchronization Signal (SSS) from the 5G Synchronization Signal Block [144], are detailed in Table 5.3.

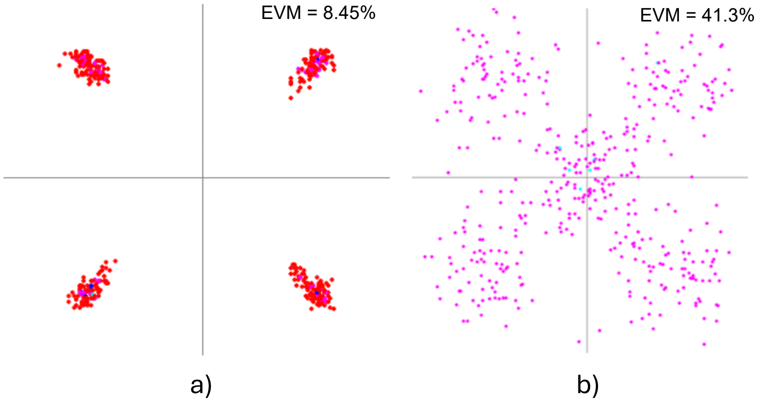

Figure 5.10: Demodulated constellation diagram for the scenario D (PBCH channel). a) With the RIS reconfigured targeting the RX antenna. b) With a metallic plate.

Figure 5.10 shows a screenshot of the demodulator both when using the RIS towards the correct direction (scenario D), and after replacing it with the GND. It is obvious that the RIS improves the demodulation quality, given that the GND is only reflecting the impinging waves towards the specular (normal) direction, while the RIS can effectively reflect the radiation towards the RX antenna in each scenario.

It is worth noting that the measurement results for both deployments across the two scenarios exhibit remarkably similar trends. This consistency suggests that the performance of the deployed systems remains stable under the given experimental conditions, highlighting the robustness and reliability of the setup in these controlled environments.

Even though a single panel has been manufactured, its functionality as electronically switchable RIS is as expected. Therefore, the behaviour of a larger RIS made of several of these panels can be predicted by considering the specific impinging field on the new structure and the designed reflection coefficients. For instance, for the 2 × 2 modular configuration of Figure 5.2, a gain improvement of around 6dB would be attained.

Chapter 6

Discussion

In the previous chapters, different aspects of SFPS based on LC have been examined, improved and implemented. In this Chapter, the results obtained in those are linked and discussed, and the completion of the objectives outlined in Section 1.5 is analyzed.

A precise manufacturing of SFPS devices is crucial for extracting reliable conclusions that allow elaborating on more complex designs and models, which in turn can enable further developments. As such, following a manufacturing protocol like the one described in Chapter 2 is needed. This process is rarely described in detail and depends on the specific device features, such as size, thickness, materials, and so on, making necessary an optimization of each fabrication process. However, typically few information, such as only the device thickness, is provided when a device is presented. Here, all the followed steps, resulting of those optimizations, are thoroughly described, and serve as a basis for all the devices manufactured in the thesis. Therefore, the objective 1.5.1 was tackled.

The reflectarray introduced in Chapter 3 is the first LC antenna capable of independently controlling dual polarization while having a low complexity, both in terms of manufacturing and analysis and design process. This served to tackle the objective 1.5.5. As compared to other works targeting polarization control with LC, even though the manufactured antenna is electrically larger [50, 48, 73], it has a reduced cost and is overall simpler thanks to its single-layer structure. The manufacturing is elaborated with the learnings of Chapter 2. The device allows for an independent scanning of each polarization while keeping low cross-polarization levels, due to a careful unit cell design, while achieving a SLL of at least 9dB in the entire scanning range and both polarizations.

Note that for a fixed illumination, the achieved gain and the measured SLL level are the result of the phase errors produced on the antenna surface, which can be the result of the manufacturing tolerances, phase quantization, the accuracy of the electromagnetic modeling used to design the structure and the design process itself. Therefore, even when the phase-range of the cell does not cover 360º, the obtained results for this antenna highlight that both the modeling and the followed design process are suitable to develop these type of antennas with great accuracy and with predictable results. The introduced efficient model allowed predicting the measured beam configurations with excellent concordance with simulations,

Technique	**Advantages**	**Disadvantages**
OD	• Preserves tunability • Great improvement in excitation transitions	• High voltage required • Small improvement in decay transitions
PNLC	• Great improvement in decay transitions	• High voltage required • Tunability reduction • Considerable losses
DFLC	• Great improvement in decay transitions • Preserves tunability • Can be jointly used with overdrive	• Very lossy mixtures available • Slightly increased circuitry complexity

Table 6.1: Comparison of advantages and disadvantages of different LC acceleration techniques for mm-wave devices.

facing objective 1.5.4, while the optimized phase synthesis further improved the radiation patterns.

Later on in the thesis, the slow dynamics of LC devices have been tackled by several ways, in order to face objective 1.5.2. The different advantages and disadvantages of the acceleration techniques studied in Chapter 4 are summarized in Table 6.1. Note that the development of these techniques required the manufacturing and measurement of several SFPS in different conditions, as well as the following of mixture characterization procedures, for which the contents of Chapter 2, and to a lesser extent of Chapter 3, were indispensable.

Given that the knowledge of the LC transition in RF terms was inexistent, a dynamic model capable of capturing the molecule rotation and predict the transient phase response had to be developed, which in turn helped contribute to objective 1.5.4. Although it was known that overdrive and underdrive techniques could be used in optics, their usage in mm-wave devices was not tested, and required of such model to not rely on experimental measurements only. However, those measurements can help to refine the model if required. This allowed for the first time a significant acceleration towards intermediate states, while keeping the natural LC tunability, although the decaying was still limiting the devices speed.

The PNLC technique was then tested to tackle this transition. Note that the manufacturing steps of PNLC, once the specific combination of RM mixture is known, is exactly the same as in regular LC devices and that obtaining such mixture does not add any complexity to the process. Although there were some early works targeting polymeric mixtures for RF phase shifters based on transmission lines [104, 105], it was shown for the first time a significant reduction of the decay times in SFPS. The introduced effective anisotropic model, as opposed to the isotropic ones, allowed certain generalization of the mixture properties to a reflectarray cell with enough phase range. This comes, however, at a high-voltage, lossy and low-tunability cost.

Finally, objective 1.5.2 could be fulfilled by using DFLC, which were only tested previously, and without any mixture knowledge at RF bands. The identification of DFLC materials potentially usable at mm-wave frequencies allowed designing a fast reflecting surface, exhibiting the smallest reconfiguration times in the literature but high loss.

Table 6.2 shows a comparison of the different results obtained through this thesis in LC acceleration, considering as T_{ON}/T_{OFF} the fastest rise/decay molecule time, and a $h_{LC} = 45\mu m$. As can be seen, the acceleration in the decay transitions is achieved through PNLC and DFLC, although the major improvement comes with using DFLC in combination of overdrive. This is the technique that allows reducing the most the decay time while maintaining a large phase range at a reduced driving voltage.

Technique	T_{ON}	T_{OFF}	**Phase Range**	**V required**
Conventional LC	$5s$	$10s$	360º	20V
LC + OD	$50ms$	$5s$	360º	45V
LC + PN + OD	$10ms$	$200ms$	180º	150V
DFLC	$5s$	$2s$	360º	20V
DFLC + OD	$20ms$	$10ms$	360º	45V

Table 6.2: Quantitative comparison of different SFPS LC acceleration techniques.

The RIS introduced in Chapter 5, which is electronically reconfigurable by means of LC, represents another contribution to the objective 1.5.5. The device has been tested indoors and can dynamically improve the coverage under different conditions and beam configurations. However, the associated difficulties in terms of manufacturing at frequencies below 60 GHz (where the required cavity thickness to avoid critically coupled resonances is usually above $100\mu m$) are more limiting than in optics or sub-THz. Specifically, the main issue is related to these large thicknesses required, which are difficult to attain consistently and in an homogeneous way for large panels, especially when microwave substrates are involved. This generates considerable phase errors in the aperture, and potential undesired antiresonances. Increasing the thickness also requires more LC material, which is not only detrimental because of the response time (thicker cavities slow down the devices if no acceleration technique is applied), but also because of the LC cost. In fact, the cost of the raw LC operating at mm-wave frequencies is, because of the lack of mass-production, still orders of magnitude larger than the widespread LC mixtures used in optics. Another setback is given by the dispersive nature of the LC, which is not properly characterized for many mixtures and it is usually characterized only in narrow bandwidths very close to the central frequency under study. Therefore, although the manufacturing was tackled in objective 1.5.1, with the developed procedures aiming at W-band, Chapter 5 gave rise to further challenges related to that objective, which will be specified as future research lines.

Regarding objective 1.5.3, a unit cell with reduced losses could not be attained. In SFPS based on LC, the introduction of losses is related to both the material complex permittivity and the dielectric anisotropy, as well as the cavity thickness. For a resonant structure to exhibit a reflection coefficient close to 1, the cavity thickness cannot be too thin in terms of λ. However, a resonance with low Q-factor is directly related with a smooth phase variation. If LC mixtures with high dielectric anisotropy (well above the current values of 0.8 - 1.2) were available, this smooth phase variation would be enough to provide a significant phase range (of around 300º with a single resonance) to scan and focus a beam. However, the limited available dielectric anisotropy forces designs with abrupt phase variations, that is, high Q-factor, thus introducing losses. Moreover, even if a high-anisotropy mixture was available, the required cavity thickness for obtaining a smooth resonance would be at least of $\lambda/30$, which is undesirably large at frequencies below 60 GHz for properly driving the LC in a reasonable time and voltage. Therefore, this might be easier to attain in higher frequencies, given that the thickness scales with the wavelength. Thus, the lossy behaviour results from a trade-off considering not only the material $tan\delta$, but also its $\Delta\varepsilon$ and structure, and manufacturing and control difficulties. A possible solution would be to limit the operation to 1-bit, sacrificing gain and SLL. By choosing a central frequency of operation in-between the resonant frequencies for the extreme biasings, and provided that enough dielectric anisotropy is available, a high Q-factor resonance could be used with practical reflection coefficients close to the unit. Alternatively, new unit cell topologies, including complex structures or dielectric resonators, could be investigated. For all of the above, the reduction of losses is left as a future line of research.

Chapter 7

Conclusions and future research lines

7.1 Conclusions

This Ph.D. thesis focuses on developing the capabilities of mm-wave reconfigurable surfaces based on Liquid Crystals (LC). These devices are capable of manipulating the radiation of electromagnetic waves by means of an electronic bias of the material, which provides varying volumetric permittivities caused by a molecular rotation. Then, to design the electric field reflection coefficients throughout the surface, each unit cell composing the array is biased with the corresponding voltage. This allows shaping the phase of the reflected field at the surface, from which the radiation pattern will ultimately depend. There exist several working prototypes of such technology, but important challenges must yet be faced, which requires further research.

The study of these structures in this thesis has been mainly centered in (i) adding novel functionalities, (ii) reducing their temporal response to varying biasing excitations, and (iii) the design of electrically large structures. Moreover, to do so, several LC mixtures have been electromagnetically characterized. The results are validated through measurements, which are obtained from in-house manufactured devices. Therefore, the work presented in this document has a fundamental experimental component. The manufacturing has been carried out by the author in the clean room facilities of the CEMDATIC I+D Center at UPM, and both the manufacturing and measurement procedures have been detailed.

The first main contribution presented consists of designing a multi-functional unit cell, specifically an independently biased dual-polarization cell. The operating principle of this multi-functionality relies on separate biasing conditions for the LC beneath the different resonant elements within a single cell. It has been observed that in order to enable a simultaneously fast and accurate characterization of the liquid crystal states upon biasing, a model which partitions the LC material in the unit cell is required to account for the transversal inhomogeneity, which must also consider the longitudinal inhomogeneity in each block. Moreover, after analyzing the effect of the bias lines, it was understood that they play an important role in a polarization-sensitive device, which can easily modify the entire response. Therefore, a dedicated impact study of the biasing lines is required, which will lead to a certain geometrical layout that minimizes polarization conversion. The manufactured surface, containing 55 × 55 unit cells featuring an independent resonance per polarization, together with the macroscopically measured cell behaviour under periodic conditions, confirmed the modeling accuracy. These measurements validated the unit cell modeling strategy, showing precise results while gaining in compute efficiency. Therefore, this allowed designing a complete electronically reconfigurable reflectarray antenna, which is the first of its kind to show independent beam-steering for orthogonal linear polarizations at W-band. The antenna, measured at an anechoic chamber with excellent agreement to simulations, is capable of scanning from 5º to 40º in one plane, showing 25dBi gain with a minimum SLL of 9dB, for each polarization. This opens the door to the design and manufacture of other multi-functional unit cells based on this technology.

The second main contribution is related to accelerating the switching response of LC-based mm-wave surfaces. Given their thick cavities, and that the decay molecule transitions cannot be actively controlled by the external excitation, the natural response time is in the order of tenths of seconds, which is excessive for many applications. To tackle this, and considering the substantial errors made by other temporal approximations, the lack of a dynamic model is identified, which has been first introduced and experimentally validated at the cell level. The model allowed not only to obtain the evolution of the reflection coefficient phase upon varying states, but also to model it with realistic biasing waveforms and to predict transient far-field radiation patterns. It is therefore concluded that, in order to obtain a precise knowledge of the cell-level (reflection coefficient) and antenna-level (radiation pattern) metrics, an anisotropic tensorial model which includes the temporal dependence of the LC is required. It has been observed how, similarly to the static case, in this dynamic model a multi-layer description (for each voltage and time) can be simplified by means of an effective homogeneous (single layer) tensorial model that encompasses the longitudinal inhomogeneity, which results in small phase errors.

Then, three methods have been evaluated: overdrive and underdrive, polymer network liquid crystals (PNLC) and dual-frequency liquid crystals (DFLC). Overdrive and underdrive demand engineering the biasing waveforms of the unit cells, which requires using the dynamic model to predict the material behaviour during the transient states. For the former, it has been seen how depending on the initial and final states, providing high-voltage signals during few microseconds accelerates the transitions up to 250X and an average of 100X in the evaluated scenarios, which are experimentally measured. For the latter, the improvements of dropping the voltage to zero are reduced, up to 2X, which occurs for the limiting case of a decay transition. Therefore, this is a partial solution only.

PNLC are polymer-stabilized mixtures, that can be manufactured such that LC molecules are so strongly attached at the repose state that their decay response is dramatically reduced. An effective anisotropic model for such mixtures has been developed and validated through measurements, which allowed designing and manufacturing a working reflectarray surface. As a main takeaway, it has been observed how the model, although assuming uniaxiality in the mixture as in conventional LC, generalizes well to varying geometries and angles of incidence. The results show that, by using PNLC as dielectric substrate, the tunability is reduced by 3X, which limits the phase range and the instantaneous bandwidth of the device.

The achieved decay times are around 200ms, improving by far the state-of-the-art, although requiring high operating voltages. Thus, even though the acceleration is remarkable, in this case the drawbacks outweigh the improvements.

The usage of DFLC materials is examined as a final approach to reduce the temporal response. These materials are sensible to the frequency of the biasing waveforms, showing a sign inversion to their dielectric anisotropy, which allows to actively rotate the molecules for both rise and decay transitions through the voltage excitations. First, several commercially available mixtures are identified to obtain their permittivity tensor values, which enabled predicting the tunability and performing a reflecting surface design. The manufactured device, although showing large losses, can achieve reduced times in all kinds of transitions. If used in conjunction with overdrive, the response between extreme states is of only 10ms. Therefore, it is concluded that the combination of DFLC and an overdriving technique is the best approach, although a low-loss mixture is yet to be commercially available. Using overdrive alone is possible if certain beam switch combinations are prioritized. In such transitions, at the most representative unit cells located at the center of the array, a voltage increase should be enforced.

The third main contribution is the design of a LC-based electrically large reconfigurable intelligent surface (RIS). The concept of RIS slightly differs from that of an antenna since the purpose is to improve the coverage of a certain zone, for which the surface is typically illuminated from a far-away feed, with large spillover. A modular design composed of 27 GHz LC RIS panels, of 38×36 unit cells each, is proposed, and a single panel is manufactured and measured. By evaluating such device in different scenarios, both near-field and far-field, two main takeaways have been collected. First, the measured system-level metrics undoubtedly show how using an electronically reconfigurable RIS based on LC can result in important coverage improvements, in terms of SINR and symbol EVM. It is observed through these field work experiments that RIS devices can improve the quality of a received 5G signal, especially for changing conditions in which a dynamic beam configuration is needed, and when the system operates under realistic low power conditions. The measurement campaign included the use of commercially available and 3GPP compliant transceiver equipment, which validates the previous statements. Second, it is concluded that the manufacturing of electrically large devices that operate at such frequencies entails new challenges, and demands for new fabrication protocols adapted to the sizes of these devices. With the manufacturing processes described for W-band LC planar devices, difficulties such as the resulting cavity inhomogeneity hinder the fabrication repeatability.

In close, this thesis sheds light to the different processes related to the design, manufacture and measure of LC-based SFPS with enhanced capabilities, as well as the methodology for mixture characterization and modeling.

7.2 Future Research Lines

There are still important drawbacks in which this technology must be improved. The most limiting one is perhaps the lossy behaviour of the mixtures. Although there have been efforts on the side of LC developers to obtain a LC material with low $tan\delta$ values, they are still an order of magnitude above the dielectric materials commonly found in microwave devices. This, together with the resonant behaviour of SFPS, and the tight trade-off happening because of the limited material tunability at mm-wave, has a relevant impact. It is possible to design structures that avoid these losses as much as possible, and to alleviate its effects by a proper device control. However, it still represents the major problem to overcome, and if there is no further development on high anisotropy or low-loss mixtures, novel research in unit cell topologies (e.g. based on dielectric resonators) will be required.

A second important future research line is related to the 2D addressing scheme. A truly scalable solution for a LC surface capable of beam-steer and focus in two planes is needed, since current direct addressing implementations are too complex to bias electrically large devices. The most straightforward solution consists on implementing an active matrix scheme, similar to those in large LCD panels. However, the unit cell modifications that this addressing entails will require en exhaustive analysis at the RF level, once again demanding innovative cell structures. In turn, the LC modeling in those structures might be challenging, for which new efficient models might be needed.

Related to the previous point, more advanced unit cells are required to tackle complex functionalities. For instance, the concept of multi-functional unit cell introduced here could be expanded to design dual-band or multi-band cells. Other polarization manipulation, such as conversion or circular polarization beam-steering antennas, are other possible examples.

When developing complex unit cells, the placing of the biasing lines often limits the designer freedom, and sacrifices must be made in terms of performance, such as increased period size, or by adding unnecessary complexity to the structure. In order to avoid such issues, novel materials must be introduced that allow biasing unit cells without any RF impact whatsoever. At the same time, modeling the LC would be easier because greater homogeneity molecule rotation could be achieved. These materials must be conductive for AC frequencies but transparent at RF.

There is also a lack of solutions in the manufacturing of low-frequency devices (e.g. K-band) which employ LC. The related processes must be improved to provide repeatability, especially at the LC cavity thickness, which must ensure homogeneity through large panels. When using materials optimized for microwave frequencies, an analysis on their suitability for LC structures might be needed, considering their mechanical properties.

Current characterization methods for LC materials rarely consider their dispersion. Therefore, when certain permittivity parameters are used in full-wave simulators, which might have been obtained either through an extraction process or provided by the manufacturer, the wideband results might be inaccurate. The used permittivity tensor values are typically valid for a specific frequency of reference only, and the dispersion models used in commercial software simulators only ensure convergence at other frequencies. Thus, a dispersion analysis for different mixtures must be performed, to test whether the current models are accurate enough. Together with them, a thermal analysis of the LC behaviour to assess the phase changes under different conditions, including the LC dynamics, would also provide relevant information for a real deployment.

Finally, there has been recent interest for optically transparent SFPS that could be seamlessly integrated in building windows while improving signal coverage or enabling certain wireless communications. Additional potential applications for such devices include their installation on top of commercial advertisement displays or on top of solar cells. However, current prototypes show limited performance, and the LC bias characterization in those structures is challenging.

7.3 Publications and research stays related to this thesis

7.3.1 Journal papers

- R. Guirado, G. Perez-Palomino, M. Ferreras, E. Carrasco and M. Caño-García, "Dynamic Modeling of Liquid Crystal-Based Metasurfaces and Its Application to Reducing Reconfigurability Times," in IEEE Transactions on Antennas and Propagation, vol. 70, no. 12, pp. 11847-11857, Dec. 2022.
- R. Guirado, G. Perez-Palomino, M. Caño-García, M. A. Geday and E. Carrasco, "mm-Wave Metasurface Unit Cells Achieving Millisecond Response Through Polymer Network Liquid Crystals," in IEEE Access, vol. 10, pp. 127928-127938, 2022.
- R. Guirado, P. de la Rosa, G. Perez-Palomino, M. Caño-García, E. Carrasco and X. Quintana, "Characterization and Application of Dual-Frequency Liquid-Crystal Mixtures in mm-Wave Reflectarray Cells to Improve Their Temporal Response," in IEEE Transactions on Antennas and Propagation, vol. 71, no. 8, pp. 6535-6545, Aug. 2023.
- R. Guirado, G. Perez-Palomino, P. de la Rosa, E. Carrasco and X. Quintana, "Electronically Reconfigurable Reflectarray Antenna Based on Single-Layer Liquid Crystal With Independent Dual-Polarization Control," in IEEE Transactions on Antennas and Propagation, vol. 72, no. 7, pp. 5626-5636, Jul. 2024.
- P. Aghabeyki, P. de la Rosa, M. Caño-García, X. Quintana, R. Guirado and S. Zhang, "Optically Transparent Beam-Steering Reflectarray Antennas Based on a Liquid Crystal for Millimeter-Wave Applications," in IEEE Transactions on Antennas and Propagation, vol. 72, no. 1, pp. 614-627, Jan. 2024.
- J.R. Montejo-Garai, J.E. Page, G. Perez-Palomino and R. Guirado, "Band-Stop Frequency-Selective Surface (FSS) with Elliptic Response Designed by the Extracted Pole Technique," in Sensors, 2024, 24, 4452.

7.3.2 International conferences

- S. García-Ruano, R. Guirado, G. Perez-Palomino, J.A. Encinar and E. Carrasco, "Dual Polarization Reflectarray Elements with Dynamic Reconfiguration Based on Liquid Crystal," 2022 16th European Conference on Antennas and Propagation (EuCAP), Madrid, Spain, 2022.
- R. Guirado, G. Perez-Palomino and E. Carrasco, "Impact of Addressing Techniques on Liquid Crystal-Based mm-Wave Reflectarrays," 2022 International Symposium on

Antennas and Propagation (ISAP), Sydney, Australia, 2022, pp. 383-384.

- R. Guirado, G. Perez-Palomino and E. Carrasco, "Dynamic Effects of Scaling and Biasing on Liquid Crystal-based Reflectarray Antennas," 2023 17th European Conference on Antennas and Propagation (EuCAP), Florence, Italy, 2023.
- P. de la Rosa, R. Guirado, G. Perez-Palomino, M. Caño-García and E. Carrasco, "Preliminary study of reconfigurable Orbital Angular Momentum beams with Liquid Crystal metasurface at mmWave," 9th International Conference on Antennas and Electromagnetic Systems (AES), Torremolinos, Spain, 2023.
- G. Gomez-Bravo, R. Guirado, R. Teschl, G. Perez-Palomino, E. Carrasco and W. Bösch, "Low-Cost Liquid Crystal Based Reflectarray Antenna for Indoor Wireless Localization Applications Operating in the Ka-Band," 2023 IEEE International Symposium on Antennas and Propagation and USNC-URSI Radio Science Meeting (USNC-URSI), Portland, OR, USA, 2023, pp. 1509-1510.
- P. De la Rosa, R. Guirado, G. Pérez-Palomino, E. Carrasco and M. Caño-García, "Reflective Surfaces Based on Semi-Passive Reconfigurable Polymer Network Liquid Crystal," 2024 18th European Conference on Antennas and Propagation (EuCAP), Glasgow, United Kingdom, 2024.
- E. Carrasco, R. Guirado, G. Pérez-Palomino, P. de la Rosa, M. A. Geday, "Liquid Crystal Technology for Implementing Smart Electromagnetic Skins in Next Generations of mm-Waves Wireless Systems," 10th International Conference on Antennas and Electromagnetic Systems (AES), Rome, Italy, 2024.
- G. Gomez-Bravo, R. Guirado, P. Hodl, R. Teschl, G. Perez-Palomino, K. Witrisal, T. Wilding, E. Carrasco, W. Bosch, "Utilization of Liquid Crystal Based Reflectarray Antennas for Multipath-Assisted Localization," 54th European Microwave Conference (EuMC), Paris, France, 2024.
- R. Guirado, G. Perez-Palomino and E. Carrasco, "Transient Far-Field Radiation of Reconfigurable Liquid Crystal Reflectarray Antennas," 2024 International Symposium on Antennas and Propagation (ISAP), Incheon, South Korea, 2024.

7.3.3 Spanish conferences

- R. Guirado, G. Perez-Palomino and E. Carrasco, "Improvement of Liquid Crystal Transition Times in Thick mm-Wave Devices," XXXVII Simposium Nacional de la URSI, Málaga, Spain, 2022.
- P. de la Rosa, R. Guirado, G. Perez-Palomino, E. Carrasco and M. Caño-García, "Superficies Reflectantes, Reconfigurables y Semi-Pasivas Basadas en Redes de Cristal Líquido Polimérico," XXXVIII Simposium Nacional de la URSI, Cáceres, Spain, 2023.
- R. Guirado, G. Pérez-Palomino, P. de la Rosa and E. Carrasco, "Design of a Liquid-Crystal Dual-Polarization Reflectarray Antenna," XXXIX Simposium Nacional de la URSI, Cuenca, Spain, 2024.

7.3.4 Research stays

A 6-month international research stay has been carried out as part of this thesis, as detailed below. The host research group has extensive experience in the characterization of liquid crystal mixtures and in the design of liquid crystal devices.

- **Host institution:** Huawei Munich Research Center
- **Department:** Optical & Quantum Communications Lab
- **Supervisor:** Grigory Lazarev
- **Location:** Munich, Germany
- **Period:** 15/01/2024 - 14/07/2024

7.4 Listing of manufactured samples and devices

The following list enumerates the produced samples in the clean room facilities in relation to this thesis, where the purpose of each fabrication is also detailed:

#	Amount	Purpose	Final device
1	6 × 3	SU8 thickness characterization on glass	No
2	5 × 3	SU8 thickness characterization on glass	No
3	5 × 3	SU8 thickness characterization on glass	No
4	5 × 3	SU8 thickness characterization on glass	No
5	4	SU8 thickness characterization on Rogers	No
6	4	Polyimide curing test on Rogers	No
7	12	Photolithography optimization	No
8	5	Sputtering thickness characterization	No
9	2	Fiber optic spacers test	No
10	5	GT7-29001 LC characterization	No
11	1	GT7-29001 PNLC polymerization test	No
12	4	PNLC RF characterization samples	No
13	6	PNLC optical characterization samples	No
14	2	PNLC reflectarray device (20 × 20 elem.)	Yes
15	14	DFLC samples (50 × 50 elem.)	Yes
16	5	Dual polarization reflectarray (55 × 55 elem.)	Yes
17	3	RIS panels (36 × 38 elem .)	Yes

Table 7.1: Outline of the most relevant manufactured cells during this thesis.

References

[1] Marco Di Renzo et al. “Smart Radio Environments Empowered by Reconfigurable Intelligent Surfaces: How It Works, State of Research, and The Road Ahead”. In: *IEEE Journal on Selected Areas in Communications* 38.11 (2020), pp. 2450–2525. DOI: `10.1109/JSAC.2020.3007211`.

[2] Oscar Quevedo-Teruel et al. “Roadmap on metasurfaces”. In: *Journal of Optics* 21 (July 2019), p. 073002. DOI: `10.1088/2040-8986/ab161d`.

[3] Borja Imaz-Lueje, Marcos R. Pino, and Manuel Arrebola. “Deployable Multi-Faceted Reflectarray Antenna in Offset Configuration With Band Enhancement”. In: *IEEE Transactions on Antennas and Propagation* 70.12 (2022), pp. 11686–11696. DOI: `10.1109/TAP.2022.3209753`.

[4] Yuanwei Liu et al. “Reconfigurable Intelligent Surfaces: Principles and Opportunities”. In: *IEEE Communications Surveys & Tutorials* 23.3 (2021), pp. 1546–1577. DOI: `10.1109/COMST.2021.3077737`.

[5] John Huang and Jose Antonio Encinar. *Reflectarray antennas*. John Wiley & Sons, 2007.

[6] M.E. Bialkowski and H.J. Song. “Dual linearly polarized reflectarray using aperture coupled microstrip patches”. In: *IEEE Antennas and Propagation Society International Symposium. 2001 Digest. Held in conjunction with: USNC/URSI National Radio Science Meeting (Cat. No.01CH37229)*. Vol. 3. 2001, 486–489 vol.3. DOI: `10.1109/APS.2001.960140`.

[7] J.A. Encinar. “Design of two-layer printed reflectarrays using patches of variable size”. In: *IEEE Transactions on Antennas and Propagation* 49.10 (2001), pp. 1403–1410. DOI: `10.1109/8.954929`.

[8] M. Bozzi, S. Germani, and L. Perregrini. “Performance comparison of different element shapes used in printed reflectarrays”. In: *IEEE Antennas and Wireless Propagation Letters* 2 (2003), pp. 219–222. DOI: `10.1109/LAWP.2003.819687`.

[9] Daniel Martinez-De-Rioja et al. “A Simple Beamforming Technique for Intelligent Reflecting Surfaces in 5G Scenarios”. In: *2022 International Workshop on Antenna Technology (iWAT)*. 2022, pp. 249–252. DOI: `10.1109/iWAT54881.2022.9811009`.

[10] Hirokazu Kamoda et al. “60-GHz Electronically Reconfigurable Large Reflectarray Using Single-Bit Phase Shifters”. In: *IEEE Transactions on Antennas and Propagation* 59.7 (2011), pp. 2524–2531. DOI: `10.1109/TAP.2011.2152338`.

[11] Shi-Guo Zhou et al. "A Wideband 1-Bit Reconfigurable Reflectarray Antenna at Ku-Band". In: *IEEE Antennas and Wireless Propagation Letters* 21.3 (2022), pp. 566–570. DOI: 10.1109/LAWP.2021.3138438.

[12] Jiaqi Han et al. "A Wideband 1 bit 12 × 12 Reconfigurable Beam-Scanning Reflectarray: Design, Fabrication, and Measurement". In: *IEEE Antennas and Wireless Propagation Letters* 18.6 (2019), pp. 1268–1272. DOI: 10.1109/LAWP.2019.2914399.

[13] Na Zhang et al. "A Dual-polarized Reconfigurable Reflectarray Antenna Based on Dual-channel Programmable Metasurface". In: *IEEE Transactions on Antennas and Propagation* (2022), pp. 1–1. DOI: 10.1109/TAP.2022.3165872.

[14] Elham Baladi et al. "Dual-Band Circularly Polarized Fully Reconfigurable Reflectarray Antenna for Satellite Applications in the Ku-Band". In: *IEEE Transactions on Antennas and Propagation* 69.12 (2021), pp. 8387–8396. DOI: 10.1109/TAP.2021.3090577.

[15] David Rotshild and A. Abramovich. "Realization and validation of continuous tunable metasurface for high resolution beam steering reflector at K-band frequency". In: *International Journal of RF and Microwave Computer-Aided Engineering* 31 (2021). DOI: 10.1002/mmce.22559.

[16] Hamid Moghadas et al. "Monolithic-Integrated MEMS-Tunable Reflective Cell for Ku-Band Mobile Satellite Two-Way Connectivity". In: *IEEE Transactions on Antennas and Propagation* 63.4 (2015), pp. 1384–1392. DOI: 10.1109/TAP.2015.2391275.

[17] Eduardo Carrasco et al. "Characterization of a Reflectarray Gathered Element With Electronic Control Using Ohmic RF MEMS and Patches Aperture-Coupled to a Delay Line". In: *IEEE Transactions on Antennas and Propagation* 60.9 (2012), pp. 4190–4201. DOI: 10.1109/TAP.2012.2207046.

[18] Tomislav Debogovic and Julien Perruisseau-Carrier. "Low Loss MEMS-Reconfigurable 1-Bit Reflectarray Cell With Dual-Linear Polarization". In: *IEEE Transactions on Antennas and Propagation* 62.10 (2014), pp. 5055–5060. DOI: 10.1109/TAP.2014.2344100.

[19] Lixue Lu et al. "A Mechanical Reconfigurable Reflectarray Based on Magnetic Force Tuning". In: *IEEE Antennas and Wireless Propagation Letters* 23.2 (2024), pp. 528–532. DOI: 10.1109/LAWP.2023.3329104.

[20] Xue Yang et al. "A Mechanically Reconfigurable Reflectarray With Slotted Patches of Tunable Height". In: *IEEE Antennas and Wireless Propagation Letters* 17.4 (2018), pp. 555–558. DOI: 10.1109/LAWP.2018.2802701.

[21] Eduardo Carrasco, Michele Tamagnone, and Julien Perruisseau-Carrier. "Tunable graphene reflective cells for THz reflectarrays and generalized law of reflection". In: *Applied Physics Letters* 102.10 (Mar. 2013), p. 104103. DOI: 10.1063/1.4795787.

[22] Liping Shi et al. "Accurate Characterization of Graphene Reconfigurable Reflectarray Antenna Element by SVR". In: *IEEE Journal on Multiscale and Multiphysics Computational Techniques* 6 (2021), pp. 50–55. DOI: 10.1109/JMMCT.2021.3062147.

[23] Robert R. Romanofsky. "Advances in Scanning Reflectarray Antennas Based on Ferroelectric Thin-Film Phase Shifters for Deep-Space Communications". In: *Proceedings of the IEEE* 95.10 (2007), pp. 1968–1975. DOI: 10.1109/JPROC.2007.905065.

[24] Kalyan K. Karnati, Michael E. Trampler, and Xun Gong. "A Monolithically BST-Integrated K_a -Band Beamsteerable Reflectarray Antenna". In: *IEEE Transactions on Antennas and Propagation* 65.1 (2017), pp. 159–166. DOI: 10.1109/TAP.2016.2627007.

[25] Randy Matos and Nezih Pala. “VO2-based ultra-reconfigurable intelligent reflective surface for 5G applications”. In: *Scientific Reports* 12 (2022). DOI: 10.1038/s41598-022-08458-9.

[26] J. A. Ramsey et al. “Low-loss vanadium dioxide-enabled mmWave tunable reflective electromagnetic surface with complementary unit cells for wave manipulation”. In: *Journal of Applied Physics* 135.21 (June 2024), p. 214901. DOI: 10.1063/5.0211712.

[27] Eduardo Carrasco et al. “Design of Microfluidic Reflectarray Elements for Multi-Reconfiguration Using Liquid Metal”. In: *IEEE Open Journal of Antennas and Propagation* 3 (2022), pp. 425–434. DOI: 10.1109/OJAP.2022.3166232.

[28] Kevin Xu and Jun H. Choi. “Liquid-Metal-Tuned Patch Element for Flexible and Reconfigurable Reflectarrays/Intelligent Surfaces”. In: *2021 IEEE International Symposium on Antennas and Propagation and USNC-URSI Radio Science Meeting (APS/URSI)*. 2021, pp. 79–80. DOI: 10.1109/APS/URSI47566.2021.9704431.

[29] Deng-Ke Yang and Shin-Tson Wu. “Fundamentals of Liquid Crystal Devices”. In: *Wiley Series in Display Technology, 2nd Ed.* (2014), pp. 1–570. DOI: 10.1002/9781118751992.

[30] P.G. de Gennes and J. Prost. *The Physics of Liquid Crystals*. International Series of Monographs on Physics. Clarendon Press, 1993.

[31] William C. O’Mara. *Liquid Crystal Flat Panel Displays: Manufacturing Science & Technology*. English. New York, 1993.

[32] Kristina M Johnson, Douglas J McKnight, and Ian Underwood. “Smart spatial light modulators using liquid crystals on silicon”. In: *IEEE Journal of Quantum Electronics* 29.2 (1993), pp. 699–714.

[33] Kun Yin et al. “Advanced liquid crystal devices for augmented reality and virtual reality displays: principles and applications”. In: *Light: Science & Applications* 11.1 (May 2022), p. 161. DOI: 10.1038/s41377-022-00851-3.

[34] W. Hu et al. “Tunable liquid crystal reflectarray patch element”. In: *Electronics Letters* 42.9 (2006). DOI: 10.1049/el:20060571.

[35] Alexander Moessinger et al. “Electronically reconfigurable reflectarrays with nematic liquid crystals”. In: *Electronics Letters* 42 (2006), pp. 899–900.

[36] Wenfei Hu et al. “Liquid-crystal-based reflectarray antenna with electronically switchable monopulse patterns”. In: *Electronics Letters* 43 (Feb. 2007). DOI: 10.1049/el:20071098.

[37] Wenfei Hu et al. “Design and Measurement of Reconfigurable Millimeter Wave Reflectarray Cells With Nematic Liquid Crystal”. In: *IEEE Transactions on Antennas and Propagation* 56.10 (2008), pp. 3112–3117. DOI: 10.1109/TAP.2008.929460.

[38] R. Marin et al. “77 GHz Reconfigurable Reflectarray with Nematic Liquid Crystal”. In: *The Second European Conference on Antennas and Propagation, EuCAP 2007*. 2007, pp. 1–5. DOI: 10.1049/ic.2007.0940.

[39] G. Perez-Palomino et al. “Design and evaluation of multi-resonant unit cells based on liquid crystals for reconfigurable reflectarrays”. In: *IET Microwaves, Antennas & Propagation* 6 (3 2012), pp. 348–354. DOI: 10.1049/iet-map.2011.0234.

[40] Gerardo Perez-Palomino et al. “Design and Experimental Validation of Liquid Crystal-Based Reconfigurable Reflectarray Elements With Improved Bandwidth in F-Band”. In: *IEEE Transactions on Antennas and Propagation* 61.4 (2013), pp. 1704–1713. DOI: 10.1109/TAP.2013.2242833.

[41] Gerardo Perez-Palomino et al. “Accurate and Efficient Modeling to Calculate the Voltage Dependence of Liquid Crystal-Based Reflectarray Cells”. In: *IEEE Transactions on Antennas and Propagation* 62.5 (2014), pp. 2659–2668. DOI: 10.1109/TAP.2014.2308521.

[42] Gerardo Perez-Palomino et al. “Design and Demonstration of an Electronically Scanned Reflectarray Antenna at 100 GHz Using Multiresonant Cells Based on Liquid Crystals”. In: *IEEE Transactions on Antennas and Propagation* 63.8 (2015), pp. 3722–3727. DOI: 10.1109/TAP.2015.2434421.

[43] Xiaoyu Li et al. “Broadband Electronically Scanned Reflectarray Antenna With Liquid Crystals”. In: *IEEE AWPL* 20.3 (2021), pp. 396–400. DOI: 10.1109/LAWP.2021.3051797.

[44] Dayan Pérez-Quintana et al. “Reconfigurable Millimeter-Wave Reflectarray Based on Low-Loss Liquid Crystals”. In: *IEEE Transactions on Antennas and Propagation* 72.1 (2024), pp. 531–541. DOI: 10.1109/TAP.2023.3329666.

[45] Hogyeom Kim, Jongyeong Kim, and Jungsuek Oh. “Liquid-Crystal-Based X-Band Reactively Loaded Reflectarray Unit Cell to Reduce Reflection Loss”. In: *IEEE Antennas and Wireless Propagation Letters* 20.10 (2021), pp. 1898–1902. DOI: 10.1109/LAWP.2021.3099818.

[46] Weiquan Zhang, Yue Li, and Zhijun Zhang. “A Reconfigurable Reflectarray Antenna With an 8 um-Thick Layer of Liquid Crystal”. In: *IEEE Transactions on Antennas and Propagation* 70.4 (2022), pp. 2770–2778. DOI: 10.1109/TAP.2021.3125378.

[47] Hogyeom Kim, Jongyeong Kim, and Jungsuek Oh. “Communication A Novel Systematic Design of High-Aperture-Efficiency 2D Beam-Scanning Liquid-Crystal Embedded Reflectarray Antenna for 6G FR3 and Radar Applications”. In: *IEEE Transactions on Antennas and Propagation* 70.11 (2022), pp. 11194–11198. DOI: 10.1109/TAP.2022.3209178.

[48] Peyman Aghabeyki et al. “A Dual-Polarized Reconfigurable Reflectarray with A Thin Liquid Crystal Layer and 2D Beam Scanning”. In: *IEEE Transactions on Antennas and Propagation* (2023), pp. 1–1. DOI: 10.1109/TAP.2023.3240853.

[49] Xiaotong Li et al. “Development of Two-Dimensional Steerable Reflectarray With Liquid Crystal for Reconfigurable Intelligent Surface Applications”. In: *IEEE Transactions on Antennas and Propagation* 72.3 (2024), pp. 2108–2123. DOI: 10.1109/TAP.2024.3354054.

[50] Hogyeom Kim et al. “Independently Polarization Manipulable Liquid- Crystal -Based Reflective Metasurface for 5G Reflectarray and Reconfigurable Intelligent Surface”. In: *IEEE Transactions on Antennas and Propagation* 71.8 (2023), pp. 6606–6616. DOI: 10.1109/TAP.2023.3283136.

[51] Rolf Jakoby, Alexander Gaebler, and Christian Weickhmann. “Microwave Liquid Crystal Enabling Technology for Electronically Steerable Antennas in SATCOM and 5G Millimeter-Wave Systems”. In: *Crystals* 10.6 (2020). DOI: 10.3390/cryst10060514.

[52] Robin Neuder et al. *Architecture for sub-100 ms Liquid Crystal Reconfigurable Intelligent Surface Based on Defected Delay Lines*. Sept. 2023. DOI: 10.21203/rs.3.rs-3296270/v1.

[53] Hogyeom Kim et al. “Low Voltage Controlled Fast Switchable Liquid Crystal-Based Reflectarray With Transverse Rubbing Layer”. In: *IEEE Antennas and Wireless Propagation Letters* (2024), pp. 1–4. DOI: 10.1109/LAWP.2024.3438367.

[54] Guangsheng Deng et al. “Design and experimental investigation of interdigitated electrode architecture for tunable liquid crystal-based metasurfaces with rapid responses”. In: *Infrared Physics & Technology* 133 (2023), p. 104768. DOI: https://doi.org/10.1016/j.infrared.2023.104768.

[55] G. Perez-Palomino, J. A. Encinar, and M. Barba. “Method for accurately solving the scattering in planar reflectarrays under an arbitrary excitation”. In: *2012 6th European Conference on Antennas and Propagation (EUCAP)*. 2012, pp. 1081–1085. DOI: 10.1109/EuCAP.2012.6206445.

[56] *Merck KGaA*. [Online] www.merckgroup.com. Accessed: 2024-9-17.

[57] Henning Tesmer et al. “Temperature Characterization of Liquid Crystal Dielectric Image Line Phase Shifter for Millimeter-Wave Applications”. In: *Crystals* 11.1 (2021). DOI: 10.3390/cryst11010063.

[58] *CST Studio*. [Online] www.cst.com. Accessed: 2024-9-11.

[59] R. Dickie et al. “Electrical characterisation of liquid crystals at millimetre wavelengths using frequency selective surfaces”. In: *Electronics Letters* 48 (11 May 2012), 611–612(1).

[60] Jinfeng Li. “Rethinking Figure-of-Merits of Liquid Crystals Shielded Coplanar Waveguide Phase Shifters at 60 GHz”. In: *J* 4.3 (2021), pp. 444–451. DOI: 10.3390/j4030034.

[61] Dimitrios C. Zografopoulos, Antonio Ferraro, and Romeo Beccherelli. “Liquid-Crystal High-Frequency Microwave Technology: Materials and Characterization”. In: *Advanced Materials Technologies* 4.2 (2019), p. 1800447. DOI: 10.1002/admt.201800447.

[62] Carsten Fritzsch et al. “77-1: Invited Paper: Liquid Crystals beyond Displays: Smart Antennas and Digital Optics”. In: *SID Symposium Digest of Technical Papers* 50 (June 2019), pp. 1098–1101. DOI: 10.1002/sdtp.13120.

[63] Sebastian Strunck et al. “Reliability study of a tunable Ka-band SIW-phase shifter based on liquid crystal in LTCC-technology”. In: *International Journal of Microwave and Wireless Technologies* 7 (July 2014), pp. 1–7. DOI: 10.1017/S175907871400083X.

[64] Ersin Polat et al. “Reconfigurable Millimeter-Wave Components Based on Liquid Crystal Technology for Smart Applications”. In: *Crystals* 10.5 (2020). DOI: 10.3390/cryst10050346.

[65] S. Christie et al. “Electronically scanned Rotman lens antenna with liquid crystal phase shifters”. In: *Electronics Letters* 49.7 (2013), pp. 445–447. DOI: https://doi.org/10.1049/el.2013.0020.

[66] Sandra Costanzo et al. “Dual-Band Dual-Linear Polarization Reflectarray for mmWaves/5G Applications”. In: *IEEE Access* 8 (2020), pp. 78183–78192. DOI: 10.1109/ACCESS.2020.2989581.

[67] Eduardo Martinez-de-Rioja et al. “Dual Polarized Reflectarray Transmit Antenna for Operation in Ku- and Ka-Bands With Independent Feeds”. In: *IEEE Transactions on Antennas and Propagation* 65.6 (2017), pp. 3241–3246. DOI: 10.1109/TAP.2017.2689059.

[68] Julien Perruisseau-Carrier. “Dual-Polarized and Polarization-Flexible Reflective Cells With Dynamic Phase Control”. In: *IEEE Transactions on Antennas and Propagation* 58.5 (2010), pp. 1494–1502. DOI: 10.1109/TAP.2010.2044333.

[69] Pei-Shen Wei et al. “Miniaturized Dual-Band FSS Suitable for Curved Surface Application”. In: *IEEE Antennas and Wireless Propagation Letters* 19.12 (2020), pp. 2265–2269. DOI: 10.1109/LAWP.2020.3029820.

[70] José R. Montejo-Garai et al. “Band-Stop Frequency-Selective Surface (FSS) with Elliptic Response Designed by the Extracted Pole Technique”. In: *Sensors* 24.14 (2024). DOI: 10.3390/s24144452.

[71] E. Doumanis et al. “Electronically Reconfigurable Liquid Crystal Based Mm-Wave Polarization Converter”. In: *IEEE Transactions on Antennas and Propagation* 62.4 (2014), pp. 2302–2307. DOI: 10.1109/TAP.2014.2302844.

[72] Hiromi Matsuno et al. “Development of a Dual-Polarized Direction-Variable Liquid-Crystal Meta-Surface Reflector for Intelligent Reflecting Surface”. In: *IEEE Access* 11 (2023), pp. 95757–95767. DOI: 10.1109/ACCESS.2023.3276231.

[73] Peyman Aghabeyki and Shuai Zhang. “A Wideband Reflectarray with Reconfigurable Polarization and Beam-Scanning by using Liquid Crystal Delay Line for Millimeter-wave”. In: *2024 18th European Conference on Antennas and Propagation (EuCAP)*. 2024, pp. 1–5. DOI: 10.23919/EuCAP60739.2024.10501301.

[74] Byeongju Moon et al. “Simultaneously Dual-Polarization Convertible Sub- THz Reconfigurable Intelligent Surface Enabled by Through-Quartz VIAs”. In: *2024 18th European Conference on Antennas and Propagation (EuCAP)*. 2024, pp. 1–5. DOI: 10.23919/EuCAP60739.2024.10501659.

[75] Rafael Florencio et al. “Cross-polar reduction in reflectarray antennas by means of element rotation”. In: *2016 10th European Conference on Antennas and Propagation (EuCAP)*. 2016, pp. 1–5. DOI: 10.1109/EuCAP.2016.7481103.

[76] Fernando Conde-Pumpido et al. “Generalized Bimode Equivalent Circuit of Arbitrary Planar Periodic Structures for Oblique Incidence”. In: *IEEE Transactions on Antennas and Propagation* 70.10 (2022), pp. 9435–9448. DOI: 10.1109/TAP.2022.3184518.

[77] Gerardo Perez-Palomino et al. “A Design Technique Based on Equivalent Circuit and Coupler Theory for Broadband Linear to Circular Polarization Converters in Reflection or Transmission Mode”. In: *IEEE Transactions on Antennas and Propagation* 66.5 (2018), pp. 2428–2438. DOI: 10.1109/TAP.2018.2809664.

[78] *COMSOL Multiphysics*. [Online] www.comsol.com. Accessed: 2024-9-11.

[79] *TICRA GRASP*. [Online] www.ticra.com/software/grasp/. Accessed: 2024-10-14.

[80] Manuel Caño-Garcia et al. “Dynamic multilevel spiral phase plate generator”. In: *Scientific Reports* 8 (Oct. 2018). DOI: 10.1038/s41598-018-34041-2.

[81] Mario García de Blas. “Tunable Diffractive Liquid Crystal Photonic Devices”. PhD Thesis. 2022.

[82] Kalyan K. Karnati et al. “Theoretical Analysis on Reflection Properties of Reflectarray Unit Cells Using Quality Factors”. In: *IEEE Transactions on Antennas and Propagation* 61.1 (2013), pp. 201–210. DOI: 10.1109/TAP.2012.2214753.

[83] J. L. Ericksen. “Conservation Laws for Liquid Crystals”. In: *Transactions of the Society of Rheology* 5.1 (1961), pp. 23–34. DOI: 10.1122/1.548883.

[84] Frank M. Leslie. “Some constitutive equations for liquid crystals”. In: *Archive for Rational Mechanics and Analysis* 28 (1968), pp. 265–283.

[85] S. Chandrasekhar and Morton D Hull. *Liquid Crystals*. Cambridge monographs on physics. Cambridge University Press, 1992.

[86] Haiying Wang et al. “Method to estimate the Leslie coefficients of liquid crystals based on MBBA data”. In: *Liquid Crystals* 33 (Jan. 2006), pp. 91–98. DOI: `10.1080/02678290500446111`.

[87] Shin-Tson Wu and Chiung-Sheng Wu. “Small angle relaxation of highly deformed nematic liquid crystals”. In: *Appl. Physics Letters* 53.19 (1988). DOI: `10.1063/1.99783`.

[88] Xiangyi Nie et al. “Pretilt Angle Effects on Liquid Crystal Response Time”. In: *J. Display Technol.* 3.3 (Sept. 2007), pp. 280–283.

[89] Haiying Wang et al. “Correlations between liquid crystal director reorientation and optical response time of a homeotropic cell”. In: *Journal of Applied Physics* 95.10 (2004), pp. 5502–5508. DOI: `10.1063/1.1707210`.

[90] Dongwei Wang et al. “Fast and Miniaturized Phase Shifter With Excellent Figure of Merit Based on Liquid Crystal and Nanowire-Filled Membrane Technologies”. In: *IEEE Journal of Microwaves* 2.1 (2022), pp. 174–184. DOI: `10.1109/JMW.2021.3131648`.

[91] Huanhuan Yang et al. “A Study of Phase Quantization Effects for Reconfigurable Reflectarray Antennas”. In: *IEEE AWPL* 16 (2017), pp. 302–305. DOI: `10.1109/LAWP.2016.2574118`.

[92] H. Okumura and H. Fujiwara. “A new low-image-lag drive method for large-size LCTVs”. In: *Journal of the Society for Information Display* 1.3 (1993), pp. 335–339. DOI: `10.1889/1.1984882`.

[93] Shin-Tson Wu and Chiung-Sheng Wu. “High-speed liquid-crystal modulators using transient nematic effect”. In: *J. Appl. Phys.* 65.2 (1989), pp. 527–532. DOI: `10.1063/1.343135`.

[94] M. Grinfeld, M. Langer, and N.J. Mottram. “Nematic viscosity estimation using director kickback dynamics”. In: *Liquid Crystals* 38.8 (2011), pp. 981–987. DOI: `10.1080/02678292.2011.588969`.

[95] Dwight W. Berreman. “Liquid-crystal twist cell dynamics with backflow”. In: *Journal of Applied Physics* 46.9 (1975), pp. 3746–3751. DOI: `10.1063/1.322159`.

[96] Ya-Di Zhang et al. “Backflow Effect Enabling Fast Response and Low Driving Voltage of Electrophoretic E-ink Dispersion by Liquid Crystal Additives”. In: *Scientific Reports* 9 (Sept. 2019). DOI: `10.1038/s41598-019-50382-y`.

[97] Jie Sun, Shin-Tson Wu, and Yasuhiro Haseba. “A low voltage submillisecond-response polymer network liquid crystal spatial light modulator”. In: *Applied Physics Letters* 104.2 (2014). DOI: `10.1063/1.4862474`.

[98] Jie Sun and Shin-Tson Wu. “Recent advances in polymer network liquid crystal spatial light modulators”. In: *Journal of Polymer Science Part B: Polymer Physics* 52.3 (2014), pp. 183–192. DOI: `https://doi.org/10.1002/polb.23391`.

[99] Yun-Hsing Fan et al. “Fast-response and scattering-free polymer network liquid crystals for infrared light modulators”. In: *Applied Physics Letters* 84.8 (2004), pp. 1233–1235. DOI: `10.1063/1.1649816`.

[100] Gordon D. Love, Andrew K. Kirby, and Robert A. Ramsey. "Sub-millisecond, high stroke phase modulation using polymer network liquid crystals". In: *Opt. Express* 18.7 (Mar. 2010), pp. 7384–7389. DOI: 10.1364/OE.18.007384.

[101] John L. West et al. "Fast birefringent mode stressed liquid crystal". In: *Applied Physics Letters* 86.3 (2005). DOI: 10.1063/1.1852720.

[102] Zhiping Yin et al. "Fast-Tunable Terahertz Metamaterial Absorber Based on Polymer Network Liquid Crystal". In: *Appl. Sciences* 8.12 (2018). DOI: 10.3390/app8122454.

[103] Fenglin Peng et al. "Fast-response infrared phase modulator based on polymer network liquid crystal". In: *Opt. Mater. Express* 5.2 (Feb. 2015), pp. 265–273. DOI: 10.1364/OME.5.000265.

[104] Hideo Fujikake et al. "Thick polymer-stabilized liquid crystal films for microwave phase control". In: *Journal of Appl. Physics* 89.10 (2001), pp. 5295–5298. DOI: 10.1063/1.1365081.

[105] Thanh Nguyen et al. "Improvement of decay time in nematic-liquid-crystal-loaded coplanar-waveguide-type microwave phase shifter by polymer stabilizing method". In: *Japanese Journal of Applied Physics* 53 (Jan. 2014). DOI: 10.7567/JJAP.53.01AE08.

[106] Deng-Ke Yang et al. "Modeling aligning effect of polymer network in polymer stabilized nematic liquid crystals". In: *Journal of Appl. Physics* 114.24 (2013), p. 243515. DOI: 10.1063/1.4856295.

[107] Hogyeom Kim et al. "Waveguide-Thru Closed-Form Characterization of Anisotropic Polymer Network Liquid-Crystal for mmWave Reconfigurable RF Devices". In: *IEEE Transactions on Antennas and Propagation* 72.7 (2024), pp. 5447–5457. DOI: 10.1109/TAP.2024.3403939.

[108] Carlos Carrasco Vela. *Diseño y fabricación de dispositivos basados en cristal líquido polimérico (Spanish)*. pp. 198. PhD thesis, 2012.

[109] P. A. Sakhare and Jayasri Dontabhaktuni. "Ultra Fast Switching of DFLC Based Dynamic Metasurfaces". In: *Frontiers in Physics* 10 (2022). DOI: 10.3389/fphy.2022.849470.

[110] Xiao Liang et al. "Dual-Frequency Addressed Variable Optical Attenuator with Sub-millisecond Response Time". In: *Japanese Journal of Applied Physics* 44.3R (Mar. 2005), p. 1292. DOI: 10.1143/JJAP.44.1292.

[111] Haiqing Xianyu, Shin-Tson Wu, and Chih-Lung Lin. "Dual frequency liquid crystals: a review". In: *Liquid Crystals* 36.6-7 (2009), pp. 717–726. DOI: 10.1080/02678290902755598.

[112] Olha Melnyk et al. "Electro-Optical Switching of Dual-Frequency Nematic Liquid Crystals: Regimes of Thin and Thick Cells". In: *Crystals* 9.6 (2019). DOI: 10.3390/cryst9060314.

[113] Y. W. Li and H. S. Kwok. "Bistable twisted-bend and twisted-nematic liquid crystal display". In: *Applied Physics Letters* 95.18 (2009), p. 181107. DOI: 10.1063/1.3254212.

[114] Bing-Xiang Li et al. "Dye-doped dual-frequency nematic cells as fast-switching polarization-independent shutters". In: *Opt. Express* 27.4 (Feb. 2019), pp. 3861–3866. DOI: 10.1364/OE.27.003861.

[115] Thorsten Gobel et al. "Dual-frequency switching Liquid Crystal based tunable THz Filter". In: *2009 Conference on Lasers and Electro-Optics and 2009 Conference on*

Quantum electronics and Laser Science Conference. 2009, pp. 1–2. DOI: 10.1364/CLEO.2009.CThFF4.

[116] Stefan Mueller et al. “Passive Phase Shifter for W-Band Applications using Liquid Crystals”. In: *2006 European Microwave Conference*. 2006, pp. 306–309. DOI: 10.1109/EUMC.2006.281317.

[117] Jason E Nobles et al. “Eight-element liquid crystal based 32 GHz phased array antenna with improved time response”. In: *Engineering Research Express* 3.4 (Nov. 2021), p. 045033. DOI: 10.1088/2631-8695/ac3848.

[118] Guangsheng Deng et al. “Liquid crystal-based wide-angle metasurface absorber with large frequency tunability and low voltage”. In: *Opt. Express* 30.13 (June 2022), pp. 22550–22561. DOI: 10.1364/OE.462307.

[119] Alejandro Jiménez-Sáez et al. “Liquid Crystals: The way to Scalable and Practical Reconfigurable Intelligent Surfaces in 6G”. In: *TechRxiv* (Oct. 2022). DOI: 10.36227/techrxiv.21335733.v1.

[120] Robert Guirado et al. “Characterization and Application of Dual-Frequency Liquid-Crystal Mixtures in mm-Wave Reflectarray Cells to Improve Their Temporal Response”. In: *IEEE Transactions on Antennas and Propagation* 71.8 (2023), pp. 6535–6545. DOI: 10.1109/TAP.2023.3281076.

[121] Haiqing Xianyu et al. “High performance dual frequency liquid crystal compounds and mixture for operation at elevated temperature”. In: *Liquid Crystals* 37 (Dec. 2010), pp. 1493–1499. DOI: 10.1080/02678292.2010.528803.

[122] *Military University of Technology*. [Online] www.wojsko-polskie.pl. Accessed: 2023-1-10.

[123] *HCCH*. [Online] www.hcch.net.cn. Accessed: 2023-1-10.

[124] Bartłomiej Klus et al. “All-optical measurement of elastic constants in nematic liquid crystals”. In: *Opt. Express* 22.24 (Dec. 2014), pp. 30257–30266. DOI: 10.1364/OE.22.030257.

[125] Gexing Kong et al. “Design of an Electronically Beam-Scanned High-Power Capacity Reflectarray Antenna Based on Liquid Crystals for Airborne Radar Application”. In: *Proceedings of the 10th Chinese Society of Aeronautics and Astronautics Youth Forum*. 2023.

[126] Keiji Yoshikawa, Takuya Ohto, and Takahiro Hayashi. “User and Passive Beam Scheduling Scheme for Liquid Crystal IRS-assisted mmWave Communications”. In: *18th European Conference on Antennas and Propagation (EuCAP)*. 2024. DOI: 10.23919/EuCAP60739.2024.10501342.

[127] T.N. Ruckmongathan. *Addressing Techniques of Liquid Crystal Displays*. Wiley Series in Display Technology. Wiley, 2014.

[128] Ilias Pappas, Stylianos Siskos, and Charalambos A. Dimitriadis. “Active-Matrix Liquid Crystal Displays - Operation, Electronics and Analog Circuits Design”. In: *New Developments in Liquid Crystals*. IntechOpen, 2009. Chap. 8. DOI: 10.5772/9686.

[129] Patricia Fratilescu et al. “W-Band Confocal Antenna System Based on Liquid Crystal Reflectarray for Beam Scanning Applications”. In: *2021 15th European Conference on Antennas and Propagation (EuCAP)*. 2021, pp. 1–5. DOI: 10.23919/EuCAP51087.2021.9410896.

[130] W. den Boer. *Active Matrix Liquid Crystal Displays: Fundamentals and Applications*. Elsevier Science, 2011.

[131] Dr Cristaldi, Salvatore Pennisi, and Francesco Pulvirenti. *Liquid Crystal Display Drivers*. Springer, 2009. DOI: 10.1007/978-90-481-2255-4.

[132] Alejandro Jiménez-Sáez et al. *Reconfigurable Intelligent Surfaces with Liquid Crystal Technology: A Hardware Design and Communication Perspective*. Aug. 2023. DOI: 10.48550/arXiv.2308.03065.

[133] Jinfeng Li. "From liquid crystal on silicon and liquid crystal reflectarray to reconfigurable intelligent surfaces for post-5G networks". In: *Applied Sciences* 13.13 (2023), p. 7407.

[134] Jingbo Wu et al. "Liquid crystal programmable metasurface for terahertz beam steering". In: *Applied Physics Letters* 116.13 (Mar. 2020), p. 131104. DOI: 10.1063/1.5144858.

[135] Eduardo Martinez-de-Rioja et al. "Dual-Band Electromagnetic Skin With Independent Reflection Performance at 28 GHz and 39 GHz for 5G Millimeter-Wave Communications". In: *IEEE Antennas and Wireless Propagation Letters* 23.10 (2024), pp. 3138–3142. DOI: 10.1109/LAWP.2024.3427772.

[136] Stefano Maci. "Reflective Intelligent Surfaces and metasurface antennas". In: *2023 IEEE Radio and Antenna Days of the Indian Ocean (RADIO)*. 2023, pp. 1–1. DOI: 10.1109/RADIO58424.2023.10146076.

[137] Marco Di Renzo et al. "Smart radio environments empowered by reconfigurable AI meta-surfaces: an idea whose time has come". In: *EURASIP Journal on Wireless Communications and Networking* 2019 (May 2019). DOI: 10.1186/s13638-019-1438-9.

[138] Álvaro F. Vaquero et al. "Smart Electromagnetic Skin to Enhance Near-Field Coverage in mm-Wave 5G Indoor Scenarios". In: *IEEE Transactions on Antennas and Propagation* 72.5 (2024), pp. 4311–4326. DOI: 10.1109/TAP.2024.3383216.

[139] Ze Shen et al. "A liquid crystal-based multi-bit terahertz reconfigurable intelligent surface". In: *APL Photonics* 9.1 (Jan. 2024), p. 016109. DOI: 10.1063/5.0176272.

[140] Youngno Youn et al. "Liquid-Crystal-Driven Reconfigurable Intelligent Surface With Cognitive Sensors for Self-Sustainable Operation". In: *IEEE Transactions on Antennas and Propagation* 71.12 (2023), pp. 9415–9423. DOI: 10.1109/TAP.2023.3312814.

[141] Yue Cui et al. "A Low-Cost Structure for Reducing Reflection Loss in Intelligent Reflecting Surface of Liquid Crystal". In: *IEEE Antennas and Wireless Propagation Letters* 22.12 (2023), pp. 3027–3031. DOI: 10.1109/LAWP.2023.3309304.

[142] Lu Xu et al. "Fully Electrically Driven Liquid Crystal Reconfigurable Intelligent Surface for Terahertz Beam Steering". In: *IEEE Transactions on Terahertz Science and Technology* 14.5 (2024), pp. 708–717. DOI: 10.1109/TTHZ.2024.3435506.

[143] Jaehoon Kim et al. "Asymmetrically Layered Unit Cell Topology to Reduce Cell Gap of Liquid Crystals for 5G Millimeter-Wave Transmissive Reconfigurable Intelligent Surface Applications". In: *IEEE Transactions on Antennas and Propagation* 72.3 (2024), pp. 2950–2955. DOI: 10.1109/TAP.2023.3338863.

[144] 3GPP. *3rd Generation Partnership Project; Technical Specification; Physical Layer Procedures for Control*. Tech. rep. 3GPP-ETSI TS 38.213 (version 16). 2020.